Creation of Erbium-Dysprosium Dipolar Quantum Mixtures and Their Interspecies Feshbach Resonances

DISSERTATION

by

Gianmaria Durastante, M.Sc., B.Sc.

submitted to the Faculty of Mathematics, Computer Science, and Physics of the University of Innsbruck, in partial fulfillment of the requirements for the degree of Doctor of Philosophy (PhD)

Advisors:

Univ.-Prof. Dr. Francesca Ferlaino,
Institute for Experimental Physics, University of Innsbruck
Institute for Quantum Optics and Quantum Information of the Austrian Academy of Sciences

Univ.-Prof. Mag. Dr. Paul Scheier,
Institute of Ion Physics and Applied Physics, University of Innsbruck

Innsbruck, 31 August 2020

Creation of Erbium-Dysprosium Dipolar Quantum Mixtures and Their Interspecies Feshbach Resonances

Gianmaria Durastante

So remember to look up at the stars and not down at your feet. Try to make sense of what you see and wonder about what makes the universe exist. Be curious. And however difficult life may seem, there is always something you can do and succeed at. It matters that you don't just give up. Unleash your imagination. Shape the future.

Stephen Hawking

Dedicated to my family.

Abstract

Ultracold quantum gases are a powerful platform for research in the field of quantum simulation as well as few- and many-body physics. They provide the possibility to precisely control a wide range of parameters, ensuring the realization of simplified versions of more complex systems typical of condensed matter, high-energy, and nuclear physics. Among the great experimental control, they allow for an accurate tuning of the interparticle contact interactions by means of Feshbach resonances. Since the creation of the first Bose-Einstein condensate, great progress has been made moving from single-component alkali experiments to multi-component ones. More recently, aiming to further the complexity and extending the possibilities of such systems, elements with permanent large magnetic dipole moments (chromium, dysprosium, and erbium overall) arouse interest due to the long-range and anisotropic character of the dipole-dipole interactions, paving the way towards the realization of novel scenarios.

In this panorama, on the basis of the knowledge achieved on the topic, a further step led our group to the world-first realization of a dipolar quantum gas mixture experiment combining erbium and dysprosium atoms — two highly magnetic lanthanides. After a designing and building phase with a duration of about three years, we are now able to compete at the forefront of the research in the field of ultracold atoms. The initial part of this manuscript briefly summarizes the development of such state-of-the-art experiment from the review of erbium and dysprosium properties, to the design of the experimental apparatus, to the achievement of quantum degeneracy in the two-components sample.

As the main topic of discussion, this thesis reports on the observation of heteronuclear magnetic Feshbach resonances in dipolar ultracold mixtures of erbium and dysprosium atoms. We investigated several isotopic combinations including Bose-Bose, Bose-Fermi, and Fermi-Fermi mixtures. Our research provides accessible experimental tools to control interactions in dipolar quantum gases of erbium-dysprosium and it will help to understand fundamental properties of the system such as the scattering dynamics. Furthermore, this work discloses new possibilities for the investigation of dipolar polarons, miscibility/imiscibility phase diagram, vortex formation, and binary magnetic quantum droplets. Eventually, it will be possible to transfer this knowledge into the creation of erbium-dysprosium Feshbach molecules via magnetoassociation with both electric and magnetic dipole moments.

Contents

Abstract i

1 Introduction 1
- 1.1 Motivation . . . 1
- 1.2 Thesis overview . . . 2
  - 1.2.1 List of publications . . . 3
  - 1.2.2 Additional publications . . . 4

2 Ultracold erbium-dysprosium atoms 5
- 2.1 Erbium and dysprosium properties . . . 6
  - 2.1.1 Physical properties . . . 6
  - 2.1.2 Energy levels and atomic polarizabilities . . . 7
- 2.2 Experimental setup . . . 10
  - 2.2.1 General description of the apparatus . . . 11
  - 2.2.2 Magnetic-field calibration . . . 13
  - 2.2.3 Magnetic field system . . . 13
- 2.3 Publication: Two-species five-beam magneto-optical trap for erbium and dysprosium . . . 23

3 Quantum mixtures 31
- 3.1 Theory of quantum mixture . . . 31
  - 3.1.1 Contact and dipolar interactions . . . 32
  - 3.1.2 Mean-field description and Gross-Pitaevskii equation . . . 33
  - 3.1.3 Solutions to the Gross-Pitaevskii equation . . . 34
- 3.2 Mixture experiments overview . . . 36
  - 3.2.1 Alkali-alkali mixtures . . . 37
  - 3.2.2 Alkali-nonalkali mixtures . . . 38
  - 3.2.3 Erbium-dysprosium mixture . . . 39
- 3.3 Publication: Dipolar Quantum Mixtures of Erbium and Dysprosium Atoms . 41

4 Feshbach resonances 49
- 4.1 Theory of Feshbach resonances . . . 50
  - 4.1.1 Ultracold collision . . . 50
  - 4.1.2 Open- and closed-channel picture . . . 51
  - 4.1.3 Resonance strength . . . 52
  - 4.1.4 Hamiltonian . . . 53
- 4.2 Experimental aspects . . . 54
  - 4.2.1 Inelastic collisions and trap-loss spectroscopy . . . 55
  - 4.2.2 Alkali . . . 55
  - 4.2.3 Mixtures and complex systems . . . 56

4.3 Feshbach resonances in lanthanides . . . 56
4.3.1 Role of anisotropy . . . 56
4.3.2 Experimental observations . . . 57
4.4 Publication: Feshbach Resonances in an Erbium-Dysprosium Dipolar Mixture 59
4.5 Additional measurements . . . 73
4.5.1 Feshbach resonance at 34 G in ^{166}Er-^{164}Dy . . . 73
4.5.2 Additional measurements on the feature at 161 G in ^{161}Dy . . . 73

5 Conclusion and outlook **77**
5.1 Conclusion . . . 77
5.2 Further studies . . . 78

A Additional publications **79**
A.1 Publication: Long-Lived and Transient Supersolid Behaviors in Dipolar Quantum Gases . . . 81
A.2 Publication: Phase coherence in out-of-equilibrium supersolid states of ultracold dipolar atoms . . . 103

B Extensive Feshbach scans **117**

C Coil systems' cooling **125**

Bibliography **129**

Acknowledgments **145**

List of Figures

2.1 Energy level diagrams . . . 8
2.2 Atomic polarizabilities . . . 10
2.3 Vacuum system . . . 11
2.4 Coils setup . . . 15
2.5 Small-field coils numerical calculation . . . 18
2.6 Small-field bias coils characterization . . . 19
2.7 Large-field coils numerical calculation . . . 20
2.8 Compensation coils numerical calculation . . . 22
3.1 Dipole-dipole interactions in polarized dipoles . . . 32
4.1 Feshbach resonance two channels model . . . 52
4.2 Numerically calculated Feshbach spectrum for ^{164}Dy . . . 57
4.3 Feshbach resonance at 34 G in ^{166}Er-^{164}Dy . . . 74
4.4 Temperature dependence of the 161 G Feshbach resonance . . . 75
4.5 Er/Dy ratio dependence of the 161 G Feshbach resonance . . . 76
B.1 Extensive scan for ^{166}Er-^{164}Dy . . . 118
B.2 Extensive scan for ^{168}Er-^{164}Dy . . . 119
B.3 Extensive scan for ^{170}Er-^{164}Dy . . . 120
B.4 Extensive scan for ^{166}Er-^{161}Dy . . . 121
B.5 Extensive scan for ^{167}Er-^{161}Dy . . . 122
B.6 Extensive scan for ^{168}Er-^{161}Dy . . . 123
B.7 Extensive scan for ^{170}Er-^{161}Dy . . . 124
C.1 Large-field coils temperature . . . 126
C.2 Small-field coils temperature . . . 127

List of Tables

2.1 Atomic properties of erbium and dysprosium . . . 6
2.2 Employed optical transitions . . . 9
2.3 Coils technical description . . . 14
3.1 Dipolar lengths comparison . . . 37

Chapter 1

Introduction

1.1 Motivation

From its very beginning [Pla06], quantum physics has transformed our view of the world and provided us with a deeper understanding along with even more challenging questions. As a matter of fact, natural phenomena might be too complicated to be described analytically or they happen on a scale too small or fast to be directly observable. High-temperature superconductivity, quark-gluon plasma, or quantum behavior of electrons in semiconductors are typical examples of such challenges. In extreme cases, some systems are not accessible at all on Earth, like neutron stars and white dwarfs. More generally, quantum many-body systems are highly non-trivial and their numerical simulation gets exponentially demanding with the increase in the number of particles involved [Gar14]. Beyond a few involved particles, exact calculations including all correlations are challenging, getting eventually impossible even with supercomputers for a few tens of particles. Complications may arise also in the other direction, when trying to validate a theory or a model. In strongly correlated or interacting many-body systems, exact theoretical descriptions break down, and experiments need to benchmark the limits and the approximations of such a model.

Scientists have searched for a solution to these issues for long time and one possibility is to follow a bottom-up approach. That is, building a simpler system in which the fundamental laws are identical to the one governing such complex systems. In the case of quantum physics, these model systems are known as *quantum simulators* [Fey82]. In this panorama, *ultracold atoms* have proven to be an excellent platform to investigate nature [Blo12, Tö14]. Their strength lies in the extreme precision to which all the different external and internal degrees of freedom can be controlled. Particularly important is the possibility to accurately tune interparticle interactions, e. g. by means of Feshbach resonances, exploiting non-interacting as well as strongly interacting regimes [Chi10].

The field of ultracold gases began along with the investigation of simple systems featuring purely short-range contact interactions, that is alkali-metal atoms. The major achievement of those years has been the attainment of quantum degeneracy in bosonic [And95, Dav95] and fermionic [DeM99] samples, 70 years after the prediction of such a novel state of matter [Bos24, Ein24]. After the success set by this milestone, the field has seen remarkable technological progresses covering several fields of fundamental research and precision measurement as well [Cor02, Kuh16, Pez18]. Nevertheless, scientists have tried to push back the

limits and delve further into the physics accessible with ultracold atoms. In this direction, new intriguing scenarios — always dominated by contact interactions — have been introduced by using heteronuclear mixtures [Had02, Mod02] or more complex elements, e. g. ytterbium and strontium [Tak03, Ste09].

More recently, in the spirit of integrating new types of interactions into quantum simulators, the interest has moved to *dipole-dipole interactions* (DDI) displaying long-range and anisotropic characters. Systems characterized by such DDI are: magnetic atoms, ground-state heteronuclear molecules, and Rydberg atoms, in order of dipolar strength [Lah09, Car09, Saf10]. In this thesis, we are interested in the peculiar case of magnetic atoms for the immediate access to the dipolar regime they offer thanks to their permanent magnetic dipole moment, avoiding complicated experimental procedures for molecule formations or Rydberg excitation.

In the advent of dipolar quantum gases, bosonic chromium has been the first magnetic species in which quantum degeneracy was attained [Gri05]. A number of different pioneering experiments demonstrated the importance of dipolar interactions in such a system, including demagnetization cooling, its stability diagram, and d-wave collapse [Lah09]. Nevertheless, the turning point was reached with the realization of degenerate quantum gases of highly magnetic species such as dysprosium and erbium [Lu11a, Lu12, Aik12, Aik14b]. The strong dipolarity together with their intrinsic complexity have led to a vast amount of observations proving the potentialities of such systems. Among these we mention the observation of Feshbach resonances and quantum chaos [Bau14, Mai15b], Fermi surface deformation [Aik14a] and extended Bose-Hubbard models [Bai16], roton excitation [Cho18], the discovery of quantum droplets [FB16, Cho16] and supersolid states of matter [BÏ9, Tan19, Cho19].

To combine the manipulation schemes available with lanthanides together with the additional complexity of heteronuclear mixtures, our group worked towards the realization of the world-first dipolar quantum gas mixture experiment combining erbium and dysprosium atoms. Only recently the interest in such binary dipolar systems aroused notable attention thanks to the striking prospects they offer. Phenomena arising from the complex parameter landscape of heteronuclear dipolar mixture which have been already theoretically investigated include the miscibility of two-components BECs [Kum17a], vortices and vortex lattices formation [Kum17b, Mar17], binary magnetic quantum droplets [Smi20], and dipolar polarons [PA18, Wen18].

1.2 Thesis overview

This thesis reviews the first experimental realization of dipolar quantum gases of erbium-dysprosium isotopic mixtures with tunable interaction. The line followed by this work is given by the chronological development of the experiment: from the realization of a dual-species intercombination-line magneto-optical trap in a novel open-top configuration, to the achievement of quantum degeneracy in several isotopic combinations, to conclude with the observation of interspecies Feshbach resonances in highly dipolar erbium-dysprosium mixtures. The work carried out until the achievement of quantum degeneracy is also included in the thesis of Philipp Ilzhöfer [Ilz20].

Personally, I joined the group in the late 2015 when the design and planning of the experiment were coming to an end but at the very beginning of the building process (two empty optical tables were the only components already set up). It took about three years to move from an empty room to a fully operational quantum gas experiment competing at the forefront of the research in the field.

This thesis resulted in three scientific publications setting the main discussion of the manuscript. Two additional publications on the topic of supersolidity in dipolar quantum gases — in which I contributed but not part of the main discussion of this manuscript — are included at the end of the thesis. As a general overview, this manuscript is structured as follows:

Chapter 2 summarizes the knowledge and the relevant properties of erbium and dysprosium atoms and gives details on the experimental setup. Particular attention is drawn to the magnetic field generation and control. It further describes the production of an erbium-dysprosium cold thermal cloud as part of our first publication [Ilz18].

Chapter 3 reviews the state-of-the-art knowledge in the research topic of quantum mixtures from a theoretical as well as an experimental point of view. The chapter reports the production of different heteronuclear dipolar BECs of several isotopic mixtures of erbium and dysprosium as part of our second publication [Tra18].

Chapter 4 is dedicated to the topics of Feshbach resonance theory and experiments in ultracold atoms. The chapter develops from simple alkali system towards more complex dipolar systems. The first experimental observation of Feshbach resonances in a heteronuclear lanthanide mixture is reported as part of the publication [Dur20].

Chapter 5 closes the thesis and discusses further steps to pursue as an outlook to future investigations. The work performed during the development of this manuscript makes the employment of erbium-dysprosium quantum mixtures with tunable interactions for the purposes of quantum simulation and fundamental research possible.

Appendix A-C include the publications not covered by the main topic of this thesis [Cho19, Ilz19], complete sets of measurement performed for the publication [Dur20] and additional information regarding the coils system.

1.2.1 List of publications

The publications discussed in the main text of this thesis are listed here in a chronological order.

- *Two-species five-beam magneto-optical trap for erbium and dysprosium*
  Philipp Ilzhöfer, Gianmaria Durastante, Alexander Patscheider, Arno Trautmann, Manfred J. Mark, and Francesca Ferlaino
  Physical Review A **97**, 023633 (2018)

- *Dipolar Quantum Mixtures of Erbium and Dysprosium Atoms*
  Arno Trautmann, Philipp Ilzhöfer, Gianmaria Durastante, Claudia Politi, Maximilian Sohmen, Manfred J. Mark, and Francesca Ferlaino
  Physical Review Letters **121**, 213601 (2018)

- *Feshbach Resonances in an Erbium-Dysprosium Dipolar Mixture*
  Gianmaria Durastante, Claudia Politi, Maximilian Sohmen, Philipp Ilzhöfer, Manfred J. Mark, Matthew A. Norcia, and Francesca Ferlaino
  Physical Review A — accepted, in press (2020)

1.2.2 Additional publications

During my PhD work, I also contributed to study many-body dipolar physics, culminated in the observation of supersolid phases in dysprosium quantum gases. The corresponding publications, which I co-authored, are listed below. Such publications are included in Appendix A as "additional" since their subject is not part of the core topic of this thesis.

- *Long-Lived and Transient Supersolid Behaviors in Dipolar Quantum Gases*
  Lauriane Chomaz, Daniel Petter, Philipp Ilzhöfer, Gabriele Natale, Arno Trautmann, Claudia Politi, Gianmaria Durastante, Rick M. W. van Bijnen, Alexander Patscheider, Maximilian Sohmen, Manfred J. Mark, and Francesca Ferlaino
  Physical Review X **9**, 021012 (2019)

- *Phase coherence in out-of-equilibrium supersolid states of ultracold dipolar atoms*
  Philipp Ilzhöfer, Maximilian Sohmen, Gianmaria Durastante, Claudia Politi, Arno Trautmann, Giacomo Morpurgo, Thierry Giamarchi, Lauriane Chomaz, Manfred J. Mark, and Francesca Ferlaino
  arXiv:1912.10892

Chapter 2

Ultracold erbium-dysprosium atoms

In the periodic table, and more precisely in the sixth period from lanthanum to lutetium, a series of elements has recently attracted great interest in the ultracold atom community. Indeed, in the *lanthanide series*, several elements show peculiar properties which make them excellent candidates to expand the physics accessible by quantum gas experiments. Typically, lanthanide elements offer several bosonic as well as fermionic isotopes with high natural abundance increasing the experiment flexibility. Due to the unpaired electrons in the f-orbital, most of the lanthanides possess a strong permanent magnetic dipole moment, among the strongest on the periodic table, leading to new and fascinating few- and many-body phenomena in the ultracold regime. This dipole moment is particularly important to create dipolar quantum gases unaccompanied by the technical difficulties of working with molecules (see Chap. 3) or Rydberg states. Furthermore, their complex electronic structure leads to a wealth of possible manipulation schemes. In this panorama, erbium and dysprosium are the two most widely used to date with large magnetic moments. After their laser cooling and trapping has been demonstrated [McC06, Lu10], several groups followed the path towards quantum degeneracy [Lu11a, Lu12, Aik12, Aik14b, Tra18].

More generally, lanthanides are widely used in industrial applications as catalysts, luminescent devices, superconductors, magnets, and so on [McG00, Kri15]. Their ions are used in optoelectronics such us lasers (e. g. Nd:YAG) and as a dopant in optical fibers (e. g. erbium-doped fiber amplifiers in optical-fiber telecommunication) due to their favorable optical properties. Lanthanide atoms feature 58 core electrons in a xenon-like configuration and, the majority of them, a complicated valence electronic configuration with unpaired electrons in the $4f$ (even $5d$) orbital. Peculiar is the submerged structure of the f-shell which is surrounded by the filled $6s$-shell leading to the anisotropic electronic ground state (exceptions are Eu and Yb) and the complex energy level distribution [Rum20].

In this chapter, the experimental apparatus needed to produce a cold thermal sample of erbium and dysprosium is presented. Sec. 2.1 reviews and compares the relevant atomic properties of erbium and dysprosium. The experimental setup is described in Sec. 2.2 with special attention focused on the magnetic field generation and control. Sec. 2.3 includes our first publication *Two-species five-beam magneto-optical trap for erbium and dysprosium* [Ilz18].

Table 2.1: List of erbium and dysprosium isotopes relevant for our experiment together with selected properties. The sign on the nuclear spin **I** describes its relative orientation. B and F refer to bosonic and fermionic isotopes, respectively. Values taken from Ref. [Rum20].

	^{166}Er	^{167}Er	^{168}Er	^{170}Er	^{161}Dy	^{162}Dy	^{163}Dy	^{164}Dy
Atomic mass (u)	165.9	166.9	167.9	169.9	160.9	161.9	162.9	163.9
Abundance (%)	33.50	22.87	26.98	14.91	18.89	25.48	24.90	28.26
Nuclear spin	0	$+\frac{7}{2}$	0	0	$+\frac{5}{2}$	0	$-\frac{5}{2}$	0
Statistics	B	F	B	B	F	B	F	B

2.1 Erbium and dysprosium properties

Erbium and dysprosium are next-nearest neighbors on the periodic table with atomic numbers of 68 and 66 and atomic mass of 167.26 u and 162.50 u, respectively. They were discovered in the XVIII century and, like all the lanthanide elements, they can't be found as isolated elements in nature but always bound in mineral ores (*dysprosium* means indeed *hard to get* from Greek). Their abundance on the Earth's crust is about 3.5 ppm for erbium and 5.2 ppm for dysprosium [Rum20]. The natural abundance and other properties for each isotope are reported in Tab. 2.1.

In the following, Sec. 2.1.1 reviews the relevant properties of such elements in order to plan and build an ultracold atoms experiment. Sec. 2.1.2 focuses on the energy level diagrams and the atomic polarizabilities of both species highlighting the most important aspects of them.

2.1.1 Physical properties

Erbium and dysprosium are solid under standard conditions with densities of $9.07\,\mathrm{g/cm^3}$ and $8.55\,\mathrm{g/cm^3}$, respectively. The melting temperatures are $T_\mathrm{m}^{Er} = 1529\,^\circ\mathrm{C}$ and $T_\mathrm{m}^{Dy} = 1412\,^\circ\mathrm{C}$ and this difference impacts their vapor pressures. At 1100 °C, temperature regime around which we evaporate the material, Dy has a vapor pressure ten times higher than Er.

As said in the introduction to this chapter, lanthanide elements have a peculiar electronic configuration. In the specific case of erbium and dysprosium, it is

$$\mathrm{Er} : [\mathrm{Xe}]4f^{12}6s^2 \quad \text{and} \quad \mathrm{Dy} : [\mathrm{Xe}]4f^{10}6s^2 \tag{2.1}$$

which leads to the respective electronic ground state

$$\mathrm{Er} : {}^3\mathrm{H}_6 \quad \text{and} \quad \mathrm{Dy} : {}^5\mathrm{I}_8. \tag{2.2}$$

Here, the presence of a large total orbital momentum **L** — $L_\mathrm{Er} = 5$ and $I_\mathrm{Dy} = 6$ for erbium and dysprosium respectively — modifies the scattering properties by introducing a strong anisotropy in the electronic ground state. **L** adds to the total spin **S** into the total electronic angular momentum **J** leading to a fine structure with three states for Er and five for Dy ($J_\mathrm{Er} \in \{4, 5, 6\}$ and $J_\mathrm{Dy} \in \{4, 5, 6, 7, 8\}$ respectively). Remarkably, all the bosonic isotopes have no nuclear spin ($\mathbf{I} = 0$) leading to the absence of a hyperfine structure [Foo05].

Whereas, in the case of fermionic isotopes, the situation is different with $I_{\mathrm{Er}} = 7/2$ and $I_{\mathrm{Dy}} = 5/2$. The hyperfine coupling of $\mathbf{I}$ with $\mathbf{J}$ to the total atomic angular momentum $\mathbf{F}$ introduce a hyperfine structure for a total of eight states $F_{\mathrm{Er}} \in \{5/2, 7/2, \ldots, 19/2\}$ in erbium and six $F_{\mathrm{Dy}} \in \{11/2, 13/2, \ldots, 21/2\}$ in dysprosium with quantum number F.

In the case of erbium and dysprosium, the unpaired electrons in the valence f-shell give rise to their large magnetic moment. A complete derivation is possible by following Ref. [Foo05]. As reported in Tab. 3.1, the magnetic moment in the ground state manifold is $\mu_{\mathrm{Er}} \simeq 7.0\mu_{\mathrm{B}}$ and $\mu_{\mathrm{Dy}} \simeq 10\mu_{\mathrm{B}}$ (μ_{B} is the Bohr magneton). The strong dipolarity, hence the strong long-range anisotropic dipole-dipole interaction, triggers the interest of using erbium and dysprosium in quantum regimes as it opens new ways for understanding nature (see Chap. 3 and Chap. 4).

2.1.2 Energy levels and atomic polarizabilities

Erbium and dysprosium show profound similarities in their energy level diagrams. In particular, the two transitions for both species used in our experiment to prepare and probe the atomic sample promote a $6s$ valence electron to the $6p$ state (see colored arrows in Fig. 2.1) [Mar78]. In both cases, a $\Delta J = +1$ transitions to a singlet (triplet) $^1P_1$- ($^3P_1$-) configuration of such $6s$ and $6p$ electrons is induced. For our purposes, we can distinguish the transitions in two pairs: broad and narrow (see also Tab. 2.2).

Broad transitions This is the strongest transition to the singlet $^1P_1$-configuration in both species, particularly useful in cases where a large amount of photons need to be scattered in a short time. It is employed in the initial transversal cooling of the atomic beam, the Zeeman slower section, and for absorption imaging. The wavelength of this transition in erbium (dysprosium) is $\lambda_{\mathrm{Er}} = 400.910\,\mathrm{nm}$ ($\lambda_{\mathrm{Dy}} = 421.290\,\mathrm{nm}$), with a natural linewidth of 29.4 MHz (32.2 MHz).

Narrow transitions Also referred as *intercombination-line transition*, it couples to the triplet $^3P_1$-configuration. It is employed in the magneto-optical trap (MOT) with wavelength $\lambda_{\mathrm{Er}} = 582.842\,\mathrm{nm}$ and $\lambda_{\mathrm{Dy}} = 626.082\,\mathrm{nm}$. Due to the dipole-forbidden nature, the natural linewidth is 186 kHz and 135 kHZ, respectively. This comparative narrow linewidth leads to a favorable low Doppler temperature of $\sim$4 µK, allowing to reach a final temperature of the sample after the MOT stage of about 10 µK.

This MOT scheme has been efficiently employed in the single-species experiments described in Refs. [Fri12, Mai14]. The decision of adopting for such approach simplifies the experiment for the following reasons. Firstly, both transitions for both species are either nearly closed (the broad) or completely closed (the narrow) transitions, therefore there is no need for repumpers reducing the complexity of the laser source. Secondly, the wavelengths for the transitions are close enough to facilitate the design of the coatings of optics and viewports. Additionally, the final temperature of the sample is low enough to allow for a direct loading of the double-species MOT into an optical dipole trap beam. Nonetheless, in the pioneering experiments described in Refs. [McC06, Lu10], the authors obtained single-species MOTs on

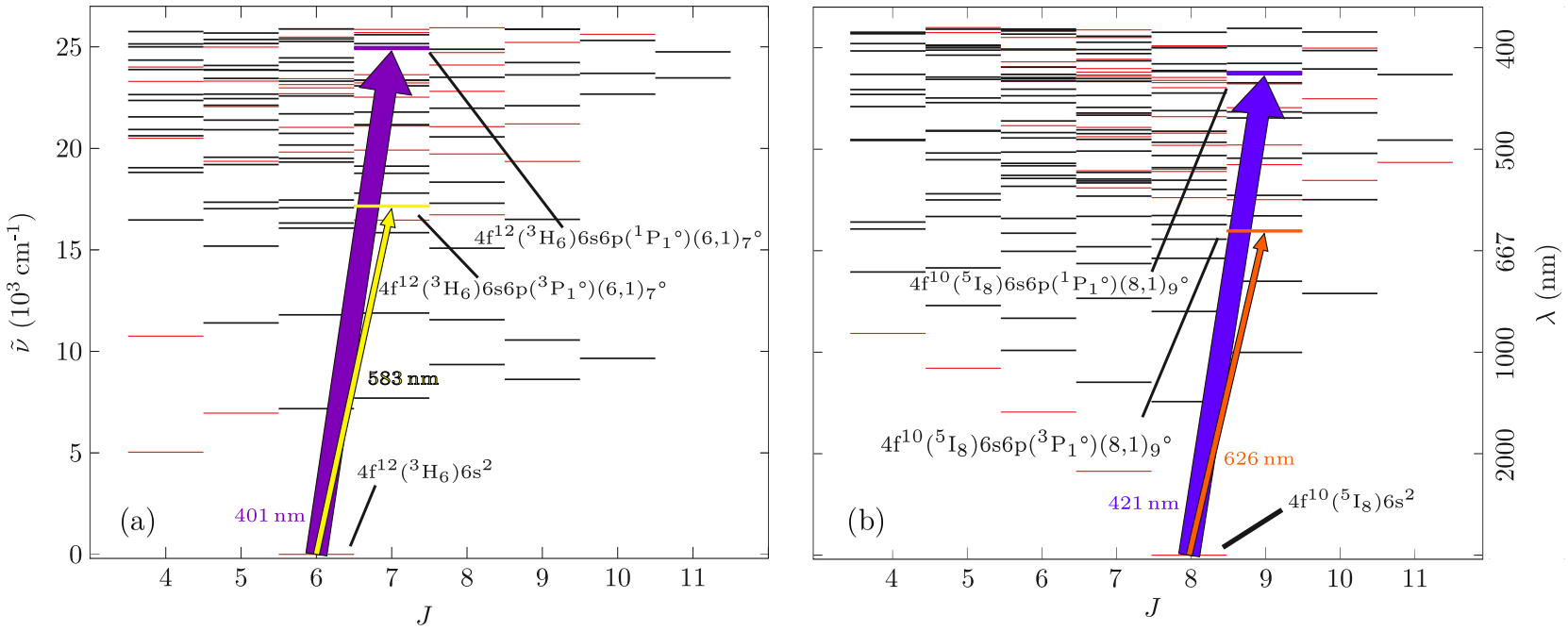

Figure 2.1: Energy level diagram for erbium (a) and dysprosium (b) highlighting the optical transitions employed in the experiment described in Tab. 2.2. J is the total angular momentum. (a) The violet (yellow) arrow indicate the 401 nm (583 nm) broad (narrow) transition. (b) The blue (orange) arrow indicate the 421 nm (626 nm) broad (narrow) transition. The broad transitions are used for transversal cooling, Zeeman slower, and for absorption imaging whereas the narrower transitions are used to generate the double-species MOT.

Table 2.2: Optical transitions employed in our experiment. The broad ∼30 MHz transitions are used in the transversal cooling and Zeeman slowing stage and for absorption imaging. The narrower ∼100 kHz transitions are used to generate the double-species magneto-optical trap. Values are extracted or calculated from Refs. [Law10, Lu11b, Kra19].

Transition property	Erbium		Dysprosium	
Wavelength (nm)	400.910	582.842	421.290	626.082
Lifetime	5.41 ns	0.85 µs	4.94 ns	1.2 µs
Natural linewidth	29.4 MHz	186 kHz	32.2 MHz	135 kHz
Saturation intensity	59.7 $\frac{\mathrm{mW}}{\mathrm{cm}^2}$	123 $\frac{\mu\mathrm{W}}{\mathrm{cm}^2}$	56.4 $\frac{\mathrm{mW}}{\mathrm{cm}^2}$	72 $\frac{\mu\mathrm{W}}{\mathrm{cm}^2}$
Doppler temperature (µK)	707	4.5	774	3.2

the broad transition instead. In the dysprosium case, this method required an additional MOT stage on a 8 kHz transition in order to load the atoms into a dipole trap for evaporative cooling towards quantum degeneracy [Lu11a].

A relevant property directly connected to the level diagram is the atomic polarizability α [Met99, Foo05]. Peculiar for every atomic species, α plays a fundamental role in techniques involving light trapping such as optical-dipole traps and optical lattices [Gri00, Blo05]. Neutral atoms in an external electric field $\mathbf{E}$ exhibit an induced electric dipole moment $\mathbf{d} = \alpha \cdot \mathbf{E}$. Worth to be noticed is that α depends on the field's angular frequency and it is generally a complex-numbered tensor of rank-two. In a laser field, the atomic polarizability dictates the light potential seen by the atoms and the photon scattering rate through its real ($\Re\{\alpha\}$) and imaginary part ($\Im\{\alpha\}$), respectively [Lep14, Bec18]. α itself can be decomposed in scalar α_s, vectorial α_v, and tensorial α_t polarizabilty where the scalar one is the dominant term in our application [Bec18, Rav18a]. Despite its importance, the theoretical determination of α for complex atomic species is a delicate and non-trivial task requiring deep understanding of the energy level diagrams and transition dipole moments. For erbium and dysprosium such understanding is still limited compared to alkali species. In Fig. 2.2, the real parts of the scalar atomic polarizabilities for erbium and dysprosium are plotted. Here, the large number of transitions in the range 300 nm to 700 nm gives rise to the interesting possibility of implementing species-selective manipulation schemes [LeB07, Lud15]. Above this range, and especially at 1064 nm, there exists a relatively flat region in which the polarizabilities converge becoming similar. This is of particular interest because, together with the similar atomic masses, it allows for the implementation of a standard red-detuned far-off resonance optical dipole trap [Gri00] able to work efficiently on both atomic species (see also Sec. 3.2). Experimentally determined values at 1064 nm are [Bec18, Rav18a]:

$$\begin{aligned} \Re\{\alpha\}_\mathrm{Er} &= (166 \pm 3_\mathrm{stat} \pm 61_\mathrm{syst})\,\mathrm{a.u.} \quad \text{and} \quad \Re\{\alpha_\mathrm{t}\}_\mathrm{Er} = (-1.9 \pm 0.8_\mathrm{stat} \pm 1.2_\mathrm{syst})\,\mathrm{a.u.} \\ \Re\{\alpha_\mathrm{s}\}_\mathrm{Dy} &= 184.4(2.4)\,\mathrm{a.u.} \quad \text{and} \quad \Re\{\alpha_\mathrm{t}\}_\mathrm{Dy} = 1.7(6)\,\mathrm{a.u.} \end{aligned} \tag{2.3}$$

where a.u. stands for *atomic unit* (1 a.u. $= 4\pi\epsilon_0 a_0^3$ with ϵ_0 the vacuum permittivity and a_0 the Bohr radius).

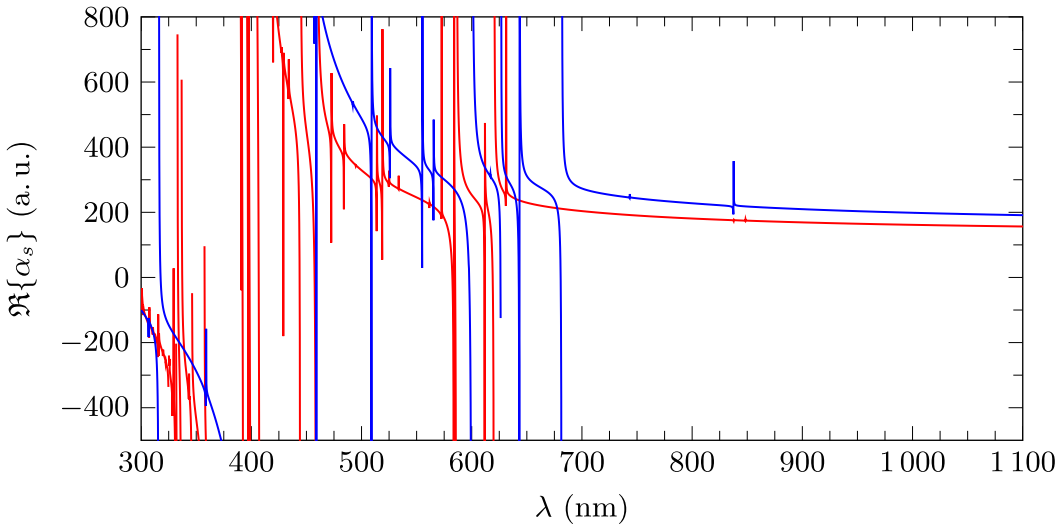

Figure 2.2: Calculated real part of the scalar atomic polarizabilities $\Re\{\alpha_s\}$ for erbium and dysprosium (red and blue, respectively) versus wavelength. At 1064 nm, value relevant for our optical trapping scheme, the calculated atomic polarizabilities are $\Re\{\alpha_s\}_{Er} = 161.8$ a.u. and $\Re\{\alpha_s\}_{Dy} = 198.6$ a.u..

2.2 Experimental setup

The experimental apparatus to prepare a quantum-degenerate heteronuclear mixture consists of an ultra-high vacuum (UHV) system in which hot erbium and dysprosium atoms coming from a high-temperature oven are trapped and cooled by means of laser lights and magnetic fields (see Fig. 2.3). The general layout of the system resembles more a single-component quantum gas experiment rather than a dual-species one. Such similarity is due to the similar atomic properties of the two species allowing for a fairly simple design. It consists of an effusion cell to evaporate at about 1400 K both species simultaneously, a transversal cooling (TC) section to collimate the atomic beam, a Zeeman slower (ZS) to decelerate longitudinally the atoms, and a dual-species magneto-optical trap (MOT) to cool and trap the atoms down to few µK. The last step towards the degeneracy implies an evaporative cooling scheme in a red-detuned far-off resonance optical dipole trap (ODT) described in Chap. 3.

In this section we describe the key features and performances of our experimental apparatus. Sec. 2.2.1 treats the UHV system and the laser cooling and trapping of an erbium-dysprosium sample. Sec. 2.2.2 describes our procedure for magnetic-field calibration and Sec. 2.2.3 focuses on the generation and control of the magnetic fields in the main chamber section of the apparatus. More information including extensive technical descriptions and details are available in Ref. [Ilz20].

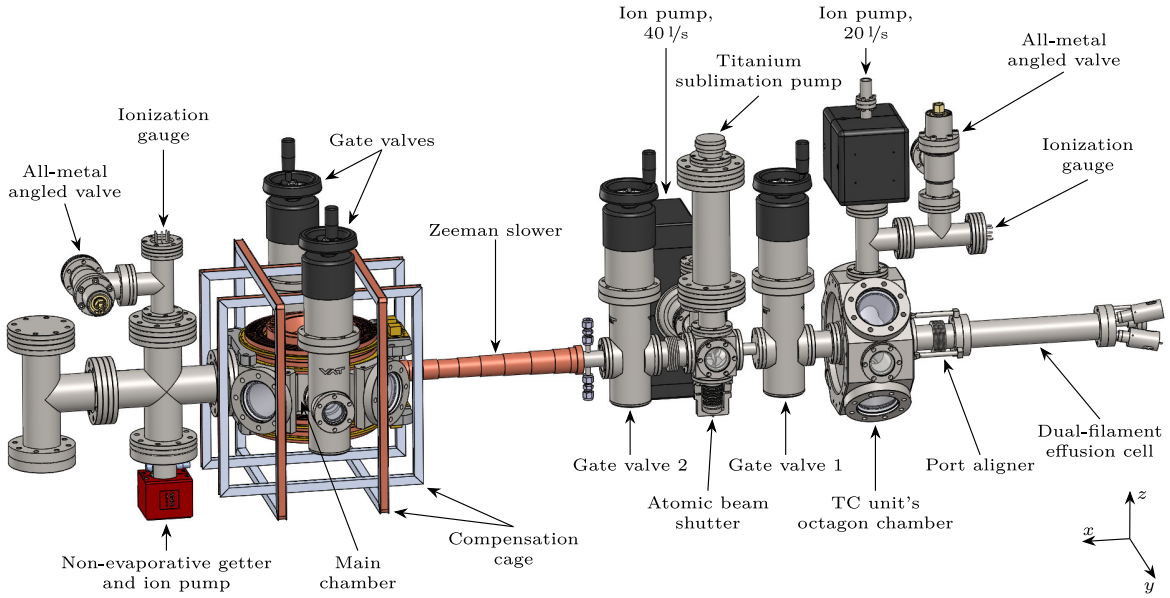

Figure 2.3: Sketch of the vacuum system of the erbium-dysprosium experiment. The major highlights of the setup are indicated with arrows. The atomic beam generated in the effusion cell travels from right to left through a transversal cooling and Zeeman slower section. The atoms are then trapped and cooled to quantum degeneracy in the main chamber. Here, several coil pairs allow a complete tuning of magnetic fields. Figure adapted from [Ilz20].

2.2.1 General description of the apparatus

Vacuum chamber

The whole apparatus is constructed with components made out of 1.4404 and/or 1.4429 stainless steel to ensure low magnetic permeability. This is particularly important to reduce the risk of magnetizing the components themselves. The TC chamber and main chamber feature an electrolytic-polished surface to reduce roughness and improve the vacuum quality [VV04]. Shown in Fig. 2.3, the vacuum system can be divided into three parts: the atomic beam source module, the atomic beam shutter module, and the main chamber module. These modules are separable via gate valves and they feature pressures on the low 10^{-10} mbar, few 10^{-11} mbar, and low 10^{-11} mbar level respectively due to two ion pumps and an ion pump combined with a non-evaporative getter. A titanium sublimation pump allows for refreshing the vacuum in case of oven refilling procedures. Additionally, two gate valves on the main chamber's sides allow for possible extensions of the experiment with two more vacuum modules for future dedicated experiments.

The high-temperature oven has a dual-filament effusion cell design with a tantalum crucible typically heated up to 1100 °C. An outer hot-lip section at about 1200 °C prevents evaporated material to condense on the crucible's aperture. The temperatures of both sections can be controlled independently. The crucible is filled with granulated alloy composed from 33 % erbium and 67 % dysprosium. To compensate for the higher vapor pressure of dysprosium, the hot-lip is filled with additional pure granulated erbium.

In the atomic beam shutter module, an in-vacuum stainless steel plate can be moved by a servo driver and placed into the atomic beam to forbid atoms from traveling through the ZS into the main chamber. This shutter is actuated after every MOT loading cycle. This module also acts as a differential pumping stage between the first and the third module, using the Zeeman slower tube and a short tube between the beam shutter and the first gate valve as apertures maintaining the pressure difference.

The main chamber section is the heart of the experiment. Here, the double-species MOT is produced and the sample is brought to quantum degeneracy. It consists of a custom-made vacuum chamber with full optical access thanks to eight viewports. Particularly important are the two CF100 inverted viewports along the vertical direction. Such design allows for a reduced working distance from the atoms and a large field-of-view supporting the installation of a high-resolution imaging along the z-axis. Moreover, it opens up the possibility of implementing a series of coils for magnetic-field generation close to the atomic sample (see Sec. 2.2.3).

Laser cooling and imaging

The laser cooling employed in our experiment makes use of a robust three-stage scheme. First, the TC section cools the transversal velocity components of the atomic beam, thereby collimating it and increasing the atomic flux through the ZS to the main chamber. Its operating principle is based on a red-detuned two-dimensional molasses technique[Met99] on the $\sim$30 MHz broad transitions $\lambda_{\mathrm{Er}} = 401\,\mathrm{nm}$ and $\lambda_{\mathrm{Dy}} = 421\,\mathrm{nm}$ of erbium and dysprosium, respectively. The laser beams are elliptical to maximize the overlap with the atomic beam and increase the amount of scattered light.

Secondly, the 350 mm spin-flip ZS stage simultaneously decelerate the two-components atomic beam from velocity classes of up to 370 m/s down to 5 m/s, smaller than MOT capture velocities of about 16 m/s. It operates on the same broad transitions employed in the TC section.

Finally, the dual-species MOT traps and cools the atoms in the center of the main chamber down to a temperature of about 10 µK. The MOT operates at the same time on the two species on the narrower $\sim$100 kHz broad transitions $\lambda_{\mathrm{Er}} = 583\,\mathrm{nm}$ and $\lambda_{\mathrm{Dy}} = 626\,\mathrm{nm}$ of erbium and dysprosium, respectively. Because of the narrow-line character, the large-detuning operation, and the gravitational sag, the MOT spin-polarizes the atoms into the lowest Zeeman sublevel and it has the advantage of allowing for an open-top configuration along the z-axis. In fact, the vertical down-propagating beam becomes redundant and it can be removed without detrimental effects on the general performances ensuring an easy full optical access from the top viewport. More details on the characterization of the MOT operation are available in the publication Ref. [Ilz18] reported in Sec. 2.3.

The atomic sample is probed in time-of-flight (TOF) expansion by using a standard low-field absorption imaging technique [Ket99]. The pictures are recorded under a $\sim$45° in the horizontal $x-y$ plane with respect to the transversal y-axis. The open-top MOT will support the implementation of an additional µm-resolution vertical imaging suitable for in-situ as well as TOF imaging.

2.2.2 Magnetic-field calibration

To know precisely the value of each magnetic-field applied in the experiment at the main chamber, we calibrate our bias coils by means of radio-frequency spectroscopy on a cold thermal cloud of either erbium or dysprosium in trap. This is done by fixing the current flowing in a specific coil pair and varying the frequency of the RF radiation[1]. When the Zeeman splitting matches the RF energy, atoms are transferred to higher m_j states. In these states they experience dipolar relaxation processes heating up the atoms which induce losses from the ODT. By recording such frequency-dependent atom-loss curves and because of the known value of the Zeeman splitting ($\Delta E_{\mathrm{Z,Er}} = 1.63\,\mathrm{MHz/G}$ and $\Delta E_{\mathrm{Z,Dy}} = 1.74\,\mathrm{MHz/G}$ for bosonic erbium and dysprosium, respectively), it is possible to connect the applied current with the real magnetic field value at the atoms' position. By repeating this procedure for several values of the current, we extract precise calibration curves for our coil pairs and we get insights on the overall magnetic-field stability. In the following Sec. 2.2.3, values extracted by applying such technique are reported. Note that not all the coils have been characterized, and in particular, measuring magnetic field gradients would require completely different techniques [Xu17].

2.2.3 Magnetic field system

In a quantum gas experiment, magnetic fields are employed in ZS, MOT, and interaction-tuning techniques, hence magnetic fields and the ability of control them are of fundamental importance for a successful and reliable operation [Met99, Ket99]. In the following, we leave aside the detailed description of the ZS to focus on the coil systems at the main chamber. Our system is composed by eight coil pairs divided in three modules: inverted-viewport coils, large-field coils, and compensation cage coils surrounding the main chamber itself (see Fig. 2.4). In Tab. 2.3, technical details about the coils system are reported. In the following, we define the total magnetic field $B_{\mathrm{tot}}^{x,y,z} = \sqrt{B_{\mathrm{x}}^2 + B_{\mathrm{y}}^2 + B_{\mathrm{z}}^2}$ along x-, y-, and z-axis, respectively. The gradient is then calculated as $\boldsymbol{\nabla} B_{\mathrm{tot}}^{x,y,z} = \partial_{x,y,z}(B_{\mathrm{tot}}^{x,y,z})$. Moreover, the vertical and horizontal extension of a coil are indicated as *windings* and *layers*, respectively.

Several temperature sensors[2] and resettable thermal fuses[3] monitor the status of the system preventing overheating and switching off the power supplies in that case. In search for the best heat-exchange performances, the copper wires are wound with high-thermal conductivity glue[4].

[1] RF source: in-house direct digital synthesizer (DDS), amplifier: Frankonia FFL-25A

[2] 10 kΩ NTC thermistor

[3] Temperature thresholds ranging from 40 °C to 60 °C are used depending on their position

[4] Fischer Elektronik WLK-10 and WLK-DK-50 for the large- and small-field coils and Electrolube ERTCER75S for the compensation cage coils

Table 2.3: Details of the coil system employed at the main chamber. See Fig. 2.4 for the exact location of the coils in the experimental setup. The vertical and horizontal extension of a coil are indicated as *windings* × *layers*, respectively. Resistance and inductance are measured values. The current-to-field conversion is reported as numerical calculated value (th) from the Biot–Savart law at the center of the main chamber and as measured value (exp) from RF spectroscopy on a cold atomic sample. The measured value is an average over independent repetitions on different days.

Coil purpose	Extension	Resistance (mΩ)	Inductance (µH)	Current-to-field	
				th	exp
Large bias	2×27	150	1590	4.37 G/A	4.80(1) G/A
Large gradient	2×27	150	1590	0.48 (G/cm)/A	
small bias	1×6	42	14	0.78 G/A	0.822(5) G/A
small gradient	10×6	330	796	1.55 (G/cm)/A	
RF fields	1×1	30	0.50	0.14 G/A	
Fast field	1×4	70	7	0.57 G/A	
Compensation x-axis	2×11	346	1006	1.06 G/A	1.06(2) G/A
Compensation y-axis	2×11	326	898	1.16 G/A	1.13(2) G/A

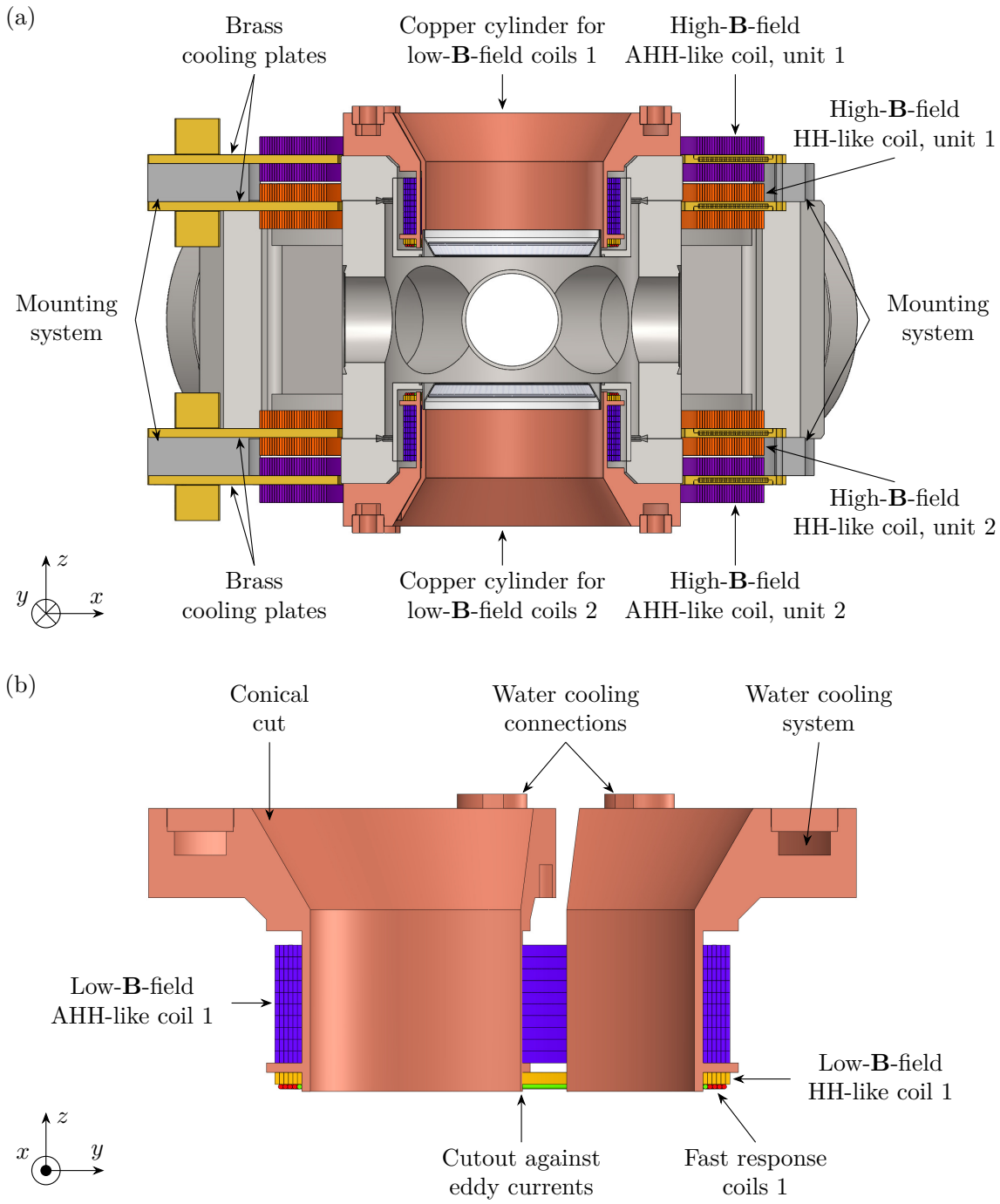

Figure 2.4: Sectional view of the main chamber along the x-axis highlighting the coil system composed by six independent coil pairs. (a) The *large-bias* (orange) and *large-gradient* coils (violet) are in Helmholtz and anti-Helmholtz configuration, respectively. They are mounted on a water-cooled brass plate featuring a small cutout against eddy current. Four additional coil pairs are meant for small magnetic field generation and are wound on copper cylinders. Both mounting systems are rigidly connected to the main chamber and symmetric with respect to its center. (b) Zoom of a water-cooled copper block in the $y-z$ plane. The cutout helps against eddy currents. The *small-gradient* coils (blue) are in anti-Helmholtz configuration to generate small gradients. The *small-bias* coils (yellow) are in Helmholtz configuration to generate small bias. The *fast coils* (red) are meant for fast-field generation. The single-winding single-layer *RF coils* (green) are meant to apply RF on the atoms. Figure taken from [Ilz20].

Inverted viewport coils

This module (see Fig. 2.4 (b)) is composed by four pairs of independent coils designed to create small magnetic-fields and wound around a copper cylinder of 81 mm of inner diameter. This copper block is rigidly connected to the vacuum apparatus and it holds in place the coils and cools them down thanks to an internal water cooling system. If the coil pairs are activated at the maximum operating current of 10 A, the cooling system keeps the entire module at a maximum steady-state temperature of ∼28 °C with 1 l/min of running water at about 23 °C (see Fig. C.2). Due to the low resistivity of these four coil pairs, the power dissipated is quite low and, even without water cooling, the temperature does not rise above ∼50 °C. Worth to be noted is the presence of a cutout on the copper block and an additional thin isolating layer between it and the viewport which prevent the buildup of large eddy currents. The main characteristics of the four coil pairs in this module are summarized in the following list:

- **Small-gradient coils** Ten-windings six-layers coil built with a 2.7 mm × 1.0 mm copper wire. The coils in the pair are at 100 mm distance and they are in anti-Helmholtz configuration for quadrupole-field generation. They are employed in the creation of gradients used in the MOT loading and/or for levitation of the atomic sample.

  At the center of the main chamber, the calculated quadrupole field produced by the coil pair is $|\boldsymbol{\nabla} B^{x,y}_{\mathrm{tot}}| = 0.78\,(\mathrm{G/cm})/\mathrm{A}$ and $|\boldsymbol{\nabla} B^{z}_{\mathrm{tot}}| = 1.55\,(\mathrm{G/cm})/\mathrm{A}$ (see Fig. 2.5 (a)). Even though the actual value of the current-to-gradient conversion has not been measured, the performance of the double-species MOT was optimized by tuning the current directly.

- **Small-bias coils** Single-winding six-layers coil built with a 2.7 mm × 1.0 mm copper wire. The coils in the pair are at 70 mm distance and they are in Helmholtz configuration for homogeneous-field generation to control the bias field along the z-axis. They are used to generate the MOT-bias field and for precise intra-/inter-species interaction tuning in the ODT.

  By employing RF spectroscopy on a cold sample (described in Sec. 2.2.2), we measure a current-to-field conversion at the atoms' position of $B^{x,y,z}_{\mathrm{tot}} = 0.822(5)\,\mathrm{G/A}$ over independent repetitions on different days (see Fig. 2.6 (a) for a typical measurement). As a comparison, the numerically calculated value is $B^{x,y,z}_{\mathrm{tot}} = 0.78\,\mathrm{G/A}$ with a relative flatness of 10^{-4} within ±0.5 mm (see Fig. 2.5 (b)). By setting the magnetic field with a step function, we are able to follow the time-variation of the field at the atoms and extract a time constant τ from an exponential decay fit (see Fig. 2.6 (b)). We estimate $\tau = 0.62(9)$ ms. The main limitation comes most likely from eddy currents in the systems.

- **RF coils** Single-winding single-layer coil built with a 1 mm diameter copper wire. The main purpose is radio-frequency generation. These coils are used e. g. to perform RF spectroscopy for magnetic-field calibration.

- **Fast coils** Single-winding four-layers coil built with a 1 mm diameter copper wire. They are meant for fast-field generation and/or precision tuning. Currently not employed.

The small-bias and -gradiend coils are driven with two independent self-build bipolar current sources based on high-voltage/high-current operational amplifier[5] capable of ±10 A of constant current.

High-field coils

This module (see Fig. 2.4 (a)) is composed of two pairs of independent coils dedicated to large-gradient and large-bias generation. Each coil of each pair is composed of two single-winding 27-layers parts of 165 mm of inner diameter separated by a 4 mm hollow brass plate. The brass plates rigidly connect the coils to the vacuum apparatus and cool them down as a result of an internal water cooling system. In the inside of the cooling channel, the surface of the brass is machined with a high roughness in order to increase the surface and leading to a turbulent water flow improving the heat exchange. If operated at the maximum steady-state current of 100 A, the temperature is kept at a maximal value of 40 °C (see Fig. C.1). Cutouts on the brass plates work against eddy currents. Both pairs are manufactured by using a 8 mm × 1 mm copper wire. The basic features of the two coil pairs are listed in the following:

- **Large-gradient coils** The coils in the pair are at 145 mm distance between each other and they are in anti-Helmholtz configuration for quadrupole-field generation. Their purpose is creating large-gradient fields useful for e. g. Stern-Gerlach separation.

  The calculated quadrupole field generated at the center of the main chamber is $|\boldsymbol{\nabla} B^{x,y}_{\mathrm{tot}}| = 0.24\,(\mathrm{G/cm})/\mathrm{A}$ and $|\boldsymbol{\nabla} B^{z}_{\mathrm{tot}}| = 0.48\,(\mathrm{G/cm})/\mathrm{A}$ (see Fig. 2.7 (a)). If changed to Helmholtz configuration, they can produce and homogeneous field of $B^{x,y,z}_{\mathrm{tot}} = 3.24\,\mathrm{G/A}$ with a flatness of 10^{-4} within ±1 mm of the center. Alternatively, using the pair in Helmholtz configuration, it can be used to extend the magnetic field generated by the large-bias coils up to ∼800 G in steady-state operation. At the moment of the submission of this thesis, the large-gradient coils were not actively employed in the experiment.

- **Large-bias coils** The coils in the pair are 105 mm apart and they are in Helmholtz configuration for homogeneous-field generation. They are used to create large bias used for interaction tuning out of the magnetic-field range achievable with the small-bias coils. These large-bias coils are used to perform Feshbach spectroscopy (see Sec. 4.4).

  At the position of the atoms we measure a current-to-field conversion of $B^{x,y,z}_{\mathrm{tot}} = 4.80(1)\,\mathrm{G/A}$ over independent repetitions on different days. As a comparison, the numerically calculated value is $B^{x,y,z}_{\mathrm{tot}} = 4.37\,\mathrm{G/A}$ with a flatness of 10^{-4} within ±1.5 mm of the center (see Fig. 2.7 (b)). We checked that the response of the current flowing in this coil pair can follow time ramps on the millisecond time-scale. By setting the field with a step function of 10 G and following the time-variation of the generated field, we measure an effective change of the field at the sample position in the order of 10 ms to settle at the part per thousand level.

[5] OPA549T

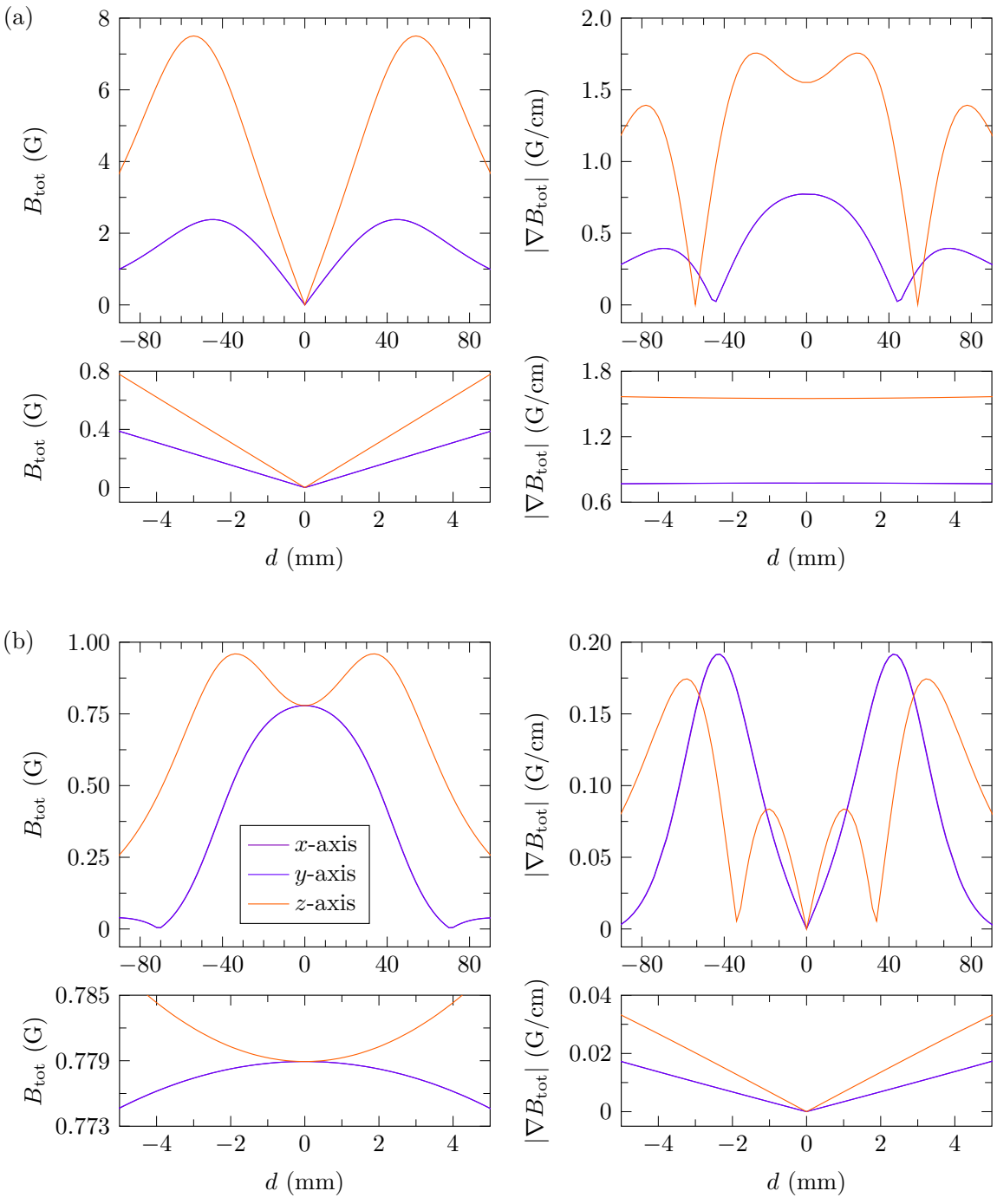

Figure 2.5: Calculated magnetic-field values $B_{\mathrm{tot}}^{x,y,z}$ (left column) and gradient $|\boldsymbol{\nabla} B_{\mathrm{tot}}^{x,y,z}|$ (right column) as a function of the distance d from the main chamber center for a constant 1 A current for the small-field coils. The orange curve shows the behavior along the z-axis. The violet and blue curves show the behavior along the x- and y-axis, respectively. Each rectangular panel beneath the respective square one is a zoom-in of the field in the center. (a) Small-gradient coils in anti-Helmholtz configuration. (b) Small-bias coils in Helmholtz configuration. Figure taken from [Ilz20].

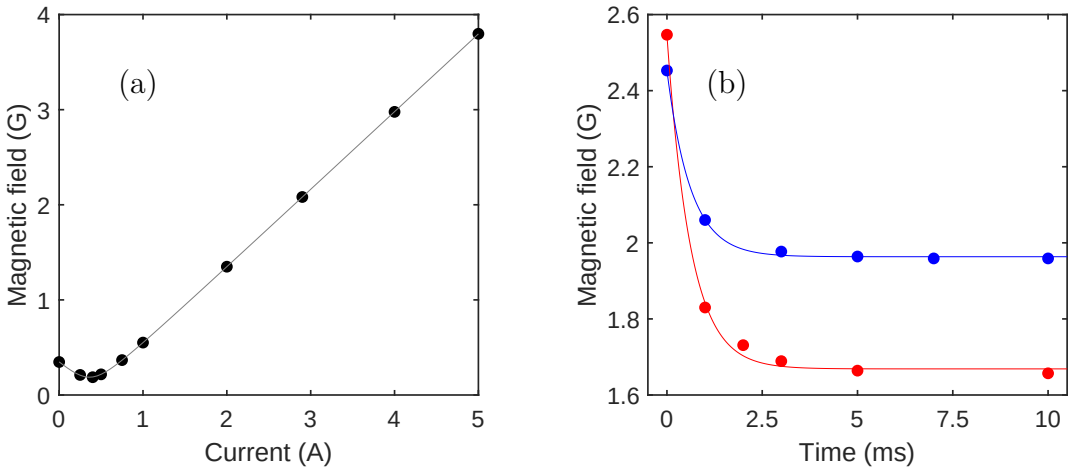

Figure 2.6: Characterization of the magnetic field produced by the small-bias coil pair by employing radio-frequency spectroscopy on either erbium or dysprosium (see Sec. 2.2.2). (a) Typical current-to-field measurement for magnetic-field calibration in which we fix the current flowing into a specific coil pair and we measure the field by RF spectroscopy. Black points are experimental values whereas the gray line is the fit over the datapoints. From independent repetitions of such measurement on different days we extract a conversion factor of $B_{\mathrm{tot}}^{x,y,z} = 0.822(5)\,\mathrm{G/A}$. (b) Time variation of the magnetic-field measured at the atoms position when the field is set at 0 ms with a jump of 0.5 G (blue points) and 1 G (red points). The blue and red curves are exponential decay fits over the respective dataset. We extract a time constant of 0.62(9) ms.

For each of the two pairs of coil, the field is controlled by stabilizing the current in the coils by an active feedback loop. The current is provided by two independent DC power supplies[6] and monitored by high-precision current transducers[7]. The current is set via temperature-stabilized 18-bit digital-to-analog converters (DAC)[8] resulting in an ideal shot-to-shot accuracy of $\pm 1.7\,\mathrm{mG}$.

Compensation cage coils

This module composed by two square coil pairs in Helmholtz configuration is meant for canceling the Earth's magnetic field and other external stray fields at the sample's position along the x- and y-axis. In addition, two independent bipolar power supplies (identical to the one used for the small-bias and small-gradient coils) allow for rotations of the magnetic field on the $x-y$ plane e. g. towards the imaging axis to perform absorption imaging of the sample. Each coil features a two-winding eleven-layers design and it is manufactured with a $4\,\mathrm{mm} \times 1\,\mathrm{mm}$ copper wire. The wire is wound inside an aluminum frame which is then rigidly connected to the main chamber (see Fig. 2.3). The size of the two coil pairs is slightly different to simplify the assembly in a configuration as close as possible to a perfect Helmholtz scheme and, at the same time, able to surround the entire main chamber. Although the module is only passively cooled, the temperature at the maximum steady-state current of 10 A does not raise above $\sim 30\,^{\circ}\mathrm{C}$. By optimizing the absorption imaging signal, it

[6] Delta Elektronica SM30-200
[7] LEM IT200-S ULTRASTAB
[8] DAC based on a LTC2757

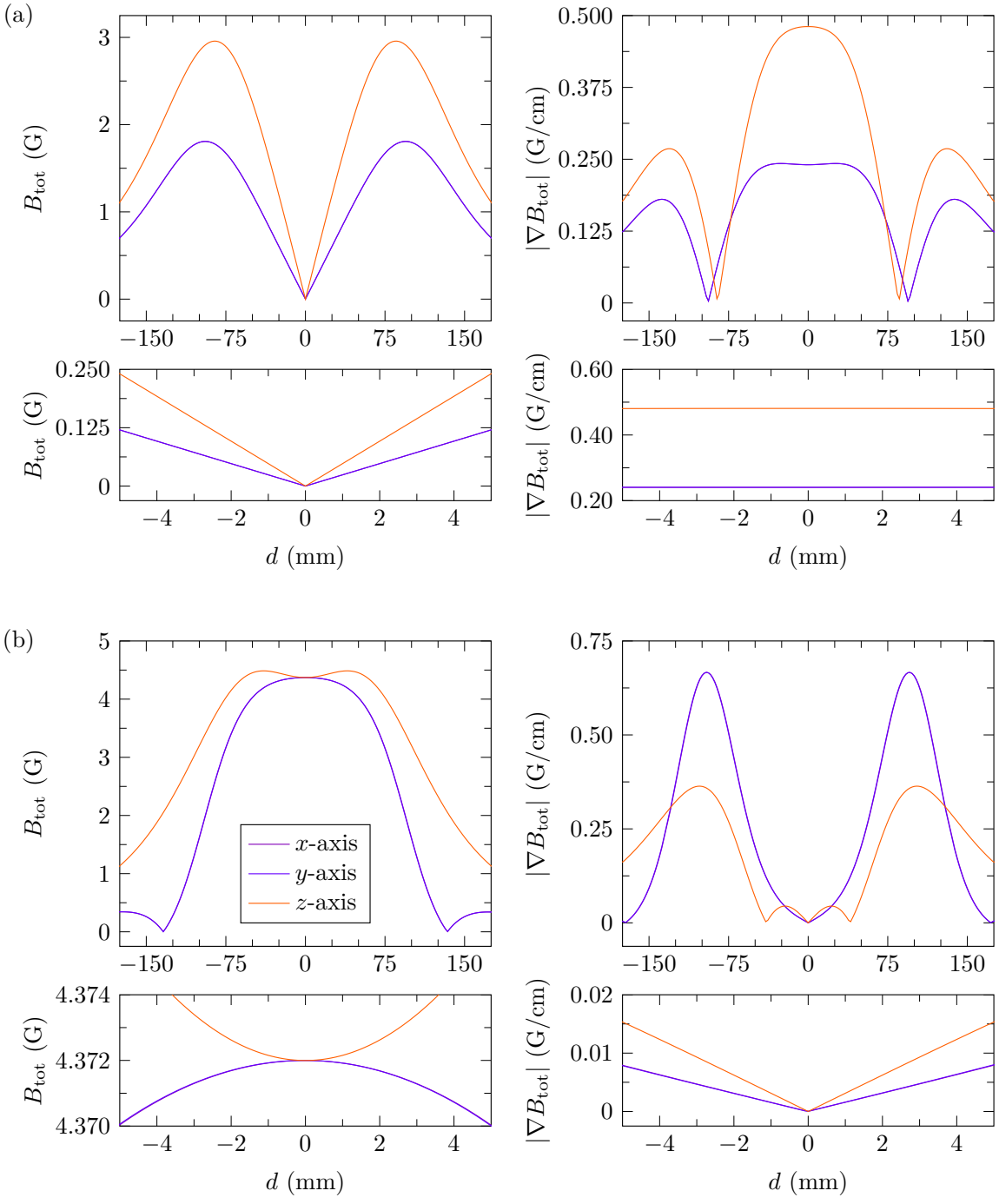

Figure 2.7: Calculated magnetic-field values $B_{\mathrm{tot}}^{x,y,z}$ (left column) and gradient $|\boldsymbol{\nabla} B_{\mathrm{tot}}^{x,y,z}|$ (right column) as a function of the distance d from the main chamber center for a constant 1 A current for the large-field coils. The orange curve shows the behavior along the z-axis. The violet and blue curves show the behavior along the x- and y-axis, respectively. Each rectangular panel beneath the respective square one is a zoom-in of the field in the center. (a) Large-gradient coils in anti-Helmholtz configuration. (b) Large-bias coils in Helmholtz configuration. Figure taken from [Ilz20].

has been possible to estimate the time for the field to settle after a change in its amplitude in the few-ms timescale.

- **Compensation x-axis** The dimension of each coil compensating for magnetic fields along the x-axis is 380 mm × 380 mm with a distance between each other of 175 mm. The field produced at the center of the main chamber by such configuration is calculated to be $B_{\text{tot}}^{x,y,z} = 1.04\,\text{G/A}$ with a flatness of 2×10^{-6} within ±0.5 mm (see Fig. 2.8 (a)). We measure $B_{\text{tot}}^{x,y,z} = 1.06(2)\,\text{G/A}$ over different days.

- **Compensation y-axis** The dimension of each coil compensating for magnetic fields along the y-axis is 350 mm × 350 mm with a distance between each other of 155 mm. The field produced at the center of the main chamber is calculated to be $B_{\text{tot}}^{x,y,z} = 1.12\,\text{G/A}$ with a flatness of 2×10^{-6} within ±0.5 mm (see Fig. 2.8 (b)). We measure $B_{\text{tot}}^{x,y,z} = 1.13(2)\,\text{G/A}$ over different days.

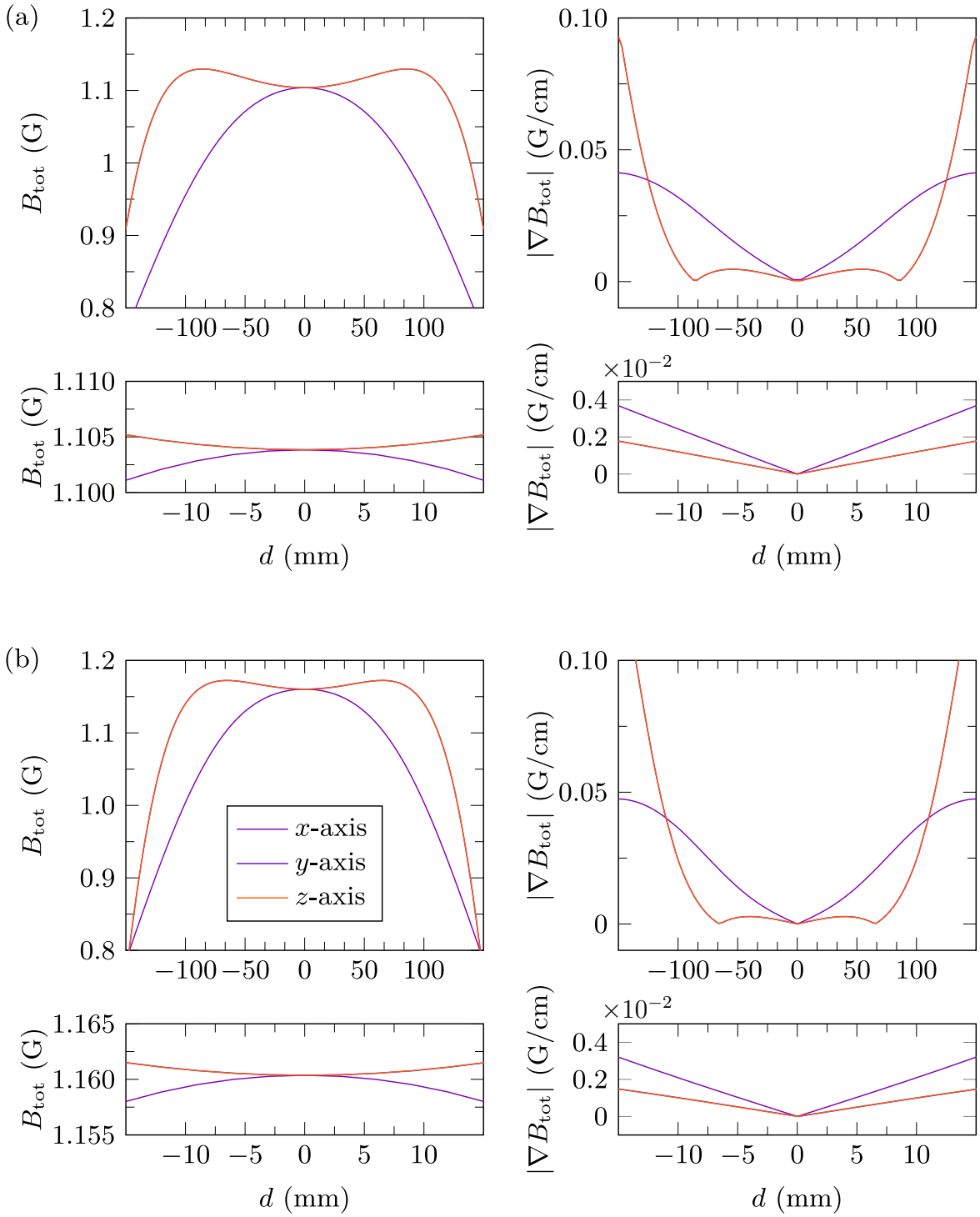

Figure 2.8: Calculated magnetic-field values $B_{\mathrm{tot}}^{x,y,z}$ (left column) and gradient $|\nabla B_{\mathrm{tot}}^{x,y,z}|$ (right column) as a function of the distance d from the main chamber center for a constant 1 A current for the compensation coils. The orange curve shows the behavior along the z-axis. The violet and blue curves show the behavior along the x- and y-axis, respectively. Each rectangular panel beneath the respective square one is a zoom-in of the field in the center. (a) Compensation x-axis. (b) Compensation y-axis.

2.3 Publication: Two-species five-beam magneto-optical trap for erbium and dysprosium[†]

Philipp Ilzhöfer[1,2], Gianmaria Durastante[1,2], Alexander Patscheider[1,2], Arno Trautmann[2], Manfred J. Mark[1,2], and Francesca Ferlaino[1,2]

[1] *Institut für Experimentalphysik and Zentrum für Quantenphysik, Universität Innsbruck, Technikerstraße 25, 6020 Innsbruck, Austria*
[2] *Institut für Quantenoptik und Quanteninformation, Österreichische Akademie der Wissenschaften, Technikerstraße 21a, 6020 Innsbruck, Austria*

Physical Review A **97**, 023633 (2018)
submitted 20 Nov 2017; published 26 Feb 2018
DOI: 10.1103/PhysRevA.97.023633

[†] The author of the present thesis helped in developing the experimental procedure, taking the data, and contributed in writing the manuscript. This publication is also part of the PhD thesis of Philipp Ilzhöfer.

Two-species five-beam magneto-optical trap for erbium and dysprosium

P. Ilzhöfer,[1,2] G. Durastante,[1,2] A. Patscheider,[1,2] A. Trautmann,[2,*] M. J. Mark,[1,2] and F. Ferlaino[1,2,†]
[1]*Institut für Experimentalphysik und Zentrum für Quantenoptik, Universität Innsbruck, Technikerstrasse 25, 6020 Innsbruck, Austria*
[2]*Institut für Quantenoptik und Quanteninformation, Österreichische Akademie der Wissenschaften, 6020 Innsbruck, Austria*

(Received 20 November 2017; published 26 February 2018)

We report on the first realization of a two-species magneto-optical trap (MOT) for the highly magnetic erbium and dysprosium atoms. The MOT operates on an intercombination line for the respective species. Owing to the narrow-line character of such a cooling transition and the action of gravity, we demonstrate a trap geometry employing only five beams in the orthogonal configuration. We observe that the mixture is cooled and trapped very efficiently, with up to 5×10^8 Er atoms and 10^9 Dy atoms at temperatures of about 10 μK. Our results offer an ideal starting condition for the creation of a dipolar quantum mixture of highly magnetic atoms.

DOI: 10.1103/PhysRevA.97.023633

Within the very active research field of ultracold quantum gases, heteronuclear mixtures of different atomic species offer unique possibilities to study a broad range of quantum phenomena. In the past 15 years, various atomic species have been combined to produce quantum degenerate mixtures. Each such quantum mixture has its own characteristic traits. Among the widely used alkali mixtures (e.g., [1,2]), the mass imbalance and the selective tuning of the intra- and interspecies interaction have allowed to investigate fascinating phenomena, such as heteronuclear Efimov states [3–6], polaron and impurity physics in both bosonic and fermionic backgrounds [7–11], and heteronuclear molecules with large electric dipole moments [12–14].

The latter development is mainly driven by the interest in studying phenomena arising from long-range and anisotropic dipole-dipole interactions among the molecules [15]. As an alternative approach, magnetic atoms have proven to be a robust system for study of few- and many-body dipolar physics. The strength of magnetic atoms for the study of dipolar physics was first shown using Bose-Einstein condensates of chromium atoms [16,17]. More recently, both erbium (Er) and dysprosium (Dy), among the most magnetic and isotope-rich atomic species, have been individually brought to quantum degeneracy [18–21]. Using these species, remarkable many-body dipolar phenomena have been observed, including the observation of deformed Fermi surfaces [22], quantum droplets [23–25], and roton excitations [26] and the recent study of thermalization in many-body dipolar gases [27].

Adding the flexibility of mixtures to the richness of magnetic atoms, we here report on the first combination of the two highly magnetic atomic species Er and Dy in a single experimental apparatus. The Er-Dy system extends the collection of available quantum mixtures by an unexplored case, as the interplay between the interspecies contact and dipolar interactions and the dipolar imbalance among the two species provides a new dimension in the parameter space of accessible quantum phenomena. This impacts, e.g., the miscibility properties of the mixture [28]. Although imbalanced dipolar mixture systems have not yet been considered in theory, they are good candidates for observation of, e.g., long-range dominated polarons, dipolar pairing, and the anisotropic BEC-BCS crossover with deformed Fermi surfaces.

While single-species magneto-optical traps (MOTs) of Er [29–31] and Dy [32–34] as well as other lanthanoid atoms [35–37] have already been attained, we simultaneously cool and trap Er and Dy in a two-species MOT operating on intercombination lines. We observe a remarkably robust operation of the dual MOT, with atom numbers similar or even surpassing the typical ones recorded in the single-species Er or Dy experiments. Moreover, we demonstrate magneto-optical trapping using a unique beam configuration, allowing us to efficiently operate the MOT using only five beams (5B) in an orthogonal *open-top* configuration; see Fig. 1(b). The working principle of our orthogonal 5B MOT relies on the combined effect of the narrow-line cooling and gravity [30,31,33–35,38] and contrasts with the classical six-beam (6B) approach.

A beneficial factor for combining the multivalence-electron atoms Er and Dy is their similarity in atomic properties [see table in Fig. 1(e)]. They both have several stable isotopes with a high natural abundance, >14%; in total, five bosonic (^{166}Er, ^{168}Er, ^{170}Er, ^{162}Dy, ^{164}Dy) and three fermionic (^{167}Er, ^{161}Dy, ^{163}Dy) isotopes. This isotope variety will allow us to prepare ultracold Bose-Bose, Bose-Fermi, and Fermi-Fermi quantum mixtures of Er and Dy. Whereas all bosonic isotopes have zero nuclear spin, the fermionic isotopes possess nuclear spins of $I_{\mathrm{Er}} = 7/2$ and $I_{\mathrm{Dy}} = 5/2$, leading to eight and six hyperfine states in the electronic ground state, respectively. Both elements exhibit a rich atomic energy spectrum, arising from their submerged-shell electronic configuration, featuring a [Xe] core, a partially filled inner $4f$ shell, and a closed outer $6s$ shell. The electron vacancy in the $4f$ shell is responsible for the large orbital quantum numbers and the respective high magnetic moments, i.e., $7\mu_B$ and $10\mu_B$ for Er and Dy, with μ_B being the Bohr magneton.

Figures 1(c) and 1(d) show the electronic levels of Er and Dy for wave numbers up to 26 000 cm^{-1} [39]. While most of

*arno.trautmann@uibk.ac.at
†Corresponding author: Francesca.Ferlaino@uibk.ac.at

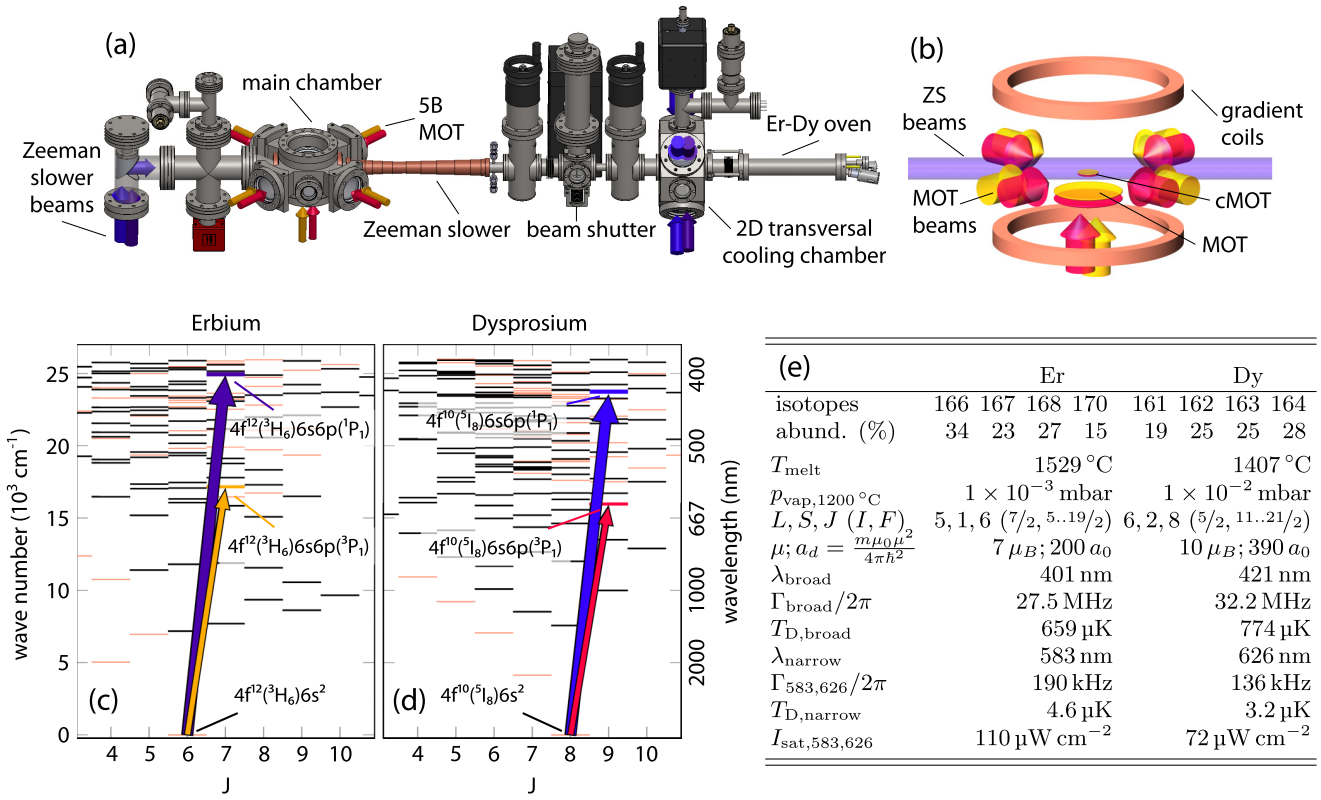

(e)

	Er				Dy			
isotopes	166	167	168	170	161	162	163	164
abund. (%)	34	23	27	15	19	25	25	28
T_{melt}	1529 °C				1407 °C			
$p_{\mathrm{vap,1200\,°C}}$	1×10^{-3} mbar				1×10^{-2} mbar			
$L,S,J\ (I,F)_2$	$5,1,6\ (^7/_2,{}^{5..19}/_2)$				$6,2,8\ (^5/_2,{}^{11..21}/_2)$			
$\mu;a_d=\frac{m\mu_0\mu^2}{4\pi\hbar^2}$	$7\,\mu_B;200\,a_0$				$10\,\mu_B;390\,a_0$			
λ_{broad}	401 nm				421 nm			
$\Gamma_{\mathrm{broad}}/2\pi$	27.5 MHz				32.2 MHz			
$T_{\mathrm{D,broad}}$	659 µK				774 µK			
$\lambda_{\mathrm{narrow}}$	583 nm				626 nm			
$\Gamma_{583,626}/2\pi$	190 kHz				136 kHz			
$T_{\mathrm{D,narrow}}$	4.6 µK				3.2 µK			
$I_{\mathrm{sat},583,626}$	110 µW cm^{-2}				72 µW cm^{-2}			

FIG. 1. Illustration of the vacuum apparatus, including the optical setup for the 5B MOT, and atomic properties of Er and Dy. (a) Er-Dy vacuum apparatus, including the high-temperature oven, transversal cooling chamber, Zeeman slower (ZS), and main chamber. The atomic beam propagates from right to left. The ZS beam is reflected by a metallic mirror in vacuum. (b) Sketch of the working principle of the open-top MOT. Arrows depict MOT beams, and the blue region indicates the ZS beam. For clarity, we depict the atomic clouds displaced from each other. (c, d) Energy level diagrams for Er and Dy up to 26 000 cm^{-1} at different total electronic angular momentum quantum numbers J. States with odd (even) parity are indicated by black (orange) horizontal lines. Arrows show the broad and narrow laser-cooling transitions. (e) Table listing the atomic properties of Er and Dy.

the possible transitions are dipole forbidden, both species offer one particularly broad transition, suitable for laser cooling, to the respective singlet $6s6p$ state [blue arrows in Figs. 1(c) and 1(d)], which we label *broad* in the following. The blue transition light has a wavelength of 401 nm(421 nm), and the transition line width is $\Gamma_{\mathrm{broad}}/2\pi = 27.5$ MHz (32.2 MHz) for Er (Dy) [30,33]. We use this transition for transversal cooling, Zeeman slowing, and absorption imaging. The laser light, driving the broad transition, is derived from grating-stabilized laser diodes, followed by tapered amplifiers and frequency-doubling cavities. The laser systems emit more than 1W of power each. Both systems are frequency-stabilized using signals from modulation-transfer spectroscopy in hollow-cathode lamps [30].

Following previous single-species experiments with Yb [35], Er [30], and Dy [33,34], we produce the MOT using an intercombination line driving the transition from the ground state to the triplet $6s6p$ state [yellow (red) arrow in Figs. 1(c) and 1(d)] at a wavelength of 583 nm(626 nm) in Er (Dy) and a line width of $\Gamma_{583}/2\pi = 190$ kHz($\Gamma_{626}/2\pi = 136$ kHz). The narrow-width character of these transitions leads to the conveniently low Doppler temperatures of $T_{\mathrm{D,Er}} = 4.6\ \mu$K and $T_{\mathrm{D,Dy}} = 3.2\ \mu$K. The laser system for the Er MOT is based on a Raman fiber-amplified diode laser at 1166 nm and a single-pass frequency-doubling stage, with an output power above 1.7 W. The laser system for the Dy MOT is based on two fiber lasers operating at 1050 and 1550 nm, which are amplified and frequency-converted in a single-pass sum-generation stage, resulting in more than 1.6 W of output power. Both MOT laser systems are frequency-stabilized against long-term drifts on a home-built ultralow expansion cavity via a Pound-Drever-Hall lock [40] and have line widths below 100 kHz.

The experimental procedure generalizes our previously demonstrated single-species MOT approach [30] to two-species operation. The very similar strengths and wavelengths of the laser-cooling transitions of Er and Dy and their similar masses and melting points greatly simplify the design of the vacuum apparatus and the experimental procedure for the mixture. Figure 1(a) shows the experimental apparatus. Er and Dy atoms are emitted from a single high-temperature oven, consisting of two sections: The first section (effusion cell) operates at a temperature of 1100 °C, and the second one (hot lip) operates at 1200 °C, unless otherwise stated. Three apertures of different diameters, placed inside the oven, geometrically collimate the Er-Dy atomic beam before it enters the transversal-cooling chamber. We operate the transversal cooling resonantly on the broad transitions with total powers of 300 mW(120 mW) for Er (Dy) and elliptic waists of

approximately $w_{\text{horiz}} = 30$ mm and $w_{\text{vert}} = 6$ mm. We observe that the transversal cooling increases the MOT loading rate by a factor of 10 (6) for Er (Dy). The two-species atomic beam is slowed down to about 5 m/s using a two-species Zeeman slower (ZS) about 35 cm long in the spin-flip configuration. The magnetic-field values along the ZS are experimentally optimized for Dy and work equally well for Er. The two light beams for the ZS of Er and Dy are overlapped using dichroic optics and guided through the ZS via a metallic in-vacuum mirror [41]; see Fig. 1(a). The optimal performance of the ZS has been found for laser powers of 57 mW(121 mW) with beam waists of 4 mm at a detuning of −520 MHz(−530 MHz) for Er (Dy).

The slow atoms are then captured into a two-species MOT, operating on the respective intercombination line. Taking advantage of the similar wavelengths, we combine the MOT beams for both species into the same fibers. The MOT light is spectrally broadened utilizing electro-optic modulators with resonance frequencies of 139 kHz(102 kHz) for Er (Dy), which increases the capture range and thus the number of atoms in the MOT by a factor of 5 (2). The recapture volume is further enhanced by using large MOT beams, with diameters of about 36 mm. We observe an optimal loading for peak intensities of each laser beam of $I_{583} = 50 I_{\text{sat},583}$ and $I_{626} = 160 I_{\text{sat},626}$. Additionally, we endow our main chamber with inverted top and bottom view ports with large clear apertures of 64 mm. As discussed later, our special 5B MOT geometry allows us to completely free the top view, where we will implement a high-resolution *in situ* imaging with a numerical aperture of 0.45, which can resolve structures down to 600 nm. A pair of vertical coils creates a magnetic quadrupole field for the MOT of $\nabla B = 4.6$ G/cm. A vertical bias field of $B_0 = 2.9$ G shifts the zero point of the quadrupole field downwards. Additional coil pairs in the horizontal plane compensate for external magnetic fields.

We produce and study the Er-Dy MOT using two beam configurations. In the first one, we use a standard 6B geometry with three pairs of orthogonal retroreflected beams. For the second configuration, we remove the top → bottom MOT beam, demonstrating for the first time a 5B geometry with an open top; see Fig. 1(b). Although this 5B MOT would not work for alkali MOTs [42], we here demonstrate a very robust operation for our lanthanoid mixture. In the first set of experiments, we study the loading performance of our two-species MOT in both the 6B and the 5B configurations for ^{168}Er and ^{164}Dy. For all atom numbers we report in this paper, we load the MOTs at the optimized detuning for each setting as discussed later (see Fig. 3), apply a compression phase after MOT loading, and detect the atomic clouds using absorption imaging, as described later. Figure 2 shows the Er and Dy atom numbers as a function of the MOT loading time. From a fit to the data using a standard loading function, $N(t) = N_{\text{ss}}(1 - e^{-\gamma t})$, we extract the loading rate R and decay rate γ with the steady-state atom number $N_{\text{ss}} = R/\gamma$ (see Table I). In both the 6B and the 5B configurations, we observe a very efficient loading of the two-species MOT. After about 10 s of loading, the atom numbers approach their steady-state value of some 10^8 atoms (see Table I). We do not observe any mutual influence of one species on the other, as reported for some alkaline mixtures, as, e.g., shown in Refs. [43] and [44].

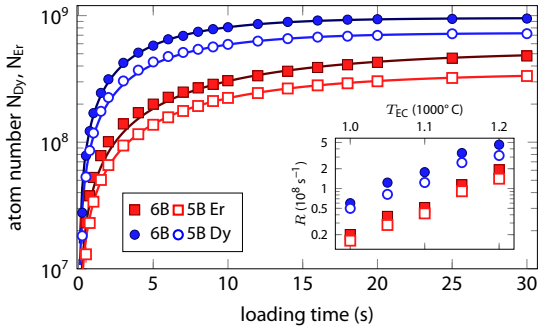

FIG. 2. Loading curve of the two-species MOT for the 6B and 5B configurations. Filled and open squares (circles) show data for the 6B and 5B Er (Dy) MOTs, respectively. The corresponding lines are fits to the data, as detailed in the text. Fit parameters are listed in Table I. Inset: Loading rate of the two species dependent on the effusion cell temperature T_{EC}. Note that the hot lip is always kept at $T_{\text{HL}} = T_{\text{EC}} + 100\,^{\circ}$C.

Given the complex scattering properties and optical spectra of multielectron lanthanoids, this surprising result enables the simultaneous MOT operation and greatly simplifies the experimental sequence.

The difference in the loading curves between Er and Dy is due to their different vapor pressures. The ratio of vapor pressures of Er and Dy is typically higher than 10 at the same temperature [45] and strongly temperature dependent, which would prevent an efficient simultaneous MOT loading. To mitigate this, we selectively heat up the atoms exploiting the two-section design of the oven. We fill the effusion cell with a 33%/67% alloy of Er/Dy and the hot-lip section with pure Er. We operate the oven with a differential temperature of 100 °C between the two sections. In the temperature range from 1000 °C to 1200 °C for the first section, we expect to reduce the vapor-pressure ratio among the two species to about 2.3. We investigate this effect by repeating the loading experiments for different temperatures of the effusion cell, while keeping the hot lip always 100 °C hotter; see Fig. 2 (inset). We observe a roughly constant loading ratio of between 2.5 and 3.5, which confirms the above expectations and shows that our concept of differential heating works very efficiently.

We remarkably find that the performance of the 5B MOT is only slightly below that of the 6B MOT. Moreover, even our 5B double-species MOT shows atom numbers similar to or larger than those previously reported for single-species Er or Dy MOT experiments [29,30,32–34]. Judging from our experience with

TABLE I. Loading rates R, decay rates γ, and steady-state atom numbers N_{ss} obtained from fits to the data shown in Fig. 2. Values for both species in the 5B and 6B configurations are listed. Also listed are the lifetimes obtained from the data in Fig. 4.

	Er		Dy	
	5B	6B	5B	6B
R (10^8 s^{-1})	0.35(1)	0.45(2)	1.21(4)	1.79(3)
γ (s^{-1})	0.100(2)	0.086(6)	0.166(7)	0.187(5)
N_{ss} (10^8)	3.5(1)	4.5(3)	7.3(4)	9.6(3)
Lifetime cMOT (ms)	515(65)	475(50)	374(44)	345(23)

Er [30], we are thus confident that these numbers are sufficient for reaching quantum degeneracy. The 5B MOT configuration has the advantage of automatically spin-polarizing the atoms and providing full optical access through the vertical top view port, allowing implementation of optical setups which require large numerical apertures, e.g., high-resolution imaging or angle-resolved Bragg spectroscopy.

The simultaneous cooling and polarization of the intercombination MOT in lanthanoids has been studied for single-species Er [30] and Dy [34] 6B MOTs. In brief, the combined effects of a narrow-line MOT and gravity yield a peculiar semi-shell-shaped MOT with its center lying below the zero of the magnetic quadrupole field; see Fig. 1(b). The center position of the MOT can be adjusted by changing the MOT detuning. For large enough vertical displacement of the MOT, i. e., detuning, the atoms predominantly absorb σ^--polarized photons, which are coming from the bottom-top beam. As a consequence, the atoms are spin-polarized into the lowest Zeeman sublevel. For lower detuning, the atoms can absorb both σ^+ and σ^- light and the sample is unpolarized [34]. With our 5B MOT, we bring this concept to the extreme: We completely remove the (σ^+) top-bottom beam and force the atoms to sit only below the zero of the magnetic field. We verified the spin polarization by performing spin-resolved absorption imaging using the Stern-Gerlach technique. Within our experimental resolution, we do not detect atoms in higher Zeeman sublevels [46]. Thanks to this spontaneous spin polarization, optical-pumping schemes are not necessary. The spin purity is very beneficial for future loading of the mixture into an optical dipole trap, where the presence of additional spin states can lead to atomic losses via inelastic dipolar relaxation processes.

In the second set of experiments, we systematically study the effect of MOT-light detuning from the respective resonant atomic frequency on the atom number and compare the results for the 6B and 5B configurations after 5s of loading; see Fig. 3. For both species, we see a clear rise of atom numbers with increasing detuning. After reaching a maximum value the numbers undergo a sharp decrease at large detunings. This decrease can be simply explained by the spatial downshift of the MOT position with increasing detuning, eventually causing the atoms to leave the recapture volume. Here, the equal behavior of the 6B and 5B MOTs indicates that the top-bottom beam does not play a significant role. At intermediate detunings, however, the two configurations clearly show different behaviors. In particular, the 6B MOT has a much broader range of operation than the 5B configuration. We believe that this difference is due to the fact that the central cloud position approaches the magnetic-field zero point with decreasing detuning. In the absence of the top-bottom beam, atoms above the magnetic-field zero do not experience a restoring light force towards the trap center and may escape from the MOT. Contrariwise, in the 6B approach, these atoms are retrapped, resulting in the broader operation range in terms of detuning.

As observed in previous experiments [33], the Dy atom number shows a small dip at detunings around $-70\Gamma_{626\,\mathrm{nm}}$. We attribute this feature to a partial overlap of the cloud with the ZS light beam, which drives off-resonant pumping processes resulting in atom losses [30]. For Er, the influence of the ZS light is weaker due to its lower light intensity and larger relative detuning, and this effect is not observed.

Finally, we study the lifetime of the mixture in the compressed MOT (cMOT). The compression phase is essential to efficiently load an optical dipole trap in future experiments, as the compression reduces the temperature and increases the density of the mixture. After loading the MOT, we switch off the spectral broadening electro-optic modulators, the ZS beams, and block the atomic beam with a mechanical shutter. The compression has a duration of 200 ms, during which we (i) reduce the detuning of the MOT light to $10\,\Gamma_{583}$ ($18\,\Gamma_{626}$), (ii) decrease the MOT-beam power to $I_{583} = 0.17 I_{\mathrm{sat},583}$ and $I_{626} = 0.6 I_{\mathrm{sat},626}$, (iii) ramp down the magnetic-field gradient to $\nabla B = 4.3$ G cm^{-1}, and (iv) switch off the vertical bias magnetic field. As shown in Fig. 4, we observe that the double-species cMOT has a lifetime that is fully sufficient for loading of atoms into an optical dipole trap, which typically requires a holding time of about 100 ms. The data are taken in dual operation, with both species present in all settings. Again,

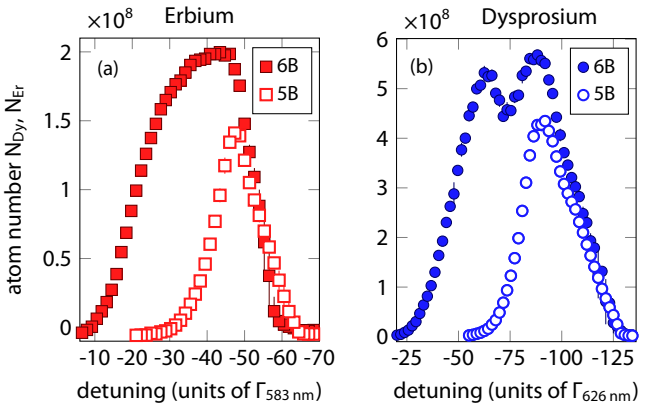

FIG. 3. Dependence of atom numbers in the cMOT on the initial MOT detuning, in units of the respective linewidth of the narrow transition of $\Gamma_{583}/2\pi = 190$ kHz($\Gamma_{626}/2\pi = 136$ kHz) for Er (Dy). Both species show broad ranges of detuning for efficient MOT loading in the 6B configuration, while 5B shows a narrower range. The optimal detunings are nearly equal for the 5B and 6B configurations. Data were taken for 5 s of MOT loading.

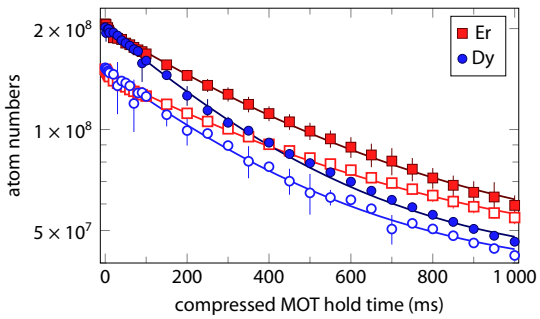

FIG. 4. Lifetime of the cMOT for both Er (red) and Dy (blue) in the 5B (open symbols) and 6B (filled symbols) configurations. We adjust the MOT loading time to compare samples with equal atom numbers. Solid lines show exponential fits to the respective data. From the fits we extract lifetimes of 515(65) and 475(5) ms [374(44) and 345(23) ms] for Er [Dy] in the 5B and 6B cMOTs, respectively.

we do not see any interplay between the species. The results of fits to the lifetime data are listed in Table I. Additionally, we extract temperatures of 11(1) μK [10(1) μK] for Er [Dy] in both the 5B and the 6B configurations from time-of-flight measurements. We observe that lower temperatures close to the Doppler temperatures can be achieved with different sets of parameters, at the expense of lower atom numbers. From our experience, we are certain that the observed lifetimes and temperatures are fully sufficient for efficient loading into an optical dipole trap as the next step towards quantum degeneracy.

The data we present here refer to the mixture of ^{168}Er and ^{164}Dy. Moreover, we are also able to trap and cool all other abundant bosonic isotopes with equally good performance, except for the ^{170}Er MOT, which has smaller numbers, as expected from its low natural abundance. For future studies of the fermionic isotopes, no changes in the experimental apparatus are necessary.

In conclusion, we have demonstrated efficient cooling and trapping of an Er-Dy mixture in a two-species MOT operating on narrow-line transitions. In addition, we demonstrate a beam geometry for our two-species MOT which consists of only five laser beams in an open-top orthogonal setting. This geometry has the big advantage of providing free optical access from the top with a large numerical aperture, greatly simplifying the implementation, e.g., of high-resolution imaging, as well as optical lattices. Our recorded temperatures and atom numbers provide ideal conditions for subsequent evaporative cooling, towards the first production of a quantum-degenerate dipolar mixture. Optimization of the optical-trap loading and evaporative cooling is under way in our laboratory.

We acknowledge A. Frisch, T. Pyragius, and C. Zhang for support in the initial phase of the experiment. We thank the ERBIUM and the Dy-K teams in Innsbruck, the Er team at Harvard, and M. Sohmen and C. Politi for fruitful discussions. This work was supported by an ERC Consolidator Grant (RARE; No. 681432) and a FET Proactive Project (RySQ; No. 640378) of EU H2020. G.D. acknowledges support from the Austrian Science Fund FWF within DK-ALM: W1259-N27.

[1] Z. Hadzibabic, C. A. Stan, K. Dieckmann, S. Gupta, M. W. Zwierlein, A. Görlitz, and W. Ketterle, Phys. Rev. Lett. **88**, 160401 (2002).
[2] G. Roati, F. Riboli, G. Modugno, and M. Inguscio, Phys. Rev. Lett. **89**, 150403 (2002).
[3] G. Barontini, C. Weber, F. Rabatti, J. Catani, G. Thalhammer, M. Inguscio, and F. Minardi, Phys. Rev. Lett. **103**, 043201 (2009).
[4] R. Pires, J. Ulmanis, S. Häfner, M. Repp, A. Arias, E. D. Kuhnle, and M. Weidemüller, Phys. Rev. Lett. **112**, 250404 (2014).
[5] S.-K. Tung, K. Jiménez-García, J. Johansen, C. V. Parker, and C. Chin, Phys. Rev. Lett. **113**, 240402 (2014).
[6] L. J. Wacker, N. B. Jørgensen, D. Birkmose, N. Winter, M. Mikkelsen, J. Sherson, N. Zinner, and J. J. Arlt, Phys. Rev. Lett. **117**, 163201 (2016).
[7] A. Schirotzek, C.-H. Wu, A. Sommer, and M. W. Zwierlein, Phys. Rev. Lett. **102**, 230402 (2009).
[8] M. Koschorreck, D. Pertot, E. Vogt, B. Fröhlich, M. Feld, and M. Köhl, Nature **485**, 619 (2012).
[9] C. Kohstall, M. Zaccanti, M. Jag, A. Trenkwalder, P. Massignan, G. M. Bruun, F. Schreck, and R. Grimm, Nature **485**, 615 (2012).
[10] T. Rentrop, A. Trautmann, F. A. Olivares, F. Jendrzejewski, A. Komnik, and M. K. Oberthaler, Phys. Rev. X **6**, 041041 (2016).
[11] N. B. Jørgensen, L. Wacker, K. T. Skalmstang, M. M. Parish, J. Levinsen, R. S. Christensen, G. M. Bruun, and J. J. Arlt, Phys. Rev. Lett. **117**, 055302 (2016).
[12] K.-K. Ni, S. Ospelkaus, M. H. G. de Miranda, A. Pe'er, B. Neyenhuis, J. J. Zirbel, S. Kotochigova, P. S. Julienne, D. S. Jin, and J. Ye, Science **322**, 231 (2008).
[13] T. Takekoshi, L. Reichsöllner, A. Schindewolf, J. M. Hutson, C. R. Le Sueur, O. Dulieu, F. Ferlaino, R. Grimm, and H.-C. Nägerl, Phys. Rev. Lett. **113**, 205301 (2014).
[14] P. K. Molony, P. D. Gregory, Z. Ji, B. Lu, M. P. Köppinger, C. R. Le Sueur, C. L. Blackley, J. M. Hutson, and S. L. Cornish, Phys. Rev. Lett. **113**, 255301 (2014).
[15] G. Pupillo, A. Micheli, H. P. Büchler, and P. Zoller, in *Cold Molecules: Creation and Applications*, edited by R. V. Krems, B. Friedrich, and W. C. Stwalley (Taylor & Francis, London, 2004), pp. 266–290.
[16] A. Griesmaier, J. Werner, S. Hensler, J. Stuhler, and T. Pfau, Phys. Rev. Lett. **94**, 160401 (2005).
[17] Q. Beaufils, R. Chicireanu, T. Zanon, B. Laburthe-Tolra, E. Maréchal, L. Vernac, J.-C. Keller, and O. Gorceix, Phys. Rev. A **77**, 061601 (2008).
[18] M. Lu, N. Q. Burdick, S. H. Youn, and B. L. Lev, Phys. Rev. Lett. **107**, 190401 (2011).
[19] M. Lu, N. Q. Burdick, and B. L. Lev, Phys. Rev. Lett. **108**, 215301 (2012).
[20] K. Aikawa, A. Frisch, M. Mark, S. Baier, A. Rietzler, R. Grimm, and F. Ferlaino, Phys. Rev. Lett. **108**, 210401 (2012).
[21] K. Aikawa, A. Frisch, M. Mark, S. Baier, R. Grimm, and F. Ferlaino, Phys. Rev. Lett. **112**, 010404 (2014).
[22] K. Aikawa, S. Baier, A. Frisch, M. Mark, C. Ravensbergen, and F. Ferlaino, Science **345**, 1484 (2014).
[23] H. Kadau, M. Schmitt, M. Wenzel, C. Wink, T. Maier, I. Ferrier-Barbut, and T. Pfau, Nature **530**, 194 (2016).
[24] M. Schmitt, M. Wenzel, F. Böttcher, I. Ferrier-Barbut, and T. Pfau, Nature **539**, 259 (2016).
[25] L. Chomaz, S. Baier, D. Petter, M. J. Mark, F. Wächtler, L. Santos, and F. Ferlaino, Phys. Rev. X **6**, 041039 (2016).
[26] L. Chomaz, R. M. W. van Bijnen, D. Petter, G. Faraoni, S. Baier, J. H. Becher, M. J. Mark, F. Waechtler, L. Santos, and F. Ferlaino, arXiv:1705.06914.
[27] Y. Tang, W. Kao, K.-Y. Li, S. Seo, K. Mallayya, M. Rigol, S. Gopalakrishnan, and B. L. Lev, arXiv:1707.07031.
[28] R. K. Kumar, P. Muruganandam, L. Tomio, and A. Gammal, J. Phys. Commun. **1**, 035012 (2017).
[29] A. J. Berglund, S. A. Lee, and J. J. McClelland, Phys. Rev. A **76**, 053418 (2007).
[30] A. Frisch, K. Aikawa, M. Mark, A. Rietzler, J. Schindler, E. Zupanič, R. Grimm, and F. Ferlaino, Phys. Rev. A **85**, 051401 (2012).

[31] J. Ulitzsch, D. Babik, R. Roell, and M. Weitz, Phys. Rev. A **95**, 043614 (2017).
[32] M. Lu, S. H. Youn, and B. L. Lev, Phys. Rev. Lett. **104**, 063001 (2010).
[33] T. Maier, H. Kadau, M. Schmitt, A. Griesmaier, and T. Pfau, Opt. Lett. **39**, 3138 (2014).
[34] D. Dreon, L. A. Sidorenkov, C. Bouazza, W. Maineult, J. Dalibard, and S. Nascimbene, J. Phys. B **50**, 065005 (2017).
[35] T. Kuwamoto, K. Honda, Y. Takahashi, and T. Yabuzaki, Phys. Rev. A **60**, R745(R) (1999).
[36] D. Sukachev, A. Sokolov, K. Chebakov, A. Akimov, S. Kanorsky, N. Kolachevsky, and V. Sorokin, Phys. Rev. A **82**, 011405 (2010).
[37] J. Miao, J. Hostetter, G. Stratis, and M. Saffman, Phys. Rev. A **89**, 041401 (2014).
[38] H. Katori, T. Ido, Y. Isoya, and M. Kuwata-Gonokami, Phys. Rev. Lett. **82**, 1116 (1999).
[39] A. Kramida, Yu. Ralchenko, J. Reader, and NIST ASD Team, *NIST Atomic Spectra Database (version 5)* [online]. Available at: http://physics.nist.gov/asd. Accessed: 13 February 2018.
[40] R. W. P. Drever, J. L. Hall, F. V. Kowalski, J. Hough, G. M. Ford, A. J. Munley, and H. Ward, Appl. Phys. B **31**, 97 (1983).
[41] The atomic beam of Er and Dy might deposit an additional metallic layer on the mirror. However, we have tested this effect in our running Er machine and did not observe any sizable reduction in the reflectivity of the mirror.
[42] For the sake of completeness, we note that early MOT experiments on alkali atoms have explored MOT geometries with five non–orthogonally intersecting beams (e.g., at an angle of 120°) [47,48], which constitutes a very different scenario compared to our open-top approach.
[43] U. Schlöder, H. Engler, U. Schünemann, R. Grimm, and M. Weidemüller, Eur. Phys. J. D **7**, 331 (1999).
[44] M. Taglieber, A.-C. Voigt, F. Henkel, S. Fray, T. W. Hänsch, and K. Dieckmann, Phys. Rev. A **73**, 011402 (2006).
[45] C. E. Habermann and A. H. Daane, J. Chem. Phys. **41**, 2818 (1964).
[46] Since the large spatial extension of the MOT might mask residual atoms in higher spin states, we performed preliminary Stern-Gerlach mapping after loading the atoms into an optical dipole trap. Again, we did not detect atoms in higher Zeeman sublevels.
[47] J. Arlt, P. Bance, S. Hopkins, J. Martin, S. Webster, A. Wilson, K. Zetie, and C. J. Foot, J. Phys. B **31**, L321 (1998).
[48] A. di Stefano, D. Wilkowski, J. Müller, and E. Arimondo, Appl. Phys. B **69**, 263 (1999).

Chapter 3

Quantum mixtures

Ultracold atoms have proved to be a great system for fundamental research, precision measurements, and quantum simulations [Cor02, Chi15]. Their high degree of control allows for an investigation of a multitude of phenomena beyond atomic physics: complex systems typical of condensed matter, few-body and many-body physics, and cold chemistry — to name some of the possibilities. A natural step beyond the intriguing physics available in homonuclear systems consists of studying more complex systems such as mixtures. They include homonuclear systems in different spin states, isotopic combinations of the same atomic species, and heteronuclear mixtures of multiple elements. More examples, not discussed within this thesis, are mixtures involving metastable noble gases [Vas12], trapped cold molecules [Car09], and hybrid atom-ion systems [Tom19].

Mass and population imbalance, mixed statistic, species-selective manipulations, and intrinsic distinct properties are all tools made available by using mixtures. They become suitable platforms to investigate new physical phenomena, e. g. impurity physics, polarons, exotic phases and molecule formations. In most of these applications, an important role is played by Feshbach resonances, allowing the tuning of the interparticle interactions and the magnetoassociation of weakly bound molecules (see Chap. 4).

In this chapter, we present the first experimental realization of a quantum-degenerate dipolar mixture of erbium-dysprosium atoms in several isotopic combinations. Up to our knowledge, this is the first experiment which approached the further step of combining two magnetic lanthanide species. The chapter begins with a theoretical introduction to the topic of quantum degeneracy in heteronuclear mixtures described in Sec. 3.1. Thereafter, Sec. 3.2 reviews the advances in the field by comparing the results achieved in mixture experiments. In the same section, a digression on the particular case of lanthanide mixture of erbium-dysprosium can be found. Sec. 3.3 includes the publication *Quantum Mixtures of Erbium and Dysprosium Atoms* [Tra18].

3.1 Theory of quantum mixture

Predicted in the early 1920s by Satyendra Nath Bose and Albert Einstein [Bos24, Ein24, Ein25], a Bose-Einstein condensate is a state of matter in which a large fraction of particles of a system occupies the lowest quantum state. In an ideal non-interacting dilute gas in

thermodynamic equilibrium at a temperature T, quantum-statistical effects become relevant when the particles' extension associated with de Broglie wavelength λ_{dB} is on the same order of the interparticle spacing n^{-3}. In other words, when the phase space density (PSD)

$$PSD = n\lambda_{\mathrm{dB}}^3 = n\left(\frac{2\pi\hbar}{mk_{\mathrm{B}}T}\right)^{3/2} \tag{3.1}$$

is larger than one [Ket99]. Here $\hbar$ is the reduced Planck constant, k_{B} is the Boltzmann constant, and m the particle's mass. By further increasing the PSD, there is a critical value for which the system undergoes a purely quantum-statistical phase transition. In a three-dimensional box, the condition is $PSD \gtrsim 2.612$.

To capture the behavior of a many-body system, the treatment must include interactions. A very common mean-field description of BECs is based on the *Gross-Pitaevskii equation* (GPE) approach [Pit16]. In the following, we make use of this approach for a dilute gas in a harmonic trap.

This section introduces the reader to the physics of quantum gases and, in particular, to the case of quantum mixtures. We first develop the mean-field description of an interacting Bose gas in a harmonic trap in Sec. 3.1.2. Thereafter, we discuss the solutions of the GPE in Sec. 3.1.3 in both cases of heteronuclear and dipolar systems. This section follows the theoretical treatment proposed in Ref. [Pet08].

3.1.1 Contact and dipolar interactions

To understand a dipolar quantum gas in the mean-field description, we need to introduce the concept of pseudo-potential, that is a simplified version of the complex interatomic potential. In the case of dipolar atoms, for two particles at distance $\mathbf{r}$, we can write such potential $V_{\mathrm{int}}(\mathbf{r})$ as a sum of the contributions coming from the contact $V_{\mathrm{c}}(\mathbf{r})$ and dipolar $V_{\mathrm{dd}}(\mathbf{r})$ interactions:

$$V_{\mathrm{int}}(\mathbf{r}) = V_{\mathrm{c}}(\mathbf{r}) + V_{\mathrm{dd}}(\mathbf{r}). \tag{3.2}$$

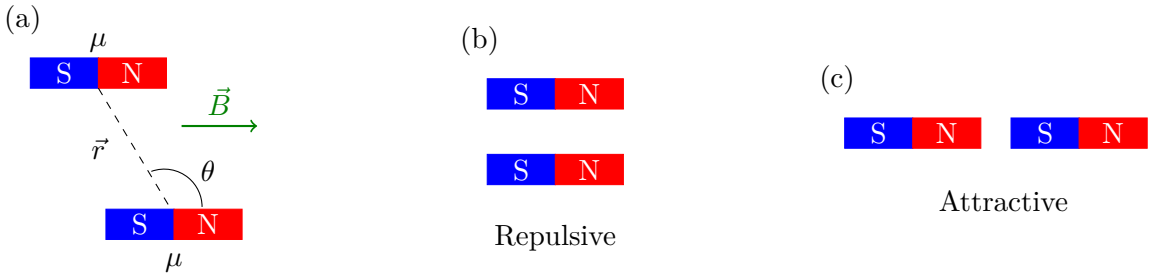

Figure 3.1: Dipole-dipole interactions of two polarized dipoles. (a) Sketch of the geometry. (b) In a side-by-side configuration, the DDI are repulsive. (c) In a head-to-tail configuration, the DDI are attractive.

Contact interactions At low energy, we can replace the contact interaction term with a spherically symmetric zero-range contact potential in the form:

$$V_{\mathrm{c}}(\mathbf{r}) = g_{1,2}\delta(\mathbf{r}) = \frac{2\pi\hbar^2}{m_{12}} a_{1,2}\delta(\mathbf{r}) \tag{3.3}$$

where m_{12} is the particles' reduced mass, $\delta(\mathbf{r})$ is the Dirac delta function, g accounts for the coupling strength and a is the s-wave scattering length as discussed in Chap. 4. For the ease of reading, in the case of single-species interactions, we write $g_{\mathrm{i,i}} = g_{\mathrm{i}}$.

Dipole-dipole interactions The long-range and anisotropic DDI for two dipoles aligned by an external magnetic field can be written as:

$$V_{\mathrm{dd}}(\mathbf{r}) = \frac{\mu_1\mu_2\mu_0}{4\pi} \frac{1 - 3\cos^2\theta}{|\mathbf{r}|^3} \tag{3.4}$$

where μ_0 is the vacuum permeability, μ_1 and μ_2 are the particles' magnetic moments, and θ is the angle between $\mathbf{r}$ and the magnetic field (see Eq. 3.1). In analogy with Eq. 3.3, we can define the *characteristic dipolar length*:

$$a_{\mathrm{dd}} = \frac{\mu_1\mu_2\mu_0 m_{12}}{6\pi\hbar^2} \tag{3.5}$$

in such a way to compare directly contact and dipolar strength via the ratio

$$\epsilon_{\mathrm{dd}} = \frac{a_{\mathrm{dd}}}{a}. \tag{3.6}$$

For $\epsilon_{\mathrm{dd}} > 1$, the system is DDI dominated. It is worth to note that, a — therefore ϵ_{dd} — can be tuned by means of Feshbach resonances (see Chap. 4), thus entering different regimes of dipolarity. For the sake of completeness, a itself is generally dependent on the DDI even though such dependency is weak and it is usually accounted in the experimental measurements [Ron06].

3.1.2 Mean-field description and Gross-Pitaevskii equation

In a mean-field description, every particle interacts with a mean-field potential (see Sec. 3.1.1) reproducing the complex interaction pattern coming from the rest of the system in a simplified way. Now, let's consider an interacting gas of N identical bosonic particles trapped in an external harmonic potential V_{ext}. We can define the condensate wave-function $\psi(\mathbf{r})$ and its density distribution $n(\mathbf{r}) = |\psi(\mathbf{r})|^2$. The time-dependent GPE acquires the form:

$$i\hbar\frac{\partial}{\partial t}\psi(\mathbf{r},t) = \left[-\frac{\hbar^2}{2m}\boldsymbol{\nabla}^2 + V_{\mathrm{ext}}(\mathbf{r}) + V_{\mathrm{int}}(\mathbf{r})\right]\psi(\mathbf{r},t) \tag{3.7}$$

where V_{int} is described in Eq. 3.9. If we assume that $\psi(\mathbf{r},t) = \psi(\mathbf{r})\,\mathrm{e}^{-i\mu_{\mathrm{c}}t/\hbar}$ with μ_{c} being the chemical potential, we can derive the time-independent GPE

$$\mu_{\mathrm{c}}\psi(\mathbf{r}) = \left[-\frac{\hbar^2}{2m}\boldsymbol{\nabla}^2 + V_{\mathrm{ext}}(\mathbf{r}) + V_{\mathrm{int}}(\mathbf{r})\right]\psi(\mathbf{r}). \tag{3.8}$$

In the mean-field approach, Eq. 3.2 becomes

$$V_{\text{int}}(\mathbf{r}) = gn(\mathbf{r}) + \int \frac{\mu^2\mu_0}{4\pi}\frac{1-3\cos^2\theta}{|\mathbf{r}|^3}n(\mathbf{r})\,\mathrm{d}\mathbf{r} \tag{3.9}$$

and, given trap frequencies $(\omega_x, \omega_y, \omega_z)$, the harmonic trapping potential can be written as

$$V_{\text{ext}}(\mathbf{r}) = \frac{m}{2}\left(\omega_x^2 x^2 + \omega_z^2 z^2 + \omega_z^2 z^2\right). \tag{3.10}$$

It is useful to define $\bar{\omega} = (\omega_{\text{x}}\omega_{\text{y}}\omega_{\text{z}})^{1/3}$ denoting the geometric mean of the trap frequencies. From here on, we work under the so called *Thomas-Fermi approximation* (TF) which neglects the kinetic term in the GPE. Such approximation is true for a sufficiently large particle number and leads to

$$\mu_{\text{c}} = V_{\text{ext}}(\mathbf{r}) + V_{\text{int}}(\mathbf{r}). \tag{3.11}$$

Heteronuclear dipolar BECs

After preparing the formalism for a one-component BEC, the next step consists of extending it to the case of two-components BECs. The problem results now in a system of coupled equations where the interspecies interactions (both contact and DD) have to be taken into account. For two species 1 and 2, we can write:

$$\begin{aligned}\mu_{\text{c},1} &= V_{\text{ext},1}(\mathbf{r}) + V_{\text{int},1}(\mathbf{r}) + V_{\text{int},12}(\mathbf{r})\\ \mu_{\text{c},2} &= V_{\text{ext},2}(\mathbf{r}) + V_{\text{int},2}(\mathbf{r}) + V_{\text{int},21}(\mathbf{r})\end{aligned} \tag{3.12}$$

where $V_{\text{ext},1}$ and $V_{\text{ext},2}$ are written like in Eq. 3.9 and, for $i \neq j$ and $i, j = 1, 2$,

$$V_{\text{int,ij}}(\mathbf{r}) = \frac{2\pi\hbar^2}{m_{12}}a_{\text{i,j}}n_{\text{j}}(\mathbf{r}) + \int \frac{\mu_{\text{i}}\mu_{\text{j}}\mu_0}{4\pi}\frac{1-3\cos^2\theta}{|\mathbf{r}|^3}n_{\text{j}}(\mathbf{r})\,\mathrm{d}\mathbf{r}\,. \tag{3.13}$$

Note that, $a_{12} = a_{21}$ indicates the interspecies scattering length which is unknown in erbium-dysprosium mixtures. Here, we did not consider the case of spinor condensate in which the particle number is not conserved.

3.1.3 Solutions to the Gross-Pitaevskii equation

Although the study of systems described by Eq. 3.12 might be complicated, we review two simpler cases: one-component dipolar BEC and two-component contact-interacting BECs. The heteronuclear dipolar BEC case is only mentioned for completeness due to the intrinsic difficulties of the methods required for achieving numerical solutions, going beyond the scope of this thesis. For a more systematic treatment, the reader is encouraged to follow the references highlighted in the respective paragraph.

Homonuclear dipolar system

Let's consider the time-independent GPE in the TF approximation leading to Eq. 3.11. For simplicity, we assume the BEC to be confined in a cigar-shaped trap with radial (ρ)

$\omega_x = \omega_y = \omega_\perp$ and axial (z) $\omega_\parallel$ confinement and dipoles oriented along the z-axis. The condensate's profile deviates from the typical Gaussian shape of the non-interacting gas to a quadratic shape

$$n(\mathbf{r}) = n_0 \left(1 - \frac{\rho^2}{R_\rho^2} - \frac{z^2}{R_z^2}\right) = \frac{15}{8\pi}\frac{N}{R_\rho^2 R_z}\left(1 - \frac{\rho^2}{R_\rho^2} - \frac{z^2}{R_z^2}\right) \tag{3.14}$$

where R_ρ and R_z are the TF radii and n_0 the peak density. The profile of the BEC is modified due to the influence of the DDI term over the contact one and $R_\rho = \kappa R_z$ differs from $\omega_\parallel = \lambda\omega_\perp$ where the cloud's aspect ratio κ and the trap's aspect ratio λ follow the condition

$$3\kappa^2\epsilon_{dd}\left[\left(\frac{\lambda^2}{2}+1\right)\frac{f_{dip}(\kappa)}{1-\kappa^2}\right] + (\epsilon_{dd}-1)(\kappa^2-\lambda^2) = 0. \tag{3.15}$$

The function

$$f_{dip}(\kappa) = \frac{1+2\kappa^2}{1-\kappa^2} - \frac{3\kappa^2 \arctan\left(\sqrt{1-\kappa^2}\right)}{(1-\kappa^2)^{3/2}} \tag{3.16}$$

is called *dipolar anisotropic function* and allows us to write the chemical potential as $\mu_c = gn_0[1 - \epsilon_{dd} f_{dip}(\kappa)]$. The TF radii are then written as

$$\begin{aligned} R_\rho &= \left(\frac{15gN\kappa}{4\pi m\omega_\perp^2}\left[1 + \epsilon_{dd}\left(\frac{3}{2}\frac{\kappa^2 f_{dip}(\kappa)}{1-\kappa^2} - 1\right)\right]\right)^{1/5} \\ R_z &= \frac{1}{\kappa}R_\rho \end{aligned} \tag{3.17}$$

and one of the typical effects arising from this is the so-called *magnetostriction* [Stu07]. In this picture, a dipolar condensate is stable when the TF energy per particle is positive

$$\frac{E}{N} = \frac{1}{14}m\omega_\perp^2 R_\rho^2\left(2 + \frac{\lambda^2}{\kappa^2}\right) + \frac{15\hbar^2}{7m}\frac{aN}{R_\rho^2 R_z}(1 - \epsilon_{dd} f_{dip}(\kappa)) \tag{3.18}$$

and one of the most known effects is the d-wave collapse reported for the first time in a BEC of Cr atoms [Lah08].

Heteronuclear contact-interacting system

In the case of purely contact interacting BECs, we can neglect the DDI term in the GPE leading to:

$$\begin{aligned} \mu_{c,1} &= V_{ext,1}(\mathbf{r}) + g_1 n_1(\mathbf{r}) + g_{1,2} n_2(\mathbf{r}) \\ \mu_{c,2} &= V_{ext,2}(\mathbf{r}) + g_2 n_2(\mathbf{r}) + g_{1,2} n_1(\mathbf{r}). \end{aligned} \tag{3.19}$$

If the gas is homogeneous and the densities n_i of the two components are constant, the stability is obtained when the energy increases under densities' deviations. Such condition can be put down in formula as

$$\frac{\partial\mu_{c,1}}{\partial n_1} > 0, \quad \frac{\partial\mu_{c,2}}{\partial n_2} > 0, \quad \text{and} \quad \frac{\partial\mu_{c,1}}{\partial n_1}\frac{\partial\mu_{c,2}}{\partial n_2} - \frac{\partial\mu_{c,1}}{\partial n_2}\frac{\partial\mu_{c,2}}{\partial n_1} > 0. \tag{3.20}$$

If the gases are trapped in isotropic and harmonic potentials for which $V_{\mathrm{ext},2} = \lambda V_{\mathrm{ext},1}$ and $\lambda = m_2\omega_2^2/m_1\omega_1^2$, the density profiles can be derived to be as

$$\begin{aligned} n_1(r) &= \frac{\mu_{\mathrm{c},1}}{g_1}\frac{1}{1-g_{1,2}^2/g_1g_2}\left[1-\frac{\mu_{\mathrm{c},2}}{\mu_{\mathrm{c},1}}\frac{g_{1,2}}{g_2}-\frac{r^2}{R_1^2}\left(1-\lambda\frac{g_{1,2}}{g_2}\right)\right] \\ n_2(r) &= \frac{\mu_{\mathrm{c},2}}{g_2}\frac{1}{1-g_{1,2}^2/g_1g_2}\left[1-\frac{\mu_{\mathrm{c},1}}{\mu_{\mathrm{c},2}}\frac{g_{1,2}}{g_1}-\frac{r^2}{R_2^2}\left(1-\frac{1}{\lambda}\frac{g_{1,2}}{g_1}\right)\right] \end{aligned} \tag{3.21}$$

where the length R_{i} is defined by $\mu_{\mathrm{c,i}} = m_{\mathrm{i}}\omega_{\mathrm{i}}^2R_{\mathrm{i}}^2/2$. Depending on the interplay between interspecies and intraspecies interactions, the two gases might merge in some region of space and might not in others. In such formalism, we recover the one-component case when one of the species is absent. If one of the two components is a minority, it can be treated like an impurity. Such an impurity moves either to the center or to the surface of the majority species depending on $g_{1,2}$.

Heteronuclear dipolar system

The coupled GPEs problem with magnetic species (Eq. 3.12) is rather non-trivial and it is solvable only numerically. The interest in such a system started to rise recently and the exploration of a variety of phenomena just began. Among these, theoretical investigation on the miscibility of two-components BECs [Gac10, Wil12, Kum17a], on binary magnetic quantum droplets [Smi20], and on vortices and vortex lattices [Zha15, Kum17b, Mar17] has been done. In Refs. [Kai14, PA18, Wen18], the authors follow an impurity-physics approach to study properties of dipolar polarons.

3.2 Mixture experiments overview

In the introduction of this chapter we saw how single-component and multi-component ultracold gases are a valuable platform to approach physics on many different levels. Since their prediction in the 1920's, it took about 70 years of technical development to observe the first BEC [And95, Dav95]. Subsequent to such milestone, many other elements were brought to degeneracy from several groups around the world and many experiments with different degrees of complexity are spreading new light on the topic every year. Up to now, a total of 13 elements were brought to degeneracy, either BEC or DFG. Listed in order of appearance on the periodic table, they are: hydrogen [Fri98], helium [Rob01, PDS01, McN06], lithium [Bra95, Tru01, Sch01], sodium [Dav95], potassium [DeM99, Mod01], rubidium [And95], cesium [Web03], calcium [Kra09], strontium [Ste09, dE09, DeS10, Tey10], chromium [Gri05, Nay15], dysprosium [Lu11a, Lu12], erbium [Aik12, Aik14b], thulium [Dav20], and ytterbium [Tak03, Fuk07].

Over the years, ultracold atoms experiments have advanced so far that single-component quantum gases can be controlled and probed down to individual atom precision (e. g. single atom detection and quantum gas microscopy [Ott16, Kuh16]). From this point of view, experiments moved towards more complex objects and the focus has shifted to the creation of multi-component mixtures. Whether the final goal is the research performed on independent

Table 3.1: Dipole moments and dipolar lengths for different atomic and molecular species. Dipole moments are in unit of μ_B for magnetic dipoles and D for electric dipoles. The dipolar length in units of a_0 allows for a direct comparison across species. Values from Ref. [Gad16].

Species	Dipole moment	$a_{dd}(a_0)$
^{87}Rb	$0.5\,\mu_B$	0.18
^{52}Cr	$6\,\mu_B$	15
^{164}Dy	$10\,\mu_B$	130
^{168}Er	$7\,\mu_B$	67
^{168}Er$_2$	$14\,\mu_B$	533
KRb	0.57 D	3.9×10^3
RbCs	1.2 D	3×10^4
NaK	2.7 D	4.4×10^4
NaRb	3.3 D	1.1×10^5
KCs	1.9 D	6×10^4
LiK	3.5 D	5.3×10^4
LiRb	4.1 D	2×10^5
LiCs	5.5 D	4×10^5
RbSr	1.5 D	3.9×10^4
RbYb	0.21 D	1.1×10^3
LiYb	<0.1 D	<200
*OH	1.7 D	4.5×10^3
KBr	10.4 D	1.2×10^6

components or associating them in ultracold molecules (eventually by magnetoassociation over Feshbach resonances, see Chap. 4), the scientific interest and the techniques used are widely shared. Often, these two directions of investigation move together and they can be two parts of the same project. It has to be kept in mind that, in most of the cases, knowledge about the mixture's scattering properties is limited to theoretical prediction or completely absent.

Despite single-component combinations of different spin states or different isotopes [Mya97, Ste98, Tru01, Sch01], considerable importance has been given to heteronuclear mixtures for the possibility of further enriching the properties of the system. In this section, we review the progress achieved on alkali-alkali (Sec. 3.2.1) and alkali-nonalkali (Sec. 3.2.2) experiments. In Sec. 3.2.3, our erbium-dysprosium system is introduced.

3.2.1 Alkali-alkali mixtures

Following the earliest advances and considering the extensive knowledge on single-species alkali systems, the most straightforward candidates to realize more complex ultracold objects were heteronuclear mixtures of alkali. Such mixtures offer a wide spectrum of possibilities in terms of masses (from ^{6}Li to ^{133}Cs), statistics (B-B, B-F, and F-F), and properties (e. g. electronegativity). Note that the common approach involves the combination of two species but a pioneering work proposed in Ref. [Tag08] demonstrated the possibility to extend the method to three species (Rb-K-Li).

Nowadays, nine out of the ten possible combinations of two alkali have been brought to quantum degeneracy. Among these we enumerate: Li-Na [Had02], Li-K [Spi10, Wu17], Li-Rb [Sil05], Li-Cs [DeS17], Na-K [Par12, Sch18], Na-Rb [Wan15], K-Rb [Mod02, Roa02, Wac15], K-Cs [Grö16], and Rb-Cs [McC11, Ler11]. The remaining combination of Na and Cs was never combined in a degenerate regime but it has been used recently to create cold polar molecules in tweezers [Liu18].

Bialkali quantum gases offer a powerful tool to study phenomena arising from population- and mass-imbalance: impurity physics and polaron, pairing beyond the standard BCS theory and superconductivity, BEC-BCS crossover, non-trivial Efimov physics, magnetic ordering and itinerant/localized ferromagnetism, and many more [Blo08, Blu12, Mas14].

The scientific interest is strongly driven by the possibility to create ground-state molecules with large electric dipole moments [Boh17]. For a comparison of the dipolar strengths across such species, see Tab. 3.1. However, reaching quantum degeneracy in gases of diatomic molecules is particularly challenging due to low densities and high losses in the sample. So far deeply bound state molecules in the ultracold regime have been produced in Na-K [Par15, See18, Vog20], Rb-K [Ni08], Rb-Cs [Tak14, Mol14], Na-Rb [Guo16], and Li-Na [Rva17]. After many years of research, in Ref. [DM19], the authors observed a degenerate sample of fermionic polar molecules of ^{40}K-^{87}Rb for the first time.

3.2.2 Alkali-nonalkali mixtures

At the same time of the achievement of the first non-alkali quantum gas, a rising interest in the field led to experimental and theoretical efforts to combine chemically different elements. In this direction, the most promising mixtures include alkali together with alkali-earth (Rb-Sr [Pas13] and Li-Sr [Ye20]), transitions metal (Li-Cr [Ner20]), or lanthanides (Li-Yb [Han11, Har11], Rb-Yb [Vai15], Cs-Yb [Gut18], and K-Dy [Rav18b]). Two additional experiments are being set up: Li-Er in Tübingen and Li-Dy in China.

These mixtures offer a wide variety of statistics: Sr, Cr, Dy, Er, and Yb have several bosonic and fermionic isotopes with a high natural abundance. The mass scalability is great as well, covering a broad range of values from a mass-ratio of about one for Rb-Sr to the Li-Yb case where Efimov physics can be studied in the extreme regime of $m_{\mathrm{Yb}}/m_{\mathrm{Li}} \simeq 29$ [Bra06, End11].

Generally speaking, heteronuclear mixtures of atoms with diverse properties extend the possibilities in designing Hamiltonians to simulate quantum many-body and few-body problems, testing of fundamental symmetries and creating scalable platforms for quantum information. In addition to the applications of heteronuclear systems explained in the previous Sec. 3.2.1, going beyond bialkali mixtures allows other fields to be explored. They are good candidates for creating ground-state molecule exhibiting both electric and magnetic dipole moments (see Tab. 3.1). Moreover, such molecules possess an unpaired electron, leading to a dense spin structure and a rich spectrum for manipulation. The scientific interest in polar molecules is vast and reviews on the topic can be found in Ref. [Mos17, Gad16]. Among them we find: novel superfluid phases, studies of lattice-spin models, geometrical phases, collective spin excitations, and the investigation of fundamental questions e. g. the determination of

electron's electric-dipole moment and proton-to-electron mass ratio.

3.2.3 Erbium-dysprosium mixture

Due to the dissimilar properties of the atomic species involved, mixture experiments are typically challenging from a scientific and technical point of view. Different melting temperatures and vapor pressures might require a special design of the apparatus with individual lines for each species. Different atomic transitions — thus laser wavelengths — might lead to difficulties in planning the optical setup and anti-reflection coatings. Moreover, Zeeman slower and the magneto optical trap conditions could be inadequate for a simultaneous operation on the two components requiring sequential loading of the species. Different polarizabilities and masses strongly affect the confinement in optical dipole traps and the evaporative cooling might be inefficient to reach quantum degeneracy. On top of these issues, the interspecies scattering length is usually not accurately accessible a priori. For example, ^{6}Li-^{87}Rb has a small background scattering length [Sil05, Deh08] leading to an inefficient sympathetic cooling, whereas in Rb-Cs or Rb-Sr, a_{bg} is large [And05, McC11, Pas13, Bar18], reducing the miscibility of the two condensates or leading to important atomic losses. Therefore, only a direct study of interspecies Feshbach resonances can give further information on the possibility of interaction tuning in the mixture to achieve good parameter regimes and experimental conditions.

From this point of view, an Er-Dy mixture defines an exceptionally favorable starting point for a two-species experiment. The technical knowledge on the two species required by a quantum gas experiment is well established [Lu11a, Lu12, Aik12]. Moreover, the physical properties of erbium and dysprosium are similar enough to allow a fairly simple experimental apparatus with a dual-species oven, a ZS optimized for both components and full simultaneous operation (see Chap. 2). Worth to be noted is the similarity in atomic polarizabilities at 1064 nm resulting in a comparable trapping potential seen by the two species into the ODT (see Eq. 2.3 in Sec. 2.1.2) [Gri00]. Only towards the end of the evaporation, the small difference (of about 6 %) plays an important role, leading to sympathetic cooling of Dy through Er.

A more subtle issue regards the interspecies interaction properties of Er and Dy. Experimental values are not available and predictions are highly complicated (see Chap. 4). In such species, even the intraspecies background scattering length is under debate for the difficulties in identifying a real background value [FB18, Luc18]. Nevertheless, by tuning the magnetic field to the mG precision, we reach double Bose-Einstein condensation with five isotopic combinations and one Bose-Fermi degenerate mixture of ^{168}Er-^{161}Dy. Only the Bose-Bose ^{166}Er-^{162}Dy mixture has revealed not to be adequate for the condensation in the magnetic field 0.1 G-5 G, probably due to a non optimal intraspecies vs. interspecies interactions regime. Further investigations might find a more favorable value of magnetic field to enhance evaporation efficiency. In the following Sec. 3.3, the experimental sequence from a cold thermal sample down to degeneracy is presented in more details. Additional information about the setup and an in-depth view on the evaporation scheme is part of Ref. [Ilz20].

3.3 Publication: Dipolar Quantum Mixtures of Erbium and Dysprosium Atoms[†]

Arno Trautmann[1], Philipp Ilzhöfer[1,2], Gianmaria Durastante[1,2], Claudia Politi[1], Maximilian Sohmen[1,2], Manfred J. Mark[1,2], and Francesca Ferlaino[1,2]

[1] *Institut für Quantenoptik und Quanteninformation, Österreichische Akademie der Wissenschaften, Technikerstraße 21a, 6020 Innsbruck, Austria*
[2] *Institut für Experimentalphysik and Zentrum für Quantenphysik, Universität Innsbruck, Technikerstraße 25, 6020 Innsbruck, Austria*

Physical Review Letters **121**, 213601 (2018)
submitted 20 Jul 2018; published 21 Nov 2018
DOI: 10.1103/PhysRevLett.121.213601

Editors' suggestion
Featured in *Physics* 11, s135. Synopsis: Making Mixtures of Magnetic Condensates

[†] The author of the present thesis helped in developing the experimental procedure, taking the data, and contributed in writing the manuscript. This publication is also part of the PhD thesis of Philipp Ilzhöfer.

Editors' Suggestion | Featured in Physics

Dipolar Quantum Mixtures of Erbium and Dysprosium Atoms

A. Trautmann,[1,*] P. Ilzhöfer,[1,2,*] G. Durastante,[1,2] C. Politi,[1] M. Sohmen,[1,2] M. J. Mark,[1,2] and F. Ferlaino[1,2]
[1]*Institut für Quantenoptik und Quanteninformation, Österreichische Akademie der Wissenschaften, 6020 Innsbruck, Austria*
[2]*Institut für Experimentalphysik und Zentrum für Quantenoptik, Universität Innsbruck, Technikerstraße 25, 6020 Innsbruck, Austria*

(Received 20 July 2018; revised manuscript received 8 October 2018; published 21 November 2018)

We report on the first realization of heteronuclear dipolar quantum mixtures of highly magnetic erbium and dysprosium atoms. With a versatile experimental setup, we demonstrate binary Bose-Einstein condensation in five different Er-Dy isotope combinations, as well as one Er-Dy Bose-Fermi mixture. Finally, we present first studies of the interspecies interaction between the two species for one mixture.

DOI: 10.1103/PhysRevLett.121.213601

In recent years, the field of atomic dipolar quantum gases has witnessed an impressive expansion as researchers have made substantial headway in using and controlling a novel class of atoms, the highly magnetic rare-earth species. Since the first experimental successes in creating Bose and Fermi quantum gases of Dy [1,2] or Er [3,4], fascinating many-body phenomena based on the dipole-dipole interaction (DDI) have been observed, including Fermi surface deformation [5], quantum-stabilized droplet states [6–8], and roton quasiparticles [9]. Remarkably, for Dy and Er, the intriguing physics within reach comes with comparatively simple experimental approaches to achieve quantum degeneracy. Several research groups have either recently reported on new experimental realizations of quantum gases with Dy [10,11] or Er [12] or are actively pursuing it [13,14].

An alternative route to access dipolar quantum physics is provided by polar molecules, possessing an electric dipole moment. Up to now, ultracold gases of polar molecules have been created from nondipolar binary quantum mixtures of alkali atoms [15–18] and dipolar spin-exchange interactions have been recently observed with lattice-confined molecules [19]. Besides molecule creation, heteronuclear quantum mixtures have been used as powerful resources to realize a broad class of many-body quantum states (e.g., [20–27]), in which intra- and interspecies short-range contact interactions are at play.

In the experiment described in this Letter, we merge for the first time the physics of heteronuclear mixtures with the one of magnetic dipolar quantum gases. Our motivations to create quantum mixtures by combining two different dipolar species, Er and Dy, are numerous. First, the coupling between the two components acquires an anisotropic and long-range character due to the strong interspecies DDI, in contrast to purely contact-interacting mixtures. The emergent physical richness of the system has only begun to be uncovered by theory. Recent studies include the prediction of anisotropic boundaries in the dipolar immiscibility-miscibility phase diagram [28,29], roton immiscibility [30], vortex lattice formation [31], and impurity physics both in dipolar quantum droplets [32] and dipolar Binary Bose-Einstein condensates (BECs) [33,34]. Moreover, the magnetic moments are large, yet different (7 bohr magneton for Er and 10 for Dy), leading to a DDI twice as strong in Dy as in Er. Such a difference is on one hand advantageous to deeper elucidate the complex scattering and many-body physics by performing comparative single-species studies with Er and Dy in the same experimental environment. On the other hand, we also anticipate

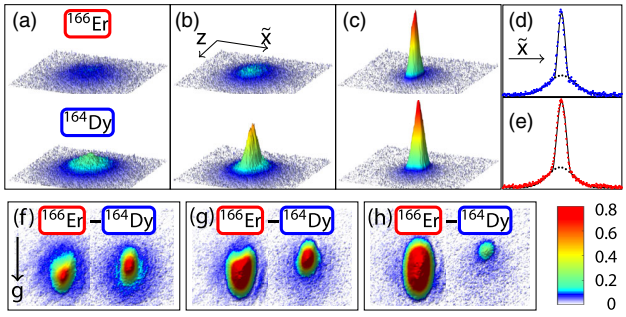

FIG. 1. Binary Bose-Einstein condensation in a ^{166}Er-^{164}Dy mixture. (a)–(c) Pairs of TOF absorption images at different evaporation stages, showing (a) a thermal mixture at about 180 nK, (b) an Er cloud at the onset of condensation coexisting with a thermal Dy gas at about 80 nK, and (c) the binary dipolar BEC with total atom numbers $N = 3.4 \times 10^4 (2.6 \times 10^4)$ for Er(Dy) with condensate fractions of about 45%. $\tilde{x}$ denotes the horizontal axis perpendicular to the imaging axis. (d),(e) Density profiles integrated along z, extracted from (c). Solid lines depict the 1D bimodal fit, the dotted lines show Gaussian fits to the thermal components. (f)–(h) BECs with a controlled number imbalance giving about $N^{\mathrm{Er}} = (3.2, 6.4, 9.2) \times 10^4$ with (35, 70, 85)% condensate fraction and $N^{\mathrm{Dy}} = (3.1, 2.9, 0.9) \times 10^4$ with (30, 55, 30)% condensate fraction for (f)–(h), respectively. The deformations and the relative displacement of the clouds are caused by interspecies interaction (see main text). The color bar indicates the optical density.

that, in mixture experiments, the imbalance in dipolar strength, combined with the interspecies interactions, promises fascinating prospects for creating long-lived quantum-droplet states and for accessing exotic fermionic superfluidity, for which the degree of deformation of the Fermi surface is species-dependent [5].

Second, the rich, but different atomic spectra of Er and Dy open promising prospects for implementing species-dependent optical manipulations schemes, including species-selective optical potentials at magic wavelengths and checkerboard-pattern-like lattice structures. Third, Er and Dy feature many stable bosonic and fermionic isotopes (both elements have four isotopes with natural abundances above 15%). Such an isotope variety allows us to create dipolar Bose-Bose, Bose-Fermi, and Fermi-Fermi heteronuclear mixtures. Last, mixtures composed of two different magnetic species serve as an ideal platform to produce ground-state polar molecules with both an electric and magnetic dipole moment, offering novel degrees of control and competing long-range interactions [35–37].

We here report on the first experimental realization of quantum-degenerate dipolar mixtures of Er and Dy atoms, using an all-optical approach for trapping and cooling. Taking advantage of the isotope richness in Er and Dy, we produce dipolar Bose-Bose mixtures with five different isotope combinations, as well as one Bose-Fermi mixture. We note that, prior to this work, the production of a Dy isotope mixture of a degenerate Fermi gas and a Bose gas near condensation has been reported [2] and, more recently, a doubly degenerate Fermi-Fermi mixture has been created from two Er spin states [39]. Experimental efforts are also devoted to creating Dy-K mixtures [40].

In the following, we detail the production of a double dipolar Bose-Einstein condensate (ddBEC) of ^{166}Er and ^{164}Dy. The same procedure is used for the other isotope mixtures. Our experiment starts with a double magneto-optical trap (MOT) of Er and Dy, as reported in our recent work [41]. For both species, the MOT operates on narrow intercombination lines and yields cold and spin-polarized samples in the absolute lowest Zeeman sublevels [10,13,41,42]. After loading the double MOT, we optically compress the mixture in 400 ms (cMOT phase) by reducing the detuning and power of the MOT beams as well as the magnetic-field gradient.

We then transfer the mixture into an optical dipole trap (ODT) by superposing it with the cMOT for 100 ms. Initially, the ODT consists of a single laser beam at 1064 nm, propagating along the horizontal (y) axis. The beam has a fixed vertical (z) focus of about 22 μm, whereas the horizontal waist can be controlled via a time-averaging-potential technique (see, e.g., [43]). This leads to an elliptic beam with variable aspect ratio (AR). Best transfer efficiency is observed for a beam power of 32 W and an AR of 4, which provides good spatial overlap between the cMOT and the ODT. We then switch off the MOT beams and magnetic-field gradient, and start a 5-sec evaporation sequence, during which we apply a bias magnetic field B_{evap} along the gravity (z) axis to preserve spin polarization.

Our strategy for evaporative cooling can be divided into three main stages. (i) During the initial 600 ms, we reduce the AR to unity while lowering the power of the single-beam ODT. This increases the density of the mixture at a roughly constant trap depth. (ii) We start forced evaporation in the horizontal ODT and add a vertically propagating dipole trap beam. The vertical beam is derived from the same laser source as the horizontal one and has a power of 15 W and a waist of 130 μm. (iii) We proceed with forced evaporation in the crossed ODT by reducing the powers of both beams nearly exponentially until the mixture is close to quantum degeneracy. In the final stage of the evaporation, we increase the AR to 5 to create a pancakelike trapping geometry and further decrease the trap depth until we reach double quantum degeneracy. To probe the atomic mixture, we switch off the ODT and, after a time-of-flight (TOF) expansion of 25 ms, we perform sequential absorption imaging with a resonant light pulse at 401 nm for Er and 500 μs later at 421 nm for Dy [3,44]; both pulses have a duration of 50 μs. The imaging light propagates horizontally with an angle of 45° with respect to the y axis.

Unlike many alkali mixtures [45–48], Er and Dy exhibit very comparable atomic polarizabilities α because of their similar atomic spectra. From single-species experiments [14,49], a ratio $\alpha_{\mathrm{Dy}}/\alpha_{\mathrm{Er}} = 1.06$ at 1064 nm is expected. For our initial ODT parameters, we calculate trap frequencies of about $\nu^{\mathrm{Er}} = (490, 5, 1980)$ Hz and $\nu^{\mathrm{Dy}} = (505, 5, 2050)$ Hz [50], corresponding to trap depths of 380 and 410 μK for Er and Dy, respectively. Although small, the difference in trap depths has an important effect on the evaporation trajectory of the mixture. We observe that the more weakly trapped Er atoms act as a coolant for Dy and are preferentially evaporated from the trap ("sympathetic losses" [47,51]). To sustain Er atom numbers high enough to achieve double quantum degeneracy, we imbalance the initial atom number in the MOT with Er as the majority component. The atom number imbalance can be easily controlled by individually changing the MOT loading time and beam power. This strategy is often employed in multispecies experiments, e.g., [52,53].

Figures 1(a)–1(c) show the phase transition from a thermal Er-Dy mixture (a) to a ddBEC (c). The TOF absorption images reveal the textbooklike fingerprint of condensation, the emergence of a bimodal density distribution, as plotted in Fig. 1(d). The condensation series [Figs. 1(a)–1(c)] is taken for an Er(Dy) MOT loading time of 3 s (1 s), for which we transfer 8×10^6 (7×10^5) Er(Dy) atoms into our ODT and measure a temperature of about 35 μK; this parameter set allows us to create number-balanced ddBECs. In agreement with the expected polarizabilities, we measure ODT trap frequencies of $\nu^{\mathrm{Er}} = (48.6(3), 29.7(9), 144(1))$ Hz and $\nu^{\mathrm{Dy}} = (50.6(3), 30.2(9),$

160(1)) Hz [54]. The resultant gravitational sag between the two species is 2.1(2) μm. By varying the imbalance of the MOT loading, we can produce degenerate mixtures with different atom number ratios and condensate fractions, which is exemplified in Figs. 1(f)–1(h). For large condensates, one directly observes a deformation of the density profiles due to interspecies interaction, as we discuss later in more detail.

To quantify the cooling efficiency, we plot the normalized phase-space density ($\mathrm{PSD}/\mathrm{PSD}_0$) as a function of normalized atom numbers (N/N_0) during the evaporation stages ii and iii [see Fig. 2(a)]. PSD_0 and N_0 are the respective initial values at stage ii. From this plot, we extract $\gamma = -d\ln(\mathrm{PSD}/\mathrm{PSD}_0)/d\ln(N/N_0)$ [55], which captures the evaporation efficiency, via a linear fit to the data. In the single-beam ODT (stage ii), we see similar efficiencies both in mixture and single-species operations, with $\gamma \approx 1.2$. In the crossed ODT (stage iii), we find $\gamma^{\mathrm{Er}} = 2.4(9)$ for Er in the mixture operation. This value is comparable to state-of-the-art single-species Er experiments [56] and, as expected, little affected by a small admixture of Dy atoms. Contrarily, the cooling efficiency of Dy in stage (iii) strongly benefits from the sympathetic cooling by Er: We observe a steep increase of the Dy PSD in the mixture and extract $\gamma^{\mathrm{Dy}}_{\mathrm{sym}} = 7(2)$, whereas for the same N_0^{Dy} but in single-species operation, the evaporation efficiency is considerably lower and would not suffice for condensation. However, with higher N_0^{Dy} we can still produce large Dy BECs in single-species operation.

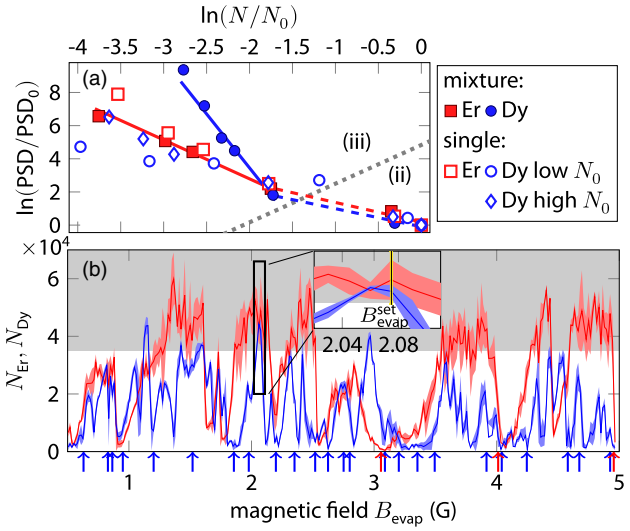

FIG. 2. (a) Evaporation trajectories: $\mathrm{PSD}/\mathrm{PSD}_0$ as a function of N/N_0. Filled squares (circles) indicate the Er(Dy) trajectory in mixture operation. The lines are linear fits to the data for evaporation in the single-beam (ii) and crossed-beam (iii) ODT (see main text). Open symbols show the single-species operation for Er (squares) and for Dy with small (circles) and large (diamonds) initial atom numbers. In the latter case, Dy condenses alone. (b) Atom numbers in the mixture of Er (red) and Dy (blue) at the onset of condensation as a function of the magnetic-field value during evaporation. Condensation is reached for atom numbers above about 3.5×10^4 (gray region). We record the best performance for a ddBEC around 2.075 G. Arrows indicate the position of known single-species Feshbach resonances [57–59].

The proper choice of B_{evap} plays an important role for cooling magnetic rare-earth atoms and becomes even more critical in mixture operation. It has indeed been observed in single-species experiments [57–59] that both Er and Dy exhibit extremely dense and temperature-dependent spectra of homonuclear Feshbach resonances. Figure 2(b) shows the atom numbers of the ^{166}Er-^{164}Dy mixture at the onset of condensation as a function of B_{evap} in a small magnetic-field range from 0.5 to 5 G. As expected, we find a number of broad and narrow loss features. Some of them are connected to known homonuclear Feshbach resonances [57–59], others we attribute to unknown high-temperature resonances or detrimental interspecies scattering conditions. In a few narrow magnetic-field windows, we observe atom numbers large enough for both components to condense. Our magnetic-field stability of about 2 mG is sufficient to reliably operate in most of these small windows. The optimal value of B_{evap}, listed in Table I, depends on the isotope combination.

Combining Er and Dy offers an unprecedented variety of heteronuclear mixtures with 16 possible isotope configurations, including Bose-Bose, Bose-Fermi, and Fermi-Fermi quantum gases (see Table I). Using the cooling and trapping procedure optimized for ^{166}Er-^{164}Dy, we are able to produce five ddBECs and one Bose-Fermi mixture. Concerning the remaining combinations, we know from previous experiments that both ^{167}Er and ^{163}Dy need a different experimental approach since ^{167}Er undergoes light-induced losses in a 1064-nm ODT [4], whereas ^{163}Dy, never brought to quantum degeneracy so far, has an inverted hyperfine structure, requiring most probably additional optical pumping stages. Both isotopes will be investigated for future studies of Fermi-Fermi mixtures.

Figures 3(a)–3(d) show absorption pictures of our doubly degenerate isotope mixtures. We are able to

TABLE I. (Left) List of optimal B_{evap} and $\gamma^{\mathrm{Dy}}_{\mathrm{sym}}$ for the quantum-degenerate Er-Dy mixtures. (Right) Chart of the available isotope mixtures: (✓) realized double-degenerate mixtures, (×) thermal mixtures, where degeneracy is not yet reached. (⋯) Mixtures with ^{167}Er and ^{163}Dy are not investigated here.

mixture	B_{evap}(G)	$\gamma^{\mathrm{Dy}}_{\mathrm{sym}}$
^{166}Er-^{164}Dy	2.075	7(2)
^{168}Er-^{162}Dy	3.300	6(2)
^{168}Er-^{164}Dy	3.300	6(2)
^{170}Er-^{162}Dy	1.540	11(7)
^{170}Er-^{164}Dy	3.210	3(1)
^{168}Er-^{161}Dy	3.455	4(1)

Dy \ Er	166	167	168	170
161	×	⋯	✓	×
162	×	⋯	✓	✓
163	⋯	⋯	⋯	⋯
164	✓	⋯	✓	✓

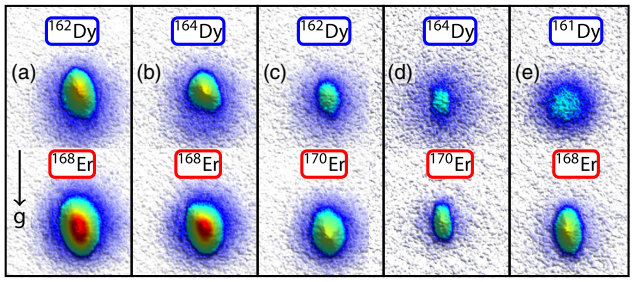

FIG. 3. Absorption pictures of the double-degenerate Bose-Bose mixtures (a)–(d) and the Bose-Fermi mixture (e). The pictures are averaged over 5–10 single shots. For all combinations, degeneracy is reached with the evaporation ramp optimized for the ^{166}Er-^{164}Dy mixture (cf. Fig. 1). B_{evap} is listed in Table I. Typical condensate fractions are around 30%, total atom numbers range between 1×10^4 and 3.5×10^4 atoms. For the imbalanced case, higher condensate fractions can be achieved (see Fig. 1). For the ^{161}Dy Fermi gas, $N = 8 \times 10^3$, $T/T_F \approx 0.5$, and TOF $= 15$ ms.

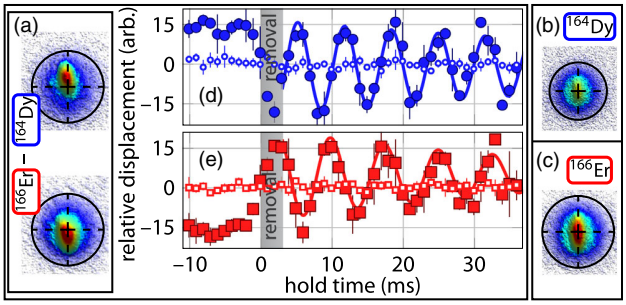

FIG. 4. Evidence of interspecies interactions in the ^{166}Er-^{164}Dy mixture: absorption pictures of Er and Dy in mixture (a) and single-species (b),(c) operation. (d),(e) Filled symbols show the c.m. position along z of the Dy BEC (d) and the Er BEC (e) after removal of the other species with resonant light. The gray region indicates the transient time until full removal. The solid lines are damped sine fits to the oscillations. For comparison, open symbols show the c.m. position in a thermal mixture.

condense all Bose-Bose isotope mixtures with the exception of ^{166}Er-^{162}Dy, for which we record severe losses during the evaporation, potentially due to a very large interspecies scattering length. For all degenerate mixtures, we observe sympathetic cooling of Dy by Er. The atom numbers in the ddBECs differ significantly for the different mixtures, while the initial atom numbers in the MOT are very similar. This points to different intra- and interspecies scattering properties during evaporation. The optimal B_{evap} and the extracted $\gamma_{\mathrm{sym}}^{\mathrm{Dy}}$ are listed in Table I.

We also prepare one Bose-Fermi mixture [see Fig. 3(e)], in which a ^{168}Er BEC coexists with a degenerate Fermi gas of ^{161}Dy. Although the cooling process of spin-polarized fermions can differ substantially from bosons, we are able to reach Bose-Fermi degeneracy with a similar evaporation scheme [60]. We measure a temperature of the Fermi gas of $T/T_F \approx 0.5$, with the Fermi temperature $T_F = 140$ nK. We expect that deeper degeneracy might be reached by using smaller ODT beam waists [4].

Remarkably, in the TOF images in Figs. 1 and 3 hints of interspecies interactions can be spotted: in mixture operation, the center-of-mass (c.m.) position of each BEC is vertically displaced with respect to its thermal-cloud center [see also Fig. 4(a)]. The two BECs are displaced in opposite directions, with the heavier (lighter) Er(Dy) always shifted down (up). Contrarily, in single-species operation the condensates and their thermal clouds are centered [see Figs. 4(b) and 4(c)].

To confirm that the displacement after TOF originates from in-trap interspecies interaction, we prepare a ddBEC, let it equilibrate for 50 ms, and then selectively remove either of the two species from the ODT using a resonant light pulse [61]. After a variable hold time in the ODT, we release the remaining cloud and record its c.m. position after TOF. As shown in Figs. 4(d) and 4(e), we observe a very pronounced c.m. oscillation of the remaining BEC component with a frequency close to its bare trap frequency. The oscillations of Er [removing Dy, Fig. 4(d)] and of Dy [removing Er, Fig. 4(e)] proceed in counterphase, as expected from their initial separation in trap. Repeating the same measurement with a thermal-thermal mixture, or a mixture with just one condensed component (not shown), yields negligible or significantly weaker oscillations, respectively.

The spatial separation between the two condensed components and their oscillating behavior after removal indicate that, for our trap geometry, the overall interspecies interaction—contact plus dipolar—has a repulsive character. We note that the interspecies scattering length, governing the contact interaction, and its Feshbach tuning are presently unknown and beyond reach of state-of-the-art scattering models [57,62]. To isolate the different sources of interaction and determine their signs, future dedicated experiments studying the interplay between trap geometry, dipole orientation, and interspecies scattering length, combined with simulations based on generalized coupled Gross-Pitaeskvii equations are necessary. Indeed, the DDI breaks the angular symmetry of the mean-field interspecies potentials and is expected to render the strength and the sign of the overall interspecies interaction anisotropic and trap dependent.

In conclusion, we have produced heteronuclear dipolar quantum mixtures by combining two strongly magnetic atomic species, Er and Dy. Their isotope variety, the richness of their interactions, the imbalance in the dipolar strength, and simple laser-cooling schemes make Er-Dy mixtures a powerful experimental platform to access many-body quantum phenomena, in which contact and dipolar intra- and interspecies interactions are at play.

This work is supported by the ERC Consolidator Grant (RARE, No. 681432) and a NFRI Grant (MIRARE,

No. ÖAW0600) from the Austrian Academy of Science. G. D. and M. S. acknowledge support by the Austrian Science Fund FWF within the DK-ALM: W1259-N27. We thank the ERBIUM team and the Dy-K team in Innsbruck and the ERBIUM team of Markus Greiner for fruitful discussions.

*These authors contributed equally to this work.

[1] M. Lu, N. Q. Burdick, S. H. Youn, and B. L. Lev, Strongly Dipolar Bose-Einstein Condensate of Dysprosium, Phys. Rev. Lett. **107**, 190401 (2011).
[2] M. Lu, N. Q. Burdick, and B. L. Lev, Quantum Degenerate Dipolar Fermi Gas, Phys. Rev. Lett. **108**, 215301 (2012).
[3] K. Aikawa, A. Frisch, M. Mark, S. Baier, A. Rietzler, R. Grimm, and F. Ferlaino, Bose-Einstein Condensation of Erbium, Phys. Rev. Lett. **108**, 210401 (2012).
[4] K. Aikawa, A. Frisch, M. Mark, S. Baier, R. Grimm, and F. Ferlaino, Reaching Fermi Degeneracy via Universal Dipolar Scattering, Phys. Rev. Lett. **112**, 010404 (2014).
[5] K. Aikawa, S. Baier, A. Frisch, M. Mark, C. Ravensbergen, and F. Ferlaino, Observation of Fermi surface deformation in a dipolar quantum gas, Science **345**, 1484 (2014).
[6] H. Kadau, M. Schmitt, M. Wenzel, C. Wink, T. Maier, I. Ferrier-Barbut, and T. Pfau, Observing the Rosensweig instability of a quantum ferrofluid, Nature (London) **530**, 194 (2016).
[7] L. Chomaz, S. Baier, D. Petter, M. J. Mark, F. Wächtler, L. Santos, and F. Ferlaino, Quantum-Fluctuation-Driven Crossover from a Dilute Bose-Einstein Condensate to a Macrodroplet in a Dipolar Quantum Fluid, Phys. Rev. X **6**, 041039 (2016).
[8] M. Schmitt, M. Wenzel, F. Böttcher, I. Ferrier-Barbut, and T. Pfau, Self-bound droplets of a dilute magnetic quantum liquid, Nature (London) **539**, 259 (2016).
[9] L. Chomaz, R. M. W. van Bijnen, D. Petter, G. Faraoni, S. Baier, J. H. Becher, M. J. Mark, F. Wächtler, L. Santos, and F. Ferlaino, Observation of roton mode population in a dipolar quantum gas, Nat. Phys. **14**, 442 (2018).
[10] T. Maier, H. Kadau, M. Schmitt, A. Griesmaier, and T. Pfau, Narrow-line magneto-optical trap for dysprosium atoms, Opt. Lett. **39**, 3138 (2014).
[11] E. Lucioni, L. Tanzi, A. Fregosi, J. Catani, S. Gozzini, M. Inguscio, A. Fioretti, C. Gabbanini, and G. Modugno, Dysprosium dipolar Bose-Einstein condensate with broad feshbach resonances, Phys. Rev. A **97**, 060701 (2018).
[12] J. Ulitzsch, D. Babik, R. Roell, and M. Weitz, Bose-Einstein condensation of erbium atoms in a quasielectrostatic optical dipole trap, Phys. Rev. A **95**, 043614 (2017).
[13] D. Dreon, L. A. Sidorenkov, C. Bouazza, W. Maineult, J. Dalibard, and S. Nascimbene, Optical cooling and trapping of highly magnetic atoms: The benefits of a spontaneous spin polarization, J. Phys. B **50**, 065005 (2017).
[14] C. Ravensbergen, V. Corre, E. Soave, M. Kreyer, S. Tzanova, E. Kirilov, and R. Grimm, Accurate Determination of the Dynamical Polarizability of Dysprosium, Phys. Rev. Lett. **120**, 223001 (2018).
[15] K.-K. Ni, S. Ospelkaus, M. H. G. de Miranda, A. Pe'er, B. Neyenhuis, J. J. Zirbel, S. Kotochigova, P. S. Julienne, D. S. Jin, and J. Ye, A high phase-space-density gas of polar molecules, Science **322**, 231 (2008).
[16] T. Takekoshi, L. Reichsöllner, A. Schindewolf, J. M. Hutson, C. R. Le Sueur, O. Dulieu, F. Ferlaino, R. Grimm, and H.-C. Nägerl, Ultracold Dense Samples of Dipolar RBCS Molecules in the Rovibrational and Hyperfine Ground State, Phys. Rev. Lett. **113**, 205301 (2014).
[17] P. K. Molony, P. D. Gregory, Z. Ji, B. Lu, M. P. Köppinger, C. R. Le Sueur, C. L. Blackley, J. M. Hutson, and S. L. Cornish, Creation of Ultracold $^{87}Rb^{133}Cs$ Molecules in the Rovibrational Ground State, Phys. Rev. Lett. **113**, 255301 (2014).
[18] S. Moses, J. Covey, M. Miecnikowski, D. Jin, and J. Ye, New frontiers for quantum gases of polar molecules, Nat. Phys. **13**, 13 (2016).
[19] B. Yan, S. A. Moses, B. Gadway, J. P. Covey, K. R. A. Hazzard, A. M. Rey, D. S. Jin, and J. Ye, Observation of dipolar spin-exchange interactions with lattice-confined polar molecules, Nature (London) **501**, 521 (2013).
[20] T.-L. Ho and V. B. Shenoy, Binary Mixtures of Bose Condensates of Alkali Atoms, Phys. Rev. Lett. **77**, 3276 (1996).
[21] S. Ospelkaus, C. Ospelkaus, O. Wille, M. Succo, P. Ernst, K. Sengstock, and K. Bongs, Localization of Bosonic Atoms by Fermionic Impurities in a Three-Dimensional Optical Lattice, Phys. Rev. Lett. **96**, 180403 (2006).
[22] S. Will, T. Best, S. Braun, U. Schneider, and I. Bloch, Coherent Interaction of a Single Fermion with a Small Bosonic Field, Phys. Rev. Lett. **106**, 115305 (2011).
[23] J. Heinze, S. Götze, J. S. Krauser, B. Hundt, N. Fläschner, D.-S. Lühmann, C. Becker, and K. Sengstock, Multiband Spectroscopy of Ultracold Fermions: Observation of Reduced Tunneling in Attractive Bose-Fermi Mixtures, Phys. Rev. Lett. **107**, 135303 (2011).
[24] N. Spethmann, F. Kindermann, S. John, C. Weber, D. Meschede, and A. Widera, Dynamics of Single Neutral Impurity Atoms Immersed in an Ultracold Gas, Phys. Rev. Lett. **109**, 235301 (2012).
[25] N. B. Jørgensen, L. Wacker, K. T. Skalmstang, M. M. Parish, J. Levinsen, R. S. Christensen, G. M. Bruun, and J. J. Arlt, Observation of Attractive and Repulsive Polarons in a Bose-Einstein Condensate, Phys. Rev. Lett. **117**, 055302 (2016).
[26] M.-G. Hu, M. J. Van de Graaff, D. Kedar, J. P. Corson, E. A. Cornell, and D. S. Jin, Bose Polarons in the Strongly Interacting Regime, Phys. Rev. Lett. **117**, 055301 (2016).
[27] T. Rentrop, A. Trautmann, F. A. Olivares, F. Jendrzejewski, A. Komnik, and M. K. Oberthaler, Observation of the Phononic Lamb Shift with a Synthetic Vacuum, Phys. Rev. X **6**, 041041 (2016).
[28] G. Gligorić, A. Maluckov, M. Stepić, L. Hadžievski, and B. A. Malomed, Transition to miscibility in linearly coupled binary dipolar Bose-Einstein condensates, Phys. Rev. A **82**, 033624 (2010).
[29] R. K. Kumar, P. Muruganandam, L. Tomio, and A. Gammal, Miscibility in coupled dipolar and non-dipolar Boseeinstein condensates, J. Phys. Commun. **1**, 035012 (2017).
[30] R. M. Wilson, C. Ticknor, J. L. Bohn, and E. Timmermans, Roton immiscibility in a two-component dipolar Bose gas, Phys. Rev. A **86**, 033606 (2012).

[31] R. K. Kumar, L. Tomio, B. A. Malomed, and A. Gammal, Vortex lattices in binary Bose-Einstein condensates with dipole-dipole interactions, Phys. Rev. A **96**, 063624 (2017).
[32] M. Wenzel, T. Pfau, and I. Ferrier-Barbut, A fermionic impurity in a dipolar quantum droplet, Phys. Scr. **93**, 104004 (2018).
[33] B. Kain and H. Y. Ling, Polarons in a dipolar condensate, Phys. Rev. A **89**, 023612 (2014).
[34] L. A. P. Ardila and T. Pohl, Ground-state properties of dipolar bose polarons, arXiv:1804.06390.
[35] E. Abrahamsson, T. V. Tscherbul, and R. V. Krems, Quantum chaos in ultracold collisions of gas-phase erbium atoms, J. Chem. Phys. **127**, 044302 (2007).
[36] T. M. Rvachov, H. Son, A. T. Sommer, S. Ebadi, J. J. Park, M. W. Zwierlein, W. Ketterle, and A. O. Jamison, Observation of Low-Field Fano-Feshbach Resonances in Ultracold Gases of Dysprosium, Phys. Rev. Lett. **119**, 143001 (2017).
[37] The electric dipole moment of ErDy is currently unknown; Ref. [38] reports the calculation for another rare-earth combination, EuYb, with −0.13 D. Based on electronegativity arguments, a similar value can be expected in ErDy.
[38] M. Tomza, Ab initio properties of the ground-state polar and paramagnetic europium–alkali-metal-atom and 5 europium–alkaline-earth-metal-atom molecules, Phys. Rev. A **90**, 022514 (2014).
[39] S. Baier, D. Petter, J. H. Becher, A. Patscheider, G. Natale, L. Chomaz, M. J. Mark, and F. Ferlaino, Realization of a Strongly Interacting Fermi Gas of Dipolar Atoms, Phys. Rev. Lett. **121**, 093602 (2018).
[40] R. Grimm (private communication).
[41] P. Ilzhöfer, G. Durastante, A. Patscheider, A. Trautmann, M. J. Mark, and F. Ferlaino, Phys. Rev. A **97**, 023633 (2018).
[42] A. Frisch, K. Aikawa, M. Mark, A. Rietzler, J. Schindler, E. Zupanič, R. Grimm, and F. Ferlaino, Narrow-line magneto-optical trap for erbium, Phys. Rev. A **85**, 051401 (2012).
[43] S. Baier, An optical dipole trap for Erbium with tunable geometry, Master's thesis, University of Innsbruck, 2012.
[44] M. Lu, S. H. Youn, and B. L. Lev, Trapping Ultracold Dysprosium: A Highly Magnetic Gas for Dipolar Physics, Phys. Rev. Lett. **104**, 063001 (2010).
[45] G. Modugno, M. Modugno, F. Riboli, G. Roati, and M. Inguscio, Two Atomic Species Superfluid, Phys. Rev. Lett. **89**, 190404 (2002).
[46] Z. Hadzibabic, C. A. Stan, K. Dieckmann, S. Gupta, M. W. Zwierlein, A. Görlitz, and W. Ketterle, Two-Species Mixture of Quantum Degenerate Bose and Fermi Gases, Phys. Rev. Lett. **88**, 160401 (2002).
[47] M. Mudrich, S. Kraft, K. Singer, R. Grimm, A. Mosk, and M. Weidemüller, Sympathetic Cooling with Two Atomic Species in an Optical Trap, Phys. Rev. Lett. **88**, 253001 (2002).
[48] M. Gröbner, P. Weinmann, F. Meinert, K. Lauber, E. Kirilov, and H.-C. Nägerl, A new quantum gas apparatus for ultracold mixtures of K and Cs and KCs ground-state molecules, J. Mod. Opt. **63**, 1829 (2016).
[49] J. H. Becher, S. Baier, K. Aikawa, M. Lepers, J.-F. Wyart, O. Dulieu, and F. Ferlaino, Anisotropic polarizability of erbium atoms, Phys. Rev. A **97**, 012509 (2018).
[50] We use the notation $\nu^{\mathrm{Er,Dy}} = (\nu_x, \nu_y, \nu_z)$.
[51] A. Mosk, S. Kraft, M. Mudrich, K. Singer, W. Wohlleben, R. Grimm, and M. Weidemüller, Mixture of ultracold lithium and cesium atoms in an optical dipole trap, Appl. Phys. B **73**, 791 (2001).
[52] Y. Tang, A. Sykes, N. Q. Burdick, J. L. Bohn, and B. L. Lev, s-wave scattering lengths of the strongly dipolar bosons ^{162}Dy and ^{164}Dy, Phys. Rev. A **92**, 022703 (2015).
[53] C.-H. Wu, I. Santiago, J. W. Park, P. Ahmadi, and M. W. Zwierlein, Strongly interacting isotopic bose-fermi mixture immersed in a fermi sea, Phys. Rev. A **84**, 011601 (2011).
[54] The trap frequencies along the y and z axes are extracted from center-of-mass-oscillation measurement; the frequency along x is calculated based on the beam waist, calibrated via the z frequency, and our knowledge of the polarizability [14,49].
[55] W. Ketterle and N. V. Druten, in *Evaporative Cooling of Trapped Atoms*, edited by B. Bederson and H. Walther, Advances in Atomic, Molecular, and Optical Physics Vol. 37 (Academic Press, New York, 1996), pp. 181–236.
[56] A. Frisch, Dipolar quantum gases of erbium, Ph.D. thesis, University of Innsbruck, 2014.
[57] A. Frisch, M. Mark, K. Aikawa, F. Ferlaino, J. L. Bohn, C. Makrides, A. Petrov, and S. Kotochigova, Nature (London) **507**, 475 (2014).
[58] K. Baumann, N. Q. Burdick, M. Lu, and B. L. Lev, Observation of low-field fano-feshbach resonances in ultracold gases of dysprosium, Phys. Rev. A **89**, 020701 (2014).
[59] T. Maier, H. Kadau, M. Schmitt, M. Wenzel, I. Ferrier-Barbut, T. Pfau, A. Frisch, S. Baier, K. Aikawa, L. Chomaz, M. J. Mark, F. Ferlaino, C. Makrides, E. Tiesinga, A. Petrov, and S. Kotochigova, Emergence of Chaotic Scattering in Ultracold Er and Dy, Phys. Rev. X **5**, 041029 (2015).
[60] For the Bose-Fermi mixture, slightly different final trap parameters are required, with typically $\nu^{\mathrm{Er}} = (95(5), 33(1), 120(1))$, $\nu^{\mathrm{Dy}} = (106(5), 34(1), 142(1))$.
[61] The light pulse at the respective imaging transition has a duration of 1 ms. We have checked that the resonant light of one species does not affect the other.
[62] S. Kotochigova, Controlling interactions between highly magnetic atoms with feshbach resonances, Rep. Prog. Phys. **77**, 093901 (2014).

Chapter 4

Feshbach resonances

Since the first theoretical investigation in the 1930s [Ric33, Beu35, Fan35] and the experimental evidence in the 1970s [Spe75, Bry77], Feshbach resonances are considered part of a fundamental step towards the understanding of the underlying properties of a specific system from both theoretical and experimental points of view [Fes58, Fan61, Fes62]. Firstly, the study of Feshbach resonances gives insights in the collisional properties and it provides very precise input for the calculation of interaction potentials [Tim99]. Secondly, and most importantly for the ultracold atoms community, Feshbach resonances are effective tools to tune the scattering length, thus the interaction between atoms [Chi10]. It becomes possible to investigate a wide range of interaction regimes, going from strongly attractive to non-interacting to strongly repulsive regimes. Few-body and many-body scenarios of particular interest become also accessible.

Feshbach resonances (FR) are important in several research branches such as nuclear, atomic, molecular, and chemical physics [Chi10, KÖ6]. This thesis addresses the problem from the ultracold atoms' perspective. Here, particles in the dilute gas are close to the zero-energy scattering regime. This allows a simpler description of the phenomenon of FRs. As a matter of fact, the two-body scattering in this regime can be described in terms of a single parameter, a, called s-wave scattering length [Pet08]. While in single valence-electron species (alkali) methods to calculate a_s are well established, predictive scattering models for two- and multi-electron atoms are still under development and more approximations are typically needed. In the case of complex atomic species such as lanthanides, the understanding is still rather superficial because of the required treatment is highly non-trivial, involving many potentials and complex interactions [Kot14]. The development of ultracold lanthanide-based experiments calls for more theoretical input.

In this chapter, the first experimental observations of Feshbach resonances in an ultracold atomic mixture of erbium and dysprosium are presented. The initial sections introduce the reader to the theory behind Feshbach resonances and the state-of-the-art knowledge in the case of single-species and multi-species alkali systems (Sec. 4.1 and Sec. 4.2, respectively). After that, in Sec. 4.3, the complex topic of FRs in lanthanides is discussed in more detail. Sec. 4.4 includes the publication *Feshbach Resonances in an Erbium-Dysprosium Dipolar Mixture* [Dur20]. The final Sec. 4.5, is dedicated to the presentation of additional information and measurements collected during the development of the previously-mentioned publication. In Appendix B, all the Feshbach scans performed in search of broad FRs are collected.

4.1 Theory of Feshbach resonances

The understanding of Feshbach resonances has its roots in the two- and three-body scattering processes between atoms. In this section we develop the topic of FR with a treatment based on the one presented in Refs. [KÖ6, Chi10, Kot14]. Generally speaking, collisions can be either elastic or inelastic. In the first case, the relative kinetic energy of two particles undergoing a scattering process does not change, while the kinetic energy of the individual atoms can change. In the second case, colliding particles can change their internal state during the scattering process. While elastic collisions are important for thermalization and evaporative cooling, inelastic collisions typically release enough energy to cause a loss of atoms from the trap. In the following description we neglect inelastic collisions.

4.1.1 Ultracold collision

Imagine two point-like particles of masses m_1 and m_2 colliding in an isotropic potential $V(\mathbf{r})$ with $\mathbf{r}$ being the interatomic distance. The separated atoms can be initially described by non-interacting plane waves. The plane waves can be re-written following a partial wave expansion by a sum over spherical harmonic $Y_{\mathrm{lm_l}}(\hat{\mathbf{r}})$, where l is the relative angular momentum and m_l is its projection along a fixed axis. In this picture, since there is no coupling among them, each of these partial waves $\psi_\mathrm{l}(r) = {}^{\phi_\mathrm{l}(r)}/_{r}$ is a solution of the Schrödinger equation

$$H\phi_\mathrm{l}(r) = E\phi_\mathrm{l}(r). \tag{4.1}$$

Here the Hamiltonian is written as the sum of the relative kinetic energy and the interaction potential as

$$H = H_\mathrm{k} + V(r) = -\frac{\hbar^2}{2m_{12}}\frac{\mathrm{d}^2}{\mathrm{d}r^2} + \frac{\hbar^2}{2m_{12}r^2}l(l+1) + V(r) \tag{4.2}$$

where m_{12} is the reduced mass of the pair and the second term accounts for the centrifugal potential. In the case of $l \neq 0$, an energy barrier is added to the potential with the result of preventing atoms with low energy to reach the scattering center. In the following, we use the general convention where the rotational states $l = 0, 1, 2, \ldots$ are called $s, p, d, \ldots$ waves. If we assume that $V(r) \xrightarrow{r\to\infty} 0$, every collisional channel can be expressed by its wave function

$$\phi_\mathrm{l}(R, E) \xrightarrow{r\to\infty} c\frac{\sin(kR - \pi l/2 + \eta_\mathrm{l}(E))}{\sqrt{k}}\,\mathrm{e}^{i\eta_\mathrm{l}(E)} \tag{4.3}$$

with k being the wavevector of the incoming particle, $c = \sqrt{2m_{12}/(\pi\hbar^2)}$ a normalization constant, and η_l a parameter describing the phase shift introduced by the scattering process and strongly dependent on the potential itself. Such phase shift plays a fundamental role enclosing the effect of the potential on the scattering event.

In ultracold atoms experiments, in which the relative momenta are very small, the leading scattering channel is typically the s-wave collision, and all higher partial waves can be safely neglected (this is not valid anymore in case of dipolar or anisotropic van der Waals interactions where all partial waves can contribute). The phase shift parameter η_0 assumes the form

$$k\cot\eta_0(E) = -\frac{1}{a} + \frac{1}{2}r_0k^2, \tag{4.4}$$

where r_0 is the extension of the potential and a is the s-wave scattering length. In the zero-energy limit ($k \to 0$), a further approximation leads to

$$a = -\lim_{k\to 0} \frac{\tan \eta_0(E)}{k}. \tag{4.5}$$

The parameter η_0 can take any value from 0 to 2π depending on the potential, thus the scattering length a can vary from $-\infty$ to $+\infty$. a is typically given in units of the Bohr radius $a_0 \simeq 0.53\,\text{Å}$.

4.1.2 Open- and closed-channel picture

To describe the basis of Feshbach resonances, we assume the existence of at least two molecular potentials. The first one is associated with the asymptotically free atoms with colliding energy close to the threshold and, from here on, such background potential $V_{\text{bg}}(r)$ will be called *entrance channel*, because it represents the energetically open channel. Nevertheless, this picture can change in the case of coupling from the free-body states to bound-states. The second potential $V_{\text{c}}(r)$, in which the energy of the colliding atoms is less than its asymptotic value, is called *closed channel* and supports near-threshold molecular bound-states. If one of these bound-states in the closed channel becomes energetically resonant with the asymptotic energy of the scattering state in the open channel, a small coupling can strongly impact the scattering length mixing the two channels and leading to a divergence of a. We then speak about *Feshbach resonance*. A pictorial representation of the open- and closed-channel picture is sketched in Fig. 4.1.

The separated atoms and the bound state might have different magnetic moments $\delta\mu = \mu_{\text{atoms}} - \mu_{\text{c}}$. If this is the case, the energy of the bound state in the closed channel E_{c} can be tuned relatively to the free-body open channel one by tuning the magnetic field B such as $E_{\text{c}} = \delta\mu(B - B_{\text{c}})$. This case is know as *magnetic tunable* Feshbach resonances. Here, we notice that, away from resonance, the bound-state energy is linear in B with the slope given by $\delta\mu$.

Now, let's consider the scattering phase shift η. Its background value η_{bg} is modified by the presence of a coupling between the two channels leading to an additional resonant term $\eta(E) = \eta_{\text{bg}}(E) + \eta_{\text{res}}(E)$. Without deriving the full theory, in the limit of small k, one can write the scattering length as

$$\begin{aligned} a(B) &= a_{\text{bg}} + a_{\text{res}}(B) \\ &= a_{\text{bg}} \left(1 + \frac{\Gamma_0}{-E_0 + i(\gamma/2)}\right) \end{aligned} \tag{4.6}$$

where Γ_0 and E_0 are energy-dependent constants accounting for the width and the energy-threshold resonance position of the resonance, respectively. γ takes into account the decay rate of the bound state into all possible loss channels. a_{bg} represent the background (off-resonant) scattering length due to $V_{\text{bg}}(r)$. In the case of magnetic Feshbach resonances, keeping in mind the previous paragraph, we can rewrite Eq. 4.6 in the famous expression

$$a(B) = a_{\text{bg}} \left(1 - \frac{\Delta}{B - B_0}\right) \tag{4.7}$$

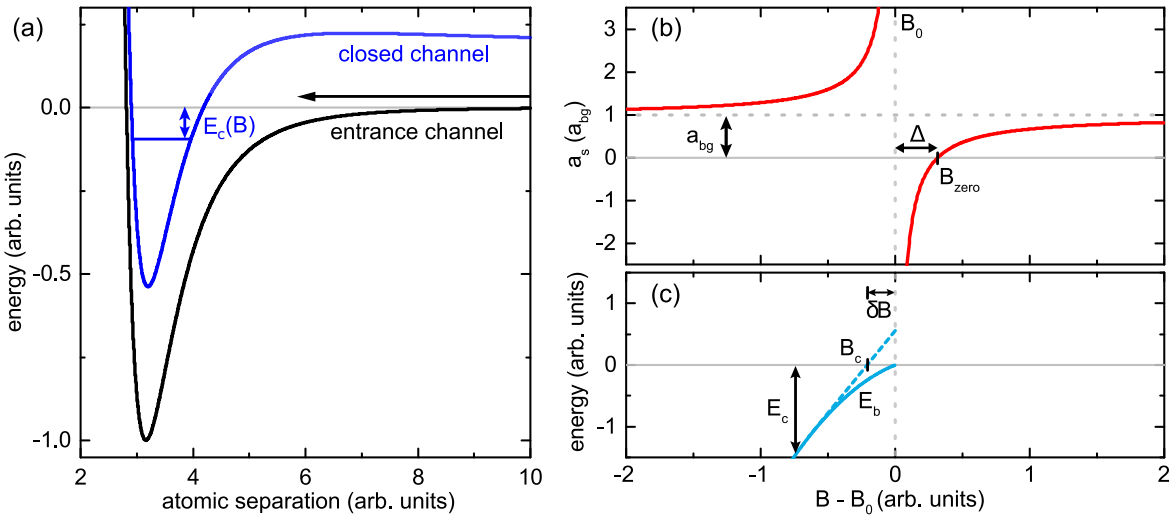

Figure 4.1: Basic description of Feshbach resonance in the two-channels model. (a) Pictorial representation of the entrance and closed channel (black and blue curve, respectively). In a magnetic FR, the energy $E_c(B)$ of a molecular bound state can be varied to resonantly couple the two channels by tuning the magnetic field. (b) Near-resonant behavior of the interparticle scattering length a_s (red curve). The FR can be described by its position B_0 and its width Δ. The width is defined as the separation between the pole and the value of magnetic field B_{zero} for which $a_s = 0$ (also called *zero crossing*). Far from the pole of the FR, a_s settle to the background scattering length a_{bg}. (c) At B_0, where a_s is very large, the binding energy E_b follows a quadratic dependence typical of the universal regime. Figure adapted from Ref. [Bai18b].

where $\Delta = \Gamma_0/\delta\mu$ and $B_0 = B_c + \delta B$ are the width and the pole respectively and $\delta B = -\delta E/\delta\mu$.

It is interesting to note that in the vicinity of the resonance's pole where $a \gg 1$, the bound-state energy bends with a quadratic dependence on the scattering length

$$E_b = \frac{\hbar^2}{2m_{12}a^2}. \tag{4.8}$$

This region of interaction is often known as *universal regime* and the state as *halo state* which in turn is a very weak bound case of a molecule [Rii94, Jen04]. The wave function of such state extends spatially on the order of a, beyond the turning point of the potential. In Fig. 4.1, the typical near-resonant behavior of a and E_b is depicted.

4.1.3 Resonance strength

In the ultracold regime, for a large distance of the colliding particles, scattering events of neutral atoms can be understood in good approximation by imagining the central potential to be of the van der Waals (vdW) type $V(r) = -C_6/r^6$ with C_6 being a coefficient. At short distances, the potential becomes repulsive and could be modeled as a hard-core repulsion potential. We can define a length scale for the vdW potential

$$R_{vdW} = \frac{1}{2}\left(\frac{2m_{12}C_6}{\hbar^2}\right)^{1/4}. \tag{4.9}$$

To simplify the physical interpretation, one can re-write this length scale as a mean scattering length $\bar{a} \approx 0.956 R_{\mathrm{vdW}}$ which defines a corresponding energy scale $\bar{E} = \hbar^2/(2m_{12}\bar{a}^2)$. In these units, it is possible to extract from Eq. 4.6 a dimensionless parameter associated with the resonance strength

$$s_{\mathrm{res}} = \frac{a_{\mathrm{bg}}}{\bar{a}} \frac{\delta\mu\Delta}{\bar{E}}. \tag{4.10}$$

If $s_{\mathrm{res}} \gg 1$, the coupling between open and closed channel is strong and the resonance is said to be "broad". These types of resonances are also called *open channel dominated* because they have the spin character of the entrance channel over a broad range of the width. Contrary to that, when $s_{\mathrm{res}} \ll 1$, the coupling is weak resulting in a "narrow" resonance which is labeled as *close channel dominated*. Open-channel dominated resonances also feature an universal regime which is much broader than the close-channel dominated case.

4.1.4 Hamiltonian

For the following development towards the complexity of lanthanides, it is necessary to do a step forward and write down a more complete Hamiltonian describing the scattering event and accounting for different interaction processes. In the following, $\mathbf{s}$ is the electronic spin, $\mathbf{l}$ the electronic orbital angular momentum coupled to the total electronic angular momentum $\mathbf{j} = \mathbf{s} + \mathbf{l}$. Then, calling $\mathbf{i}$ the nuclear spin, the total angular momentum will be $\mathbf{f} = \mathbf{j} + \mathbf{i}$. m_{f} and m_{l} are the quantum numbers accounting for the projection of $\mathbf{f}$ and l (relative angular momentum) on an external magnetic field. For two atoms (labeled as *1* and *2*), the two-atoms Hamiltonian can be written as

$$H_{12} = H_{\mathrm{k}} + H_{\mathrm{hf}} + H_{\mathrm{Z}} + H_{\mathrm{el}} + H_{\mathrm{ss}} \tag{4.11}$$

where H_{k} encloses the kinetic terms in the form of Eq. 4.2, H_{hf} is the hyperfine interaction, H_{Z} accounts for Zeeman splitting, H_{el} encloses the electronic interaction, and H_{ss} is the spin-spin interaction. Excluding the kinetic term, which was already discussed earlier in the chapter, the other terms can be summarized as follows.

The hyperfine interaction couples $\mathbf{s}$ to $\mathbf{i}$ by

$$H_{\mathrm{hf}} = \frac{1}{\hbar^2} \left(a_{\mathrm{hf},1} \mathbf{i}_1 \cdot \mathbf{s}_1 + a_{\mathrm{hf},2} \mathbf{i}_2 \cdot \mathbf{s}_2 \right) \tag{4.12}$$

with a_{hf} being the hyperfine constant.

The Zeeman term accounts for the energy-level shift of the atoms in a magnetic field B by

$$H_{\mathrm{Z}} = \frac{\mu_{\mathrm{B}}}{\hbar} B (g_{\mathrm{s}} \mathbf{s}_1 + g_{\mathrm{s}} \mathbf{s}_2 + g_{\mathrm{i},1} \mathbf{i}_1 + g_{\mathrm{i},2} \mathbf{i}_2) \tag{4.13}$$

where μ_B is the Bohr magneton and g_s and g_i are the Landé factors for electrons and nuclei.

The electronic interaction term includes the exchange term (Coulomb potential) and vdW potential $H_{\mathrm{el}} = H_{\mathrm{ex}} + H_{\mathrm{vdW}}$. The first one arises from the antisymmetry of the electronic wavefunction and can be written as

$$H_{\mathrm{ex}} = C_{\mathrm{ex}} \, \mathrm{e}^{-r/r_{\mathrm{ex}}} \left(\frac{1}{2} + 2\mathbf{s}_1 \mathbf{s}_2 \right) \tag{4.14}$$

with C_{ex} and r_{ex} being constants. The vdW potential was already discussed in Sec. 4.1.3 and follows a dependence $V(r) = -C_6/r^6$. H_{el} typically induces broad FR and it is diagonal in l and m_l, thus only even or odd partial waves are coupled together.

The last term in Eq. 4.11, encloses magnetic interactions and higher-orders spin-orbit couplings. The magnetic interaction, here called dipole-dipole interaction, depends on the relative orientation of electronic spins and atomic axes, therefore it leads to anisotropy. The higher orders spin-orbit coupling (here we just concentrate on the second order) can play an important role on heavy atoms like Cs and it shows the same spin dependence as the DDI with a different scaling law. Together they assume the shape

$$H_{\text{ss}} = -\frac{1}{2}\alpha^2 \left(\frac{1}{r^3} + C_{\text{so}}\, \mathrm{e}^{r/r_{\text{so}}} \right) (\mathbf{s}_1(3\mathbf{rr} - 1)\mathbf{s}_2) \tag{4.15}$$

where α is the fine structure constant, C_{so} and r_{so} are constants. H_{ss} instead causes narrow FR to appear. Note that H_{ss} is not diagonal in l, leading to coupling between different partial waves (off-diagonal terms).

Another important aspect in ultracold scattering relates to symmetry arguments on the wavefunctions of the atoms. Identical bosons (fermions) can collide only in even (odd) partial waves. In the case of collisions between nonidentical particles, all the values of l are in principle possible. Since all these models are highly sensitive on small variations of the interaction potentials, ideally one would need to know the exact shape of all of them. Such potentials are usually not directly accessible and a digression on their numerical calculation would require a treatment going beyond this thesis. Good approximations are reached in simple systems like alkali and alkali-alkali mixtures where H_{ss} is usually small and can be neglected, and the number of Born-Oppenheimer potentials is limited to a few. In the case of complex elements supporting a large number of bound states and/or introducing a strong H_{ss} contribution (like strongly magnetic lanthanides), the calculations become involved and predictions are hardly possible [Kot14]. As we will see later in Sec. 4.3, solving this scattering problem is highly non-trivial for alkali and even more for lanthanides.

4.2 Experimental aspects

In quantum gas experiments, Feshbach resonances are of high importance to tune the interactions between particles and, in some cases, even to attain quantum degeneracy at all. Pioneering observations of FRs in ultracold atoms were reported firstly in hydrogen [Rey86] and, at a latter time, in Na and Rb [Ino98, Cou98]. A vast number of phenomena depend on the existence of available FR: strongly and non-interacting systems, collapse and topological defects, molecule formation via *Feshbach association*, BEC-BCS crossover, Efimov physics, new phases of matter, and many more [Chi10]. In this section, we review some important experimental evidence connected to the leading role of FR in the ultracold atoms community. This contextualizes the current state-of-the-art with future steps that can be done on this topic. Firstly, we introduce the case of homonuclear alkali systems in, then we move to mixtures of alkali, and finally we discuss the last advances on more complex atomic species. A digression on the particular case of lanthanides is postponed to Sec. 4.3.

4.2.1 Inelastic collisions and trap-loss spectroscopy

In the previous theoretical approach, we considered the ultracold scattering to be dominated by elastic collisions. Nevertheless, an experimental tool used to investigate FR involves trap-loss spectroscopy methods which are related to inelastic processes. Such methods were already employed from the very first observations of FR in ultracold atom experiments [Ino98, Rob00, Web03]. Inelastic losses can be due to one-, two-, and three-body losses (α, L_2, and L_3 are the respective coefficients). In this picture, the time evolution of the trapped atom number $\dot{N}$ is expressed by the following equation:

$$\dot{N}(t) = -\alpha N(t) - \int L_2 n^2(\mathbf{r}, t)\, \mathrm{d}^3 r - \int L_3 n^3(\mathbf{r}, t)\, \mathrm{d}^3 r \tag{4.16}$$

where n is the atomic density distribution. Note that the one-body decay is usually connected to the lifetime of the sample due to background-gas collisions. L_2 and L_3 are enhanced near FR and, in the particular case of bosons, L_2 follows a Lorentzian profile while $L_3 \propto a^4$. In the case of fermions, the treatment is more complicated.

Despite their shapes, FRs are generally identified by increased atom losses with the maximum loss at the location of the resonance pole. Such a technique is extensively used in our experiment to identify and characterize FRs (see Sec. 4.4 and Appendix B).

4.2.2 Alkali

Nowadays, FRs are observed and employed in all the homonuclear alkali-metal systems (excluding francium) [Chi15]. Properties and appearance of FRs are strongly dependent on the atomic species and, even within the same element, every isotope shows dramatic differences. The direct connection between theory and experiment is intriguing: starting from the vast knowledge on alkali elements and the vast amount of spectroscopy data, theoretical calculations are possible and they are used to predict properties of FRs. In particular, between different isotopes of the same species, corrections due to mass scaling are easily implemented [Bur98, vK02]. Vice versa, their experimental observation and characterization have a direct impact on the development of interatomic potential modeling [Set00, vK04, Tie20].

Even though some alkali possess good collisional properties by themselves (^{23}Na, ^{41}K, and ^{87}Rb), interaction tuning via resonances is essential for Bose-Einstein condensation of ^{7}Li, ^{39}K, ^{85}Rb, and ^{133}Cs. Generally speaking, alkali have sparse Feshbach spectra if compared to the more complex atomic species (in the lighter elements, FRs can be hundreds of Gauss apart). The width of such resonances are also well distributed, varying from few mG to hundreds of G.

In Fermi gases and BECs of alkali-metal elements, FRs were used to successfully associate atoms into weakly-bound dimers for the production of molecular BEC [KÖ6].

4.2.3 Mixtures and complex systems

After alkali, which were the first species to be investigated, a growing attention has been focused on other species: alkaline-earth metals, transition metals, lanthanides, and various combinations of all these atomic species. The case of lanthanides will be discussed in the next Sec. 4.3.

A natural step towards an increased complexity of the system has been done by combining different alkali species in mixture experiments. Starting from K-Rb [Ino04, Fer06], the first mixture investigated to locate Feshbach resonances, observations have been reported for Li-Na [Sta04], Li-K [Wil08], Li-Cs [Rep13], Li-Rb [Deh08], Na-K [Par12], Rb-Na [Wan13], and Rb-Cs [Pil09]. There are no experimental observations for the case of Na-Cs. Isotopic mixtures of homonuclear Rb, K, and Li were also investigated and FRs characterized [Zha05, Pap06, Wu11, Tan18]. In the specific case of Li and K, both fermionic and bosonic isotopes are available leading to the possibility of interaction tuning in Bose-Fermi isotopic mixtures.

Strontium (like Ytterbium) has no electronic magnetic dipole moment due to the antiparallel alignment of the two valence-electron spin. As a consequence, Sr presents no magnetic resonances (optical FRs are possible [Bla11]). This problem does not arise in the case of mixtures of strontium with alkali atoms in which Feshbach resonances have been observed (see Sr-Rb in Ref. [Bar18]).

Chromium has been the first atom with more than one valence electron in which FRs were observed [Wer05]. In this element, the DDI term comes into play and calculations can be performed only by including such a contribution into the Hamiltonian. Indeed, in ^{52}Cr the resonances are due to the spin-spin interaction [Kot14]. Moreover, by using interaction tuning to suppress the isotropic contact interaction, it was possible to enter regimes in which DDI dominates the gas dynamics [Lah07, Koc08]. Quite recently, the creation of a cold gas of Cr-Li was announced, but no investigation on the Feshbach properties was conduced [Ner20].

4.3 Feshbach resonances in lanthanides

This section deals with the current knowledge of Feshbach resonances in lanthanide elements. In such systems, the vast amount of supported bound states combined with the complicated coupling schemes induced by the large spin-spin interaction term (see Eq. 4.11) and the anisotropy of the wave function, lead to a highly dense and intricate FR spectrum. Calculations and predictions are hardly possible, although, thanks to the great progress done on Er and Dy during the last years, the interest in the field is increasing fast.

4.3.1 Role of anisotropy

If in the case of Cr the spin-spin interaction is roughly a factor 36 stronger than alkali atoms, in lanthanides this factor can be even more substantial — in Er or Dy, it is about a hundred times higher than the alkali one. In this condition, both the long- and short-range interaction are influenced by this anisotropy and, to understand FRs at the first order, one has to consider

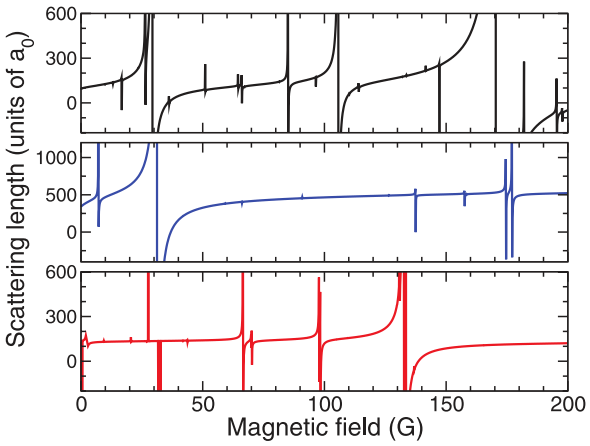

Figure 4.2: Numerically calculated scattering length as a function of magnetic field for ^{164}Dy at 30 nK. In the top panel all anisotropic interactions are included, whereas in the middle and lower panel the anisotropic dispersion and the dipole-dipole interactions are switched off, respectively. In this model, only channels of even partial waves up to $l = 10$ are included. To observe the same density as in the experiment, channels up to $l > 40$ have to be considered. Figure adapted from Ref. [Pet12]

at least the most prominent factors in the Hamiltonian (Eq. 4.11): dipole-dipole ($\propto 1/r^3$), quadrupole-quadrupole ($\propto 1/r^5$), and vdW dispersion ($\propto 1/r^6$) interactions [Pet12, Kot14]. For the sake of clarity, it has been shown that the highest contribution in the vdW potential comes from the standard isotropic term [Pet12]. However, in magnetic atoms the second highest vdW contribution is due to the so called anisotropic dispersion interaction (ADI).

Without going into too much details in the calculations, by means of a coupled-channels model, the authors in Ref. [Pet12] demonstrated that FRs in a sample of bosonic spin-polarized ^{164}Dy at 30 nK are purely caused by the anisotropic potentials. Fig. 4.2 shows the result of such calculations. By excluding the anisotropic terms, the spectrum changes drastically. However, the calculated density of resonances is much lower than the one experimentally reported. Here, the authors included channels with partial waves up to $l = 10$, although an $l > 40$ is needed to reproduce the real density. Almost simultaneously, our group has performed FR studies in erbium showing a number of resonances even higher than the predicted one [Fri14]. Another limitation comes from the temperature taken into account. In the experiments with lanthanides, a dramatic dependence of FR density on the sample temperature has been observed [Bau14, Mai15b, Khl19]. Therefore, to achieve more realistic results, calculations should include non-zero partial waves collisions and additional available channels.

Despite the difficulty of carrying out calculations, qualitative studies of different lanthanide systems were performed in Refs. [GM15, Gre16, ZK18, Fry19, Yan19, Kos20]. Nonetheless, to our knowledge, no work has been performed on heteronuclear lanthanide mixture systems.

4.3.2 Experimental observations

The first observations of FR in a lanthanides were reported by the Ferlaino's group in gases of bosonic Er atoms [Aik12]. Intensive Feshbach spectroscopy on both fermionic and bosonic

isotopes followed in Ref. [Fri14]. In Ref. [Bai18a], FR between different spin components of fermionic erbium were observed. By using magneto-association, Feshbach molecules of Er were created [Fri15]. Regarding Dy, preliminary observations of FR in gasses of bosonic and fermionic isotopes were performed by the Lev's group [Bau14] followed by deeper investigations by other groups [Mai15a, Luc18]. Recently, FRs in bosonic ^{169}Tm atoms were reported [Khl19] together with a study on their statistic distribution. In all these systems, the existence of several FRs located at low magnetic field is of particular experimental interest, as it allows for precise interaction tuning and simplifying the experimental apparatus.

Ytterbium, has zero electronic angular momentum in the ground state due to the paired electrons leading to absence of accessible and useful magnetic Feshbach resonances (beside optical FR [Eno08]). A particular type of magnetic resonances, called orbital FR, was observed in a mixture of Yt atoms in different electronic states [Pag15, Cap19].

Moving outside the purely lanthanide systems, in Ref. [Rav20] the Grimm's group reported the first experimental observation of Feshbach resonances in a lanthanide-alkali mixture of dysprosium-potassium. In Ref. [Gre20], FRs in a Yb-Li system has been reported.

As previously said, lanthanides possess a highly dense FR spectrum which in turn is a reminiscence of the intrinsic complexity of the system. A direct effect of such complexity is the so called *quantum chaos*. It has been shown that FR spectra of lanthanides follow a statistically chaotic distribution well described with the use of random-matrix theory [Fri14, Mai15b, Khl19]. In particular, the nearest-neighbor spacing between FRs resembles a Wigner-Dyson distribution (typical of chaotic systems), characterizing strongly interacting levels and level repulsion. It has also been proposed that chaos is more generally the result of systems with multiple degrees of freedom which are mixed together [Wei09]. In Refs. [Mai15b, Acv18], the authors demonstrate that this chaotic behavior in the FRs spectrum is generated by the substantial off-diagonal coupling arising from the DDI and ADI.

Worth to be noticed is also the strong dependence of FR spectra on the sample temperature. The FR density in erbium increases of 25 % when the temperature grows from 350 nK to 1.4 µK [Mai15b] and by ∼50 % in dysprosium in response to a doubling of the sample temperature [Bau14]. A similar factor is reported in thulium to a six-times temperature increase [Khl19]. This behavior is due to the increasing contribution of different partial waves of the entrance channels for increasing temperature [Mai15b], motivating the speculation in Ref. [Kot11]. In particular, resonances with $l > 0$ entrance channels are suppressed by lowering the temperature.

Up to now, no experiments or theories covered the topic of FRs in mixture of different lanthanide species such as erbium-dysprosium mixtures. In Sec. 4.4 we present the observation of several FRs in different isotopic combinations of Er-Dy including Bose-Bose, Bose-Fermi, and Fermi-Fermi mixtures. In Appendix B, the Feshbach spectra for such samples are collected and shown.

4.4 Publication: Feshbach Resonances in an Erbium-Dysprosium Dipolar Mixture[†]

Gianmaria Durastante[1,2], Claudia Politi[1], Maximilian Sohmen[1,2], Philipp Ilzhöfer[1], Manfred J. Mark[1,2], Matthew A. Norcia[1], and Francesca Ferlaino[1,2]

[1] *Institut für Quantenoptik und Quanteninformation, Österreichische Akademie der Wissenschaften, Technikerstraße 21a, 6020 Innsbruck, Austria*
[2] *Institut für Experimentalphysik and Zentrum für Quantenphysik, Universität Innsbruck, Technikerstraße 25, 6020 Innsbruck, Austria*

Physical Review A — accepted, in press
submitted 11 Jun 2020
URL: arXiv:2006.06456

[†] The author of the present thesis developed the experimental procedure, performed the measurements, analyzed the data, and wrote the manuscript with the help of the other authors. Particular support in the data analysis and writing phase came from C.P. and M.N.

Feshbach Resonances in an Erbium-Dysprosium Dipolar Mixture

Gianmaria Durastante,[1,2] Claudia Politi,[1] Maximilian Sohmen,[1] Philipp Ilzhfer,[1] Manfred J. Mark,[1,2] Matthew A. Norcia,[1] and Francesca Ferlaino[1,2]

[1] *Institut für Quantenoptik und Quanteninformation, Österreichische Akademie der Wissenschaften, 6020 Innsbruck, Austria*
[2] *Institut für Experimentalphysik und Zentrum für Quantenoptik, Universität Innsbruck, Technikerstraße 25, 6020 Innsbruck, Austria*

(Dated: June 12, 2020)

We report on the observation of heteronuclear magnetic Feshbach resonances in several isotope mixtures of the highly magnetic elements erbium and dysprosium. Among many narrow features, we identify two resonances with a width greater than one Gauss. We characterize one of these resonances, in a mixture of ^{168}Er and ^{164}Dy, in terms of loss rates and elastic cross section, and observe a temperature dependence of the on-resonance loss rate suggestive of a universal scaling associated with broad resonances. Our observations hold promise for the use of such a resonance for tuning the interspecies scattering properties in a dipolar mixture. We further compare the prevalence of narrow resonances in an ^{166}Er-^{164}Dy mixture to the single-species case, and observe an increased density of resonances in the mixture.

Ultracold quantum gases are a highly successful platform for physics research largely because it is possible to create simplified and controllable versions of condensed matter systems [1]. As the field has advanced, great progress has been made by reintroducing complexity in a carefully controlled manner. This complexity can manifest in the form of interparticle interactions [2–4], the species and statistics of the particle under study [5–7], or in the form of the potential landscape, control protocols and imaging techniques applied to the system [8, 9]. In this work, we explore interspecies Feshbach resonances as a means of generating tunable interactions between two different species of complex dipolar atoms.

Atoms with large magnetic dipole moments, such as the lanthanide series elements erbium and dysprosium, interact in a manner that is both long-range and anisotropic. This is in contrast to more commonly used atomic species, such as alkali and alkaline earth metals, which primarily interact in a short-range and isotropic way. The recent creation of degenerate Bose and Fermi gases of such atoms [10–13] has enabled the observation of a wealth of new phenomena including quantum-stabilized droplet states [14–16], roton quasi-particles [17], supersolid states [18–20], and a non-isotropic Fermi surface [21].

In a separate direction, degenerate mixtures of multiple atomic species have also provided diverse opportunities for the study of new physical phenomena. Examples include studies of polarons that arise when an impurity species interacts with a background gas [22–27], and the formation of heteronuclear molecules with large electric dipole moments [28–31].

We expect that combining dipolar interactions with heteronuclear mixtures will lead to a rich set of novel physical phenomena, the exploration of which has only recently begun. In particular, dipolar interactions are expected to have dramatic consequences for the miscibility of binary condensates [32–34], and in turn on vortex lattices that arise in such systems [35]. Further, novel properties of polarons are predicted to emerge when either the background [36] or both background and impurity [37] particles experience dipolar interactions [38].

Dipolar heteronuclear mixtures have recently been demonstrated [39], but so far the interspecies scattering properties have not been explored, either experimentally or theoretically. In these complex dipolar species, scattering properties are dictated by both anisotropic long-range dipolar interactions, which can be tuned through a combination of system geometry and magnetic field angle, and by contact interactions, which can be tuned through the use of interspecies Feshbach resonances. While scattering models and experimental demonstrations exist for mixtures of single- and two-valence electron atoms (which lack strong dipolar interactions) [40, 41], the scenario of two multi-valence electron atoms has yet to be considered, and represents a new frontier for our understanding of ultracold scattering. In many commonly used atomic systems, the strength, character, and location of magnetic Feshbach resonances can be predicted with high precision through coupled-channel calculations [3]. However, the complexity of the internal level structure and coupling mechanisms present in lanthanide atoms lead to significant challenges for the development of a microscopic theory with predictive power, and so necessitate an experimental survey to find resonances with favorable properties [42–46].

To this end, we searched for heteronuclear Feshbach resonances broad enough to provide a practical means for tuning the interspecies interaction in Bose-Bose and Bose-Fermi dipolar quantum mixtures. Using atomic-loss spectroscopy to identify resonances, we perform surveys of fermionic ^{161}Dy and bosonic ^{164}Dy together with ^{166}Er, ^{168}Er, and ^{170}Er over a magnetic-field range from zero to several hundred Gauss (the exact range varies

by isotope combination due to availability of favorable evaporation conditions). We also explored a Fermi-Fermi mixture of ^{167}Er and ^{161}Dy, but observed no broad resonances there. In Table I we summarize positions and widths of these features observed in our surveys. As an exemplary case, we present a more detailed characterization of the resonance near 13.5 G in the ^{168}Er-^{164}Dy Bose-Bose mixture, through measurements of interspecies thermalization and the dependence of atomic loss on temperature.

In addition, our dipolar mixtures host a large number of narrow interspecies resonances. In previous experiments with single species, the density and spacing of these narrow resonances has been studied to reveal a pseudo-random distribution that can be modeled well using random matrices [43, 45, 46]. By performing high resolution scans over specific magnetic-field ranges, we find that the average density of interspecies resonances exceeds the combined density of intraspecies resonances, perhaps indicating the contribution of odd partial waves or molecular states with antisymmetric electron configurations for the interspecies case, which are not present in the scattering of identical bosons.

Finally, in each Fermi-Bose mixture involving ^{161}Dy we observe a correlated loss feature between fermionic Dy and bosonic Er atoms. Strangely, the loss feature is present at the same magnetic-field value for all three bosonic erbium isotopes studied. Such behavior is inconsistent with a typical interspecies Feshbach resonance, where the magnetic field at which the resonance occurs is strongly dependent on the reduced mass of the atoms involved [47]. The mechanism behind this unusual feature is as of yet unknown and calls for further experimental and theoretical investigations.

Our experimental sequence is similar to the one introduced in our previous works [39, 48]. More details can be found in the supplemental material [49]. In brief, after cooling the desired isotope combination of erbium and dysprosium atoms into dual-species magneto-optical trap (MOT), we load the atoms into a crossed optical dipole trap (ODT) created by 1064 nm laser light. Here we perform evaporative cooling down to the desired sample temperature. During the whole evaporation sequence, we apply a constant and homogeneous magnetic field (B_{ev}), pointing along the z-direction opposite to gravity. B_{ev} preserves the spin-polarization into the lowest Zeeman sublevel of both species. We use different values of B_{ev} to optimize the evaporation efficiency depending on the isotope combination and on the range of the target magnetic field (B_{FB}) to be investigated. The final ODT has trap frequencies $\omega_{x,y,z} = 2\pi \times (222, 24, 194)\,\mathrm{s}^{-1}$. We typically obtain mixtures with atom numbers ranging from 3×10^4 to 1×10^5 atoms for each species. The sample is in thermal equilibrium at about 500 nK, which corresponds to about twice the critical temperature for condensation. Typical densities are up to a few $10^{12}\,\mathrm{cm}^{-3}$ for each species. After preparing the mixture, we linearly ramp the magnetic field from B_{ev} to B_{FB} in 5 ms, either in an increasing or decreasing manner. We hold the mixture for a time ranging between 5 ms and 400 ms depending on the experiment. At the end of the hold time, we release the atoms from the ODT in a 15 ms time-of-flight (TOF) expansion after which we record an image of the atoms using a standard low-field absorption imaging technique [12, 49]. Note that we adjust the relative amount of erbium and dysprosium in the final thermal mixture for the specific experiments by independently tuning the MOT loading time for each species between 0.5 s to 5 s.

TABLE I. Comparatively broad resonances found in specific isotope mixtures together with estimated center positions and widths (FWHM) from Gaussian fits to atom loss spectra. Each value is an average between the fit values of Er and Dy.

Combination	Resonance magnetic field (G)	Width (G)
^{168}Er-^{164}Dy	13.32(4)	1.7(1)
^{166}Er-^{164}Dy	34.09(3)	1.5(1)
^{166}Er-^{161}Dy	161.31(3)	0.84(9)
^{168}Er-^{161}Dy	161.30(2)	0.93(5)
^{170}Er-^{161}Dy	161.26(3)	0.91(8)

In the isotope combinations and range of magnetic fields that we explore here, we observe two interspecies resonances with widths greater than 1 G (see Table I). We now turn to a more detailed characterization of a feature present in the ^{168}Er-^{164}Dy combination, for which atom loss is shown in Figure 1(a). We chose to focus on this feature because it is relatively isolated from the many narrow homonuclear and heteronuclear resonances typical of lanthanides. In this experiment, the starting mixture contains 6.2×10^4 erbium and 9.1×10^4 dysprosium atoms and it is prepared by evaporation at $B_{\mathrm{ev}} = 10.9$ G. In order to compensate for loss during magnetic-field ramps and slow drifts of the atom number, we normalize measurements performed with 200 ms hold times at B_{FB} to interleaved measurements at 10 ms hold time at the same field. We further performed independent trap-loss spectra in single-species operation to confirm the interspecies nature of the resonance. Moreover, such scans allow us to identify intraspecies resonances and exclude them from the fit (see empty symbols in Figure 1(a)). As shown in the inset for erbium, a high-resolution scan reveals a narrow region with less loss near the center of our broad loss feature, probably due to the influence of a second interspecies resonance. This structure is also visible on the dysprosium loss feature but it is not shown in the inset for ease of reading.

A Gaussian fit to the loss profiles, with known narrow single-species resonance excluded, returns a center value of 13.31(2) G and 13.33(4) G and a full width at half maximum value of 1.95(5) G and 1.3(1) G for erbium and

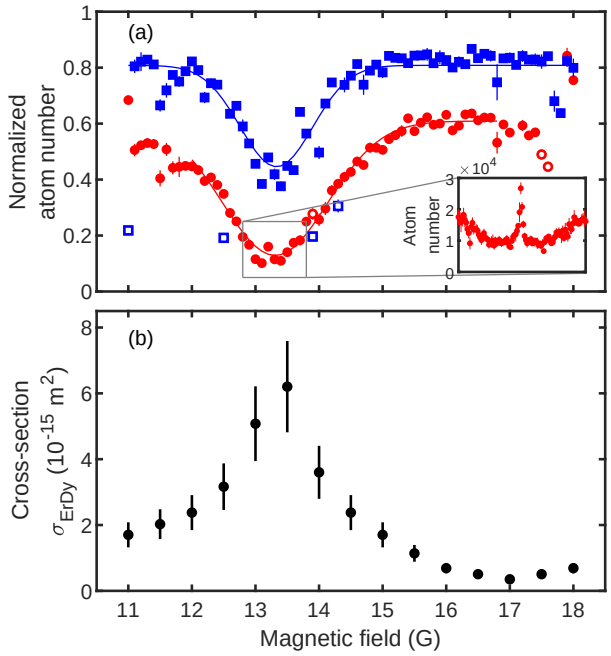

FIG. 1. (a) Trap loss from the 13.5 G resonance in the Bose-Bose mixture ^{168}Er-^{164}Dy (red circles and blue squares points respectively). Empty symbols correspond to narrow single-species resonances, which we exclude from fits. Each point is an average over four experimental repetitions. For each magnetic field, the atom number recorded after 200 ms of hold time is normalized to that at a short hold time of 10 ms. The lines are the Gaussian fits to the data. The inset shows erbium loss measured in a different dataset with 5 mG resolution, and highlights the structure present on the center of the feature. The same structure is visible also for the dysprosium atoms in the mixture. (b) Interspecies elastic cross-section σ_{ErDy} measured across the Feshbach resonance using cross-species thermalization. Each value of σ_{ErDy} is extracted from thermalization data using a numerical model for thermalization that includes temporal variation in atom number and temperature; see main text and supplemental material [49].

dysprosium, respectively. The observed difference in the fitted width of the two species can be explained by the imbalance in atom number: because this measurement was performed with fewer erbium atoms than dysprosium, the fractional loss of erbium is higher than that of dysprosium, leading to a greater saturation of loss and broadening of the erbium loss feature.

To get insights on its effective strength and width, we perform cross-species thermalization measurements across the resonance (see Fig. 1(b)). Interspecies thermalization experiments are well established techniques to extract effective thermalization cross sections, which in turn depends on the scattering length [50–52]. While inferring on a precise value of the scattering length would require the development of a detailed and rigorous model that accurately captures the temperature-dependence of the interspecies and anisotropic dipolar scattering [53], and would go beyond the scope of this work, we are able to determine a thermally averaged scattering cross-section from which we can estimate the width of the resonance.

In this cross-thermalization experiment, we selectively heat dysprosium by means of a near-resonant 421 nm light pulse along the vertical direction. We confirmed that the light pulse has no direct measurable effect on erbium. The magnetic field is then jumped to the desired value B_{FB} and held for a variable amount of time, during which the temperature of erbium rises to equilibrate with dysprosium due to elastic collisions. We record the temperature of the two species along a direction orthogonal to the heating pulse, as the effects of center of mass motion are less prevalent here [54], and use a numerical model to extract a cross section from the rate of thermalization [49]. This simple model assumes an energy independent cross section, an assumption which may break down near resonance where unitarity limits on scattering may become significant.

From these thermalization measurements, we can see a dramatic increase in the scattering cross section near resonance, as one would expect for an interspecies Feshbach resonance. Further, we observe a significant modification of the cross section associated with the resonance over a Gauss-scale range of magnetic fields, similar to the width we observe in loss measurements. For an isolated resonance and pure contact interactions, a common way to characterize the resonance width is the parameter Δ, given by the difference in magnetic field between the pole of the resonance, at which the thermalization rate is max-

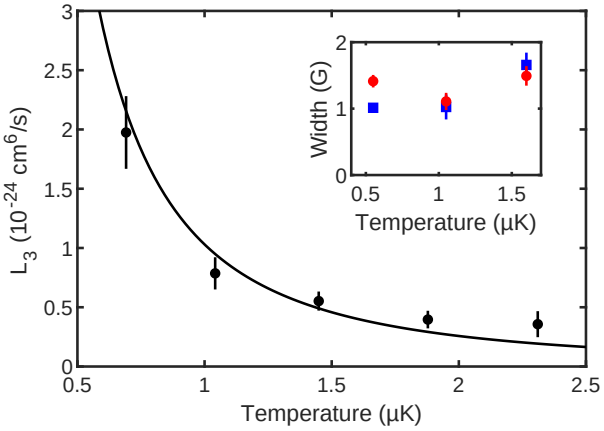

FIG. 2. Three-body loss coefficient L_3 extracted from on-resonance loss measurements at the resonance position for different temperatures (black circles), along with a fit to a $1/T^2$ scaling (black line), as expected for universal three-body loss. The inset shows the resonance width extracted as FWHM from Gaussian fits to the trap-loss spectra versus cloud temperature for a different dataset. Red circles and blue squares refer to erbium and dysprosium respectively. The reported temperature comes from a TOF estimation.

imal, and the nearest zero-crossing in the thermalization rate, which would correspond to a lack of scattering [3]. In lanthanides, the presence of anisotropic dipolar interactions leads to a scattering cross section that does not completely vanish. In addition, multiple narrow and overlapping resonances may be present, which may influence the interpretation of such a width measurement. However, to get a rough estimate of the width of the resonance, we can consider the distance between the resonance pole and the apparent minimum in the thermalization rate at 17 G. This suggests a width of $\Delta \simeq 3.5$ G.

The dependence of the loss feature on the cloud temperature can provide additional information on the nature of the resonance. For broad resonances, a universal regime is expected to emerge near resonance where the scattering cross section and loss are dictated primarily by the atomic momentum, rather than the scattering length [55]. In this regime, the three-body loss parameter L_3 follows a nearly universal form scaling as $1/T^2$, where T is the temperature. Such scaling has been observed in broad resonances of several atomic species [55–57].

We observe a temperature dependence of the loss rate near resonance that is suggestive of such universal behavior. By varying the final depth of the ODT reached during evaporation, we tune the temperature of the atomic mixture. For each temperature, we measure atom loss on resonance at 13.4 G as a function of the hold time. We then use a numerical model to extract the rate of interspecies three-body loss, and L_3 [49].

These loss coefficients are plotted as a function of temperature in Fig. 2, along with a fit to a $1/T^2$ dependence, which provides a reasonable description of our data. The universal temperature dependence arises from a maximum value of L_3 possible at a given temperature, given by:

$$L_{3,\max} = \frac{\lambda_{3,\max}}{T^2} \simeq \frac{\hbar^5}{m^3} \frac{36\sqrt{3}\pi^2}{(k_B T)^2}. \quad (1)$$

Factors associated with Efimov physics [49] can lead to a lower value for L_3, but not higher [55, 58, 59]. From our fit to a $1/T^2$ dependence for our data, we extract a value of $\lambda_3 = 1.0(2) \times 10^{-24}\,\mu\mathrm{K}^2\mathrm{cm}^6\mathrm{s}^{-1}$, which is compatible with the predicted bound of $\lambda_{3,\max} = 2.4 \times 10^{-24}\,\mu\mathrm{K}^2\mathrm{cm}^6\mathrm{s}^{-1}$.

A reduction in the peak loss rate with increasing temperature can also result from thermal broadening of the resonance, especially for very narrow resonances [45]. This is unlikely to be the dominant effect here, as for typical differential magnetic moments between entrance and closed channels in our lanthanide system [60], we would expect broadening on the scale of a few times 10 mG for temperatures near 1 µK, much narrower than the Gauss-scale width of our feature. Further, suppression of peak loss is typically accompanied by a commensurate broadening and shift of the loss feature on the scale of its width, which we do not observe (inset in Fig. 2).

In addition to the few relatively broad resonances, the lanthanides exhibit many narrow resonances, whose statistical properties have been investigated for single-species gases [43, 45, 46]. In this section we compare the abundance of interspecies resonances to single-species resonances by performing high-resolution trap-loss spectroscopy on the isotope combination ^{166}Er-^{164}Dy (see Fig. 3). Here, we investigate four different magnetic-field ranges, each 10 G wide, with a resolution 40 times higher than the one used for the exploratory surveys. To enable direct comparison with the previous works performed on single species [43, 45], we use similar experimental conditions (isotope, atom number, temperature, and hold time).

As expected, we observe many narrow homonuclear resonances [43, 45]. In addition, we also identify many narrow heteronuclear resonances. To distinguish these two types of resonance, we first label features with a fractional loss above 30% as resonances. We then categorize these resonances as interspecies if erbium and dysprosium loss features occur simultaneously within a range of ±10 mG and with a loss amplitude ratio in the range 0.5-2. Features that do not meet both of these criteria, are labelled either as homonuclear or ambiguous, based on comparison with separate scans performed with single species, either within this work or from previously published data [43, 45]. The number of ambiguous features define our confidence interval.

In order to visualize the number of resonances, we construct the staircase function $\mathcal{N}(B)$, which describes the cumulative number of resonances from the start of a scan range up to a given magnetic field B_{FB}. Figure 4(a-d) shows $\mathcal{N}(B)$ for the four investigated magnetic-field ranges. The black lines represent heteronuclear Feshbach resonances, while the blue and the red lines represent the homonuclear ^{166}Er and ^{164}Dy resonances, respectively. The shaded regions represent our confidence interval defined by the total number of ambiguous Feshbach resonances.

Our analysis results in a total number of heteronuclear resonances of $\mathcal{N}_{\mathrm{ErDy}}(\mathrm{tot}) = 339(16)$, counting all magnetic-field ranges, and a number of homonuclear resonances of $\mathcal{N}_{\mathrm{Er}}(\mathrm{tot}) = 116(16)$ and $\mathcal{N}_{\mathrm{Dy}}(\mathrm{tot}) = 144(16)$. Within our confidence intervals, we detect a total number of homonuclear resonances comparable with those of previous works [43, 45]. The corresponding total density of resonances $\bar{\rho}$, given by the total number of resonances divided by the total range of magnetic fields scanned are: $\bar{\rho}_{\mathrm{ErDy}} = 8.5(4)\,\mathrm{G}^{-1}$, $\bar{\rho}_{\mathrm{Er}} = 2.9(4)\,\mathrm{G}^{-1}$, and $\bar{\rho}_{\mathrm{Dy}} = 3.6(4)\,\mathrm{G}^{-1}$.

For our combined dataset, we find that the total number of heteronuclear resonances exceeds the combined number of homonuclear resonances for the two species: $\bar{\rho}_{\mathrm{ErDy}} = \alpha(\bar{\rho}_{\mathrm{Er}} + \bar{\rho}_{\mathrm{Dy}})$, with $\alpha = 1.3(2)$. We would expect that the average density of heteronuclear resonances should be greater than the sum of the two homonu-

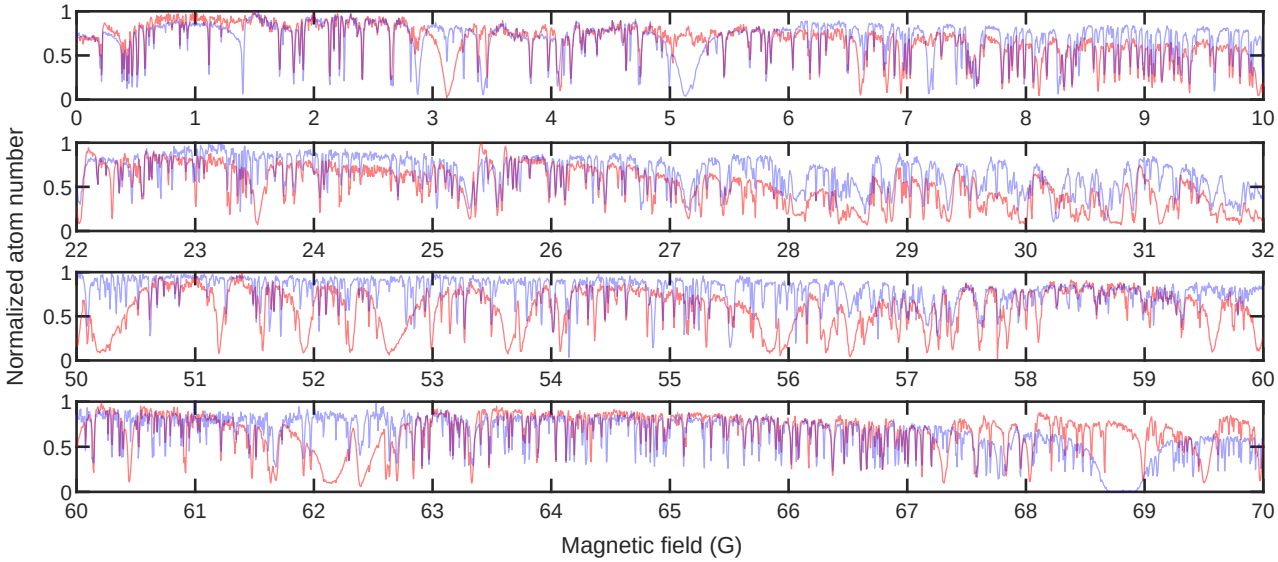

FIG. 3. High-resolution trap-loss spectroscopy for a balanced mixture of ^{166}Er and ^{164}Dy (red and blue curves respectively), with initial atom numbers of roughly 10^5 per species and a temperature of 500 nK and after 400 ms of interaction time. The measurement is composed of four datasets [0,10] G, [22,32] G, [50,60] G, and [60,70] G with a stepsize of 5 mG Each point is an average over four experimental repetitions. Atom numbers are normalized to the maximum of each dataset for ease of reading. The broad loss feature in Dy near 68.8 G was not observed in previous work [45], and may result from a technical source of loss in our experiment.

clear resonance densities. This is because each species contributes a set of internal states that can be coupled to, and the heteronuclear resonances are not subject to the same symmetrization requirements as the homonuclear resonances. In resonances involving distinguishable particles, both gerade and ungerade Born-Oppenheimer molecular potentials contribute, as well as both even and odd partial waves for the entrance channel. Our data is consistent with this expectation ($\alpha > 1$). Note that we do observe a lower number of interspecies resonances in the range [50,60] G, perhaps as a result of the non-random distribution of resonances as observed in the single-species case [43, 45], or to the presence of broad homonuclear erbium resonances that could obscure the observation of interspecies resonances.

Finally, we have also searched for broad (Gauss-range) resonances in Bose-Fermi mixtures consisting of fermionic ^{161}Dy combined with different bosonic isotopes of erbium – ^{166}Er, ^{168}Er, and ^{170}Er, as well as Fermi-Fermi mixtures of ^{161}Dy and ^{167}Er. For these combinations, we perform only coarse scans and thus only resolve broad features. In mixtures involving the bosonic isotopes of erbium we observe a correlated loss feature between erbium and dysprosium near 161 G (see Fig. 5). This loss feature is not present at our level of measurement sensitivity with either species alone, or in the mixture with the fermionic ^{167}Er. Surprisingly, the loss feature is centered at the same magnetic field (to within our resolution of 0.1 G) for all bosonic isotopes of erbium. This is quite unexpected as the magnetic-field value of the resonance position is typically highly sensitive to the reduced mass of the atoms involved [47].

Several physical mechanisms could be consistent with such a feature. One possibility is that the resonance we observe is associated with a bound state of a shallow molecular potential [61]. Mechanisms to create such potentials have been proposed for species with dipolar interactions [62, 63]. However, none are obviously applicable to magnetic atoms in the lowest energy entrance channel. Further, given the level of insensitivity to the mass of erbium, we would expect to see additional resonances of a shallow potential in the magnetic-field range over which we survey, which we do not. A second possibility is that the feature we observe is not a true interspecies resonance, but rather an intraspecies resonance in dysprosium whose loss rate is enhanced by the presence of bosonic erbium atoms. A similar effect was reported in a mixture of fermionic lithium and bosonic rubidium atoms [64]. Finally, it is possible that this feature is not a Feshbach resonance at all, but rather the result of spin-changing processes resulting from unintentional radio-frequency tones in the laboratory, or of an interspecies photoassociation resonance. We have ruled out the most likely culprits for the last effect by varying the relative detuning between our horizontal and vertical dipole traps and observing no change in the resonance position. We hope that our presentation of this mysterious feature may spur theoretical exploration of possible

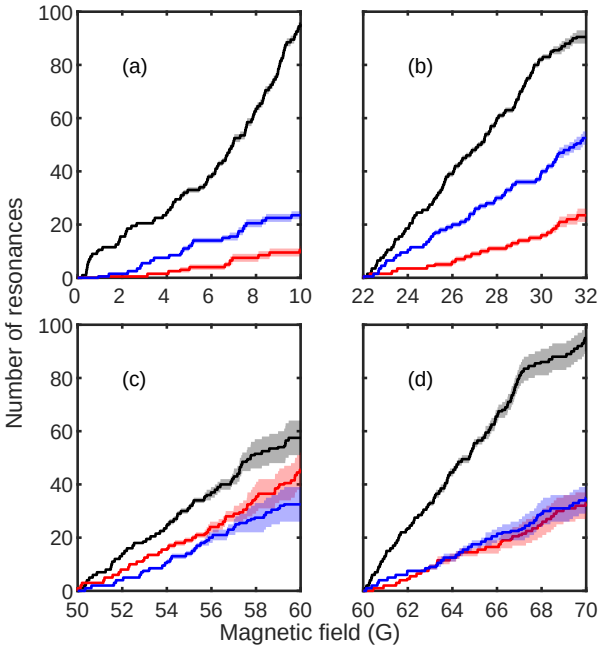

FIG. 4. (a-d) Staircase function describing the number of Feshbach resonances as a function of the four investigated magnetic-field ranges: [0,10] G, [22,32] G, [50,60] G, and [60,70] G respectively. The black line shows the number of heteronuclear resonances. The red and blue lines show the number of homonuclear resonances for ^{166}Er and ^{164}Dy, respectively. The shaded areas represent our confidence intervals (see main text).

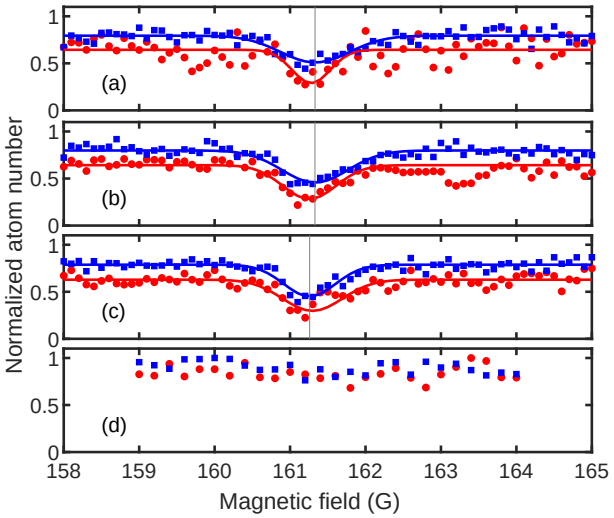

FIG. 5. Trap loss spectra for fermionic ^{161}Dy in combination with bosonic ^{166}Er, ^{168}Er, and ^{170}Er, and fermionic ^{167}Er (a-d, respectively). Red circles represent erbium, blues squares represent dysprosium and lines are Gaussian fits to the losses. The solid vertical gray lines highlight the peak centers from the fit over dysprosium losses. For the plots with bosonic erbium, the atom number after 100 ms of interaction time is normalized to a short hold time of 5 ms. In the plot with ^{167}Er, the normalization is performed using the maximum value in the dataset. For all panels, each point is an average over four experimental repetitions.

physical mechanisms.

In conclusion, we have reported experimental observation of heteronuclear magnetic Feshbach resonances in several isotope mixtures of erbium and dysprosium. Among the Gauss-broad features identified in our surveys, we have characterized one in the combination ^{168}Er-^{164}Dy by means of cross-species thermalization measurement and temperature dependence analysis. We performed high-resolution trap-loss spectroscopy in the combination ^{166}Er-^{164}Dy to compare the average resonance density of the mixture with respect to the single-species case. In mixtures of fermionic ^{161}Dy and bosonic erbium atoms, we observed a correlated loss feature which appears to be insensitive on the erbium isotope used but absent in dysprosium alone. Our observations pave the way to realize tunable interactions in quantum degenerate mixtures of dipolar atoms, which will enable varied opportunities including studies of the miscibility of binary condensates, of vortex lattices, and of dipolar polarons [32–37].

We thank Jeremy Hutson, Matthew Frye, John Bohn, Arno Trautmann, and the Erbium and DyK teams in Innsbruck for insightful discussions. This work is financially supported through an ERC Consolidator Grant (RARE, No. 681432), a NFRI Grant (MIRARE, No. ÖAW0600) from the Austrian Academy of Science, a QuantERA grant MAQS by the Austrian Science Fund FWF No I4391-N, and a DFG/FWF (FOR 2247/PI2790). M. S. and G. D. acknowledge support by the Austrian Science Fund FWF within the DK-ALM (No. W1259-N27). We also acknowledge the Innsbruck Laser Core Facility, financed by the Austrian Federal Ministry of Science, Research and Economy.

* Correspondence and requests for materials should be addressed to Francesca.Ferlaino@uibk.ac.at.

[1] I. Bloch, J. Dalibard, and W. Zwerger, Rev. Mod. Phys. **80**, 885 (2008).
[2] C. Menotti, M. Lewenstein, T. Lahaye, and T. Pfau, AIP Conference Proceedings **970**, 332 (2008).
[3] C. Chin, R. Grimm, P. S. Julienne, and E. Tiesinga, Rev. Mod. Phys. **82**, 1225 (2010).
[4] M. Saffman, T. G. Walker, and K. Mølmer, Rev. Mod. Phys. **82**, 2313 (2010).
[5] B. DeMarco and D. S. Jin, Science **285**, 1703 (1999).
[6] Z. Hadzibabic, C. A. Stan, K. Dieckmann, S. Gupta, M. W. Zwierlein, A. Görlitz, and W. Ketterle, Phys. Rev. Lett. **88**, 160401 (2002).
[7] M. Taglieber, A.-C. Voigt, T. Aoki, T. W. Hänsch, and K. Dieckmann, Phys. Rev. Lett. **100**, 010401 (2008).
[8] W. S. Bakr, J. I. Gillen, A. Peng, S. Flling, and

M. Greiner, Nature **462**, 74 (2009).
[9] C. Gross and I. Bloch, Science **357**, 995 (2017).
[10] M. Lu, N. Q. Burdick, S. H. Youn, and B. L. Lev, Phys. Rev. Lett. **107**, 190401 (2011).
[11] M. Lu, N. Q. Burdick, and B. L. Lev, Phys. Rev. Lett. **108**, 215301 (2012).
[12] K. Aikawa, A. Frisch, M. Mark, S. Baier, A. Rietzler, R. Grimm, and F. Ferlaino, Phys. Rev. Lett. **108**, 210401 (2012).
[13] K. Aikawa, A. Frisch, M. Mark, S. Baier, R. Grimm, and F. Ferlaino, Phys. Rev. Lett. **112**, 010404 (2014).
[14] H. Kadau, M. Schmitt, M. Wenzel, C. Wink, T. Maier, I. Ferrier-Barbut, and T. Pfau, Nature (London) **530**, 194 (2016).
[15] L. Chomaz, S. Baier, D. Petter, M. J. Mark, F. Wächtler, L. Santos, and F. Ferlaino, Phys. Rev. X **6**, 041039 (2016).
[16] M. Schmitt, M. Wenzel, F. Böttcher, I. Ferrier-Barbut, and T. Pfau, Nature (London) **539**, 259 (2016).
[17] L. Chomaz, R. M. W. van Bijnen, D. Petter, G. Faraoni, S. Baier, J.-H. Becher, M. J. Mark, F. Wächtler, L. Santos, and F. Ferlaino, Nat. Phys. **14**, 442 (2018).
[18] F. Böttcher, J.-N. Schmidt, M. Wenzel, J. Hertkorn, M. Guo, T. Langen, and T. Pfau, Phys. Rev. X **9**, 011051 (2019).
[19] L. Chomaz, D. Petter, P. Ilzhöfer, G. Natale, A. Trautmann, C. Politi, G. Durastante, R. M. W. van Bijnen, A. Patscheider, M. Sohmen, M. J. Mark, and F. Ferlaino, Phys. Rev. X **9**, 021012 (2019).
[20] L. Tanzi, E. Lucioni, F. Famà, J. Catani, A. Fioretti, C. Gabbanini, R. N. Bisset, L. Santos, and G. Modugno, Phys. Rev. Lett. **122**, 130405 (2019).
[21] K. Aikawa, S. Baier, A. Frisch, M. Mark, C. Ravensbergen, and F. Ferlaino, Science **345**, 1484 (2014).
[22] S. Ospelkaus, C. Ospelkaus, O. Wille, M. Succo, P. Ernst, K. Sengstock, and K. Bongs, Phys. Rev. Lett. **96**, 180403 (2006).
[23] S. Will, T. Best, S. Braun, U. Schneider, and I. Bloch, Phys. Rev. Lett. **106**, 115305 (2011).
[24] J. Heinze, S. Götze, J. S. Krauser, B. Hundt, N. Fläschner, D.-S. Lühmann, C. Becker, and K. Sengstock, Phys. Rev. Lett. **107**, 135303 (2011).
[25] N. Spethmann, F. Kindermann, S. John, C. Weber, D. Meschede, and A. Widera, Phys. Rev. Lett. **109**, 235301 (2012).
[26] N. B. Jørgensen, L. Wacker, K. T. Skalmstang, M. M. Parish, J. Levinsen, R. S. Christensen, G. M. Bruun, and J. J. Arlt, Phys. Rev. Lett. **117**, 055302 (2016).
[27] M.-G. Hu, M. J. Van de Graaff, D. Kedar, J. P. Corson, E. A. Cornell, and D. S. Jin, Phys. Rev. Lett. **117**, 055301 (2016).
[28] T. Köhler, K. Góral, and P. S. Julienne, Rev. Mod. Phys. **78**, 1311 (2006).
[29] K.-K. Ni, S. Ospelkaus, M. H. G. de Miranda, A. Pe'er, B. Neyenhuis, J. J. Zirbel, S. Kotochigova, P. S. Julienne, D. S. Jin, and J. Ye, Science **322**, 231 (2008).
[30] T. Takekoshi, L. Reichsöllner, A. Schindewolf, J. M. Hutson, C. R. Le Sueur, O. Dulieu, F. Ferlaino, R. Grimm, and H.-C. Nägerl, Phys. Rev. Lett. **113**, 205301 (2014).
[31] P. K. Molony, P. D. Gregory, Z. Ji, B. Lu, M. P. Köppinger, C. R. Le Sueur, C. L. Blackley, J. M. Hutson, and S. L. Cornish, Phys. Rev. Lett. **113**, 255301 (2014).
[32] G. Gligorić, A. Maluckov, M. Stepić, L. Hadžievski, and B. A. Malomed, Phys. Rev. A **82**, 033624 (2010).
[33] R. M. Wilson, C. Ticknor, J. L. Bohn, and E. Timmermans, Phys. Rev. A **86**, 033606 (2012).
[34] R. K. Kumar, P. Muruganandam, L. Tomio, and A. Gammal, J. Phys. Commun. **1**, 035012 (2017).
[35] R. K. Kumar, L. Tomio, B. A. Malomed, and A. Gammal, Phys. Rev. A **96**, 063624 (2017).
[36] B. Kain and H. Y. Ling, Phys. Rev. A **89**, 023612 (2014).
[37] L. A. P. Ardila and T. Pohl, Journal of Physics B: Atomic, Molecular and Optical Physics **52**, 015004 (2018).
[38] M. Wenzel, T. Pfau, and I. Ferrier-Barbut, Physica Scripta **93**, 104004 (2018).
[39] A. Trautmann, P. Ilzhöfer, G. Durastante, C. Politi, M. Sohmen, M. J. Mark, and F. Ferlaino, Phys. Rev. Lett. **121**, 213601 (2018).
[40] C. A. Stan, M. W. Zwierlein, C. H. Schunck, S. M. F. Raupach, and W. Ketterle, Phys. Rev. Lett. **93**, 143001 (2004).
[41] S. Inouye, J. Goldwin, M. L. Olsen, C. Ticknor, J. L. Bohn, and D. S. Jin, Phys. Rev. Lett. **93**, 183201 (2004).
[42] S. Kotochigova and A. Petrov, Phys. Chem. Chem. Phys. **13**, 19165 (2011).
[43] A. Frisch, M. Mark, K. Aikawa, F. Ferlaino, J. L. Bohn, C. Makrides, A. Petrov, and S. Kotochigova, Nature **507**, 475 (2014).
[44] K. Baumann, N. Q. Burdick, M. Lu, and B. L. Lev, Phys. Rev. A **89**, 020701 (2014).
[45] T. Maier, H. Kadau, M. Schmitt, M. Wenzel, I. Ferrier-Barbut, T. Pfau, A. Frisch, S. Baier, K. Aikawa, L. Chomaz, M. J. Mark, F. Ferlaino, C. Makrides, E. Tiesinga, A. Petrov, and S. Kotochigova, Phys. Rev. X **5**, 041029 (2015).
[46] V. A. Khlebnikov, D. A. Pershin, V. V. Tsyganok, E. T. Davletov, I. S. Cojocaru, E. S. Fedorova, A. A. Buchachenko, and A. V. Akimov, Phys. Rev. Lett. **123**, 213402 (2019).
[47] M. D. Frye, S. L. Cornish, and J. M. Hutson, arXiv:1910.09641 (2019).
[48] P. Ilzhöfer, G. Durastante, A. Patscheider, A. Trautmann, M. J. Mark, and F. Ferlaino, Phys. Rev. A **97**, 023633 (2018).
[49] See supplemental material.
[50] M. Anderlini, D. Ciampini, D. Cossart, E. Courtade, M. Cristiani, C. Sias, O. Morsch, and E. Arimondo, Phys. Rev. A **72**, 033408 (2005).
[51] A. Guttridge, S. A. Hopkins, S. L. Kemp, M. D. Frye, J. M. Hutson, and S. L. Cornish, Phys. Rev. A **96**, 012704 (2017).
[52] C. Ravensbergen, V. Corre, E. Soave, M. Kreyer, E. Kirilov, and R. Grimm, Phys. Rev. A **98**, 063624 (2018).
[53] J. L. Bohn and D. S. Jin, Phys. Rev. A **89**, 022702 (2014).
[54] Along the vertical direction z we observe center of mass motion caused by the momentum transfer of the resonant light pulse.
[55] B. S. Rem, A. T. Grier, I. Ferrier-Barbut, U. Eismann, T. Langen, N. Navon, L. Khaykovich, F. Werner, D. S. Petrov, F. Chevy, and C. Salomon, Phys. Rev. Lett. **110**, 163202 (2013).
[56] T. Maier, I. Ferrier-Barbut, H. Kadau, M. Schmitt, M. Wenzel, C. Wink, T. Pfau, K. Jachymski, and P. S. Julienne, Phys. Rev. A **92**, 060702 (2015).
[57] U. Eismann, L. Khaykovich, S. Laurent, I. Ferrier-Barbut, B. S. Rem, A. T. Grier, M. Delehaye, F. Chevy, C. Salomon, L.-C. Ha, and C. Chin, Phys. Rev. X **6**,

021025 (2016).
[58] K. Helfrich, H.-W. Hammer, and D. S. Petrov, Phys. Rev. A **81**, 042715 (2010).
[59] J. P. D'Incao, Journal of Physics B: Atomic, Molecular and Optical Physics **51**, 043001 (2018).
[60] A. Frisch, M. Mark, K. Aikawa, S. Baier, R. Grimm, A. Petrov, S. Kotochigova, G. Quéméner, M. Lepers, O. Dulieu, and F. Ferlaino, Phys. Rev. Lett. **115**, 203201 (2015).
[61] Private communication with Jeremy Hutson and Matthew Frye.
[62] A. V. Avdeenkov, D. C. E. Bortolotti, and J. L. Bohn, Phys. Rev. A **69**, 012710 (2004).
[63] T. Karman, M. D. Frye, J. D. Reddel, and J. M. Hutson, Phys. Rev. A **98**, 062502 (2018).
[64] B. Deh, C. Marzok, C. Zimmermann, and P. W. Courteille, Phys. Rev. A **77**, 010701 (2008).

Supplemental Material

Preparation

The experimental sequence is similar to the one introduced in our previous works [39, 48]. After cooling the erbium and dysprosium atoms into dual-species magneto-optical traps (MOTs) of the desired isotope combination, we load about $1-5\times10^6$ atoms of both erbium and dysprosium into a single-beam optical dipole trap created by 1064 nm laser light and horizontally propagating along the y-direction (hODT). We perform an initial stage of evaporative cooling of about 0.8 s. After that, a second trap beam, coming from the same laser source but detuned by 220 MHz, is shone along the vertical direction z (vODT) onto the atoms forming a crossed ODT where we continue the evaporation for an additional duration of about 4.3 s down to the desired sample temperature. During the whole evaporation sequence, a constant and homogeneous magnetic field (B_{ev}) pointing along the z-direction and opposite to gravity is applied. Different values of B_{ev} are used depending on the isotope combination and on the range of the target field (B_{FB}) to be investigated. We typically end up with $3-10\times10^4$ atoms for each species, in thermal equilibrium at about 500 nK (about twice the critical temperature for condensation). Final trap frequencies are $\omega_{x,y,z}=2\pi\times(222,24,194)\,\mathrm{s}^{-1}$.

At this point, we linearly ramp the magnetic field from B_{ev} to the target field B_{FB} in 5 ms, either in an increasing or decreasing manner. We hold the mixture for a specific time ranging between 5 ms and 400 ms depending on the experiment. At the end of the hold time, we release the atoms from the ODT in a 15 ms time-of-flight (TOF) expansion after which we record an image of the atoms using a standard low-field absorption imaging technique [12]. We use pulses of resonant light in the horizontal $x-y$ plane at an angle of $\sim 45^\circ$ with respect to our weak trap axis y. 5 ms after the clouds being released from the ODT, we linearly ramp B_{FB} to zero in 10 ms. At the same time, we activate a magnetic field of about 4 G pointing along the imaging direction.

Note that we select the relative amount of erbium and dysprosium required in the final thermal cloud by the specific experiments by independent tuning of the respective MOT loading times between 0.5 s to 5 s. B_{ev} and B_{FB} are generated by the same pair of coils in Helmholtz configuration. We ramp them up linearly in the early stage of the evaporation sequence 200 ms after loading the atoms into the hODT. We checked that the response of the current flowing in the coils can follow time ramps on the millisecond time-scale. This translates in a effective change of the field at the sample position in the order of 10 ms to settle at the part per thousand level.

Cross-species thermalization

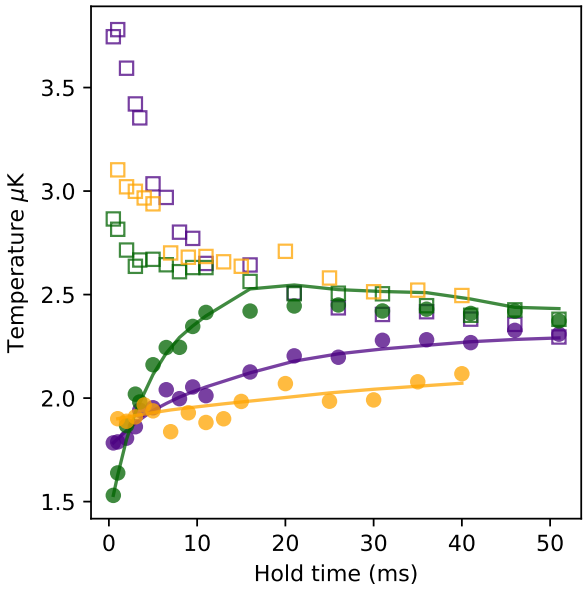

FIG. S1. Sample temperature traces for erbium (filled circles) and dysprosium (hollow squares) after dysprosium is heated. Purple, green, and orange correspond to magnetic fields of 12 G, 13.5 G, and 17 G, respectively. Fit lines represent the results of the numerical integration of equation 3, which fits the temperature profile of erbium based on its initial value and the dysprosium temperatures. Different evaporation conditions cause the curves to have slightly different initial and final conditions (see main text).

As an exemplary case, we study in more detail the resonance found in the ^{168}Er-^{164}Dy Bose-Bose mixture, near 13.5 G. To quantify reliably the value of the inter-species cross-section, we developed the following scheme for cross-species thermalization measurements [50–52]. To avoid heating of the sample by crossing Feshbach resonances, we evaporate the mixture at B_{ev} close to resonance. Specifically, when measuring on the low(high)-field side of the feature we evaporate at $B_{\mathrm{evap}}=10.8\,\mathrm{G}(16.4\,\mathrm{G})$. Once the sample is prepared as previously described (here we use an unbalanced mixture with twice as much Dy as Er), we compress the trap by linearly increasing the hODT power by a factor of five and the vODT power by two in 500 ms to prevent any plain evaporation. The final trap frequencies in the compressed trap are $\omega_{x,y,z}=2\pi\times(409,26,391)\,\mathrm{s}^{-1}$. Subsequently, we ramp the magnetic field in 5 ms to either 10 G or 16 G. Here, a pulse of near-resonant 421 nm light propagating along the magnetic field direction (z) is used to selectively heat dysprosium. We fix the duration of the pulse at 5.5 ms to roughly match the trap oscillation period along this direction and set the pulse intensity to give the

desired temperature increase of the dysprosium cloud (up to 4 μK). We confirmed that the light pulse has no direct measurable effect on erbium. Finally with a quench fast compared to the shortest thermalization rate, the magnetic field is set to the desired value B_{FB} and held for a variable amount of time, during which the temperature of erbium rises to equilibrate with dysprosium due to thermalizing collisions (Figure S1). We note that in the temperature evolution of the clouds, the initial temperatures are slightly different. This behavior is mainly due to different evaporation conditions on the two sides of the resonance, the different strength in the quench to the final B_{FB}, and the heating caused by the resonance itself. By comparing the two species' temperature, we ensure that these different conditions are consistent with general offsets on the single measurement thus not affecting the final estimation of the cross-section.

To extract a scattering cross-section from our cross-species thermalization data, we use a fit to a numerical model for the thermalization of two species. In principle, a simple exponential fit to the temperature difference between the two species could also be used, but does not account for changes in the atom number or average temperature of the sample that may arise from residual evaporation during the thermalization time. Our numerical model follows that of Ref. [50]. We treat the scattering cross section as independent of the energy of the colliding particles, an assumption that greatly simplifies the analysis, but inevitably breaks down near enough to resonance where unitarity considerations bound the scattering cross section. This assumption leads to a collision rate for each atom of species 1 with atoms of species 2 given by:

$$\gamma_{12} = \frac{N_2 m_1^{3/2} \bar{\omega}_1^3}{\pi^2 k_{\mathrm{B}} (T_1 + \beta^{-2} T_2)^{3/2}} \sqrt{\frac{T_1}{m_1} + \frac{T_2}{m_2}} \sigma_{12} \tag{2}$$

where m_1, m_2, T_1 and T_2 are the masses and temperatures of species 1 and 2, $\bar{\omega} = (\omega_x \omega_y \omega_z)^{1/3}$ characterizes the frequency of the trap, $\beta^2 = m_2 \bar{\omega}_2^2 / m_1 \bar{\omega}_1^2$, and σ_{12} is the effective interspecies cross section. We assume that the energy exchanged per collision is given by $\Delta E = \xi k_{\mathrm{B}} (T_2 - T_1)$ where $\xi = 4 m_1 m_2 / (m_1 + m_2)^2$, and that the heat capacity of each atom is $3 k_{\mathrm{B}}$. This leads to a differential equation for the temperature of erbium:

$$\frac{dT_{\mathrm{Er}}}{dt} = \frac{\xi k_{\mathrm{B}} (T_{\mathrm{Dy}} - T_{\mathrm{Er}}) N_{\mathrm{Dy}} m_{\mathrm{Er}}^{3/2} \bar{\omega}_{\mathrm{Er}}^3}{3\pi^2 k_{\mathrm{B}} (T_{\mathrm{Er}} + \beta^{-2} T_{\mathrm{Dy}})^{3/2}} \times \sqrt{\frac{T_{\mathrm{Er}}}{m_{\mathrm{Er}}} + \frac{T_{\mathrm{Dy}}}{m_{\mathrm{Dy}}}} \sigma_{\mathrm{ErDy}} \tag{3}$$

which we can numerically integrate using the instantaneous values for T_{Dy} and N_{Dy}, and from this extract the scattering cross section σ_{ErDy} that yields a thermalization profile that best matches our data, as determined through a least-squares difference. Examples of three such fits, for 12 G, 13.5 G, and 17 G are shown in Fig. S1, and generally describe our thermalization data well.

Temperature dependence of loss

We quantify the temperature dependence of three-body loss in terms of the interspecies three-body loss coefficient. For a single species, the three-body loss coefficient L_3 can be defined by: $\dot{N}/N = -L_3 \langle n^2 \rangle$ where N is the total number of atoms, and $\langle n^2 \rangle = \int d^3r \; n^3(\boldsymbol{r})/N$ represents the average squared density of scattering partners for an atom in the gas. $n(\boldsymbol{r})$ is the local density of the gas.

We define analogous quantities for our two-species mixture, containing particles denoted i and j. In this case,

$$\frac{\dot{N}_i}{N_i} = \frac{-1}{3N_i} \int d^3r \; (2L_3^{i,i,j} n_i^2(\boldsymbol{r}) n_j(\boldsymbol{r}) + L_3^{j,j,i} n_i(\boldsymbol{r}) n_j^2(\boldsymbol{r})). \tag{4}$$

Here, $L_3^{i,i,j}$ represents the loss rate due to collisions involving two atoms of species i and one of j.

To arrive at simple expressions, we make several assumptions and approximations. First, we treat the mass, temperature, and polarizability of the two atomic species as equal, which is a reasonable approximation for erbium and dysprosium isotopes in our 1064 nm wavelength ODT [39]. This assumption implies equivalent spatial distributions for the two species, which we assume to be thermal in our three-dimensional harmonic trap. We next set $L_3^{i,i,j} = L_3^{j,j,i} \equiv L_3^i$ near resonance, essentially assuming that the loss process is primarily determined by the two pairwise interactions between the minority participant and the two majority atoms. We find this assumption leads to a model consistent with our observed relative loss between the two species. With these simplifications in place, we define L_3^i using: $\dot{N}_i/N_i = -L_3^i \langle n^2 \rangle_{\mathrm{eff}}^i$, where

$$\langle n^2 \rangle_{\mathrm{eff}}^i = \frac{(2N_i N_j + N_j^2) m^3 \bar{\omega}^6}{3^{\frac{5}{2}} 8\pi^3 (k_{\mathrm{B}} T)^3} \tag{5}$$

and $\bar{\omega} = (\omega_x \omega_y \omega_z)^{1/3}$ is the geometric mean of the trap oscillation frequencies.

We extract the resonant value of L_3 by measuring remaining atom number versus hold time in mixtures prepared at different temperatures, with the magnetic field set near resonance at 13.4 G. We then fit the resulting data by numerically integrating Eq. 4. Because we observe significant single-species loss of erbium (the majority species), we treat the erbium atom number measured at each time-step as inputs to our fit, and extract the value of L_3 that best predicts the loss of dysprosium. Here, we assume that $L_3^{i,i,j} = L_3^{j,j,i} \equiv L_3$. We bound the effects of single-species loss in dysprosium by repeating the same measurement and analysis protocol off resonance at 11.5 G and 16.5 G. The error bars in Fig. 2 of the main text include a contribution corresponding to the extracted L_3 in the off-resonant condition, which contain both the effects of single-species loss and the small

effect of off-resonant interspecies loss. Also included are errors associated with the observed change in temperature during the loss measurement, and relating to the approximations made in estimating the density.

In a regime where the scattering length a exceeds the thermal wavelength $\lambda_{\mathrm{th}} = h/\sqrt{2\pi m k_{\mathrm{B}} T}$, and thermal broadening is small compared to the width of the loss feature, we expect roughly $L_3 \propto 1/T^2$, as has been observed in several experiments involving single atomic species [55–57]. This picture becomes complicated somewhat in the case of a binary mixture due to stronger Efimov effects, which lead to a temperature-dependent modulation of loss relative to the simple $1/T^2$ prediction. In particular, the parameter s_0, which characterizes the strength of the three-body Efimov potential, is equal to approximately 1.006 for identical bosons, but approximately 0.41 for our binary mixture [58, 59]. The fractional importance of these temperature-dependent modifications scale as $e^{-\pi s_0}$ [55], making them a minor correction for identical bosons, but a potentially important effect in mixtures. It is possible that such effects contribute to deviations of our data from a $1/T^2$ form, but a true calculation would require knowledge of short-range inelastic processes in our system.

4.5 Additional measurements

In this Section, we present additional measurements performed during the preparation of Ref. [Dur20] (see Sec. 4.4). If otherwise stated, the experimental procedure of these additional measurements follows the one described in the supplemental material of Ref. [Dur20]. In Sec. 4.5.1 we report the full observation of the mentioned feature observed in the mixture ^{166}Er-^{164}Dy at about 34 G. In Sec. 4.5.2, we present a deeper characterization of the feature at about 161 G in mixtures of fermionic ^{161}Dy together with bosonic isotopes of Er. For the ease of reading, all the surveys performed to identify eventual broad FRs are collected in Appendix B.

4.5.1 Feshbach resonance at 34 G in ^{166}Er-^{164}Dy

In the isotopic combination ^{166}Er-^{164}Dy, we identify by means of trap-loss spectroscopy a Gauss-broad heteronuclear resonance as reported in Fig. 4.3 (a) together with Gaussian fits to the loss feature. In this experiment, the starting sample contains a balanced mixture of about 7×10^4 erbium and dysprosium atoms at about 500 nK. The evaporation is performed at 23.1 G and the hold time at B_{FB} is 200 ms. The Gaussian fits return center values of 34.08(5) G and 34.10(7) G and FWHM values of 1.9(1) G and 1.6(2) G for erbium and dysprosium, respectively. Additionally, we performed single-species trap-loss spectra to confirm the heteronuclear nature of the resonance.

With the same procedure of Ref. [Dur20], we perform cross-species thermalization measurements at different magnetic field over the resonance to estimate the elastic interspecies cross section. More specifically for this experiment, the sample is prepared by evaporative cooling at 23.1 G (36.2 G) when performing the measurement on the low-field (high-field) side of the resonance. The mixture typically contains three times more dysprosium than erbium. The resonant light pulse is shone at 31 G or 36.2 G, respectively. The analysis is performed by fitting a numerical model to the data as already discussed. Its results are reported in Fig. 4.3 (b). Raising quantitative arguments on the strength of this resonance is hard due to the complex pattern of narrower homo and heteronuclear resonances on top of the broad resonance. Nevertheless, we observe a dramatic increase of the scattering cross-section when approaching the center of the feature.

4.5.2 Additional measurements on the feature at 161 G in ^{161}Dy

As already discussed, we observe a correlated loss feature involving fermionic ^{161}Dy and the bosonic isotopes of Er. In the publication, we report the trap-loss spectra for the different isotopic combinations. To shed more light on this puzzling feature, we conducted further investigations on the exemplary case of ^{168}Er-^{161}Dy. In the first experiment, we vary the temperatures of the sample and, in the second one, the unbalance of erbium with respect to dysprosium in the final sample. In the following, more details are reported.

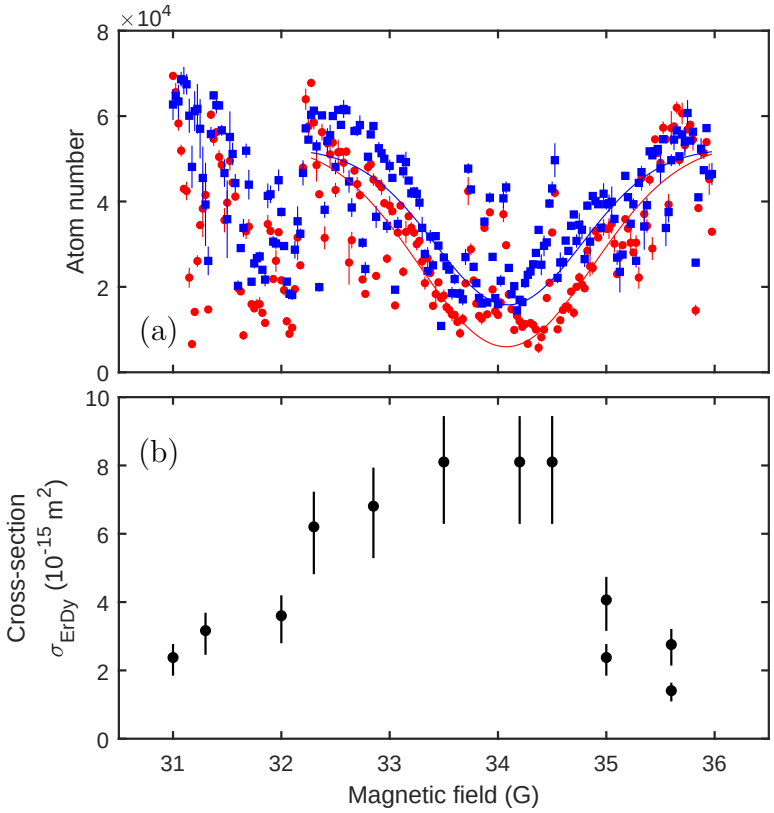

Figure 4.3: (a) Trap-loss profile from the 34 G resonance in the Bose-Bose mixture ^{166}Er-^{164}Dy (red circles and blue squares points respectively). Each point is an average over four experimental repetitions. The lines are the Gaussian fits to the data. (b) Interspecies elastic cross-section σ_{ErDy} measured across the Feshbach resonance using cross-species thermalization. Each value of σ_{ErDy} is extracted from thermalization data using a numerical model for thermalization that includes temporal variation in atom number and temperature (see Ref. [Dur20] for more details).

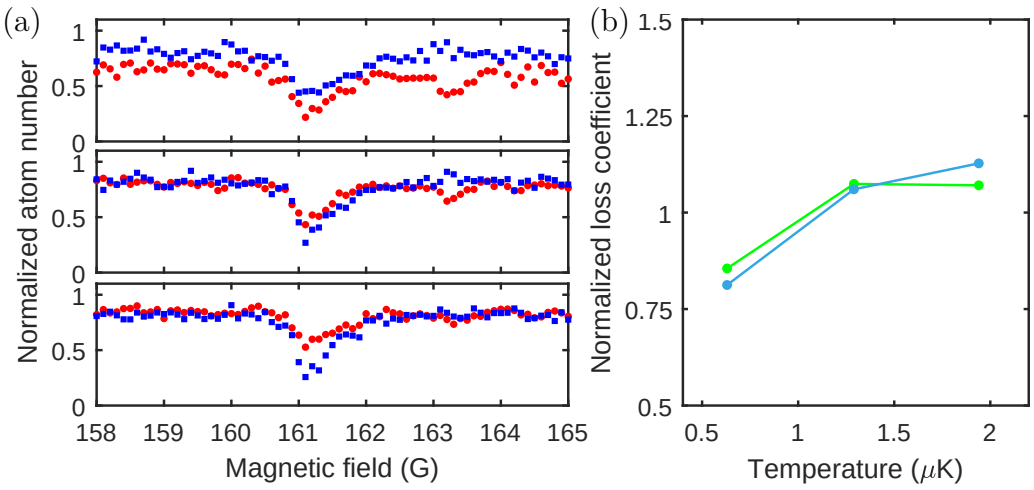

Figure 4.4: Temperature dependence of the feature present in fermionic ^{161}Dy in combination with bosonic ^{168}Er. (a) Trap-loss spectra performed at a sample temperature of 600 nK, 1.3 µK, and 2 µK, top to bottom panels, respectively. Red circles represent erbium, blues squares represent dysprosium. For each magnetic field, the atom number recorded after 100 ms of hold time is normalized to the one at a short hold time of 5 ms. For all panels, each point is an average over four experimental repetitions. (b) Simple model describing the losses as either two-body Er-Dy loss (light blue) or three-body loss with equal coefficients for Er-Er-Dy and Er-Dy-Dy (green). The traces are normalized to their means in order to better visualize the temperature dependence.

Temperature dependence By varying the final depth of the ODT, we probe three different temperature regimes of the mixture: 600 nK, 1.3 µK, and 2 µK. The hold time is 100 ms and the result is analyzed by normalizing the atom number at this value to the one at a short hold time of 5 ms to compensate for slow drifts in the experiment. The trap loss spectra are plot in Fig. 4.4 (a). To extract qualitative information, we model the losses as either two-body Er-Dy loss or three-body loss with equal coefficients for Er-Er-Dy and Er-Dy-Dy. Given the densities of the two species, we define the two-body Γ_{2B} and three-body Γ_{3B} loss coefficients as

$$\begin{aligned} \Gamma_{2B} &= \frac{\dot{n}}{2 n_{Er} n_{Dy}} \\ \Gamma_{3B} &= \frac{\dot{n}}{3(n_{Er}^2 n_{Dy} + n_{Er} n_{Dy}^2)} \end{aligned} \tag{4.17}$$

where $\dot{n}$ is the total loss rate of atoms assumed to be linear. The result of the analysis is plot in Fig. 4.4 (b) where the traces are normalized to their means in order to better visualize the temperature dependence. Although there might be a slight increase of the loss coefficients with temperature, it does not appear to be dramatic.

Er/Dy ratio dependence By varying the loading time of the Er MOT — therefore the number of atoms loaded into the ODT — we explore three different ratios of unbalance in the atom number of Er and Dy in the final sample. We performed loss measurements with erbium numbers being 1.3×10^4, 2.6×10^4, and 3×10^4 (with the number of dysprosium fixed at about 3.3×10^4). The hold time is 100 ms and the result is analyzed by normalizing

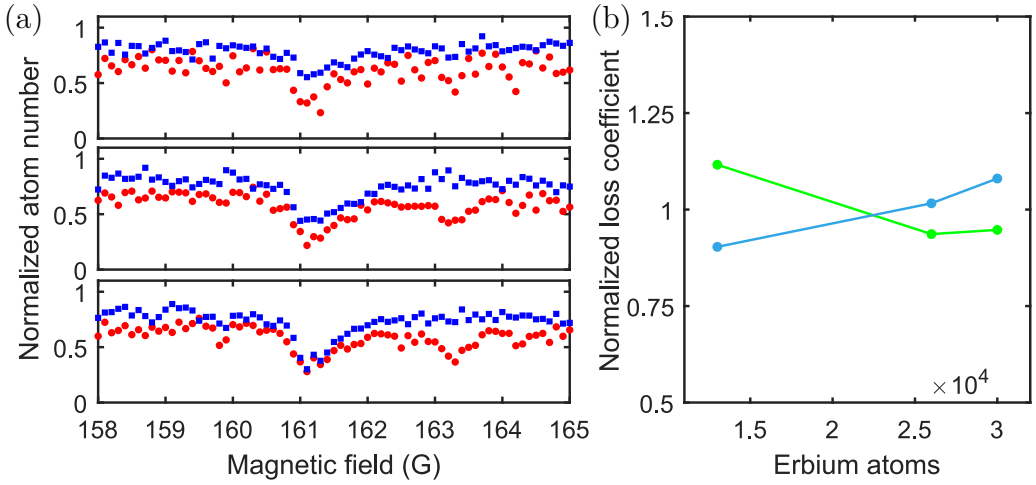

Figure 4.5: Er/Dy atoms ratio dependence of the feature present in fermionic ^{161}Dy in combination with bosonic ^{168}Er. (a) Trap-loss spectra performed with erbium numbers being 1.3×10^4, 2.6×10^4, and 3×10^4, top to bottom panels, respectively. Dysprosium atoms are fixed at about 3.3×10^4. Red circles represent erbium, blues squares represent dysprosium. For each magnetic field, the atom number recorded after 100 ms of hold time is normalized to the one at a short hold time of 5 ms. For all panels, each point is an average over four experimental repetitions. (b) Simple model describing the losses as either two-body Er-Dy loss (light blue) or three-body loss with equal coefficients for Er-Er-Dy and Er-Dy-Dy (green). The traces are normalized to their means in order to better visualize the dependence.

the atom number at this value to the one at a short hold time of 5 ms to compensate for slow drifts in the experiment. The resulting trap loss spectra are plot in Fig. 4.5 (a). In each case we found that the number of erbium lost was roughly equal to the number of dysprosium lost, and that the number of total atoms lost was roughly proportional to the number of erbium present. Following the same approach described in the previous paragraph, we analyze the loss feature in terms of two- and three-body loss coefficients as in Eq. 4.17. The result is summarized in Fig. 4.5 (b). The traces are normalized to their means in order to better visualize the dependence on the different Er/Dy ratio.

Chapter 5

Conclusion and outlook

5.1 Conclusion

This thesis reviews the experimental realization of quantum degeneracy in dipolar mixtures of erbium and dysprosium, focusing the discussion on the first observation of interspecies Feshbach resonances essential for interaction tuning.

In order to study dipolar systems in quantum regimes, we make use of mixtures of highly magnetic erbium and dysprosium atoms for the first time. These species possess among the strongest magnetic dipole moments on the periodic table — $7\mu_B$ and $10\mu_B$ for Er and Dy respectively — leading to a dipolar strength of about a hundred times the one in alkali-metal atoms. By employing their similar physical and atomic properties and the recent advances in the field [Lu11a, Aik12], we were able to build an ultracold atom experiment, competing at the forefront of the research in about three years. Remarkably, the experiment led to five publications, three of which set the main discussion in this thesis: the realization of a dual-species intercombination-line magneto-optical trap in open-top configuration [Ilz18], the achievement of quantum degeneracy in several erbium-dysprosium isotopic mixtures [Tra18], and the experimental observation of interspecies magnetic Feshbach resonances [Dur20].

Our new apparatus combines the fascinating physics of dipolar systems with the flexibility and opportunity offered by mixture experiments in which mass and population imbalance, mixed statistic, species-selective manipulations, and intrinsic distinct properties are available. This new type of experiment enters a regime of complexity in which the theoretical understanding is only at the beginning and predictive models are hardly possible, e. g. for the Er-Dy interspecies scattering properties. With this thesis, in which interspecies Feshbach resonances are investigated, we want to make a step forward into the knowledge required by more advanced experiments. In particular, the work performed will allow for the creation of dipolar heteronuclear quantum gases with tunable interaction unveiling new intriguing possibilities such as dipolar polarons, miscibility/immiscibility diagram, vortex formation, and binary magnetic quantum droplets [Dur20].

5.2 Further studies

The apparatus is designed to receive several major updates to expand the possible research topics of the experiment. Among these, the first in chronological order will be the implementation of a high-resolution imaging along the vertical z-axis in the main chamber[1]. Such a setup will allow for in-situ absorption or phase-contrast imaging with a sub-micrometer diffraction-limited resolution at the broad blue transitions. The high-resolution vertical imaging will boost the performance of the experiment in all directions, e. g. in the direct characterization of quantum droplets and supersolid states [Ilz19]. The utilization of a digital micromirror device will be of central importance to study vortexes. On top of this, another open question regards the accurate characterization of interactions in the Er-Dy quantum mixtures, fundamental to understand their miscibility/immiscibility and stability diagrams. The identification of several Feshbach resonances made the first step in this direction, whereas more investigation is needed to extract precise values of intra- and inter-species scattering lengths. For this purpose, the technique developed in Ref. [Tra18] makes use of the center-of-mass shift of the two species originating from the in-trap displacement and observable from TOF pictures. Such in-trap displacement is directly connected to the interparticle interactions and, by monitoring it for different magnetic-field values and orientations, will be possible to infer on a reliable value of a_{12} (which is currently unknown)[2].

The apparatus features the possibility to directly connect two additional vacuum modules in which the atoms can be optically transported from the main chamber. The second major change on the apparatus will regard the implementation of one of these modules dedicated to quantum-gas microscopy (QGM). Our design is based on a glass-cell chamber containing a high-NA in-vacuum objective with an estimated diffraction-limited resolution of a few hundred nanometer and designed to be achromatic for both erbium and dysprosium. Here, single-atom identification and manipulation will possibly open the path to a deeper understanding of many-body quantum systems with the additional — and so far unexplored — case of dipolar interactions. Quantum magnetism, topological quantum matter, lattice physics with fermions and bosons in periodic potentials, out-of-equilibrium systems, and atomtronic circuits are topics made available by QGM [Ott16, Gro17] on top of which the DDI will play a fundamental role.

The last planned update would have been the implementation of the third science module dedicated to Rydberg physics [Ši18]. In erbium and dysprosium, the complex electronic configuration with an open f-shell and an optically active core allow for a wealth of possible experimental techniques such as new excitation and manipulation schemes including trapping and cooling of Rydberg atoms [Ilz20]. The custom-made stainless steel chamber features a full-3D electric field control, microchannel plate detectors, and a sub-micrometer imaging scheme. However, due to the intrinsic complexity of the project and the fact that it can be optimized for a faster and more robust operation independently from the standard quantum-gas scheme proposed here, a whole new experiment will be set up[3].

[1] The employed objective is a customized commercial solution with a numerical aperture of 0.45 and a working distance of 55 mm. It is provided by *Special Optics, a Navitar company*

[2] A separate publication on this project is under preparation

[3] Tweezer array for Rydberg atoms of Erbium for Quantum Simulation (T-REQS). More information are available at the web page: http://www.erbium.at/FF/?page_id=37462

Appendix

A Additional publications

In the following appendix, two publications achieved during my PhD and which I co-authored are reported. Their subject is not part of the core of this thesis, therefore they are included as "additional" material. Such publications are:

- *Long-Lived and Transient Supersolid Behaviors in Dipolar Quantum Gases* [Cho19] reported in Sec. A.1,
- *Phase coherence in out-of-equilibrium supersolid states of ultracold dipolar atoms* [Ilz19] reported in Sec. A.2,

A.1 Publication: Long-Lived and Transient Supersolid Behaviors in Dipolar Quantum Gases[†]

Lauriane Chomaz[1], Daniel Petter[1], Philipp Ilzhöfer[2], Gabriele Natale[1], Arno Trautmann[2], Claudia Politi[2], Gianmaria Durastante[1,2], Rick M. W. van Bijnen[2], Alexander Patscheider[1], Maximilian Sohmen[1,2], Manfred J. Mark[1,2], and Francesca Ferlaino[1,2]

[1] *Institut für Experimentalphysik and Zentrum für Quantenphysik, Universität Innsbruck, Technikerstraße 25, 6020 Innsbruck, Austria*
[2] *Institut für Quantenoptik und Quanteninformation, Österreichische Akademie der Wissenschaften, Technikerstraße 21a, 6020 Innsbruck, Austria*

Physical Review X **9**, 021012 (2019)
submitted 11 Mar 2019; published 19 Apr 2019
DOI: 10.1103/PhysRevX.9.021012

Featured in *Physics* 12, 38. Viewpoint: Dipolar Quantum Gases go Supersolid

[†] The author of the present thesis helped in taking the dysprosium data, and contributed in writing the manuscript. This publication is also part of the PhD thesis of Philipp Ilzhöfer.

Featured in Physics

Long-Lived and Transient Supersolid Behaviors in Dipolar Quantum Gases

L. Chomaz,[1] D. Petter,[1] P. Ilzhöfer,[2] G. Natale,[1] A. Trautmann,[2] C. Politi,[2] G. Durastante,[1,2] R. M. W. van Bijnen,[2] A. Patscheider,[1] M. Sohmen,[1,2] M. J. Mark,[1,2] and F. Ferlaino[1,2,*]

[1]*Institut für Experimentalphysik, Universität Innsbruck, Technikerstraße 25, 6020 Innsbruck, Austria*
[2]*Institut für Quantenoptik und Quanteninformation, Österreichische Akademie der Wissenschaften, Technikerstraße 21a, 6020 Innsbruck, Austria*

(Received 11 March 2019; published 19 April 2019; corrected 25 April 2019)

By combining theory and experiments, we demonstrate that dipolar quantum gases of both ^{166}Er and ^{164}Dy support a state with supersolid properties, where a spontaneous density modulation and a global phase coherence coexist. This paradoxical state occurs in a well-defined parameter range, separating the phases of a regular Bose-Einstein condensate and of an insulating droplet array, and is rooted in the roton mode softening, on the one side, and in the stabilization driven by quantum fluctuations, on the other side. Here, we identify the parameter regime for each of the three phases. In the experiment, we rely on a detailed analysis of the interference patterns resulting from the free expansion of the gas, quantifying both its density modulation and its global phase coherence. Reaching the phases via a slow interaction tuning, starting from a stable condensate, we observe that ^{166}Er and ^{164}Dy exhibit a striking difference in the lifetime of the supersolid properties, due to the different atom loss rates in the two systems. Indeed, while in ^{166}Er the supersolid behavior survives only a few tens of milliseconds, we observe coherent density modulations for more than 150 ms in ^{164}Dy. Building on this long lifetime, we demonstrate an alternative path to reach the supersolid regime, relying solely on evaporative cooling starting from a thermal gas.

DOI: 10.1103/PhysRevX.9.021012

Subject Areas: Atomic and Molecular Physics, Condensed Matter Physics, Quantum Physics

I. INTRODUCTION

Supersolidity is a paradoxical quantum phase of matter where both crystalline and superfluid order coexist [1–3]. Such a counterintuitive phase, featuring rather antithetic properties, has been originally considered for quantum crystals with mobile bosonic vacancies, the latter being responsible for the superfluid order. Solid ^{4}He has long been considered a prime system to observe such a phenomenon [4,5]. However, after decades of theoretical and experimental efforts, an unambiguous proof of supersolidity in solid ^{4}He is still missing [6,7].

In search of more favorable and controllable systems, ultracold atoms emerged as a very promising candidate, thanks to their highly tunable interactions. Theoretical works point to the existence of a supersolid ground state in different cold-atom settings, including dipolar [8] and Rydberg particles [9,10], cold atoms with a soft-core potential [11], or lattice-confined systems [7]. Breakthrough experiments with Bose-Einstein condensates (BECs) coupled to light have recently demonstrated a state with supersolid properties [12,13]. While in these systems indeed two continuous symmetries are broken, the crystal periodicity is set by the laser wavelength, making the supersolid incompressible.

Another key notion concerns the close relation between a possible transition to a supersolid ground state and the existence of a local energy minimum at large momentum in the excitation spectrum of a nonmodulated superfluid, known as the roton mode [14]. Since excitations corresponding to a periodic density modulation at the roton wavelength are energetically favored, the existence of this mode indicates the system's tendency to crystallize [15] and it is predicted to favor a transition to a supersolid ground state [4,5,9].

Remarkably, BECs of highly magnetic atoms, in which the particles interact through the long-range and anisotropic dipole-dipole interaction (DDI), appear to gather several key ingredients for realizing a supersolid phase. First, as predicted more than 15 years ago [16,17] and recently demonstrated in experiments [18,19], the partial attraction in momentum space due to the DDI gives rise to a roton

*Corresponding author.
Francesca.Ferlaino@uibk.ac.at

minimum. The corresponding excitation energy, i.e., the roton gap, can be tuned in the experiments down to vanishing values. Here, the excitation spectrum softens at the roton momentum and the system becomes unstable. Second, there is a nontrivial interplay between the trap geometry and the phase diagram of a dipolar BEC. For instance, our recent observations have pointed out the advantage of axially elongated trap geometries (i.e., cigar shaped) compared to the typically considered cylindrically symmetric ones (i.e., pancake shaped) in enhancing the visibility of the roton excitation in experiments. Last but not least, while the concept of a fully softened mode is typically related to instabilities and disruption of a coherent quantum phase, groundbreaking works in the quantum-gas community have demonstrated that quantum fluctuations can play a crucial role in stabilizing a dipolar BEC [20–26]. Such a stabilization mechanism enables the existence, beyond the mean-field instability, of a variety of stable ground states, from a single macrodroplet [22,24,27] to striped phases [28], and droplet crystals [29]; see also related works [30–33]. For multidroplet ground states, efforts have been devoted to understanding if a phase coherence among ground-state droplets could be established [28,29]. However, previous experiments with ^{164}Dy have shown the absence of phase coherence across the droplets [28], probably due to the limited atom numbers.

Droplet ground states, quantum stabilization, and dipolar rotons have caused a huge amount of excitement with very recent advancements adding key pieces of information to the supersolid scenario. The quench experiments in an ^{166}Er BEC at the roton instability have revealed out-of-equilibrium modulated states with an early-time phase coherence over a timescale shorter than a quarter of the oscillation period along the weak-trap axis [18]. In the same work, it has been suggested that the roton softening combined with the quantum stabilization mechanism may open a promising route towards a supersolid ground state. A first confirmation came from a recent theoretical work [34], considering an Er BEC in an infinite elongated trap with periodic boundary conditions and tight transverse confinement. The supersolid phase appears to exist within a narrow region in interaction strength, separating a roton excitation with a vanishing energy and an incoherent assembly of insulating droplets. Almost simultaneously, experiments with ^{162}Dy BECs in a shallow elongated trap, performing a slow tuning of the contact interaction, reported on the production of stripe states with phase coherence persisting up to half of the weak trapping period [35]. More recently, such observations have been confirmed in another ^{162}Dy experiment [36]. Here, theoretical calculations showed the existence of a phase-coherent droplet ground state, linking the experimental findings to the realization of a state with supersolid properties. The results on ^{162}Dy show, however, transient supersolid properties whose lifetime is limited by fast inelastic losses caused by three-body collisions [35,36]. These realizations raise the crucial question of whether a long-lived or stationary supersolid state can be created despite the usually non-negligble atom losses and the crossing of a discontinuous phase transition, which inherently creates excitations in the system.

In this work, we study both experimentally and theoretically the phase diagram of degenerate gases of highly magnetic atoms beyond the roton softening. Our investigations are carried out using two different experimental setups producing BECs of ^{166}Er [22,37] and of ^{164}Dy [38] and rely on a fine-tuning of the contact-interaction strength in both systems. In the regime of interest, these two atomic species have different contact-interaction scattering lengths a_s, whose precise dependence on the magnetic field is known only for Er [18,22,39], and different three-body-loss rate coefficients. Moreover, Er and Dy possess different magnetic moments μ and masses m, yielding the dipolar lengths, $a_{\mathrm{dd}} = \mu_0\mu^2 m/12\pi\hbar^2$, of $65.5a_0$ and $131a_0$, respectively. Here, μ_0 is the vacuum permeability, $\hbar = h/2\pi$ the reduced Planck constant, and a_0 the Bohr radius. For both systems, we find states showing hallmarks of supersolidity, namely, the coexistence of density modulation and global phase coherence. For such states, we quantify the extent of the a_s parameter range for their existence and study their lifetime. For ^{166}Er, we find results very similar to the one recently reported for ^{162}Dy [35,36], both systems being limited by strong three-body losses, which destroy the supersolid properties in about half of a trap period. However, for ^{164}Dy, we have identified an advantageous magnetic-field region where losses are very low and large BECs can be created. In this condition, we observe that the supersolid properties persist over a remarkably long time, well exceeding the trap period. Based on such a high stability, we finally demonstrate a novel route to reach the supersolid state, based on evaporative cooling from a thermal gas.

II. THEORETICAL DESCRIPTION

As a first step in our study of the supersolid phase in dipolar BECs, we compute the ground-state phase diagram for both ^{166}Er and ^{164}Dy quantum gases. The gases are confined in a cigar-shaped harmonic trap, as illustrated in Fig. 1(a). Our theory is based on numerical calculations of the extended Gross-Pitaevskii equation [40], which includes our anisotropic trapping potential, the short-range contact and long-range dipolar interactions at a mean-field level, as well as the first-order beyond-mean-field correction in the form of a Lee-Huang-Yang (LHY) term [18,22–24,27]. We note that, while both the exact strength of the LHY term and its dependence on the gas characteristics are under debate [18,19,25,31,41], the importance of such a term, scaling with a higher power in density, is essential for stabilizing states beyond the mean-field instability [18,25,41]; see also Refs. [8,42–44].

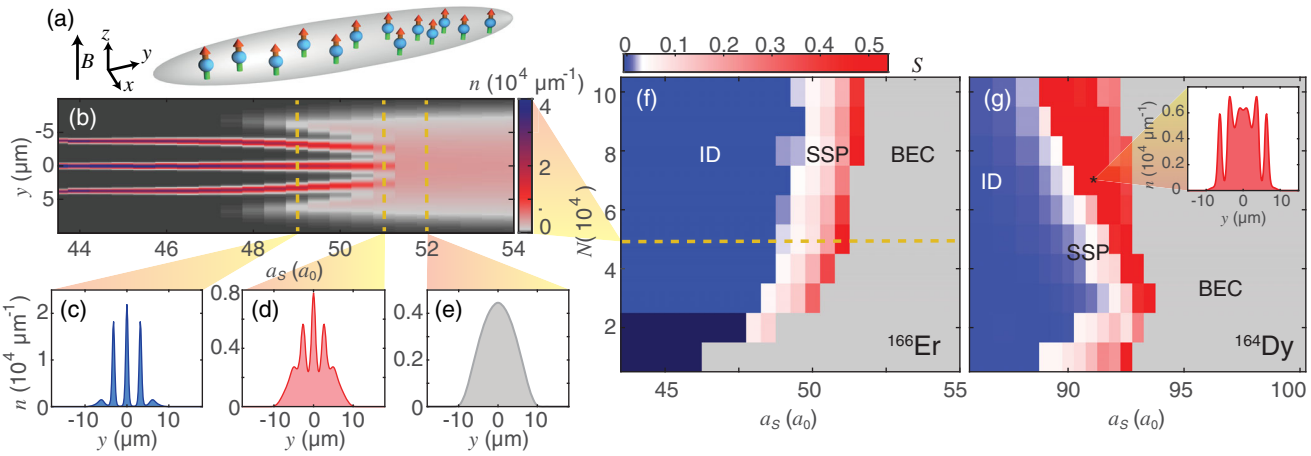

FIG. 1. Phase diagram of an ^{166}Er and a ^{164}Dy dipolar BEC in a cigar-shaped trap. (a) Illustration of the trap geometry with atomic dipoles oriented along z. (b) Integrated density profile as a function of a_s for an ^{166}Er ground state of $N = 5 \times 10^4$. In the color bar, the density scale is upper limited to 4×10^4 μm^{-1} in order to enhance the visibility in the supersolid regime. (c)–(e) Exemplary density profiles for an insulating droplet state (ID) at $a_s = 49a_0$, for a state with supersolid properties (SSP) at $51a_0$, and for a BEC at $52a_0$, respectively. (f),(g) Phase diagrams for ^{166}Er and ^{164}Dy for trap frequencies $\omega_{x,y,z} = 2\pi \times (227, 31.5, 151)$ and $2\pi \times (225, 37, 135)$ Hz, respectively. The gray color identifies ground states with a single peak in $n(y)$ of large Gaussian width, $\sigma_y > 2\ell_y$. The dark blue region in (f) shows the region where $n(y)$ exhibits a single sharp peak, $\sigma_y \leq 2\ell_y$, and no density modulation. The red-to-blue color map shows S in the case of a density-modulated $n(y)$. In (g) the color map is upper limited to use the same color code as in (f) and to enhance visibility in the low-N regime. The inset in (g) shows the calculated density profile for ^{164}Dy at $N = 7 \times 10^4$ and $a_s = 91a_0$.

Our theoretical results are summarized in Fig. 1. By varying the condensed-atom number N and a_s, the phase diagram shows three very distinct phases. To illustrate them, we first describe the evolution of the integrated *in situ* density profile $n(y)$ with fixed N for varying a_s, Fig. 1(b). The first phase, appearing at large a_s, resembles a regular dilute BEC. It corresponds to a nonmodulated density profile of low peak density and large axial size σ_y exceeding several times the corresponding harmonic oscillator length ($\ell_y = \sqrt{\hbar/m\omega_y}$); see Fig. 1(e) and the region denoted BEC in Figs. 1(f) and 1(g). The second phase appears when decreasing a_s down to a certain critical value, a_s^*. Here, the system undergoes an abrupt transition to a periodic density-modulated ground state, consisting of an array of overlapping narrow droplets, each of high peak density. Because the droplets are coupled to each other via a density overlap, later quantified in terms of the link strength S, particles can tunnel from one droplet to a neighboring one, establishing a global phase coherence across the cloud; see Fig. 1(d). Such a phase, in which periodic density modulation and phase coherence coexist, is identified as the supersolid (SSP) one [10,34]; see the SSP region in Figs. 1(f) and 1(g). When further decreasing a_s, we observe a fast reduction of the density overlap, which eventually vanishes; see Fig. 1(c). Here, the droplets become fully separated. Under realistic experimental conditions, it is expected that the phase relation between such droplets cannot be maintained; see later discussion. We identify this third phase as the one of an insulating droplet (ID) array [27,28,45]; see the ID region in Figs. 1(f) and 1(g). For low N, we find a single droplet of high peak density, as in Refs. [24,27]; see dark blue region in Fig. 1(f). Generally speaking, our calculations show that the number of droplets in the array decreases with lowering a_s or N. The existence of these three phases (BEC, SSP, ID) is consistent with recent calculations considering an infinitely elongated Er BEC [34] and a cigar-shaped ^{162}Dy BEC [36], illustrating the generality of this behavior in dipolar gases.

To study the supersolid character of the density-modulated phases, we compute the average of the wave function overlap between neighboring droplets S. As an ansatz to extract S, we use a Gaussian function to describe the wave function of each individual droplet. This is found to be an appropriate description from an analysis of the density profiles of Figs. 1(b)–1(d); see also Ref. [46]. For two droplets at a distance d and of identical Gaussian widths σ_y along the array direction, S is simply $S = \exp(-d^2/4\sigma_y^2)$. Here, we generalize the computation of the wave function overlap to account for the difference in widths and amplitudes among neighboring droplets. This analysis allows us to distinguish between the two types of modulated ground states, SSP and ID in Figs. 1(f) and 1(g). Within the Josephson-junction picture [47–49], the tunneling rate of atoms between neighboring droplets depends on the wave function overlap, and an estimate for the single-particle tunneling rate can be derived within the Gaussian approximation [46]; see also Ref. [40]. The ID phase corresponds to vanishingly small values of S, yielding

tunneling times extremely long compared to any other relevant timescale. In contrast, the supersolid phase is identified by a substantial value of S, with a correspondingly short tunneling time.

As shown in Figs. 1(f) and 1(g), a comparative analysis of the phase diagram for ^{166}Er and ^{164}Dy reveals similarities between the two species (see also Ref. [36]). A supersolid phase is found for sufficiently high N, in a narrow region of a_s, upper bounded by the critical value $a_s{}^*(N)$. For intermediate N, a_s^* increases with increasing N. We note that, for low N, the nonmodulated BEC evolves directly into a single droplet state for decreasing a_s [50]. In this case, no supersolid phase is found in between; see also Refs. [24,27]. Despite the general similarities, we see that the supersolid phase for ^{164}Dy appears for lower atom number than for Er and has a larger extension in a_s. This is mainly due to the different a_{dd} and strength of the LHY term. We note that, at large N and for decreasing a_s, Dy exhibits ground states with a density modulation appearing first in the wings, which then progresses inwards until a substantial modulation over the whole cloud is established [51]; see inset of Fig. 1(g). In this regime, we also observe that a_s^* decreases with increasing N. These types of states have not been previously reported and, although challenging to access in experiments because of the large N, they deserve further theoretical investigations.

III. EXPERIMENTAL SEQUENCE FOR ^{166}Er AND ^{164}Dy

To experimentally access the above-discussed physics, we produce dipolar BECs of either ^{166}Er or ^{164}Dy atoms. These two systems are created in different setups and below we summarize the main experimental steps; see also Ref. [40].

Erbium.—We prepare a stable ^{166}Er BEC following the scheme of Ref. [18]. At the end of the preparation, the Er BEC contains about $N = 8 \times 10^4$ atoms at $a_s = 64.5a_0$. The sample is confined in a cigar-shaped optical dipole trap with harmonic frequencies $\omega_{x,y,z} = 2\pi \times (227, 31.5, 151)$ Hz. A homogeneous magnetic field B polarizes the sample along z and controls the value of a_s via a magnetic Feshbach resonance (FR) [18,22,40]. Our measurements start by linearly ramping down a_s within 20 ms and waiting an additional 15 ms so that a_s reaches its target value [40]. We note that ramping times between 20 and 60 ms have been tested in the experiment and we do not record a significant difference in the system's behavior. After the 15-ms stabilization time, we then hold the sample for a variable time t_h before switching off the trap. Finally, we let the cloud expand for 30 ms and perform absorption imaging along the z (vertical) direction, from which we extract the density distribution of the cloud in momentum space, $n(k_x, k_y)$.

Dysprosium.—The experimental procedure to create a ^{164}Dy BEC follows the one described in Ref. [38]; see also Ref. [40]. Similarly to Er, the Dy BEC is also confined in a cigar-shaped optical dipole trap and a homogeneous magnetic field B sets the quantization axis along z and the value of a_s. For Dy, we will discuss our results in terms of magnetic field B, since the a_s-to-B conversion is not well known in the magnetic-field range considered [25,40,41,52]. In a first set of measurements, we first produce a stable BEC of about $N = 3.5 \times 10^4$ condensed atoms at a magnetic field of $B = 2.5$ G and then probe the phase diagram by tuning a_s. Here, before ramping the magnetic field to access the interesting a_s regions, we slowly increase the power of the trapping beams within 200 ms. The final trap frequencies are $\omega_{x,y,z} = 2\pi \times (300, 16, 222)$ Hz. After preparing a stable BEC, we ramp B to the desired value within 20 ms and hold the sample for t_h [40]. In a second set of measurements, we study a completely different approach to reach the supersolid state. As discussed later, here we first prepare a thermal sample at a B value where supersolid properties are observed and then further cool the sample until a transition to a coherent droplet-array state is reached. In both cases, at the end of the experimental sequence, we perform absorption imaging after typically 27 ms of time-of-flight (TOF) expansion. The imaging beam propagates horizontally under an angle α of $\approx 45°$ with respect to the weak axis of the trap (y). From the TOF images, we thus extract $n(k_Y, k_z)$ with $k_Y = \cos(\alpha)k_y + \sin(\alpha)k_x$.

A special property of ^{164}Dy is that its background scattering length is smaller than a_{dd}. This allows us to enter the supersolid regime without the need of setting B close to a FR, as is done for ^{166}Er and ^{162}Dy, which typically causes severe atom losses due to increased three-body-loss coefficients. In contrast, in the case of ^{164}Dy, the supersolid regime is reached by ramping B away from the FR pole used to produce the stable BEC via evaporative cooling, as the a_s range of Fig. 1(g) lies close to the background a_s reported in Ref. [52]; see also Ref. [40]. At the background level, three-body-loss coefficients below 1.3×10^{-41} m^6 s^{-1} have been reported for ^{164}Dy [25].

IV. DENSITY MODULATION AND PHASE COHERENCE

The coexistence of density modulation and phase coherence is the key feature that characterizes the supersolid phase and allows us to discriminate it from the BEC and ID cases. To experimentally probe this aspect in our dipolar quantum gases, we record their density distribution after a TOF expansion for various values of a_s across the phase diagram. As for a BEC in a weak optical lattice [53] or for an array of BECs [54–56], the appearance of interference patterns in the TOF images is associated with a density modulation of the *in situ* atomic distribution. Moreover, the shot-to-shot reproducibility of the patterns (in amplitude and position) and the persistence of fringes in averaged

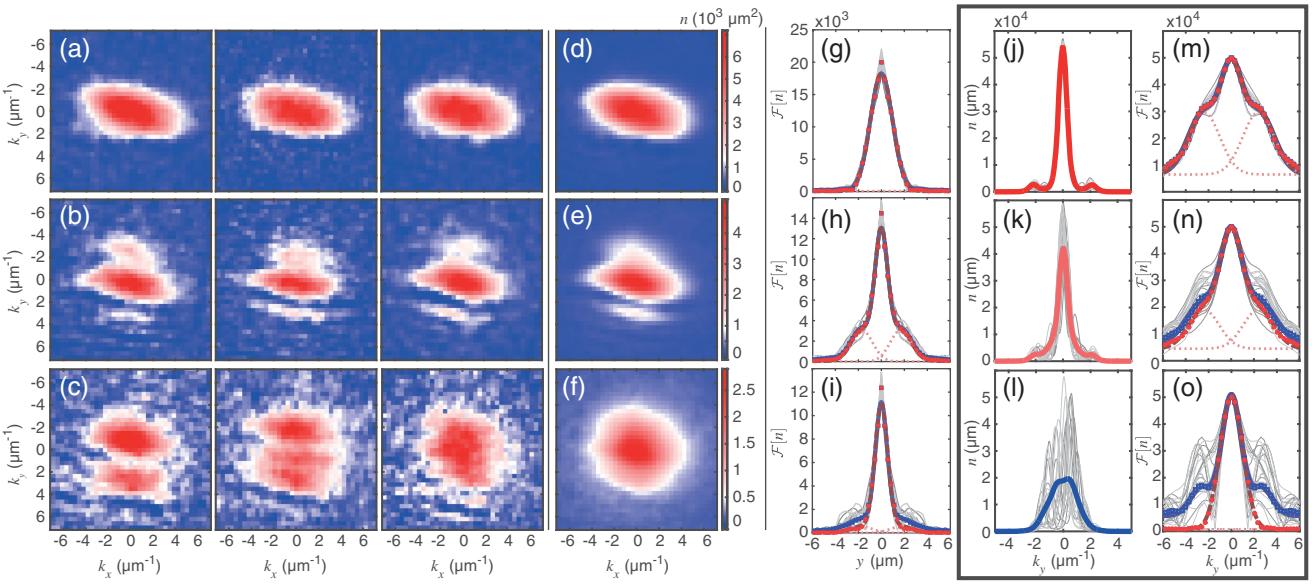

FIG. 2. Coherence in the interference patterns: measurement and toy model. (a)–(c) Examples of single TOF absorption images at $t_h = 5$ ms for ^{166}Er at $a_s = \{54.7(2), 53.8(2), 53.3(2)\}a_0$, respectively. Corresponding average pictures for 100 images obtained under the same experimental conditions (d)–(f) and their Fourier transform (FT) profiles (g)–(i). The gray lines show the FT norm $|\mathcal{F}[n](y)|$ of the individual profiles. The averages, $n_{\mathcal{M}}$ (blue squares) and n_Φ (red dots), are fitted to three-Gaussian functions (blue solid line and brown dashed line, respectively). The dotted lines show the components of the total fitted function corresponding to the two side peaks in n_Φ. (j)–(l) Interference patterns from the toy-model realizations with 100 independent draws using $N_D = 4$, $d = 2.8$ μm, $\sigma_y = 0.56$ μm (see text) and for different ϕ_i distributions: (j) $\phi_i = 0$, (k) ϕ_i normally distributed around 0 with 0.2π standard deviation, (l) ϕ_i uniformly distributed between 0 and 2π. (m)–(o) Corresponding FT profiles for the toy model, same color code as (g)–(i).

pictures, obtained from many repeated images taken under the same experimental conditions, reveals the presence of phase coherence across the sample [56].

Figure 2 exemplifies snapshots of the TOF distributions for Er, measured at three different a_s values; see Figs. 2(a)–2(c). Even if very close in scattering length, the recorded $n(k_x, k_y)$ shows a dramatic change in behavior. For $a_s = 54.7(2)a_0$, we observe a nonmodulated distribution with a density profile characteristic of a dilute BEC. When lowering a_s to $53.8(2)a_0$, we observe the appearance of an interference pattern in the density distribution, consisting of a high central peak and two almost symmetric low-density side peaks [57]. Remarkably, the observed pattern is very reproducible with a high shot-to-shot stability, as shown in the repeated single snapshots and in the average image [Figs. 2(b) and 2(e)]. This behavior indicates a coexistence of density modulation and global phase coherence in the *in situ* state, as expected in the supersolid phase. This observation is consistent with our previous quench experiments [18] and with the recent ^{162}Dy experiments [35,36]. When further lowering a_s to $53.3(2)a_0$, complicated patterns develop with fringes varying from shot to shot in number, position, and amplitude, signaling the persistence of *in situ* density modulation. However, the interference pattern is completely washed out in the averaged density profiles [Fig. 2(f)], pointing to the absence of a global phase coherence. We identify this behavior as the one of ID states.

Toy model—To get an intuitive understanding of the interplay between density modulation and phase coherence and to estimate the role of the different sources of fluctuations in our experiment, we here develop a simple toy model, which is inspired by Ref. [56]; see also Ref. [40]. In our model, the initial state is an array of N_D droplets containing in total N atoms. Each droplet is described by a one-dimensional Gaussian wave function $\psi_i(y)$ of amplitude α_i, phase ϕ_i, width σ_i, and center y_i. To account for fluctuations in the experiments, we allow α_i, $d_i = y_i - y_{i-1}$, and σ_i to vary by 10% around their expectation values. The spread of the phases ϕ_i among the droplets is treated specially as it controls the global phase coherence of the array. By fixing $\phi_i = 0$ for each droplet or by setting a random distribution of ϕ_i, we range from full phase coherence to the incoherent cases. Therefore, the degree of phase incoherence can be varied by changing the standard deviation of the distribution of ϕ_i.

To mimic our experiment, we compute the free evolution of each individual ψ_i over 30 ms, and then compute the axial distribution $n(y,t) = |\sum_i \psi_i(y,t)|^2$, from which we extract the momentum distribution $n(k_y)$, also accounting for the finite imaging resolution [40]. For each computation run, we randomly draw N_D values for ϕ_i, as well as of σ_i, d_i, and α_i, and extract $n(k_y)$. We then collect a set of $n(k_y)$

by drawing these values multiple times using the same statistical parameters and compute the expectation value, $\langle n(k_y)\rangle$; see Figs. 2(j)–2(l). The angled brackets denote the ensemble average.

The results of our toy model show large similarity with the observed behavior in the experiment. In particular, while for each single realization one can clearly distinguish multipeak structures regardless of the degree of phase coherence between the droplets, the visibility of the interference pattern in the averaged $n(k_y)$ survives only if the standard deviation of the phase fluctuations between droplets is small (roughly, below 0.3π). In the incoherent case, we note that the shape of the patterns strongly varies from shot to shot. Interestingly, the toy model also shows that the visibility of the coherent peaks in the average images is robust against the typical shot-to-shot fluctuations in droplet size, amplitude, and distance that occur in the experiments; see Figs. 2(j) and 2(k).

Probing density modulation and phase coherence.—To separate and quantify the information on the *in situ* density modulation and its phase coherence, we analyze the measured interference patterns in Fourier space [36,58–60]. Here, we extract two distinct averaged density profiles, $n_{\mathcal{M}}$ and n_{Φ}. Their structures at finite y spatial frequency (i.e., in Fourier space) quantify the two abovementioned properties.

More precisely, we perform a Fourier transform (FT) of the integrated momentum distributions $n(k_y)$ denoted $\mathcal{F}[n](y)$. Generally speaking, modulations in $n(k_y)$ induce peaks at finite spatial frequency, $y = y^*$, in the FT norm, $|\mathcal{F}[n](y)|$; see Figs. 2(g)–2(i) and 2(m)–2(o). Following the above discussion (see also Refs. [56,61]), such peaks in an individual realization hence reveal a density modulation of the corresponding *in situ* state, with a wavelength roughly equal to y^*. Consequently, we consider the average of the FT norm of the individual images, $n_{\mathcal{M}}(y) = \langle|\mathcal{F}[n](y)|\rangle$, as the first profile of interest. The peaks of $n_{\mathcal{M}}$ at finite y then indicate the mere existence of an *in situ* density modulation of roughly constant spacing within the different realizations. As the second profile of interest, we use the FT norm of the average profile $\langle n(k_y)\rangle$, $n_{\Phi}(y) = |\mathcal{F}[\langle n\rangle](y)|$. Connecting to our previous discussion, the peaks of n_{Φ} at finite y point to the persistence of a modulation in the average $\langle n(k_y)\rangle$, which we identified as a hallmark for a global phase coherence within the density-modulated state. In particular, we point out that a perfect phase coherence, implying identical interference patterns in all the individual realizations, yields $n_{\mathcal{M}} = n_{\Phi}$ and, thus, identical peaks at finite y in both profiles. We note that, by linearity, n_{Φ} also matches the norm of the average of the full FT of the individual images, i.e., $n_{\Phi}(y) = |\langle\mathcal{F}[n](y)\rangle|$; see also Ref. [40].

Figures 2(g)–2(i) and 2(m)–2(o) demonstrate the significance of our FT analysis scheme by applying it to the momentum distributions from the experiment [Figs. 2(d)–2(f)] and the momentum distributions from the toy model [Figs. 2(j)–2(l)], respectively. As expected, for the BEC case, both $n_{\mathcal{M}}$ and n_{Φ} show a single peak at zero spatial frequency, $y = 0$, characterizing the absence of density modulation, Fig. 2(g). In the case of phase-coherent droplets, Fig. 2(e), we observe that $n_{\mathcal{M}}$ and n_{Φ} are superimposed and both show two symmetric side peaks at finite y, in addition to a dominant peak at $y = 0$; see Fig. 2(h). In the incoherent droplet case, we find that, while $n_{\mathcal{M}}$ still shows side peaks at finite y, the ones in n_{Φ} wash out from the averaging, Figs. 2(f), 2(i), 2(l), and 2(o). For both coherent and incoherent droplet arrays, the toy-model results show behaviors matching the above description, providing a further justification of our FT analysis scheme; see Figs. 2(j)–2(o). Our toy model additionally proves two interesting features. First, it shows that the equality $n_{\mathcal{M}} = n_{\Phi}$, revealing the global phase coherence of a density-modulated state, is remarkably robust to noise in the structure of the droplet arrays; see Figs. 2(j) and 2(m). Second, our toy model, however, shows that phase fluctuations across the droplet array on the order of 0.2π standard deviation are already sufficient to make n_{Φ} and $n_{\mathcal{M}}$ deviate from each other; see Figs. 2(k) and 2(n). The incoherent behavior is also associated with strong variations in the side peak amplitude of the individual realizations of $|\mathcal{F}[n]|$, connecting, e.g., to the observations of Ref. [36].

Finally, to quantify the density modulation and the phase coherence, we fit a three-Gaussian function to both $n_{\mathcal{M}}(y)$ and $n_{\Phi}(y)$ and extract the amplitudes of the finite-spatial-frequency peaks, $A_{\mathcal{M}}$ and A_{Φ}, for both distributions, respectively. Note that for a BEC, which is a phase-coherent state, A_{Φ} will be zero since it probes only finite-spatial-frequency peaks; see Figs. 2(g)–2(i) and 2(m)–2(o).

V. CHARACTERIZATION OF THE SUPERSOLID STATE

We are now in the position to study two key aspects, namely, (i) the evolution of the density modulation and phase coherence across the BEC-supersolid-ID phases and (ii) the lifetime of the coherent density-modulated state in the supersolid regime.

Evolution of the supersolid properties across the phase diagram.—The first type of investigation is conducted with ^{166}Er since, contrary to ^{164}Dy, its scattering length and dependence on the magnetic field has been precisely characterized [18,22]. After preparing the sample, we ramp a_s to the desired value and study the density patterns as well as their phase coherence by probing the amplitudes $A_{\mathcal{M}}$ and A_{Φ} as a function of a_s after $t_h = 5$ ms. As shown in Fig. 3(a), in the BEC region (i.e., for large a_s), we observe that both $A_{\mathcal{M}}$ and A_{Φ} are almost zero, evidencing the expected absence of a density modulation in the system. As soon as a_s reaches a critical value a_s^*, the system's behavior dramatically changes with a sharp and simultaneous

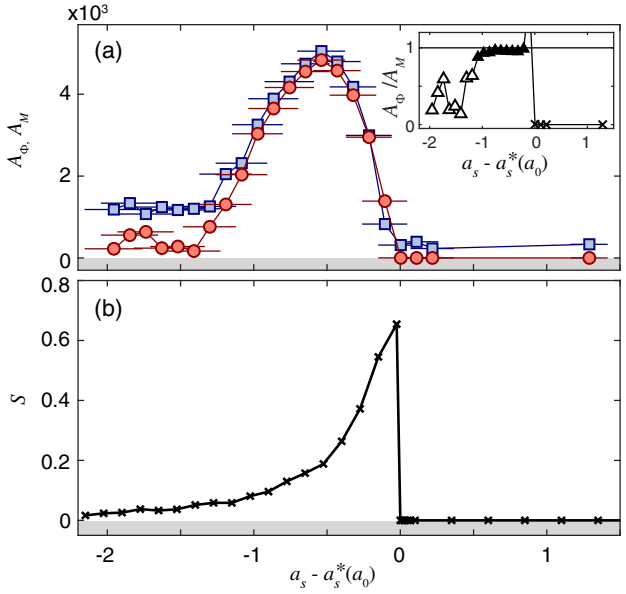

FIG. 3. Supersolid behavior across the phase diagram. Measured side peak amplitudes, A_Φ (circles) and $A_\mathcal{M}$ (squares), with their ratio in inset (a), and calculated link strength S (b) as a function of $a_s - a_s^*$ for ^{166}Er. For nonmodulated states, we set $S = 0$ in theory and $A_\Phi/A_\mathcal{M} = 0$ in experiment (crosses in inset). In the inset, open and closed symbols correspond to $A_\Phi/A_\mathcal{M} > 0.8$ and ≤ 0.8, respectively. In the experiments, we probe the system at a fixed $t_h = 5$ ms. Horizontal error bars are derived from our experimental uncertainty in B, vertical error bars corresponding to the statistical uncertainty from the fit are smaller than the data points. The measured and calculated critical scattering lengths are $a_s^* = 54.9(2)a_0$ and $51.15a_0$, respectively [62]. The numerical results are obtained for the experimental trap frequencies and for a constant $N = 5 \times 10^4$ [63].

increase of both $A_\mathcal{M}$ and A_Φ. While the strength of $A_\mathcal{M}$ and A_Φ varies with decreasing a_s—first increasing then decreasing—we observe that their ratio $A_\Phi/A_\mathcal{M}$ remains constant and close to unity over a narrow a_s range below a_s^* of $\gtrsim 1a_0$ width; see the inset of Fig. 3(a). This behavior pinpoints the coexistence in the system of phase coherence and density modulation, as predicted to occur in the supersolid regime. For $(a_s - a_s^*) < -1a_0$, we observe that the two amplitudes depart from each other. Here, while the density modulation still survives with $A_\mathcal{M}$ saturating to a lower finite value, the global phase coherence is lost with $A_\Phi/A_\mathcal{M} < 1$, as expected in the insulating droplet phase. Note that we also study the evolution of A_Φ and $A_\mathcal{M}$ in ^{164}Dy, but as a function of B, and find a qualitatively similar behavior.

To get a deeper insight on how our observations compare to the phase-diagram predictions (see Fig. 1), we study the link strength S as a function of a_s; see Fig. 3(b). Since S quantifies the density overlap between neighboring droplets and is related to the tunneling rate of atoms across the droplet array, it thus provides information on the ability of the system to establish or maintain a global phase coherence. In this plot, we set $S = 0$ in the case where no modulation is found in the ground state. At the BEC-to-supersolid transition, i.e., at $a_s = a_s^*$, a density modulation abruptly appears in the system's ground state with S taking a finite value. Here, S is maximal, corresponding to a density modulation of minimal amplitude. Below the transition, we observe a progressive decrease of S with lowering a_s, pointing to the gradual reduction of the tunneling rate in the droplet arrays. Close to the transition, we estimate a large tunneling compared to all other relevant timescales. However, we expect this rate to become vanishingly small, on the sub-Hertz level [40], when decreasing a_s 1–$2a_0$ below a_s^*. Our observation also hints at the smooth character of the transition from a supersolid to an ID phase.

The general trend of S, including the extension in a_s where it takes nonvanishing values, is similar to the a_s behavior of $A_\mathcal{M}$ and A_Φ observed in the experiments [62]. We observe in the experiments that the a_s dependence at the BEC-to-supersolid transition appears sharper than at the supersolid-to-ID interface, potentially suggesting a different nature of the two transitions. However, more investigations are needed since atom losses, finite temperature, and finite-size effects can affect, and in particular smoothen, the observed behavior [64–66]. Moreover, dynamical effects, induced by, e.g., excitations created at the crossing of the phase transitions or atom losses during the time evolution, can also play a substantial role in the experimental observations, complicating a direct comparison with the ground-state calculations. The time dynamics as well as a different scheme to achieve a state with supersolid properties is the focus of the remainder of the paper.

Lifetime of the supersolid properties.—Having identified the a_s range in which our dipolar quantum gas exhibits supersolid properties, the next central question concerns the stability and lifetime of such a fascinating state. Recent experiments on ^{162}Dy have shown the transient character of the supersolid properties, whose lifetime is limited by three-body losses [35,36]. In these experiments, the phase coherence is found to survive up to 20 ms after the density modulation has formed. This time corresponds to about half of the weak-trap period. Stability is a key issue in the supersolid regime, especially since the tuning of a_s, used to enter this regime, has a twofold consequence on the inelastic loss rate. First, it gives rise to an increase in the peak density [see Figs. 1(b)–1(d)] and, second, it may lead to an enhancement of the three-body-loss coefficient.

We address this question by conducting comparative studies on ^{166}Er and ^{164}Dy gases. These two species allow us to tackle two substantially different scattering scenarios. Indeed, the background value of a_s for ^{166}Er (as well as for ^{162}Dy) is larger than a_{dd}. Thus, reaching the supersolid regime, which occurs at $a_{dd}/a_s \approx 1.2$–1.4 in our geometry, requires us to tune B close to the pole of a FR. This tuning

also causes an increase of the three-body-loss rate. In contrast, ^{164}Dy realizes the opposite case with the background scattering length smaller than a_{dd}. This feature brings the important advantage of requiring tuning B away from the FR pole to reach the supersolid regime. As we describe below, this important difference in scattering properties leads to a strikingly longer lifetime of the ^{164}Dy supersolid properties with respect to ^{166}Er and to the recently observed behavior in ^{162}Dy [35,36].

The measurements proceed as follows. For both ^{166}Er and ^{164}Dy, we first prepare the quantum gas in the stable BEC regime and then ramp a_s to a fixed value in the supersolid regime for which the system exhibits a state of coherent droplets (i.e., $A_\Phi/A_\mathcal{M} \approx 1$); see previous discussion. Finally, we record the TOF images after a variable t_h and we extract the time evolution of both A_Φ and $A_\mathcal{M}$. The study of these two amplitudes will allow us to answer the question of whether the droplet structure—i.e., the density modulation in space—persists in time whereas the coherence among droplets is lost ($A_\mathcal{M} > A_\Phi \to 0$) or if the density structures themselves vanish in time ($A_\mathcal{M} \approx A_\Phi \to 0$).

As shown in Fig. 4, for both species, we observe that A_Φ and $A_\mathcal{M}$ decay almost synchronously with a remarkably longer lifetime for ^{164}Dy [Fig. 4(b)] than ^{166}Er [Fig. 4(a)].

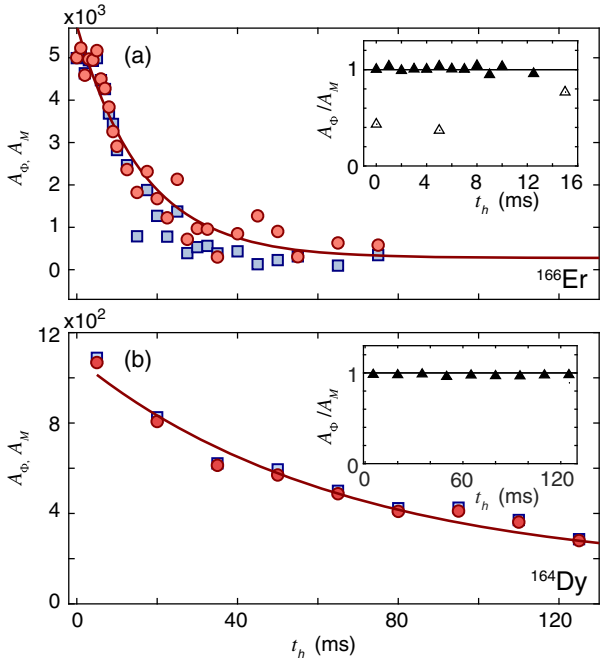

FIG. 4. Time evolution of the supersolid properties. Amplitudes A_Φ (circles) and $A_\mathcal{M}$ (squares) in the supersolid regime as a function of the holding time in trap for (a) ^{166}Er at $54.2(2)a_0$ and for (b) ^{164}Dy at 2.04 G. The solid lines are exponential fits to the data. The insets show the time evolution of $A_\Phi/A_\mathcal{M}$ for the above cases (filled triangles), and, for comparison, in the ID regime (empty triangles) for Er at $a_s = 53.1(2)a_0$ (a).

Interestingly, A_Φ and $A_\mathcal{M}$ remain approximately equal during the whole time dynamics; see insets of Figs. 4(a) and 4(b). This behavior indicates that it is the strength of the density modulation itself and not the phase coherence among droplets that decays over time. Similar results have been found theoretically in Ref. [67]. We connect this decay mainly to three-body losses, especially detrimental for ^{166}Er, and possible excitations created while crossing the BEC-to-supersolid phase transition [40]. For comparison, the inset of Fig. 4(a) shows also the behavior in the ID regime for ^{166}Er, where $A_\Phi/A_\mathcal{M} < 1$ already at short t_h and remains so during the time evolution [40].

To get a quantitative estimate of the survival time of the phase-coherent and density-modulated state, we fit a simple exponential function to A_Φ and extract t_Φ, defined as the 1/10 lifetime; see Fig. 4. For ^{166}Er, we extract $t_\Phi = 38(6)$ ms. For $t_h > t_\Phi$, the interference patterns become undetectable in our experiment and we recover a signal similar to the one of a nonmodulated BEC state [as in Figs. 2(a) and 2(d)]. These results are consistent with recent observations of transient supersolid properties in ^{162}Dy [35]. For ^{164}Dy, we observe that the coherent density-modulated state is remarkably long-lived. Here, we find $t_\Phi = 152(13)$ ms.

The striking difference in the lifetime and robustness of the supersolid properties between ^{166}Er and ^{164}Dy becomes even more visible when studying t_Φ as a function of a_s (B for Dy). As shown in Fig. 5, t_Φ for Er remains comparatively low in the investigated supersolid regime and slightly varies between 20 and 40 ms. Similarly to the recent studies with ^{162}Dy, this finding reveals the transient character of the state and opens the question of whether a stationary supersolid state can be reached with these species. On the contrary, for ^{164}Dy we observe that t_Φ first increases with B in the range from 1.8 G to about 1.98 G. Then, for $B > 1.98$ G, t_Φ acquires a remarkably large and almost constant value of about 150 ms over a wide B range. This shows the long-lived character of the supersolid properties in our ^{164}Dy quantum gas. We note that over the investigated range, a_s is expected to monotonously increase with B [40]. Such a large value of t_Φ exceeds not only the estimated tunneling time across neighboring droplets but also the weak-axis trap period, which together set the typical timescale to achieve global equilibrium and to study collective excitations.

VI. CREATION OF STATES WITH SUPERSOLID PROPERTIES BY EVAPORATIVE COOLING

The long-lived supersolid properties in ^{164}Dy motivate us to explore an alternative route to cross the supersolid phase transition, namely, by evaporative cooling instead of interaction tuning. For this set of experiments, we have modified the waists of our trapping beams in order to achieve quantum degeneracy in tighter traps with respect to

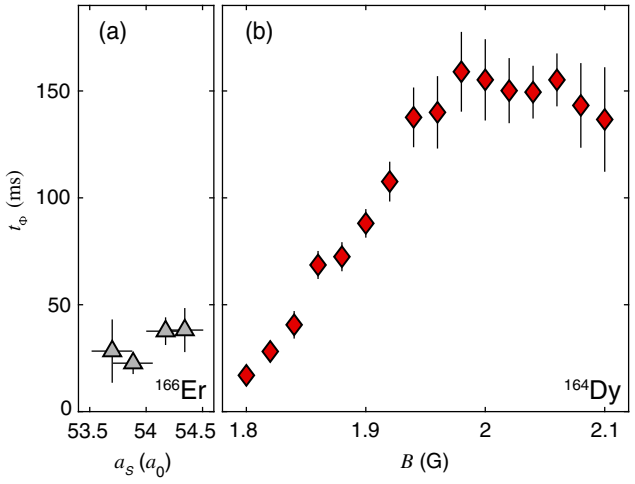

FIG. 5. Survival time of the coherent density-modulated state. t_Φ in ^{166}Er as a function of a_s (a) and ^{164}Dy as a function of B (b). The error bars refer to the statistical uncertainty from the fit. The range of investigation corresponds to the supersolid regime for which phase-coherent density-modulated states are observed. This range is particularly narrow for ^{166}Er.

the one used for condensation in the previous set of measurements. In this way, the interference peaks in the supersolid region are already visible without the need to apply a further compression of the trap since the side-to-central-peak distance in the momentum distribution scales roughly as $1/\ell_z$ [18]. Forced evaporative cooling is performed by reducing the power of the trapping beams piecewise linearly in subsequent evaporation steps until a final trap with frequencies $2\pi \times (225, 37, 134)$ Hz is achieved. During the whole evaporation process, which has an overall duration of about 3 s, the magnetic field is kept either at $B = 2.43$ G, where we observe long-lived interference patterns, or at $B = 2.55$ G, where we produce a stable nonmodulated BEC. We note that these two B values are very close without any FR lying in between [40].

Figure 6 shows the phase transition from a thermal cloud to a final state with supersolid properties by evaporative cooling. In particular, we study the phase transition by varying the duration of the last evaporation ramp, while maintaining the initial and final trap-beam power fixed. This procedure effectively changes the atom number and temperature in the final trap while keeping the trap parameters unchanged, which is important to not alter the final ground-state phase diagram of the system. At the end of the evaporation, we let the system equilibrate and thermalize for $t_h = 100$ ms, after which we switch off the trap, let the atoms expand for 26.5 ms, and finally perform absorption imaging. We record the TOF images for different ramp durations, i.e., for different thermalization times. For a short ramp, too many atoms are lost such that the critical atom number for condensation is not reached, and the atomic distribution remains thermal; see Fig. 6(a).

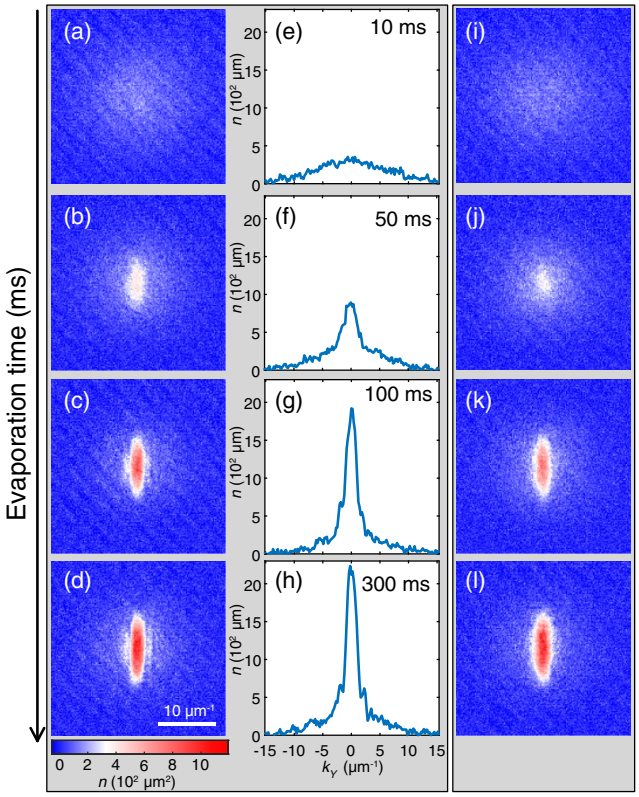

FIG. 6. Evaporative cooling to a state with supersolid properties. ^{164}Dy absorption images showing the transition to a state with supersolid properties at 2.43 G (a)–(d) and to a BEC state at 2.55 G (i)–(l), via different durations of the last evaporation step. These durations are 10 ms (a),(i), 50 ms (b),(j), 100 ms (c),(k), and 300 ms (d),(l). The density profiles (e)–(h) are integrated over the central regions of the corresponding absorption images (a)–(d). The color map indicates the atomic density in momentum space.

By increasing the ramp time, the evaporative cooling becomes more efficient and we observe the appearance of a bimodal density profile with a narrow and dense peak at the center, which we identify as a regular BEC; see Fig. 6(b). By further cooling, the BEC fraction increases and the characteristic pattern of the supersolid state emerges; see Figs. 6(c) and 6(d). The observed evaporation process shows a strikingly different behavior in comparison with the corresponding situation at $B = 2.55$ G, where the usual thermal-to-BEC phase transition is observed; see Figs. 6(i)–6(l).

We finally probe the lifetime of the supersolid properties by extracting the time evolution of both the amplitudes A_Φ and $A_\mathcal{M}$, as previously discussed. We use the same experimental sequence as the one in Fig. 6(d)—i.e., 300-ms duration of the last evaporation ramp and 100 ms of equilibration time—and subsequently hold the sample in the trap for a variable t_h. As shown in Fig. 7(a), we observe a very long lifetime with both amplitudes staying large and almost constant over more than 200 ms. At longer holding

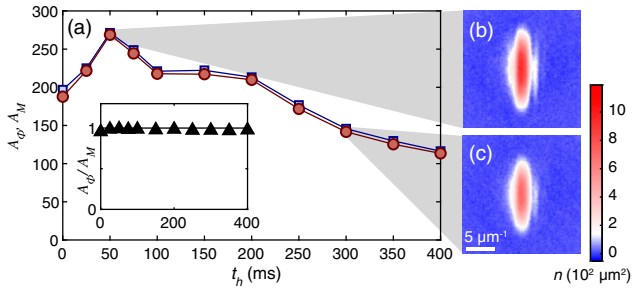

FIG. 7. Lifetime of the supersolid properties achieved via evaporative cooling. Time evolution of the amplitudes A_Φ (red circle) and $A_\mathcal{M}$ (square) after an evaporation time of 300 ms at 2.43 G and an equilibration time of 100 ms. The inset shows the time evolution of $A_\Phi/A_\mathcal{M}$. At $t_h = 0$ ms, the atom number in the phase-coherent density-modulated component is $N = 2.2(2) \times 10^4$. (b),(c) Averaged absorption images of 25 realizations after 50 and 300 ms of holding time, respectively. Note that the thermal background has been subtracted from the images. The color map indicates the atomic density in momentum space.

time, we observe a slow decay of A_Φ and $A_\mathcal{M}$, following the decay of the atom number. Moreover, during the dynamics, the ratio $A_\Phi/A_\mathcal{M}$ stays constant. The long lifetime of the phase-coherent density modulation is also directly visible in the persistence of the interference patterns in the averaged momentum density profiles [similar to Fig. 2(e)], both at intermediate and long times; see Figs. 7(b) and 7(c), respectively. For even longer t_h, we cannot resolve anymore interference patterns in the TOF images. Here, we recover a signal consistent with a regular BEC of low N.

Achieving the coherent droplet phase via evaporative cooling is a very powerful alternative path to supersolidity. We speculate that, for instance, excitations, which might be important when crossing the phase transitions by interaction tuning, may be small or removed by evaporation when reaching this state kinematically. Other interesting questions, open to future investigations, are the nature of the phase transition, the critical atom number, and the role of noncondensed atoms.

VII. CONCLUSIONS

For both ^{166}Er and ^{164}Dy dipolar quantum gases, we have identified and studied states showing hallmarks of supersolidity, namely, global phase coherence and spontaneous density modulations. These states exist in a narrow scattering-length region, lying between a regular BEC phase and a phase of an insulating droplet array. While for ^{166}Er, similarly to the recently reported ^{162}Dy case [35,36], the observed supersolid properties fade out over a comparatively short time because of atom losses, we find that ^{164}Dy exhibits remarkably long-lived supersolid properties. Moreover, we are able to directly create stationary states with supersolid properties by evaporative cooling, demonstrating a powerful alternative approach to interaction tuning on a BEC. This novel technique provides prospects of creating states with supersolid properties while avoiding additional excitations and dynamics. The ability to produce long-lived supersolid states paves the way for future investigations on quantum fluctuations and many-body correlations, as well as of collective excitations in such an intriguing many-body quantum state. A central goal of these future investigations lies in proving the superfluid character of this phase, beyond its global phase coherence [7,34,68–70].

ACKNOWLEDGMENTS

We thank R. Bisset, B. Blakie, M. Boninsegni, G. Modugno, T. Pfau, and, in particular, L. Santos for many stimulating discussions. Part of the computational results presented have been achieved using the HPC infrastructure LEO of the University of Innsbruck. We acknowledge support by the Austrian Science Fund FWF through the DFG/FWF Forschergruppe (FOR 2247/PI2790), by the ERC Consolidator Grant (RARE, No. 681432), and by a NFRI Grant (MIRARE, No. ÖAW0600) from the Austrian Academy of Science. G. D. and M. S. acknowledge support by the Austrian Science Fund FWF within the DK-ALM (No. W1259-N27).

Note added.—Recently, we became aware of related works reporting theoretical studies of the ground-state phase diagram [71,72].

[1] A. F. Andreev and I. M. Lifshitz, *Many-Body Problem in Quantum Mechanics and Quantum Statistical Mechanics*, Sov. Phys. JETP **29**, 1107 (1969).
[2] G. V. Chester, *Speculations on Bose-Einstein Condensation and Quantum Crystals*, Phys. Rev. A **2**, 256 (1970).
[3] A. J. Leggett, *Can a Solid Be "Superfluid"?*, Phys. Rev. Lett. **25**, 1543 (1970).
[4] D. A. Kirzhnits and Y. A. Nepomnyashchii, *Coherent Crystallization of Quantum Liquid*, Sov. Phys. JETP **32**, 1191 (1971).
[5] T. Schneider and C. P. Enz, *Theory of the Superfluid-Solid Transition of* ^{4}He, Phys. Rev. Lett. **27**, 1186 (1971).
[6] S. Balibar, *The Enigma of Supersolidity*, Nature (London) **464**, 176 (2010).
[7] M. Boninsegni and N. V. Prokof'ev, *Colloquium: Supersolids: What and Where Are They?*, Rev. Mod. Phys. **84**, 759 (2012).
[8] Z.-K. Lu, Y. Li, D. S. Petrov, and G. V. Shlyapnikov, *Stable Dilute Supersolid of Two-Dimensional Dipolar Bosons*, Phys. Rev. Lett. **115**, 075303 (2015).
[9] N. Henkel, R. Nath, and T. Pohl, *Three-Dimensional Roton Excitations and Supersolid Formation in Rydberg-Excited Bose-Einstein Condensates*, Phys. Rev. Lett. **104**, 195302 (2010).

[10] F. Cinti, P. Jain, M. Boninsegni, A. Micheli, P. Zoller, and G. Pupillo, *Supersolid Droplet Crystal in a Dipole-Blockaded Gas*, Phys. Rev. Lett. **105**, 135301 (2010).

[11] M. Boninsegni, *Supersolid Phases of Cold Atom Assemblies*, J. Low Temp. Phys. **168**, 137 (2012).

[12] J. Léonard, A. Morales, P. Zupancic, T. Esslinger, and T. Donner, *Supersolid Formation in a Quantum Gas Breaking a Continuous Translational Symmetry*, Nature (London) **543**, 87 (2017).

[13] J.-R. Li, J. Lee, W. Huang, S. Burchesky, B. Shteynas, F. Ç. Top, A. O. Jamison, and W. Ketterle, *A Stripe Phase with Supersolid Properties in Spin–Orbit-Coupled Bose–Einstein Condensates*, Nature (London) **543**, 91 (2017).

[14] L. D. Landau, *The Theory of Superfluidity of Helium II*, J. Phys. (Moscow) **5**, 71 (1941).

[15] P. Nozières, *Is the Roton in Superfluid* ^{4}He *the Ghost of a Bragg Spot?*, J. Low Temp. Phys. **137**, 45 (2004).

[16] D. H. J. O'Dell, S. Giovanazzi, and G. Kurizki, *Rotons in Gaseous Bose-Einstein Condensates Irradiated by a Laser*, Phys. Rev. Lett. **90**, 110402 (2003).

[17] L. Santos, G. V. Shlyapnikov, and M. Lewenstein, *Roton-Maxon Spectrum and Stability of Trapped Dipolar Bose-Einstein Condensates*, Phys. Rev. Lett. **90**, 250403 (2003).

[18] L. Chomaz, R. M. W. van Bijnen, D. Petter, G. Faraoni, S. Baier, J. H. Becher, M. J. Mark, F. Wächtler, L. Santos, and F. Ferlaino, *Observation of Roton Mode Population in a Dipolar Quantum Gas*, Nat. Phys. **14**, 442 (2018).

[19] D. Petter, G. Natale, R. M. W. van Bijnen, A. Patscheider, M. J. Mark, L. Chomaz, and F. Ferlaino, *Probing the Roton Excitation Spectrum of a Stable Dipolar Bose Gas*, arXiv:1811.12115.

[20] H. Kadau, M. Schmitt, M. Wenzel, C. Wink, T. Maier, I. Ferrier-Barbut, and T. Pfau, *Observing the Rosensweig Instability of a Quantum Ferrofluid*, Nature (London) **530**, 194 (2016).

[21] I. Ferrier-Barbut, H. Kadau, M. Schmitt, M. Wenzel, and T. Pfau, *Observation of Quantum Droplets in a Strongly Dipolar Bose Gas*, Phys. Rev. Lett. **116**, 215301 (2016).

[22] L. Chomaz, S. Baier, D. Petter, M. J. Mark, F. Wächtler, L. Santos, and F. Ferlaino, *Quantum-Fluctuation-Driven Crossover from a Dilute Bose-Einstein Condensate to a Macrodroplet in a Dipolar Quantum Fluid*, Phys. Rev. X **6**, 041039 (2016).

[23] F. Wächtler and L. Santos, *Quantum Filaments in Dipolar Bose-Einstein Condensates*, Phys. Rev. A **93**, 061603(R) (2016).

[24] F. Wächtler and L. Santos, *Ground-State Properties and Elementary Excitations of Quantum Droplets in Dipolar Bose-Einstein Condensates*, Phys. Rev. A **94**, 043618 (2016).

[25] M. Schmitt, M. Wenzel, F. Böttcher, I. Ferrier-Barbut, and T. Pfau, *Self-Bound Droplets of a Dilute Magnetic Quantum Liquid*, Nature (London) **539**, 259 (2016).

[26] I. Ferrier-Barbut, M. Wenzel, M. Schmitt, F. Böttcher, and T. Pfau, *Onset of a Modulational Instability in Trapped Dipolar Bose-Einstein Condensates*, Phys. Rev. A **97**, 011604(R) (2018).

[27] R. N. Bisset, R. M. Wilson, D. Baillie, and P. B. Blakie, *Ground-State Phase Diagram of a Dipolar Condensate with Quantum Fluctuations*, Phys. Rev. A **94**, 033619 (2016).

[28] M. Wenzel, F. Böttcher, T. Langen, I. Ferrier-Barbut, and T. Pfau, *Striped States in a Many-Body System of Tilted Dipoles*, Phys. Rev. A **96**, 053630 (2017).

[29] D. Baillie and P. B. Blakie, *Droplet Crystal Ground States of a Dipolar Bose Gas*, Phys. Rev. Lett. **121**, 195301 (2018).

[30] D. S. Petrov, *Quantum Mechanical Stabilization of a Collapsing Bose-Bose Mixture*, Phys. Rev. Lett. **115**, 155302 (2015).

[31] C. R. Cabrera, L. Tanzi, J. Sanz, B. Naylor, P. Thomas, P. Cheiney, and L. Tarruell, *Quantum Liquid Droplets in a Mixture of Bose-Einstein Condensates*, Science **359**, 301 (2018).

[32] G. Semeghini, G. Ferioli, L. Masi, C. Mazzinghi, L. Wolswijk, F. Minardi, M. Modugno, G. Modugno, M. Inguscio, and M. Fattori, *Self-Bound Quantum Droplets of Atomic Mixtures in Free Space*, Phys. Rev. Lett. **120**, 235301 (2018).

[33] P. Cheiney, C. R. Cabrera, J. Sanz, B. Naylor, L. Tanzi, and L. Tarruell, *Bright Soliton to Quantum Droplet Transition in a Mixture of Bose-Einstein Condensates*, Phys. Rev. Lett. **120**, 135301 (2018).

[34] S. M. Roccuzzo and F. Ancilotto, *Supersolid Behaviour of a Dipolar Bose-Einstein Condensate Confined in a Tube*, Phys. Rev. A **99**, 041601(R) (2019).

[35] L. Tanzi, E. Lucioni, F. Fama, J. Catani, A. Fioretti, C. Gabbanini, R. N. Bisset, L. Santos, and G. Modugno, *Observation of a Dipolar Quantum Gas with Metastable Supersolid Properties*, Phys. Rev. Lett. **122**, 130405 (2019).

[36] F. Böttcher, J.-N. Schmidt, M. Wenzel, J. Hertkorn, M. Guo, T. Langen, and T. Pfau, *Transient Supersolid Properties in an Array of Dipolar Quantum Droplets*, Phys. Rev. X **9**, 011051 (2019).

[37] K. Aikawa, A. Frisch, M. Mark, S. Baier, A. Rietzler, R. Grimm, and F. Ferlaino, *Bose-Einstein Condensation of Erbium*, Phys. Rev. Lett. **108**, 210401 (2012).

[38] A. Trautmann, P. Ilzhöfer, G. Durastante, C. Politi, M. Sohmen, M. J. Mark, and F. Ferlaino, *Dipolar Quantum Mixtures of Erbium and Dysprosium Atoms*, Phys. Rev. Lett. **121**, 213601 (2018).

[39] S. Baier, M. J. Mark, D. Petter, K. Aikawa, L. Chomaz, Z. Cai, M. Baranov, P. Zoller, and F. Ferlaino, *Extended Bose-Hubbard Models with Ultracold Magnetic Atoms*, Science **352**, 201 (2016).

[40] See Supplemental Material at http://link.aps.org/supplemental/10.1103/PhysRevX.9.021012 for details on the experimental setup, measurement schemes, analysis, and theory calculations.

[41] I. Ferrier-Barbut, M. Wenzel, F. Böttcher, T. Langen, M. Isoard, S. Stringari, and T. Pfau, *Scissors Mode of Dipolar Quantum Droplets of Dysprosium Atoms*, Phys. Rev. Lett. **120**, 160402 (2018).

[42] A. Gammal, T. Frederico, L. Tomio, and P. Chomaz, *Atomic Bose-Einstein Condensation with Three-Body Interactions and Collective Excitations*, J. Phys. B **33**, 4053 (2000).

[43] A. Bulgac, *Dilute Quantum Droplets*, Phys. Rev. Lett. **89**, 050402 (2002).

[44] D. S. Petrov, *Quantum Mechanical Stabilization of a Collapsing Bose-Bose Mixture*, Phys. Rev. Lett. **115**, 155302 (2015).

[45] F. Wächtler and L. Santos, *Ground-State Properties and Elementary Excitations of Quantum Droplets in Dipolar Bose-Einstein Condensates*, Phys. Rev. A **94**, 043618 (2016).
[46] M. Wenzel, F. Böttcher, J.-N. Schmidt, M. Eisenmann, T. Langen, T. Pfau, and I. Ferrier-Barbut, *Anisotropic Superfluid Behavior of a Dipolar Bose-Einstein Condensate*, Phys. Rev. Lett. **121**, 030401 (2018).
[47] B. D. Josephson, *Possible New Effects in Superconductive Tunnelling*, Phys. Lett. **1**, 251 (1962).
[48] J. Javanainen, *Oscillatory Exchange of Atoms between Traps Containing Bose Condensates*, Phys. Rev. Lett. **57**, 3164 (1986).
[49] S. Raghavan, A. Smerzi, S. Fantoni, and S. R. Shenoy, *Coherent Oscillations between Two Weakly Coupled Bose-Einstein Condensates: Josephson Effects, π Oscillations, and Macroscopic Quantum Self-Trapping*, Phys. Rev. A **59**, 620 (1999).
[50] A similar behavior is also seen for ^{164}Dy for $N < 4000$ [out of the scale of Fig. 1(g)].
[51] We note that a similar behavior is also found in our ^{166}Er phase diagram but for larger N than the one reported here.
[52] Y. Tang, A. Sykes, N. Q. Burdick, J. L. Bohn, and B. L. Lev, *s-Wave Scattering Lengths of the Strongly Dipolar Bosons ^{162}Dy and ^{164}Dy*, Phys. Rev. A **92**, 022703 (2015).
[53] M. Greiner, O. Mandel, T. Esslinger, T. W. Hänsch, and I. Bloch, *Quantum Phase Transition from a Superfluid to a Mott Insulator in a Gas of Ultracold Atoms*, Nature (London) **415**, 39 (2002).
[54] M. Greiner, I. Bloch, O. Mandel, T. W. Hänsch, and T. Esslinger, *Exploring Phase Coherence in a 2D Lattice of Bose-Einstein Condensates*, Phys. Rev. Lett. **87**, 160405 (2001).
[55] B. Paredes, A. Widera, V. Murg, O. Mandel, S. Fölling, I. Cirac, G. V. Shlyapnikov, T. W. Hänsch, and I. Bloch, *Tonks–Girardeau Gas of Ultracold Atoms in an Optical Lattice*, Nature (London) **429**, 277 (2004).
[56] Z. Hadzibabic, S. Stock, B. Battelier, V. Bretin, and J. Dalibard, *Interference of an Array of Independent Bose-Einstein Condensates*, Phys. Rev. Lett. **93**, 180403 (2004).
[57] In our absorption imaging a residual asymmetry can be observed between $\pm k_y$. This asymmetry, providing a sharper peak at $k_y > 0$, stems from optical aberrations in our imperfect optical setup. These imperfections make the quantitative analysis of our data more challenging, yet they do not affect the quantitative interpretation. In particular, we have checked that the peak structures are also observable along a distinct imaging axis, nonorthogonal to y, using an independent imaging setup.
[58] M. Takeda, H. Ina, and S. Kobayashi, *Fourier-Transform Method of Fringe-Pattern Analysis for Computer-Based Topography and Interferometry*, J. Opt. Soc. Am. **72**, 156 (1982).
[59] C. Kohstall, S. Riedl, E. R. S. Guajardo, L. A. Sidorenkov, J. H. Denschlag, and R. Grimm, *Observation of Interference between Two Molecular Bose–Einstein Condensates*, New J. Phys. **13**, 065027 (2011).
[60] L. Chomaz, L. Corman, T. Bienaimé, R. Desbuquois, C. Weitenberg, S. Nascimbène, J. Beugnon, and J. Dalibard, *Emergence of Coherence via Transverse Condensation in a Uniform Quasi-Two-Dimensional Bose Gas*, Nat. Commun. **6**, 6162 (2015).
[61] S. Hofferberth, I. Lesanovsky, B. Fischer, T. Schumm, and J. Schmiedmayer, *Non-Equilibrium Coherence Dynamics in One-Dimensional Bose Gases*, Nature (London) **449**, 324 (2007).
[62] The values of a_s^* extracted from experiments and from theory disagree by $3.8a_0$. Such a mismatch is similar to the one observed in our previous work on the roton instability [18,19]. This behavior might be related to the possibility that beyond-mean-field effects are not properly accounted for by the conventional LHY correction term; see main text. In addition, other effects, such as the dynamics and the atom losses [40], can affect the experimental observations.
[63] This atom number corresponds to the condensed atom number measured within the stabilization time of a_s [40].
[64] M. E. Fisher and A. E. Ferdinand, *Interfacial, Boundary, and Size Effects at Critical Points*, Phys. Rev. Lett. **19**, 169 (1967).
[65] Y. Imry and D. Bergman, *Critical Points and Scaling Laws for Finite Systems*, Phys. Rev. A **3**, 1416 (1971).
[66] Y. Imry, *Finite-Size Rounding of a First-Order Phase Transition*, Phys. Rev. B **21**, 2042 (1980).
[67] See the theoretical analysis in the revised version of Ref. [35].
[68] V. W. Scarola, E. Demler, and S. D. Sarma, *Searching for a Supersolid in Cold-Atom Optical Lattices*, Phys. Rev. A **73**, 051601(R) (2006).
[69] Z.-K. Lu, Y. Li, D. S. Petrov, and G. V. Shlyapnikov, *Stable Dilute Supersolid of Two-Dimensional Dipolar Bosons*, Phys. Rev. Lett. **115**, 075303 (2015).
[70] F. Cinti and M. Boninsegni, *Classical and Quantum Filaments in the Ground State of Trapped Dipolar Bose Gases*, Phys. Rev. A **96**, 013627 (2017).
[71] Y. Kora and M. Boninsegni, *Patterned Supersolids in Dipolar Bose Systems*, arXiv:1902.08256.
[72] Y.-C. Zhang, F. Maucher, and T. Pohl, *Supersolidity around a Critical Point in Dipolar Bose Einstein Condensates*, arXiv:1903.06161.

Correction: The inadvertent omission of a marker indicating "Featured in Physics" has been fixed.

Supplemental Material: Long-lived and transient supersolid behaviors in dipolar quantum gases

L. Chomaz,[1] D. Petter,[1] P. Ilzhöfer,[2] G. Natale,[1] A. Trautmann,[2] C. Politi,[2] G. Durastante,[1,2] R. M. W. van Bijnen,[2] A. Patscheider,[1] M. Sohmen,[1,2] M. J. Mark,[1,2] and F. Ferlaino[1,2,*]

[1] *Institut für Experimentalphysik, Universität Innsbruck, Technikerstraße 25, 6020 Innsbruck, Austria*

[2] *Institut für Quantenoptik und Quanteninformation, Österreichische Akademie der Wissenschaften, Technikerstraße 21a, 6020 Innsbruck, Austria*

(Dated: March 27, 2019)

GROUND STATE CALCULATIONS

We perform numerical calculations of the ground state following the procedure detailed in the supplementary information of Ref. [1]. The calculations are based on the conjugate-gradients technique to minimize the energy functional of an eGPE [2]. In particular, the eGPE accounts for the effect of quantum fluctuations, by including the LHY term $\Delta\mu[n] = 32g(na_s)^{3/2}(1+3\epsilon_{dd}^2/2)/3\sqrt{\pi}$ in the system's Hamiltonian (here $g = 4\pi\hbar^2 a_s/m$ and $n = |\psi|^2$ is the spatial density of the macroscopic state ψ). $\Delta\mu[n]$ has been obtained under a local density approximation in Refs. [3, 4]. The relevance of the LHY correction has been demonstrated in various studies of dipolar Bose gases close to the mean-field instability [1, 5–9] as it brings an additional repulsive potential, stabilizing the gas against mean-field collapse at large density. We note that the exact functional form of the potential, originating from beyond mean-field effects, has been questioned by several experimental results in finite-size trapped systems [1, 9–11], calling for further theory developments [12].

Our numerical calculations provide us with the three-dimensional ground-state wavefunctions $\psi(\boldsymbol{r})$. From this, we compute the axial in-situ density profile along the trap's weak axis, $n(y) = \int |\psi(\boldsymbol{r})|^2 dxdz$ and find density profiles, corresponding to the BEC, the supersolid or the ID phase, that we plot in Fig. 1. From the density profiles that exhibit a density modulation, we evaluate S by performing Gaussian fits to each droplet, i. e. to $n(y)$ with y ranging between two neighboring local density minima. From these Gaussian fits, we evaluate the sets of centers $\{y_i^{(0)}\}_i$ and widths $\{\sigma_i\}_i$ corresponding to the macroscopic Gaussian wavefunctions $\{\psi_i\}_i$ associated to the individual droplets in the array. We then approximate the droplet wavefunction via $\psi_i(y) \approx \sqrt{n(y \approx y_i^{(0)})} = \alpha_i \exp\left(-(y-y_i^{(0)})^2/2\sigma_i^2\right)$ with α_i a normalization coefficient such that $\int |\psi_i(y)|^2 dy = 1$. We then evaluate the wavefunction overlap S_i between the neighboring droplets $i-1$ and i via:

$$S_i \equiv \int \psi_{i-1}^*(y)\psi_i(y)dy \tag{1}$$

$$= \sqrt{\frac{2\sigma_i\sigma_{i-1}}{\sigma_i^2+\sigma_{i-1}^2}} \exp\left(-\frac{(y_i^{(0)}-y_{i-1}^{(0)})^2}{2(\sigma_i^2+\sigma_{i-1}^2)}\right). \tag{2}$$

The latter equation is obtained via an analytical evaluation of the Gaussian integral. The characteristic link strength defined in the paper is then computed by averaging S_i over all droplet links in the array: $S = \langle S_i \rangle_i$. In our calculation, we only consider as droplets all density peaks of at least 5 % of the global density maximum.

LINK STRENGTH AND ESTIMATE OF TUNNELING RATE

Generally speaking, the wavefunction overlap between neighboring droplets relates to a tunneling term, which sets a particle exchange term between two neighboring droplets [13–16]. Following the work of Ref. [17], we perform a first estimate of the tunneling coefficient by simply considering the single-particle part of the Hamiltonian and evaluate it between two neighboring droplets. We note that, in our particular setting where the density modulation is not externally imposed but arises from the mere interparticle interactions, the inter-droplet interaction may also play a crucial role. To perform a more precise estimation of the tunneling between droplets, one would certainly need to properly account for this effect. Here, we stress that our approach simply gives a rough idea of the magnitude of tunneling while it does not aim to be a quantitative description of it. This consideration calls for further studies making a systematic analysis of the full Hamiltonian and of the full phase diagram within the Josephson junction formalism and beyond.

Generalizing the description of Ref. [17] to neighboring droplets of different sizes and amplitudes, which are described by a three-dimensional wavefunction $\psi_i(\boldsymbol{r})$ approximated to a three-dimensional Gaussian of widths

$(\sigma_{i,x}, \sigma_{i,y}, \sigma_{i,z})$ with $\sigma_{i,y} = \sigma_i$, our estimate writes:

$$J_i = \frac{\hbar^2 S_i}{2m}\left[\sum_{k=x,y,z}\frac{1+\left(\frac{\sigma_{i,k}\sigma_{i-1,k}}{\ell_k^2}\right)^2}{\sigma_{i,k}^2+\sigma_{i-1,k}^2} + \frac{(y_i^{(0)}-y_{i-1}^{(0)})^2}{2\sigma_i\sigma_{i-1}}\frac{(\sigma_i\sigma_{i-1}/\ell_y)^4-1}{\sigma_i^2+\sigma_{i-1}^2}\right], \quad (3)$$

where $\ell_{x,y,z} = \sqrt{\hbar/m\omega_{x,y,z}}$ are the harmonic oscillator lengths.

In general, the tunnelling coefficients set two typical rates relevant for equilibration processes. The first one is the bare single-particle tunneling rate, which is equal to J_i/h, while the second accounts for the bosonic enhancement from the occupation of the droplet modes and writes $\tilde{t}_i = \sqrt{N_i N_{i-1}}|J_i|/h$ where N_i is the number of atoms in droplet i. In our analysis, we then define the average rates over the droplet arrays as characteristic rates $J/h = \langle J_i\rangle_i/h$, and $\tilde{t} = \langle \tilde{t}_i\rangle_i$; see e.g. [18]. While the ground state evolves from a BEC to a supersolid to an ID, the relevant timescale for achieving (global) equilibrium crosses from being set by the trap frequencies to the above-mentioned tunneling rates.

Using our approximate model, we here give a first estimate of the rates J/h and $\tilde{t}$ as a function of a_s, for the parameters of Fig. 1(b-d) of the main text (i.e. Er quantum gas with $N = 5\times10^4$ atoms). Here we find that, for $a_s = a_s^*$, $J/h \sim 400\,\text{Hz}$ and $\tilde{t} \sim 10\,\text{MHz}$ while for $a_s = a_s^* - 2.5\,a_0$, $J/h \sim 10^{-7}\,\text{Hz}$ and $\tilde{t} \sim 10^{-3}\,\text{Hz}$.

TOY MODEL FOR THE INTERFERENCE PATTERN

As described in the main text we use a simple toy model, adapted from Ref. [18], to identify the main features of the TOF interference patterns obtained from an insitu density-modulated state. As a quick reminder, our model considers a one-dimensional array of N_D Gaussian droplets, described by a single classical field, ψ_i, thus neglecting quantum and thermal fluctuations. We compute the TOF density distribution from the free-expansion of the individual ψ_i during a time t via $n(y,t) = |\sum_i \psi_i(y,t)|^2$. In our calculations, we also account for the finite imaging resolution by convolving the resulting $n(y,t)$ with a gaussian function of width σ_{im}. Here we allow the characteristics of the individual ψ_i to fluctuate. In this aim, we introduce noise on the corresponding parameter with a normal distribution around its expectation value and with a variable standard deviation (only ϕ_i can also have a uniform distribution). We then perform a Monte-Carlo study and perform ensemble averages, similar to our experimental analysis procedure. We note that, in this simple implementation, the noise on the different parameters – droplet amplitudes, widths and distances – are uncorrelated.

In the main text, we present results for a single set of parameters, namely $N_D = 4$, $d \equiv \langle d_i\rangle_i = 2.8\,\mu\text{m}$ (mean droplet distance), $\sigma_y \equiv \langle\sigma_i\rangle_i = 0.56\,\mu\text{m}$ (mean droplet size), $t = 30\,\text{ms}$, and $\sigma_{\text{im}} = 3\,\mu\text{m}$, typical for our experimental Er setting and the corresponding theory expectations in the supersolid regime. $\langle\cdot\rangle_i$ denotes the average over the droplets. In this section, we have a deeper look at the impact of the different parameters on both the TOF signal and our FT analysis. We study both the fully phase coherent and fully incoherent case, and the unchanged parameters are set as in Fig. 2(j,m) and (l,o).

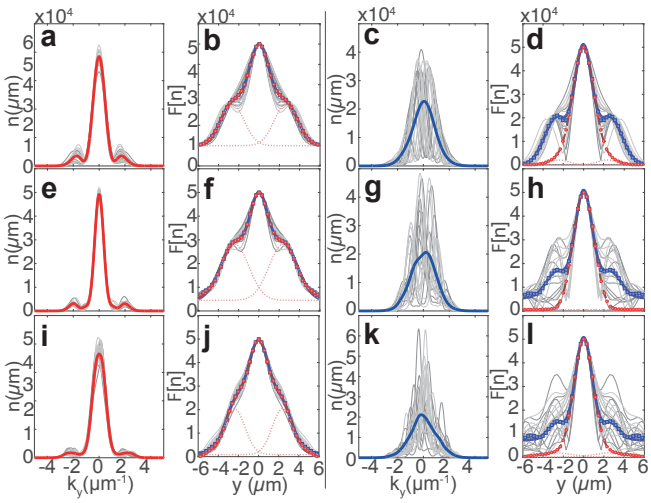

FIG. S1. **Toy model realizations with varying number of droplets** N_D. We use 100 independent draws, and expectation values $d = 2.85\,\mu\text{m}$, $\sigma_y = 0.56\,\mu\text{m}$ (with 10% noise) and either $\phi_i = 0$ (a,b,e,f,i,j), or ϕ_i uniformly distributed between 0 and 2π (c,d,g,h,k,l). (a–d) $N_D = 2$, (e–h) $N_D = 3$ and (i–l) $N_D = 8$. (a,c,e,g,i,k) TOF density profiles and (b,d,f,h,j,l) corresponding FT analysis of the interference patterns, same color code as Fig .2.

In Fig. S1, we first exemplify the TOF and FT profiles for a varying number of droplets, between 2 and 8, which cover the range of relevant N_D over the phase diagram of Fig. 1. The results remain remarkably similar to the realization of Fig. 2 with only slight quantitative changes. The main difference lies in the individual interference patterns obtained in the phase incoherent case. With increasing N_D, those profiles become more complex and made of a larger number of peaks (see (c,g,k)). Yet, in this incoherent case, a similar (non-modulated) profile is recovered in the averaged $n(k_y)$ for all N_D. Additionally, we note that for the coherent case with $N_D = 8$, the side peaks in the FT analysis (see (j)) become less visible. By performing additional tests, we attribute this behavior to the limited TOF duration, t, used in our experiment yielding a typical length scale, $\sqrt{\hbar t/m}$ ($= 3.4\mu\text{m}$), which becomes small compared to the system size ($\approx (N_D-1)d + \sigma_y$) for large N_D. This intermediate regime in the TOF expansion leads to more

complex features, including smaller-sized motifs, in the interference patterns. Finally, when accounting for our imaging resolution, it yields a broadening of the structure observed in the TOF images and less visible peaks in the FT (see (i)). We note that our experiments, because of limited N and additional losses, should rather lie in the regime $2 \leq N_D \leq 5$; see Fig. 1(b).

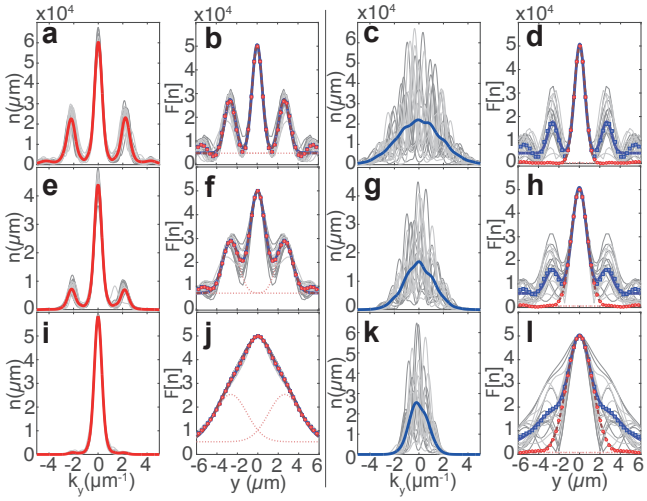

FIG. S2. **Toy model realizations with varying σ_y/d.** We use 100 independent draws, with $N_D = 4$, $d = 2.85\,\mu$m (with 10% noise) and either $\phi_i = 0$ (a,b,e,f,i,j), or ϕ_i uniformly distributed between 0 and 2π (c,d,g,h,k,l). For each realization we also compute the associated mean S. (a–d) $\sigma_y/d = 0.1$, yielding $S = 1.8\times10^{-7}$ (e–h)$\sigma_y/d = 0.15$, matching $S = 1.7\times10^{-4}$ and (i–l) $\sigma_y/d = 0.25$, matching $S = 0.028$. (a,c,e,g,i,k) TOF density profiles and (b,d,f,h,j,l) Corresponding FT analysis of the interference patterns, same color code as Fig. 2.

We then investigate the evolution of the interference patterns and their FT analysis for a varying mean droplet size, σ_y, while keeping their mean distance, d, fixed. This study is particularly relevant recalling that, within the Josephson junction formalism (see main text and corresponding section of this Supplemental Material), the key parameter controlling the tunneling rate between the droplets is set by the ratio σ_y/d, and the link strength parameter that we use to characterize the supersolid regime scales roughly as $\exp(-(d/2\sigma_y)^2)$. Thus, in our experiment, σ_y/d is intrinsically expected to decrease with the scattering length (see Fig. 3). Performing a direct estimate of the average droplet link from the initial state of our toy model, we find $S = 0.004$ for the calculations of Fig. 2(j-o), lying in an expected supersolid regime yet rather close to the supersolid-to-ID transition. Figure S2 investigates the effect of smaller and larger values of σ_y/d (and consequently of S) on the TOF and FT profiles while independently assuming phase coherence or incoherence. Qualitatively, the features remain similar as in Fig. 2(j-o). In the coherent case, side peaks are visible in the individual as well as in the mean $n(k_y)$ (see (a,e,i)) and yield side peaks in the FT profiles, with $n_{\mathcal{M}} \approx n$ (see (b,f,j)). Increasing (decreasing) σ/d mainly results in a stronger (weaker) signal both in the interference pattern and their FT analysis. Within our toy model, we find that, already for $\sigma/d = 0.25$, the signal nearly vanishes; see (i,j). Even if, given the approximations used in our toy model, this exact value may not fully hold for our experimental conditions, we expect a similar trend. It is interesting to keep in mind that this effect may limit our capacity of detecting an underlying supersolid state via matter-wave interference in experiments. In the incoherent case, the effect of decreasing σ_y/d mainly results in a broader shape of the mean density profile, while it remains non-modulated; see (c,g,k). In the FT analysis n_Φ remains structure-less independently of σ_y/d while the structures in $n_{\mathcal{M}}$ becomes sharper with decreasing σ_y/d, as in the coherent case; see (d,h,l).

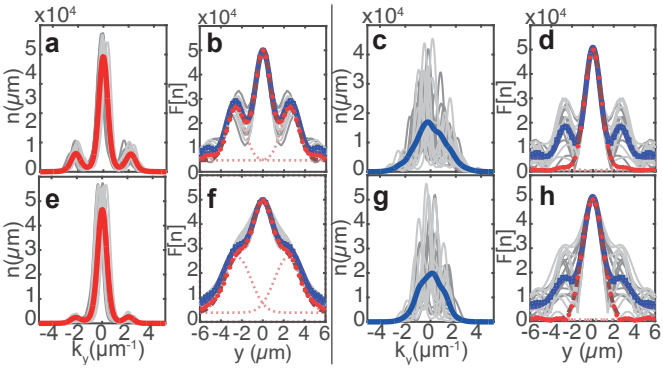

FIG. S3. **Toy model realizations allowing noise in the center position.** We use 100 independent draws, with $N_D = 4$, $d = 2.85\,\mu$m (with 10% noise), $\sigma_y/d = 0.15$ (a–d) or $\sigma_y/d = 0.2$ (e–h), and either $\phi_i = 0$ (a,b,e,f,i,j), or ϕ_i uniformly distributed between 0 and 2π (c,d,g,h,k,l). Center fluctuation are introduced as normal noise around 0 with standard deviation of $2\,\mu\text{m}^{-1}$ in situ (a,c,e,g,i,k) TOF density profiles and (b,d,f,h,j,l) corresponding FT analysis of the interference patterns, same color code as Fig. 2.

Finally, we investigate how a possible shot-to-shot noise on the position of the central interference peak could affect our observables of the density modulation and phase coherence. In the experiments, such fluctuations may occur, for instance, because of beam-pointing fluctuations or excitations of the gas. Although we compensate for such effects by recentering the individual images (see Imaging Analysis section), residual effects may remain, in particular due to center misestimation in the mere presence of the interference patterns of interest. To investigate this aspect, we repeat our toy model calculations now including noise in the global droplet array position and using a standard deviation of $2\,\mu$m for two values of σ_y/d; see Fig.S3. Again, qualitatively the observed features remains similar to our prediction in the main text. The main effect lies in the appearance of a

small discrepancy in the coherent case between n_Φ and $n_\mathcal{M}$, while the structure in the incoherent case remains similar. As the center misestimation should be the most severe in the latter case (due to the variability of the interference patterns observed here), our test shows the robustness of our analysis procedure against this issue.

IMAGING ANALYSIS: ^{164}Dy AND ^{166}Er

The density distributions in momentum space are extracted from the TOF images using the free-expansion expectation. In the Dy case, the thermal component is subtracted from the individual distribution by cutting out the central region of the cloud and performing an isotropic Gaussian fit on the outer region. This subtraction is beneficial because of the large thermal fraction. In the ^{166}Er case, such a subtraction is on the contrary complicated because of the weak thermal component and this pre-treatment may lead to improper estimation of $A_\mathcal{M}$ and A_Φ in the later analysis. The obtained momentum density distributions are then recentered and integrated numerically along $k_z(k_x)$ between $[-2.0, +2.0]\,\mu\mathrm{m}^{-1}$ ($[-1.28, +1.28]\,\mu\mathrm{m}^{-1}$) to obtain $n(k_Y)$ ($n(k_y)$) for ^{164}Dy (^{166}Er). The recentering procedure uses the result a single Gauss fit to the TOF images. The fit is performed after convoluting each image with a Gaussian function of width $0.5\,\mu$m whose purpose is to reduce the impact of the interference pattern on the center estimation [19].

In order to characterise the system's state, we use the Fourier transform, $\mathcal{F}[n](y)$ of the single density profile, $n(k_y)$. We then compute two average profiles, $n_\mathcal{M}$ and n_Φ, relying on ensemble average over all measurements under the same experimental conditions; see below for a detailed discussion on $n_\mathcal{M}$ and n_Φ. In all the measurements reported in this work we use averages over typically 15 to 100 realizations.

To quantify both the existence of a density modulation and global phase coherence on top of this modulation, we fit both $n_\mathcal{M}(y)$ and $n_\Phi(y)$ with a triple-Gaussian function, where one Gaussian accounts for the central peak and the other Gaussians are accounting for the symmetric side peaks. The amplitudes of the latter give $A_\mathcal{M}$ and A_Φ, respectively. The distance between the side peaks and the central one is allowed to vary between $[2.5, 2.7]\,\mu$m ($[2.3, 2.5]\,\mu$m) in the case of ^{164}Dy (^{166}Er).

DETAILS ON THE FOURIER ANALYSIS

In our analysis we rely on two averaged profiles, named $n_\mathcal{M}$ or n_Φ, to quantify both the density modulation and its phase coherence. Here we detail the meaning of the average performed.

The Fourier transform (FT) of the integrated momentum distributions, $n(k_y)$, which reads $\mathcal{F}[n](y) = |\mathcal{F}[n](y)|\exp(i\arg(\mathcal{F}[n](y)))$ sets the ground for our analysis. As stated in the main text, an in-situ density modulation of wavelength y^* yields patterns in $n(k_y)$ and consequently induce peaks at $y \approx y^*$, in the FT norm, $|\mathcal{F}[n](y)|$, see Fig. 2(g-i) and (m-o). Spatial variations of the phase relation within the above-mentioned density modulation translate into phase shifts of the interference patterns, which are stored in the FT argument at $y \approx y^*$, $\arg(\mathcal{F}[n](y^*))$; see also Ref. [18, 20].

The first average that we use is $n_\mathcal{M}(y) = \langle|\mathcal{F}[n](y)|\rangle$, i. e. the average of the FT norm of the individual images. As the phase information contained in $\arg(\mathcal{F}[n](y))$ is discarded from $n_\mathcal{M}$ when taking the norm, the peaks in $n_\mathcal{M}$ probe the mere existence of an insitu density modulation of roughly constant spacing within the different realizations. The second average of interest is $n_\Phi(y) = |\langle\mathcal{F}[n](y)\rangle|$, i. e. the average of the full FT of the individual images. In contrast to $n_\mathcal{M}$, n_Φ keeps the phase information of the individual realizations contained in $\arg(\mathcal{F}[n](y^*))$. Consequently, peaks in n_Φ indicate that the phase relation is maintained over the density modulation, in a similar way for all realizations. Their presence thus provides information on the global phase coherence of a density-modulated state.

EXPERIMENTAL SEQUENCE: ^{164}Dy AND ^{166}Er

^{166}Erbium - The BEC of ^{166}Er is prepared similarly to Refs. [1, 8, 21, 22]. We start from a magneto-optical trap with 2.4×10^7 ^{166}Er atoms at a temperature of 10μK, spin-polarized in the lowest Zeeman sub-level. In a next step we load about 3×10^6 atoms into a crossed optical dipole trap (ODT) operated at 1064 nm. We evaporatively cool the atomic cloud by reducing the power and then increasing the ellipticity of one of the ODT beams. During the whole evaporation a constant magnetic field of $B = 1.9\,\mathrm{G}$ ($a_\mathrm{s} = 80\,a_0$) along z is applied. We typically achieve BEC with 1.4×10^5 atoms and a condensed fraction of 70%. In a next step the ODT is reshaped in 300 ms into the final trapping frequencies $\omega_{x,y,z} = 2\pi \times (227, 31.5, 151)\,\mathrm{Hz}$. Consecutively, we ramp B linearly to $0.62\,\mathrm{G}$ ($64.5\,a_0$) in 50 ms and obtain a BEC with 8.5×10^4 atoms, which are surrounded by 3.5×10^4 thermal atoms. This point marks the start of the ramp to the final a_s.

^{164}Dysprosium - For the production of a ^{164}Dy BEC we closely follow the scheme presented in [23]. Starting from a 3 s loading phase of our 5-beam MOT in open-top configuration [24], we overlap a 1064 nm single-beam dipole trap with a $1/e^2$-waist of about $22\,\mu$m, for 120 ms. Eventually, we transfer typically 8×10^6 atoms utilizing a time averaging potential technique to increase the spatial overlap with the MOT. After an initial 1.1 s evaporative

cooling phase by lowering the power of the beam, we add a vertically propagating beam, derived from the same laser, with a $1/e^2$-waist of about 130 μm to form a crossed optical dipole trap for additional confinement. Subsequently, we proceed forced evaporative cooling to reach quantum degeneracy by nearly exponentially decreasing the laser powers in the two dipole-trap beams over 3.6 s. We achieve BECs of ^{164}Dy with typically 10^5 atoms and condensate fractions of about 40%. During the entire evaporation sequence the magnetic field is kept constant at 2.5 G pointing along the vertical (z-) axis.

To be able to condense directly into the supersolid, we modify the dipole trap to condense at a stronger confinement of $\omega_{x,y,z} = 2\pi \times (225, 37, 134)$ Hz. After a total evaporative cooling duration of 3.1 s, we achieve Bose-Einstein condensation at 2.55 G and reach a state with supersolid properties at 2.43 G, keeping the magnetic field constant throughout the entire evaporation sequence for both cases.

Time of flight and imaging for ^{166}Er *and* ^{164}Dy - In order to probe the momentum distribution of the Dy (Er) gases, we switch off the confining laser beams and let the atoms expand freely for 18 ms (15 ms), while keeping the magnetic field constant. Consecutively the amplitude of B is increased to a fixed amplitude of 5.4 G (0.6 G). In the case of ^{164}Dy, the magnetic field orientation is rotated in order to point along the imaging axis. This ensures constant imaging conditions for different a_s. After an additional 9 ms (15 ms) we perform a standard absorption imaging.

TUNING THE SCATTERING LENGTH IN ^{166}Er AND ^{164}Dy

^{166}*Erbium* - All measurements start with a BEC at 64.5 a_0. In order to probe the BEC-supersolid-ID region, we linearly ramp a_s to its target value in $t_r = 20$ ms by performing a corresponding ramp in B. Due to a finite time delay of the magnetic field in our experimental setup and the highly precise values of a_s needed for the experiment, we let the magnetic field stabilize for another 15 ms before $t_h = 0$ starts. By this, we ensure that the residual lowering of a_s during the entire hold time is $\lesssim 0.3\, a_0$. In the main text, we always give the a_s at $t_h = 0$. Furthermore, we estimate our magnetic field uncertainty to be ± 2.5 mG, leading to a $\pm 0.2\, a_0$ uncertainty of a_s in our experiments.

To choose the best ramping scheme, we have performed experiments varying t_r from 0.5 ms to 60 ms, ramping to a fixed a_s lying in the supersolid regime, and holding for $t_h = 5$ ms after a fixed 15 ms waiting time. We record the evolution of A_Φ as a function of t_r; see Fig. S4. When increasing t_r, we first observe that A_Φ increases, up to $t_r = 20$ ms, and then A_Φ gradually decreases. The initial increase can be due to diabatic effects and larger excitation when fast-crossing the phase transition. On the other hand, the slow decrease at longer t_r can be explained by larger atom loss during the ramp. We then choose $t_r = 20$ ms as an optimum value where a supersolid behavior develops and maintains itself over a significant time while the losses are minimal.

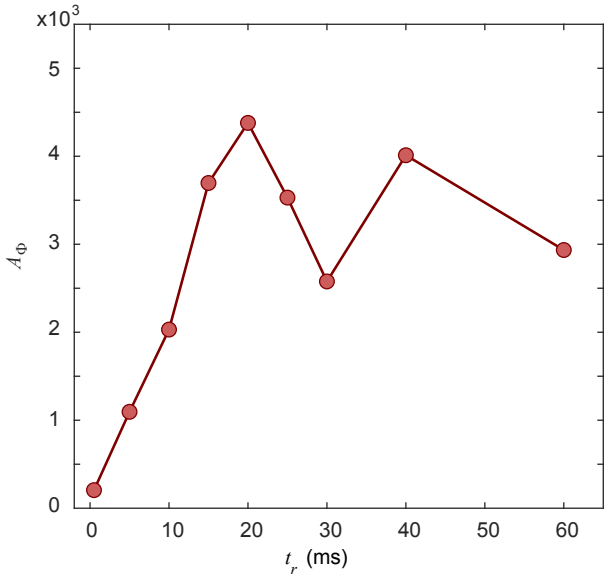

FIG. S4. **Ramp time effect on the supersolid behavior** Measured A_Φ for various durations of the scattering-length ramp with ^{166}Er and a final $a_s = 54.1(2)\, a_0$. All measurements include a 15 ms stabilization time after t_r and are performed with an additional hold of $t_h = 5$ ms.

^{164}*Dysprosium* - As the value of the background scattering, a_{bg} length for ^{164}Dy is still under debate [9, 10, 25], we discuss the experimental settings in terms of magnetic field. Yet, to gain a better understanding of the tunability of a_s in our experiment, we first perform a Feshbach spectroscopy scan on a BEC at $T = 60$ nK. After evaporative cooling at $B = 2.5$ G, we jump to B varying from 1 G to 7.5 G and we hold the sample for 100 ms. Finally, we switch off the trap, let the cloud expand for 26 ms and record the total atom number as a function of B. We then fit the observed loss features with a gaussian fit to obtain the position $B_{0,i}$ and width ΔB_i of the FRs, numbered i. We finally use the standard Feshbach resonance formula to estimate the a_s-to-B dependence via $a_s(B) = a_{bg} \prod_i (1 - \Delta B_i/(B - B_{0,i}))$. Here we account for 8 FRs located between 1.2 G and 7.2 G. Depending on the background scattering length a_{bg}, the overall magnitude of $a_s(B)$ changes. We can get an estimate of a_{bg} from literature. In Fig. S5, we use the value of a_s from Ref. [25] obtained at 1.58 G close to the B-region investigated in our experiment, $a_s = 92(8)\, a_0$. By reverting

the $a_s(B)$ formula, we set $a_{bg} = 87(8)\,a_0$. For the measurements of Figs. 4-5, we ramp B linearly from 2.5 G in 20 ms to a final value ranging from 1.8 to 2.1 G, for which we estimate a_s ranging from $97(9)\,a_0$ to $105(10)\,a_0$. We calibrate our magnetic field using RF spectroscopy, with a stability of about 2 mG. In the Dy case, we do not apply an additional stabilization time. This is justified because of the more mellow a_s-to-B dependence in the B-range of interest as well as of the wider a_s-range of the supersolid regime (see Fig. 1) compared to the Er case. For the measurements of Figs. 6–7, we use two B-values, namely 2.43 G and 2.55 G, at which we perform the evaporative cooling scheme. Here we estimate $a_s = 109(10)\,a_0$ and $a_s = 134(12)\,a_0$, respectively.

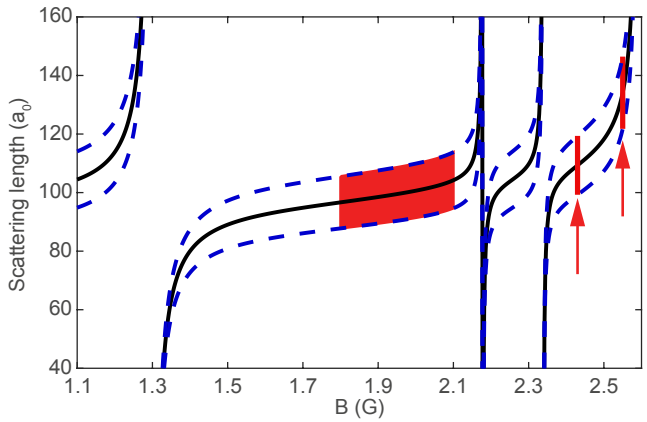

FIG. S5. **Estimated scattering length tuning in ^{164}Dy** Estimated dependence of a_s on B for ^{164}Dy. The FR positions and widths have been extracted from trap-loss spectroscopy measurements, the background scattering length is estimated to $a_{bg} = 87(8)\,a_0$, see text. The blue dashed line gives an error-estimate considering only the errorbar on a_{bg} from the mere a_s measurement of Ref. [25] and not accounting for uncertainty of the Feshhach scan. For Figs. 4-5, we use B between 1.8 G and 2.1 G (red area); for Figs. 6–7, we keep at two constant B-values, namely 2.43 G and 2.55 G (red arrows).

ATOM LOSSES IN ^{166}Er AND ^{164}Dy

As pointed out in the main text, in the time evolution of the quantum gases in both the supersolid and the ID regime, inelastic atom losses play a crucial role. The atom losses are increased in the above mentioned regime as (i) higher densities are required so that a stabilization under quantum fluctuation effects becomes relevant and (ii) the magnetic field may need to be tune close to a FR pole to access the relevant regime of interaction parameters. (i) is at play for all magnetic species but more significant for ^{166}Er due to the smaller value of a_{dd}. (ii) is relevant for both ^{166}Er and ^{162}Dy but conveniently avoided for ^{164}Dy thanks to the special short-range properties of this isotope.

To quantify the role of these losses, we report here the evolution of the number of condensed atoms, N, as a function of the hold time in parallel to the phase coherent character of the density modulation observed. We count N by fitting the thermal fraction of each individual image with a two-dimensional Gaussian function. To ensure that only the thermal atoms are fitted, we mask out the central region of the cloud associated with the quantum gas. Afterwards we subtract this fit from the image and perform a numerical integration of the resulting image (so called pixel count) to obtain N.

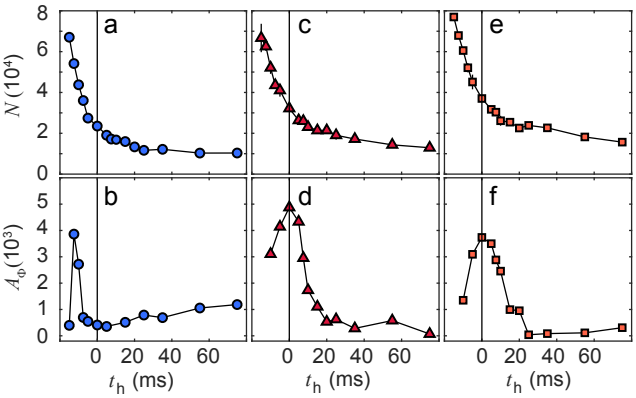

FIG. S6. **atom number and coherence decays in ^{166}Er** Time evolution of N and A_Φ for ^{166}Er at different a_s, including points before $t_h = 0$ ms in the experiment. The corresponding scattering lengths are $53.3(2)\,a_0$ (a,b), $54.0(2)\,a_0$ (c,d), $54.2(2)\,a_0$ (e,f).

^{166}Erbium - In the Er case, a 15 ms stabilization time is added to ensure that a_s is reached up to $0.3\,a_0$. During this time, i. e. for $t_h < 0$, we suspect that the time-evolution of the cloud properties is mainly dictated by the mere evolution of the scattering length. Therefore, in the main text, we report on the time evolution for $t_h \geq 0$. We note that because of the narrow a_s-range for the supersolid regime, the long stabilization time for a_s is crucial. However, because of the significant role of the atom losses in our system, in particular for ^{166}Er, the early evolution of N and the cloud's properties are intimately connected. Therefore, the early time evolution at $t_h < 0$ is certainly of high importance for our observations at $t_h \geq 0$.

To fully report on this behavior, we show the evolution of N and A_Φ during both the stabilization and the holding time in Fig. S6 for three different a_s values – either in the ID (a, b) or supersolid regime (c-f). The time evolution shows significant atom loss, prominent already during the stabilization time, and levels off towards a remaining atom number at longer holding times in which we recover small BECs. Simultaneously, in each case reported here, we observe that during the stabilization time A_Φ increases and a coherent density modulated state grows.

TABLE I. Extracted 1/10-lifetime of ^{166}Er atom number decay for $t_h \geq 0$ and remaining atom number at long holding time for data in Fig. S6.

$a_s(a_0)$	t_N (ms)	$N_r(10^4)$	t_Φ (ms)
53.3(2)	32(5)	1.03(5)	-
54.0(2)	51(9)	1.29(11)	25(6)
54.2(2)	46(12)	1.7(2)	32(9)

This density modulation starts to appear at a typical atom number of $N \gtrsim 6 \times 10^4$ and consecutively decays. For the lower $a_s = 53.3(2)\, a_0$ case, we observe that the coherent state does not survive the a_s stabilization time, and decays faster than the atoms loss; see Fig. S6 (a, b). This behavior corresponds to the ID case discussed in the main text. The central point of the present work is to identify a parameter range where the coherence of the density modulated state survives for $t_h > 0$ and its decay time scale is similar to the one of the atom loss. In order to quantify a timescale for the atom number decay, we fit an exponential decay to $t_h \geq 0$ ms. Here we allow an offset N_r of the fit, accounting for the BEC recovered at long holding times. In Table I, we report on the typical 1/10-decay times of the atom number, which are up to 50 ms. These values are of the order as the extracted t_Φ, see Table I and Fig. 5 of the main text. This reveals that in ^{166}Er the extracted lifetime of the coherent density modulated states are mainly limited by atom loss.

Furthermore we note that the extracted N_r values for the recovered BECs are smaller than 2×10^4, which is consistent with the BEC region found in the phase diagram of Fig. 1(f).

^{164}Dysprosium - Differently from the ^{166}Er case, for ^{164}Dy, we operate in a magnetic-field range in which the three-body collision coefficients are small and only moderate atom losses occur. This enables the observation of an unprecendented long-lived supersolid behavior. To understand the effects limiting the supersolid lifetime, we study the lifetime of the condensed-atom number for different B. We perform this detailed study for the data of Fig. 5 of the main text, which are obtained after preparing a stable BEC and then ramping B to the target value. Fig. S7 shows the parallel evolution of N and A_Φ for three different magnetic field values 1.8 G, 2.04 G and 2.1 G. Here we observe that, for all B values, A_Φ seems to decay faster than the atom number. This suggests that the lifetime of the density-modulated state in our ^{164}Dy experiment is not limited by atom losses. To confirm this observation, we extract the 1/10 lifetimes of both N and A_Φ; see Table II. The values confirm our observation and shows an atom number lifetime larger than t_Φ at least by a factor of ≈ 5. In addition, we find that the ratio t_N/t_Φ varies, indicating that atom losses are not the only mechanism limiting the lifetime of the supersolid properties in Dy.

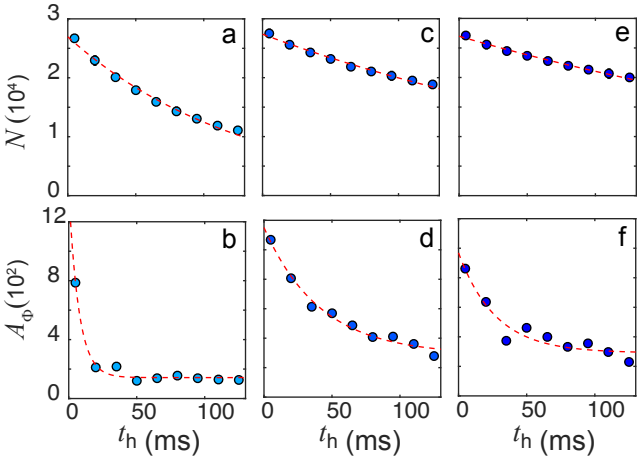

FIG. S7. **atom number and coherence decays in ^{164}Dy** Time evolution of N and A_Φ for ^{164}Dy at different B for the data of Fig. 5. The corresponding magnetic fields are 1.8 G (a,b), 2.04 G (c,d), 2.1 G (e,f).

TABLE II. Extracted 1/10-lifetime of ^{164}Dy atom number decay and A_Φ decay for data in Fig. S7.

B (G)	t_N (ms)	t_Φ (ms)
1.8	300(12)	12(5)
2.04	728(34)	152(13)
2.1	926(36)	133(25)

[1] L. Chomaz, R. M. W. van Bijnen, D. Petter, G. Faraoni, S. Baier, J. H. Becher, M. J. Mark, F. Wächtler, L. Santos, and F. Ferlaino, "Observation of roton mode population in a dipolar quantum gas," Nat. Phys. **14**, 442 (2018).

[2] S. Ronen, D. C. E. Bortolotti, and J. L. Bohn, "Bogoliubov modes of a dipolar condensate in a cylindrical trap," Phys. Rev. A **74**, 013623 (2006).

[3] A. R. P. Lima and A. Pelster, "Quantum fluctuations in dipolar Bose gases," Phys. Rev. A **84**, 041604 (2011).

[4] A. R. P. Lima and A. Pelster, "Beyond mean-field low-lying excitations of dipolar Bose gases," Phys. Rev. A **86**, 063609 (2012).

[5] F. Wächtler and L. Santos, "Quantum filaments in dipolar Bose-Einstein condensates," Phys. Rev. A **93**, 061603(R) (2016).

[6] F. Wächtler and L. Santos, "Ground-state properties and elementary excitations of quantum droplets in dipolar Bose-Einstein condensates," Phys. Rev. A **94**, 043618 (2016).

[7] R. N. Bisset, R. M. Wilson, D. Baillie, and P. B. Blakie, "Ground-state phase diagram of a dipolar condensate

with quantum fluctuations," Phys. Rev. A **94**, 033619 (2016).
[8] L. Chomaz, S. Baier, D. Petter, M. J. Mark, F. Wächtler, L. Santos, and F. Ferlaino, "Quantum-fluctuation-driven crossover from a dilute Bose-Einstein condensate to a macrodroplet in a dipolar quantum fluid," Phys. Rev. X **6**, 041039 (2016).
[9] M. Schmitt, M. Wenzel, F. Böttcher, I. Ferrier-Barbut, and T. Pfau, "Self-bound droplets of a dilute magnetic quantum liquid," Nature (London) **539**, 259–262 (2016).
[10] I. Ferrier-Barbut, M. Wenzel, F. Böttcher, T. Langen, M. Isoard, S. Stringari, and T. Pfau, "Scissors Mode of Dipolar Quantum Droplets of Dysprosium Atoms," Phys. Rev. Lett. **120**, 160402 (2018).
[11] C. R. Cabrera, L. Tanzi, J. Sanz, B. Naylor, P. Thomas, P. Cheiney, and L. Tarruell, "Quantum liquid droplets in a mixture of Bose-Einstein condensates," Science **359**, 301–304 (2018).
[12] V. Cikojevi, L. Vranje Marki, G. E. Astrakharchik, and J. Boronat, "Universality in ultradilute liquid Bose-Bose mixtures," arXiv:1811.04436 (2018).
[13] B. D. Josephson, "Possible new effects in superconductive tunnelling," Phys. Lett. **1**, 251 – 253 (1962).
[14] A. Barone and G. Patern, *Physics and applications of the Josephson effect* (Wiley, New York, NY, 1982).
[15] J. Javanainen, "Oscillatory exchange of atoms between traps containing Bose condensates," Phys. Rev. Lett. **57**, 3164–3166 (1986).
[16] S. Raghavan, A. Smerzi, S. Fantoni, and S. R. Shenoy, "Coherent oscillations between two weakly coupled bose-einstein condensates: Josephson effects, π oscillations, and macroscopic quantum self-trapping," Phys. Rev. A **59**, 620–633 (1999).
[17] M. Wenzel, F. Böttcher, J.-N. Schmidt, M. Eisenmann, T. Langen, T. Pfau, and I. Ferrier-Barbut, "Anisotropic Superfluid Behavior of a Dipolar Bose-Einstein Condensate," Phys. Rev. Lett. **121**, 030401 (2018).
[18] Z. Hadzibabic, S. Stock, B. Battelier, V. Bretin, and J. Dalibard, "Interference of an Array of Independent Bose-Einstein Condensates," Phys. Rev. Lett. **93**, 180403 (2004).
[19] We note that we have also checked our analysis without performing the recentering step and the same features remain. For instance, for our test data of Fig. 2, the effect being mainly that the side peaks in (e) are more washed out and a slight difference occurs between $n_{\mathcal{M}}$ and n_{Φ}, both showing still side peaks.
[20] S. Hofferberth, I. Lesanovsky, B. Fischer, T. Schumm, and J. Schmiedmayer, "Non-equilibrium coherence dynamics in one-dimensional Bose gases," Nature (London) **449**, 324 (2007).
[21] K. Aikawa, A. Frisch, M. Mark, S. Baier, A. Rietzler, R. Grimm, and F. Ferlaino, "Bose-Einstein condensation of Erbium," Phys. Rev. Lett. **108**, 210401 (2012).
[22] D. Petter, G. Natale, R. M. W. van Bijnen, A. Patscheider, M. J. Mark, L. Chomaz, and F. Ferlaino, "Probing the roton excitation spectrum of a stable dipolar Bose gas," arXiv:1811.12115 (2018).
[23] A. Trautmann, P. Ilzhöfer, G. Durastante, C. Politi, M. Sohmen, M. J. Mark, and F. Ferlaino, "Dipolar Quantum Mixtures of Erbium and Dysprosium Atoms," Phys. Rev. Lett. **121**, 213601 (2018).
[24] P. Ilzhöfer, G. Durastante, A. Patscheider, A. Trautmann, M. J. Mark, and F. Ferlaino, "Two-species five-beam magneto-optical trap for erbium and dysprosium," Phys. Rev. A **97**, 023633 (2018).
[25] Y. Tang, A. Sykes, N. Q. Burdick, J. L. Bohn, and B. L. Lev, "s-wave scattering lengths of the strongly dipolar bosons ^{162}Dy and ^{164}Dy," Phys. Rev. A **92**, 022703 (2015).

A.2 Publication: Phase coherence in out-of-equilibrium supersolid states of ultracold dipolar atoms[†]

Philipp Ilzhöfer[1], Maximilian Sohmen[1,2], Gianmaria Durastante[1,2], Claudia Politi[1], Arno Trautmann[1], Giacomo Morpurgo[3], Thierry Giamarchi[3], Lauriane Chomaz[2], Manfred J. Mark[1,2], and Francesca Ferlaino[1,2]

[1] *Institut für Quantenoptik und Quanteninformation, Österreichische Akademie der Wissenschaften, Technikerstraße 21a, 6020 Innsbruck, Austria*
[2] *Institut für Experimentalphysik and Zentrum für Quantenphysik, Universität Innsbruck, Technikerstraße 25, 6020 Innsbruck, Austria*
[3] *DQMP, University of Geneva, 24 Quai Ernest-Ansermet, CH-1211 Geneva, Switzerland*

arXiv:1912.10892
submitted 23 Dec 2019
URL: arXiv:1912.10892

[†] The author of the present thesis helped in taking the data, and contributed in writing the manuscript. This publication is also part of the PhD thesis of Philipp Ilzhöfer.

Phase coherence in out-of-equilibrium supersolid states of ultracold dipolar atoms

P. Ilzhöfer,[1] M. Sohmen,[1,2] G. Durastante,[1,2] C. Politi,[1] A. Trautmann,[1]
G. Morpurgo,[3] T. Giamarchi,[3] L. Chomaz,[2] M. J. Mark,[1,2] and F. Ferlaino[1,2,*]

[1]*Institut für Quantenoptik und Quanteninformation, Österreichische Akademie der Wissenschaften, 6020 Innsbruck, Austria*
[2]*Institut für Experimentalphysik und Zentrum für Quantenoptik, Universität Innsbruck, Technikerstraße 25, 6020 Innsbruck, Austria*
[3]*DQMP, University of Geneva, 24 Quai Ernest-Ansermet, CH-1211 Geneva, Switzerland*

(Dated: December 24, 2019)

A supersolid is a fascinating phase of matter, combining the global phase coherence of a superfluid with hallmarks of solids, e. g. a spontaneous breaking of the translational symmetry. Recently, states with such counter-intuitive properties have been realized in experiments using ultracold quantum gases with strong dipolar interactions. Here, we investigate the response of a supersolid state to phase excitations which shatter the global phase coherence. After the creation of those excitations, we observe a rapid re-establishment of a global phase coherence, suggesting the presence of a superfluid flow across the whole sample and an efficient dissipation mechanism. We are able to identify a well-defined region where rephasing occurs, indicating the phase boundary between the solid-like and the supersolid phase. Our observations call for the development of theoretical descriptions able to capture the non-equilibrium dynamics in the recently discovered supersolid states of quantum matter.

The notion of phase coherence lies at the foundation of quantum physics. It is considered a master property in understanding many-body quantum phenomena [1, 2], ranging from superfluidity and the Josephson effect to the more applied examples of matter-wave interference, atom lasing processes, and quantum transport in mesoscopic and macroscopic systems. A coherent state can be described in terms of single amplitude and phase fields. However, the phase itself is not a physical observable and the study of coherence relies on measurements of phase differences between a set of coherent matter waves. In the context of atomic Bose–Einstein condensates (BECs), sets of spatially separated clouds have been created, for instance, by splitting a BEC into two or more parts or by loading an ultracold gas into an optical lattice or into a double-well potential [3].

The reverse process, i. e. in-trap merging of BECs, and the related study of the phase evolution, is a much less explored and more subtle problem, invoking, for instance, the growth of thermal correlations in isolated systems [4], the complex interaction-mediated collapse and revival of many-body coherence [5], dissipative dynamics [6], or even the exponential growth of unstable modes and topological defects in connection with the Kibble-Zurek mechanism [7–9]. Despite important theoretical and experimental progress, no generic framework exists yet to understand the quantum-phase evolution and relaxation dynamics in quantum many-body systems out of equilibrium [10].

The physical understanding of the dynamical re-establishment of coherence remains even more elusive for many-body quantum states that feature a spontaneous breaking of the translational symmetry. Prime examples are the supersolid states. For a long time mainly considered a theoretical notion [11–14], such states have been recently observed in quantum gases [15–19]. These supersolids can be seen as coherent matter waves with short-wavelength modulations – shorter than the system size. Remarkably, in dipolar quantum gases the density modulation is not imprinted by external fields but truly emerges from the many-body interactions between atoms. Here, the symmetry breaking is driven by the interplay between short- (contact) and long-range (dipolar) interactions [20–25] and is connected to the softening of the roton mode in the excitation spectrum [26, 27].

The density modulation is predicted to robustly survive both in the limit of infinite system size [21] and trapped quantum gases [17, 19]. In the latter case, for a given trap geometry, the modulation contrast can be controlled by tuning the scattering length a_s – parametrizing the contact interaction – or changing the atom number, N, in the system. The different quantum phases of a cigar-shaped dipolar quantum gas with vertical dipole orientation are shown in Fig. 1a. The phase diagram is constructed by numerically solving the extended Gross-Pitaevskii equation (eGPE; Methods) [19], describing our trapped system and including the recently discovered quantum-fluctuation-driven stabilization mechanism [28–31]. The color map encodes the strength of the density modulation via the number $\widetilde{C} = 1 - C$, with $C = (n_{\max} - n_{\min})/(n_{\max} + n_{\min})$ the dimensionless modulation contrast. Here, $n_{\max}$ ($n_{\min}$) is the density maximum (minimum) in the central region of the calculated in-situ density distribution. $\widetilde{C}$ equals unity for a non-modulated and zero for a fully modulated state.

The phase diagram shows three distinct regions; see Fig. 1a. For large enough a_s, the system is a non-modulated dipolar BEC with $\widetilde{C} = 1$ (grey region). By lowering a_s, the influence of the dipolar interaction increases. When reaching a critical value of a_s, the system undergoes a phase transition to a supersolid phase (SSP). Here, a density modulation with $\widetilde{C} < 1$ appears in the ground-state density profile (red region). By further lowering a_s, the system evolves into an array of independent droplets (ID) with an exponentially vanishing density link between individual droplets and $\widetilde{C}$ approaching zero (blue region).

Recent experiments have shown a connection between the strength of the density modulation and the coherence proper-

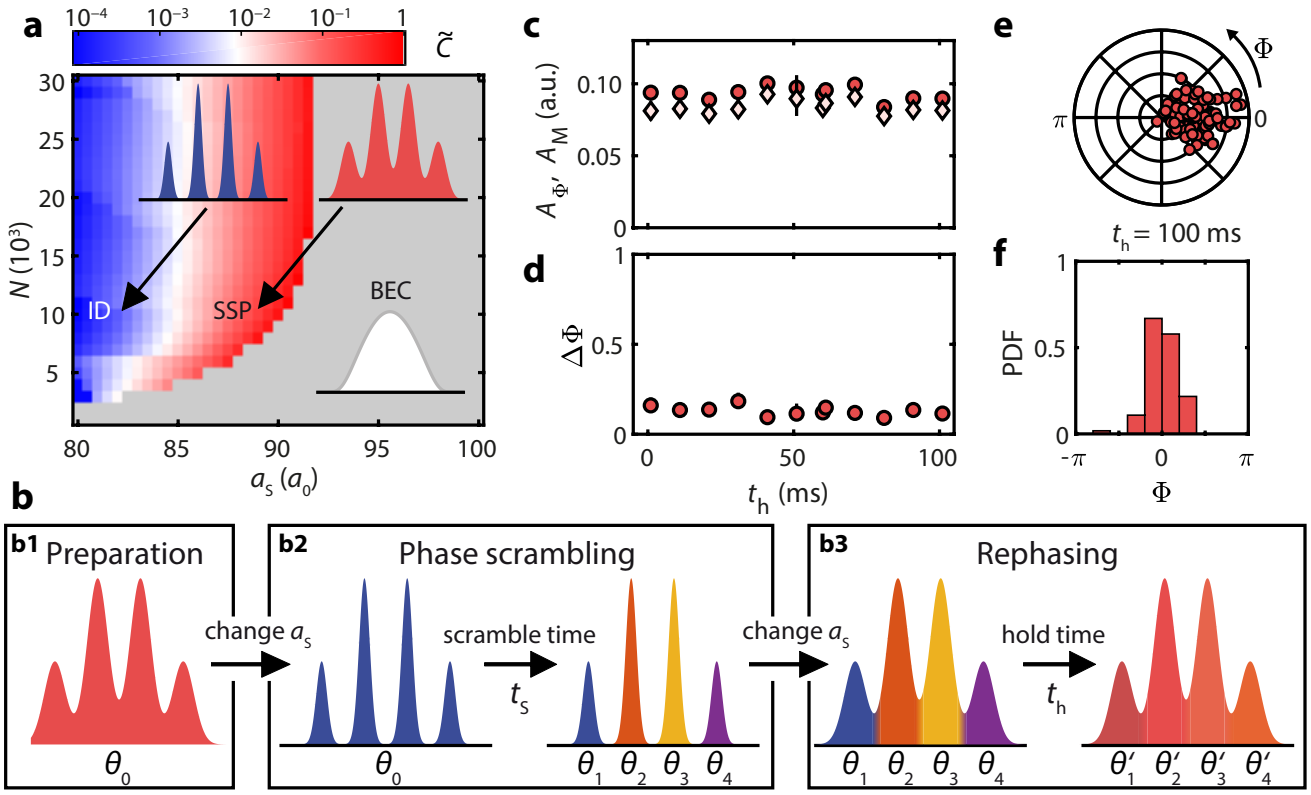

Fig. 1 | Phase diagram, experimental sequence, and starting conditions. a, Ground-state phase diagram for our cigar-shaped trapped ^{164}Dy gas. The color map shows the values of $\widetilde{C}$. The grey color indicates a non-modulated BEC, while the red and blue regions correspond to a SSP and ID phase, respectively. The insets show illustrations of the density profiles along the weak axis for the different phases. **b,** Illustration of the phase scrambling sequence: Starting from a SSP (b1), we reduce a_s to enter the ID regime (b2). During t_S, the phases of the droplets can evolve differently, leading to a phase scrambling between the individual droplets. Eventually, we jump a_s back to its initial value, re-entering the supersolid regime (b3), where we study the time evolution of the global phase coherence. **c,** Amplitudes A_M and A_Φ, and **d,** $\Delta\Phi$ for our evaporatively cooled SSP plotted over t_h. Each data point is derived from $q = 80$–90 individual experimental realizations. The error bars (almost covered by plot symbols) are the one-σ confidence intervals calculated using a bias-corrected accelerated bootstrapping analysis (Methods) [32]. **e,** Polar scatter plot for P_i and **f,** histogram of the probability density function (PDF) for Φ_i at $t_h = 100$ ms.

ties of the system, revealing a clear difference between the SSP and ID phase [17–19]. In the SSP, a global phase is present along the whole system, whereas, in the ID case, phase coherence is absent. The latter behavior can be understood by considering that any fluctuation or excitation within a single isolated droplet will drive an independent evolution of the phases, which cannot lock to each other since particle flow is absent [3]. This type of dephasing has been studied in split BECs and atomic Josephson-junction arrays [3].

While the phase evolution when moving from a SSP to an ID can be understood intuitively, highly fundamental and non-trivial questions arise when considering the opposite route, i. e. when phase-incoherent isolated droplets are linked back together. First, will the out-of-equilibrium system spontaneously re-establish phase coherence? And, if yes, will it relax into its supersolid ground state or reach a quasi-stationary state? Second, which mechanism sets the rephasing timescale? Finally, whereto will the excitation energy be dissipated? Many-body quantum descriptions, as e. g. a standard eGPE approach, are often inherently phase coherent and thus cannot capture such types of non-equilibrium dynamics.

Here, we take first steps to experimentally answer those questions by studying the out-of-equilibrium phase dynamics of a supersolid state after a *phase-scrambling* excitation. Our excitation scheme relies on an interaction quench and exploits the different coherence characters of the SSP and ID phase, as illustrated in Fig. 1b. In particular, after preparing a dipolar quantum gas in the SSP via direct evaporative cooling (b1), we drive the system into the ID regime by lowering a_s (b2). Here, we observe that the phase coherence gets quickly lost while the system remains density modulated. When going back to the parameter regime where the SSP is again the ground state (b3), we observe efficient rephasing dynamics, re-establishing the global phase coherence of the supersolid. Our measurements indicate the presence of superfluid flow with particles delocalizing across the density mod-

ulated gas as well as a dynamical mechanism dissipating the created phase excitations.

As starting point for the experiments, we produce the initial supersolid state by direct evaporative cooling from a thermal sample. As demonstrated in Ref. [19], this is a powerful approach to create a long-lived supersolid state with a high degree of phase coherence. For the present work, our supersolid state contains about $N = 1.4 \times 10^4$ ^{164}Dy atoms and is confined in an axially elongated optical-dipole trap of harmonic frequencies $\omega_{x,y,z} = 2\pi \times (225, 37, 165)\,\mathrm{s}^{-1}$. During the whole evaporation sequence, we apply a vertical magnetic field of $B = 2.430(4)\,\mathrm{G}$ to set the dipole orientation and the desired a_s-value in the SSP region.

Our investigation relies on the ability to probe the system's phase coherence and density modulation, whose co-existence is a hallmark of supersolidity. To this aim, we developed an analysis based on matter-wave-interference [17, 19, 33–36], which is capable of capturing the degree of phase coherence and the density-modulation strength (Methods). In brief, for each individual experimental realization i, we take an absorption image after a time-of-flight (TOF) expansion, which exhibits an interference pattern in case of an in-situ density modulation. Via Fourier transform, we extract the phasor $P_i = \rho_i \cdot \mathrm{e}^{-\mathrm{i}\cdot\Phi_i}$, revealing the amplitude ρ_i and phase Φ_i at the spatial frequency of the interference pattern. Whereas a single P_i characterises the degree of density modulation, the statistical average over an ensemble q of many realizations reveals information about the global phase coherence. We calculate the phase amplitude, $A_\Phi = |\langle P_i \rangle|$, and the density-modulation amplitude, $A_\mathrm{M} = \langle |P_i| \rangle$, as well as the circular phase variance $\Delta\Phi = 1 - \frac{1}{q}\sqrt{\left(\sum_{i=1}^{q}\cos(\Phi_i)\right)^2 + \left(\sum_{i=1}^{q}\sin(\Phi_i)\right)^2}$ [37]. We note that for a perfect supersolid (resp. ID) state and in the limit $q \to \infty$, $A_\Phi = A_\mathrm{M} > 0$ (resp. $A_\Phi = 0, A_\mathrm{M} > 0$) and $\Delta\Phi = 0$ (resp. 1).

To demonstrate the power of this analysis, we apply it to our initial state, whose supersolid properties have been previously investigated [19]. As shown in Fig. 1c–d, A_Φ, A_M and $\Delta\Phi$ are roughly constant during holding times t_h up to 100 ms. We observe almost equal values for A_Φ and A_M and a mean value $\langle\Delta\Phi\rangle = 0.142(8)$, confirming a high degree of global phase coherence for our density-modulated initial state. For $t_\mathrm{h} = 100\,\mathrm{ms}$, we also show a polar plot of P_i (Fig. 1e) as well as the corresponding histogram for Φ_i (Fig. 1f), both displaying a narrow distribution.

After preparing the initial supersolid state, we apply our phase-scrambling protocol; see Fig. 1b2. We ramp the B-field within 20 ms from 2.43 G (SSP) to 1.65 G (ID phase) and let the system evolve for a variable time t_S. Exploiting the magnetic-field tunability of a_s via Feshbach resonances, the B-field ramp corresponds to a change from about $a_{\mathrm{s,SSP}} = 88\,a_0$ to $a_{\mathrm{s,ID}} = 77\,a_0$ (Methods). As shown in Fig. 2a, we observe a rapid initial increase of $\Delta\Phi$ on a time scale of $t_\mathrm{S} \simeq 20\,\mathrm{ms}$ [38], after which $\Delta\Phi$ saturates close at a mean value of $\langle\Delta\Phi\rangle_{t_\mathrm{S}\geq 30\,\mathrm{ms}} = 0.92(2)$. We note that the saturation value is not expected to reach unity because of our finite sample size ($q \simeq 95$). Indeed, it is comparable to the one calculated from a toy model, which considers a sample with the same q and fully random (i. e. uniformly distributed) phases (Methods).

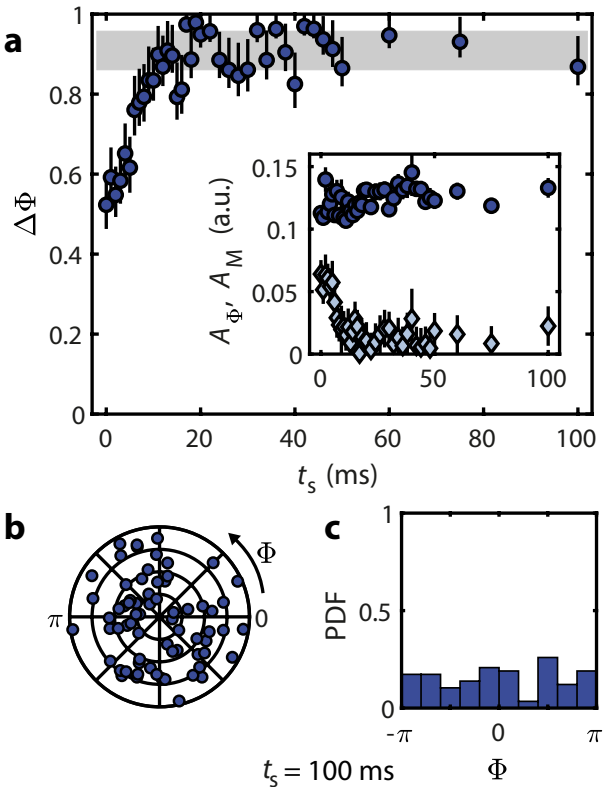

Fig. 2 | Phase scrambling. **a,** $\Delta\Phi$ as a function of t_S for the ID phase at 1.65 G ($a_{\mathrm{s,ID}} = 77\,a_0$). Each point is derived from $q = 90$–100 independent experimental realizations. The error bars are the one-σ confidence intervals calculated using a bias-corrected accelerated bootstrapping analysis (Methods) [32]. The grey shaded area indicates the theoretical one-σ confidence interval for $\Delta\Phi$ using the same sample size and a uniformly random phase. The inset shows the according A_Φ (cyan) as well as A_M (blue). **b,** Polar scatter plot for P_i and **c,** histogram of the PDF for Φ_i at $t_\mathrm{S} = 100\,\mathrm{ms}$.

Simultaneous to the increase of $\Delta\Phi$, we observe that A_Φ decreases quickly towards zero, while A_M slightly increases. This behavior shows that the density modulation is maintained while losing global phase coherence; see inset. As expected, in the ID phase, quantum and thermal fluctuations as well as atom losses can give rise to a different time evolution for the phases of the individual droplets. Apparently the vanishing small density overlap between droplets ($\widetilde{C} \simeq 0$) prevents an efficient phase locking, resulting in the observed loss of global phase coherence.

We now move to the core of our experiment and investigate the phase-relocking after the phase scrambling. We set a_s back to its initial value, i. e. where the system's ground state is a supersolid, by a B-field jump, and study the system's evolution; see Fig. 1b3. As shown in Fig. 3a, we observe first a rapid reduction of $\Delta\Phi$, occurring in the first 20 ms, and then a much slower dynamics with $\Delta\Phi$ saturating

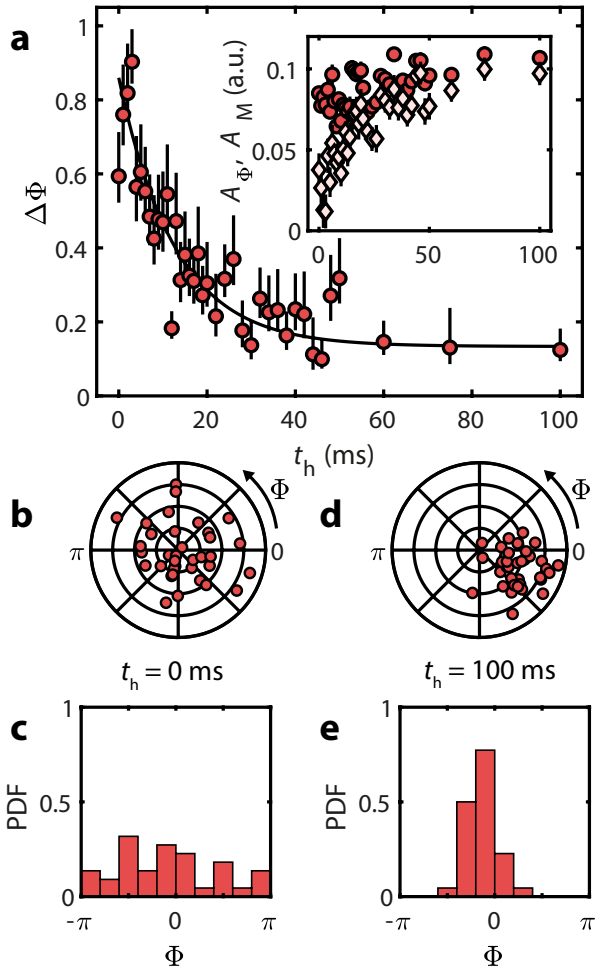

Fig. 3 | Rephasing dynamics. a, $\Delta\Phi$ as a function of t_h after a jump from the ID phase back to the SSP regime at 2.43 G ($a_{s,SSP} = 88\,a_0$). For each point $q = 66$–74. The error bars are the one-σ confidence intervals calculated using a bias-corrected accelerated bootstrapping analysis (Methods) [32]. The solid black line is an exponential fit to guide the eye. The inset shows the according A_Φ (light red) as well as A_M (red). **b,** Polar scatter plot for P_i and **c,** histogram of the PDF for Φ_i at $t_h = 0$ ms and at $t_h = 100$ ms (**d**–**e**).

to $\langle\Delta\Phi\rangle_{t_h\geq 30\,\mathrm{ms}} = 0.20(2)$. Accordingly, A_Φ approaches A_M on the same time scale, whereas A_M remains nearly constant. This re-establishment of global phase coherence is further illustrated with individual polar scatter plots and histograms in Fig. 3, confirming a reduction of the phase distribution's width with increasing t_h.

Our system of multiple superfluid parts with different phases interconnected via weak links is reminiscent of a Josephson-Junction array (JJA) [39], opening the question whether a JJA framework can capture the main ingredients of our system's dynamics. Although our array of droplets is soft, meaning that the droplets' shape and their distance change with a_s, we construct a simple model in terms of a one-dimensional array of coupled grains (Methods). This is justified as the strongest effect of the change of the system's state with a_s is the change of the wavefunction overlap between the droplets, i. e. the tunneling rate. Using this model, we simulate quenches of the tunneling rate and look at the time evolution of the correlation function of the phases in the array, which corresponds to the experimental observable A_Φ/A_M.

The model gives dephasing and rephasing dynamics, similar to the observations of Fig. 2-3. A more quantitative description goes beyond the scope of this paper. It would require (i) to find proper relations between the parameters of the JJA model and the real system, (ii) to achieve a macroscopic modelling of the dissipation mechanisms by including coupling with a thermal bath and/or with the excited droplet modes [40], or even (iii) to go beyond the hard-grain model. Even in experiments with non-dipolar coupled quasi-condensates, realizing a case closer to an ideal JJA, the observed phase dynamics and full phase-locking have no theoretical explanation up to now [41]. Another important ingredient in the phase relaxation dynamics is the phase defects formed at the boundaries between the distinct grains when they merge [6, 8, 9, 42]. These defects, forming e. g. solitons, are expected to propagate and interact with each other and with excitations from the thermal bath, and thus eventually decay.

To further investigate the role of the density links among droplets – i. e. the Josephson coupling –, we study the rephasing dynamics as a function of the theoretically calculated $\widetilde{C}$; see Fig. 1a. Although our system is out of equilibrium, we use the ground-state quantity $\widetilde{C}$ as an estimate for the strength of the density link [17–19]. For each value of a_s, we assign $\widetilde{C}$ and record the time trace of $\Delta\Phi$ for different t_h. As shown in Fig. 4a, we see different rephasing dynamics depending on $\widetilde{C}$. In the case of small $\widetilde{C}$, associated with the ID regime, no rephasing occurs with $\Delta\Phi$ remaining large (> 0.5) for all t_h (blue region). As $\widetilde{C}$ and thus the link strength increases, the system starts to rephase with $\Delta\Phi$ approaching a small saturation value (≈ 0.15) at long evolution times (red region).

The time traces clearly show the existence of two regimes for $\Delta\Phi$, one in which phase re-locking occurs and one in which the system remains incoherent. To further investigate these regimes and their interface, we study the long-time dynamics of A_Φ and A_M and record their asymptotic values. As shown in Fig. 4b, A_M remains large and shows only slight variations over the full investigated range of $\widetilde{C}$. This indicates the persistence of density modulation in the system. In contrast, a striking change is found in the evolution of the ratio between A_Φ and A_M. At large $\widetilde{C} > 0.01$, A_Φ and A_M are nearly equal. This shows the re-establishement of a global phase coherence, and the relaxation towards a SSP. Differently, at small $\widetilde{C} < 0.001$, A_Φ nearly vanishes while A_M remains large and almost constant, evidencing a final phase-incoherent state (ID regime). At intermediate $\widetilde{C}$, A_Φ and A_M show an in-between behavior with A_Φ smaller than A_M but non-vanishing, showing a partial recoherence of the state. These three distinct behaviors are also reflected in the asymptotic values of $\Delta\Phi$ (Fig. 4c), showing full recoherence ($\Delta\Phi \approx 0.15$) in the supersolid regime, persistence of a full incoherence ($\Delta\Phi \approx 0.9$) in

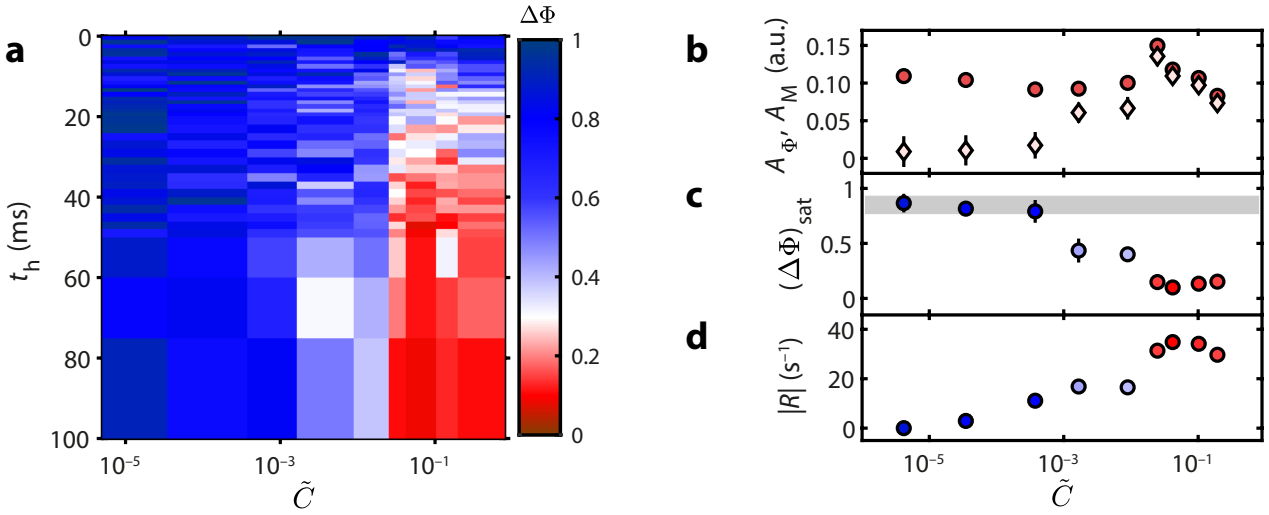

Fig. 4 | Time traces of the phase dynamics and their characterization. a, Temporal evolution of $\Delta\Phi$ (color map) after the complete phase scrambling sequence plotted as a function of t_h and $\widetilde{C}$. For each t_h we record $q \geq 35$ individual experimental realizations. In the red region ($\Delta\Phi \simeq 0$) the system has recovered its global phase coherence, while for the blue one ($\Delta\Phi \simeq 1$) no global phase coherence is present. **b,** A_Φ (light red) and A_M (red), **c,** saturation value $(\Delta\Phi)_{sat}$ and **d,** rephasing rate $|R|$ as a function of $\widetilde{C}$. A_Φ, A_M, and $(\Delta\Phi)_{sat}$ are the mean values at long t_h. The grey shaded area indicates the theoretical one-σ confidence interval for $\Delta\Phi$ using the same sample size as the experiment and a uniformly random phase.

the ID regime, and partial recoherence ($\Delta\Phi \approx 0.5$) in the intermediate regime.

A further question is whether the value of $\widetilde{C}$, i. e. the different regimes, also dictates the speed of the rephasing dynamics. To explore this aspect, we study the early time dynamics of $\Delta\Phi$ by performing a linear fit to the data for $t_h \leq 20$ ms. The extracted slope characterizes the initial rephasing rate $|R|$. As shown in Fig. 4d, in the supersolid regime, we always record a large rephasing rate, which remarkably is roughly independent of $\widetilde{C}$, with $|R| \approx 30 s^{-1}$. This value is comparable to the weak-axis trap frequency, $\omega_y/2\pi$, and compatible with the time needed for a sound wave or soliton to propagate along the system [8, 43]. In contrast, when crossing from the supersolid to the intermediate regime, we observe a sudden decrease of $|R|$ by almost a factor of two. Evolving from this intermediate regime to the ID, $|R|$ continuously decreases with decreasing $\widetilde{C}$ until it vanishes. While such a decrease of $|R|$ is consistent with a JJA picture in which the tunneling between the droplets dictates the rephasing dynamics, the underlying reason for a constant rephasing rate in the supersolid regime remains an open question. It might indicate the action of other mechanisms, related for instance to the soft nature of our JJA, or the formation and slow decay of phase defects in the array.

In conclusion, we have reported the first study of the out-of-equilibrium dynamics of a dipolar supersolid after an interaction-driven phase excitation that fully randomizes the phases. In the SSP regime, we have demonstrated that the system re-establishes a high-degree of phase coherence on the timescale of one trap period by almost perfect rephasing. When tunneling is suppressed by a too weak density link across our spontaneously-modulated quantum state, the rephasing substantially slows down at a rate depending on the tunneling and eventually ceases in the deep ID regime. Our observations might shed new light on the properties of the particle flow in a SSP and its superfluid properties, whose general understanding is still elusive. Future experimental works, combined with advanced out-of-equilibrium theoretical models, will be crucial to understand the relaxation dynamics and dissipation mechanisms in isolated and open supersolid states of quantum matter.

[1] Cohen-Tannoudji , C. & Gury-Odelin, D. *Advances in Atomic Physics: An Overview* (World Scientific, 2011). URL https://doi.org/10.1142/6631.

[2] Svistunov, B. V., Babaev, E. S. & Prokof'ev, N. V. *Superfluid States of Matter* (CRC Press, 2015). URL https://doi.org/10.1201/b18346.

[3] Bloch, I., Dalibard, J. & Zwerger, W. Many-body physics with ultracold gases. *Rev. Mod. Phys.* **80**, 885–964 (2008). URL https://doi.org/10.1103/RevModPhys.80.885.

[4] Langen, T., Geiger, R., Kuhnert, M., Rauer, B. & Schmiedmayer, J. Local emergence of thermal correlations in an isolated quantum many-body system. *Nature Physics* **9**, 640–643 (2013). URL https://doi.org/10.1038/nphys2739.

[5] Wright, E. M., Walls, D. F. & Garrison, J. C. Collapses and Revivals of Bose-Einstein Condensates Formed in Small Atomic Samples. *Phys. Rev. Lett.* **77**, 2158–2161 (1996). URL

https://doi.org/10.1103/PhysRevLett.77.2158.

[6] Jo, G.-B. *et al.* Phase-Sensitive Recombination of Two Bose-Einstein Condensates on an Atom Chip. *Phys. Rev. Lett.* **98**, 180401 (2007). URL https://doi.org/10.1103/PhysRevLett.98.180401.

[7] Scherer, D. R., Weiler, C. N., Neely, T. W. & Anderson, B. P. Vortex Formation by Merging of Multiple Trapped Bose-Einstein Condensates. *Phys. Rev. Lett.* **98**, 110402 (2007). URL https://doi.org/10.1103/PhysRevLett.98.110402.

[8] Aidelsburger, M. *et al.* Relaxation Dynamics in the Merging of *N* Independent Condensates. *Phys. Rev. Lett.* **119**, 190403 (2017). URL https://doi.org/10.1103/PhysRevLett.119.190403.

[9] del Campo , A. & Zurek, W. H. Universality of phase transition dynamics: Topological defects from symmetry breaking. *Int. J. Mod. Phys. A* **29**, 1430018 (2014). URL https://doi.org/10.1142/S0217751X1430018X.

[10] Langen, T., Geiger, R. & Schmiedmayer, J. Ultracold Atoms Out of Equilibrium. *Annu. Rev. Condens. Matter Phys* **6**, 201–217 (2015). URL https://doi.org/10.1146/annurev-conmatphys-031214-014548.

[11] Andreev , A. F. & Lifshitz, I. M. Quantum Theory of Defects in Crystals. *Sov. Phys. JETP* **29**, 1107 (1969).

[12] Chester, G. V. Speculations on Bose-Einstein Condensation and Quantum Crystals. *Phys. Rev. A* **2**, 256–258 (1970). URL https://doi.org/10.1103/PhysRevA.2.256.

[13] Leggett, A. J. Can a Solid Be "Superfluid"? *Phys. Rev. Lett.* **25**, 1543–1546 (1970). URL https://doi.org/10.1103/PhysRevLett.25.1543.

[14] Boninsegni , M. & Prokof'ev, N. V. Colloquium: Supersolids: What and where are they? *Rev. Mod. Phys.* **84**, 759–776 (2012). URL https://doi.org/10.1103/RevModPhys.84.759.

[15] Li, J.-R. *et al.* A stripe phase with supersolid properties in spinorbit-coupled BoseEinstein condensates. *Nature* **543**, 91–94 (2017). URL https://doi.org/10.1038/nature21431.

[16] Léonard, J., Morales, A., Zupancic, P., Esslinger, T. & Donner, T. Supersolid formation in a quantum gas breaking a continuous translational symmetry. *Nature* **543**, 87–90 (2017). URL https://doi.org/10.1038/nature21067.

[17] Böttcher, F. *et al.* Transient Supersolid Properties in an Array of Dipolar Quantum Droplets. *Phys. Rev. X* **9**, 011051 (2019). URL https://doi.org/10.1103/PhysRevX.9.011051.

[18] Tanzi, L. *et al.* Observation of a Dipolar Quantum Gas with Metastable Supersolid Properties. *Phys. Rev. Lett.* **122**, 130405 (2019). URL https://doi.org/10.1103/PhysRevLett.122.130405.

[19] Chomaz, L. *et al.* Long-Lived and Transient Supersolid Behaviors in Dipolar Quantum Gases. *Phys. Rev. X* **9**, 021012 (2019). URL https://doi.org/10.1103/PhysRevX.9.021012.

[20] Lu, Z.-K., Li, Y., Petrov, D. S. & Shlyapnikov, G. V. Stable Dilute Supersolid of Two-Dimensional Dipolar Bosons. *Phys. Rev. Lett.* **115**, 075303 (2015). URL https://doi.org/10.1103/PhysRevLett.115.075303.

[21] Roccuzzo , S. M. & Ancilotto, F. Supersolid behavior of a dipolar Bose-Einstein condensate confined in a tube. *Phys. Rev. A* **99**, 041601 (2019). URL https://doi.org/10.1103/PhysRevA.99.041601.

[22] Kora , Y. & Boninsegni, M. Patterned Supersolids in Dipolar Bose Systems. *J. Low Temp. Phys.* **197**, 337–347 (2019). URL https://doi.org/10.1007/s10909-019-02229-z.

[23] Wenzel, M., Böttcher, F., Langen, T., Ferrier-Barbut, I. & Pfau, T. Striped states in a many-body system of tilted dipoles. *Phys. Rev. A* **96**, 053630 (2017). URL https://doi.org/10.1103/PhysRevA.96.053630.

[24] Baillie , D. & Blakie, P. B. Droplet Crystal Ground States of a Dipolar Bose Gas. *Phys. Rev. Lett.* **121**, 195301 (2018). URL https://doi.org/10.1103/PhysRevLett.121.195301.

[25] Cinti , F. & Boninsegni, M. Classical and quantum filaments in the ground state of trapped dipolar Bose gases. *Phys. Rev. A* **96**, 013627 (2017). URL https://doi.org/10.1103/PhysRevA.96.013627.

[26] Santos, L., Shlyapnikov, G. V. & Lewenstein, M. Roton-Maxon Spectrum and Stability of Trapped Dipolar Bose-Einstein Condensates. *Phys. Rev. Lett.* **90**, 250403 (2003). URL https://doi.org/10.1103/PhysRevLett.90.250403.

[27] Chomaz, L. *et al.* Observation of roton mode population in a dipolar quantum gas. *Nat. Phys.* **14**, 442 (2018). URL https://doi.org/10.1038/s41567-018-0054-7.

[28] Ferrier-Barbut, I., Kadau, H., Schmitt, M., Wenzel, M. & Pfau, T. Observation of Quantum Droplets in a Strongly Dipolar Bose Gas. *Phys. Rev. Lett.* **116**, 215301 (2016). URL https://doi.org/10.1103/PhysRevLett.116.215301.

[29] Chomaz, L. *et al.* Quantum-Fluctuation-Driven Crossover from a Dilute Bose-Einstein Condensate to a Macrodroplet in a Dipolar Quantum Fluid. *Phys. Rev. X* **6**, 041039 (2016). URL https://doi.org/10.1103/PhysRevX.6.041039.

[30] Wächtler , F. & Santos, L. Quantum filaments in dipolar Bose-Einstein condensates. *Phys. Rev. A* **93**, 061603 (2016). URL https://doi.org/10.1103/PhysRevA.93.061603.

[31] Bisset, R. N., Wilson, R. M., Baillie, D. & Blakie, P. B. Ground-state phase diagram of a dipolar condensate with quantum fluctuations. *Phys. Rev. A* **94**, 033619 (2016). URL https://doi.org/10.1103/PhysRevA.94.033619.

[32] Efron, B. Better Bootstrap Confidence Intervals. *Journal of the American statistical Association* **82**, 171–185 (1987). URL https://doi.org/10.2307/2289144.

[33] Hadzibabic, Z., Stock, S., Battelier, B., Bretin, V. & Dalibard, J. Interference of an Array of Independent Bose-Einstein Condensates. *Phys. Rev. Lett.* **93**, 180403 (2004). URL https://doi.org/10.1103/PhysRevLett.93.180403.

[34] Takeda, M., Ina, H. & Kobayashi, S. Fourier-transform method of fringe-pattern analysis for computer-based topography and interferometry. *J. Opt. Soc. Am.* **72**, 156–160 (1982). URL https://doi.org/10.1364/JOSA.72.000156.

[35] Kohstall, C. *et al.* Observation of interference between two molecular Bose–Einstein condensates. *New J. Phys.* **13**, 065027 (2011). URL https://doi.org/10.1088/1367-2630/13/6/065027.

[36] Chomaz, L. *et al.* Emergence of coherence via transverse condensation in a uniform quasi-two-dimensional Bose gas. *Nat. Commun.* **6**, 6162 (2015). URL https://doi.org/10.1038/ncomms7162.

[37] Fisher, N. I. *Statistical Analysis Of Circular Data* (Cambridge University Press, Cambridge, 1993). URL https://doi.org/10.1017/CBO9780511564345.

[38] Note that $\Delta\Phi\,(t_S = 0) \simeq 0.5$. We attribute this large value to dephasing dynamics taking place already within the *B*-field ramp duration and the initial time of the TOF.

[39] Fazio , R. & van der Zant, H. Quantum phase transitions and vortex dynamics in superconducting networks. *Physics Reports* **355**, 235 (2001). URL https://doi.org/10.1016/S0370-1573(01)00022-9.

[40] Dalla Torre, E. G., Demler, E. & Polkovnikov, A. Universal Rephasing Dynamics after a Quantum Quench via Sudden Coupling of Two Initially Independent Condensates. *Phys. Rev. Lett.* **110**, 090404 (2013). URL https://doi.org/10.1103/PhysRevLett.110.090404.

[41] Pigneur, M. *et al.* Relaxation to a Phase-Locked Equilibrium

State in a One-Dimensional Bosonic Josephson Junction. *Phys. Rev. Lett.* **120**, 173601 (2018). URL https://doi.org/10.1103/PhysRevLett.120.173601.

[42] Frantzeskakis, D. Dark solitons in atomic Bose–Einstein condensates: from theory to experiments. *J. Phys. A: Math. Theor.* **43**, 213001 (2010). URL https://doi.org/10.1088/1751-8113/43/21/213001.

[43] Natale, G. *et al.* Excitation Spectrum of a Trapped Dipolar Supersolid and Its Experimental Evidence. *Phys. Rev. Lett.* **123**, 050402 (2019). URL https://doi.org/10.1103/PhysRevLett.123.050402.

- We are grateful to S. Erne, J. Schmiedmayer and the ERBIUM team for insightful discussions. We acknowledge R. M. W. van Bijnen for developing the code for our eGPE ground-state simulations. This work is financially supported through an ERC Consolidator Grant (RARE, No. 681432), a NFRI Grant (MIRARE, No. ÖAW0600) from the Austrian Academy of Science and a DFG/FWF (FOR 2247/PI2790), and by the Swiss National Science Fundation under Division II. M. S. and G. D. acknowledge support by the Austrian Science Fund FWF within the DK-ALM (No. W1259-N27). A. T. acknowledges support by the Austrian Science Fund FWF within the Lise-Meitner-Programm (No. M2683-N36). We also acknowledge the Innsbruck Laser Core Facility, financed by the Austrian Federal Ministry of Science, Research and Economy. Part of the computational results presented have been achieved using the HPC infrastructure LEO of the University of Innsbruck.

- Competing Interests: The authors declare no competing interests.

- Author information: Correspondence to F. F. (e-mail: Francesca.Ferlaino@uibk.ac.at).

- Author contributions: P. I. , G. D. and A T. conducted the experiment and collected the experimental data. M. S. and C. P. analyzed the data. M. J. M. performed the eGPE ground-state simulations. G. M. and T. G. contributed to the theoretical analysis. All authors contributed to the writing of the paper. F. F. supervised the project.

I. METHODS

A. Phase diagram and contrast.

Our numerical calculations of the ground-state phase diagram of a cigar-shaped ^{164}Dy dipolar quantum gas follow the procedure described in our earlier works [19, 27]. In brief, the calculations are based on minimizing the energy functional of the extended Gross-Pitaevskii equation (eGPE) using the conjugate-gradients technique [44]. The eGPE includes our anisotropic trapping potential, the short-range contact and long-range dipolar interactions at a mean-field level, as well as the first-order beyond-mean-field correction in the form of a Lee-Huang-Yang (LHY) term [29, 30] and [45]. From the derived three-dimensional wavefunction $\psi(\mathbf{r})$ we calculate the one-dimensional in-situ density profile $n(y) = \int |\psi(\mathbf{r})|^2 \mathrm{d}x\mathrm{d}z$. We evaluate the in-situ density contrast $C = (n_{\max} - n_{\min})/(n_{\max} + n_{\min})$ for profiles which feature density modulations by searching central extrema of $n(y)$ and determining the overall maximum ($n_{\max}$) and minimum ($n_{\min}$) value. For profiles without density modulation (ordinary BEC), we set $C = 0$. We use the quantity $\widetilde{C} = 1 - C$ to estimate the density link between the droplets, which is connected to the tunneling strength [19].

B. Experimental sequence.

We apply our phase scrambling protocol to the evaporatively cooled SSP of ^{164}Dy atoms [19]. For this, we initially load our 5-beam open-top magneto-optical trap (MOT) for 3 s and apply a MOT compression phase, which lasts 400 ms [46]. We then load about 8×10^6 atoms into a single-beam horizontal optical dipole trap (hODT), propagating along our y-axis. The hODT is derived from a 1064 nm focused laser beam. After loading, we apply forced evaporative cooling by exponentially reducing the optical power in the hODT for 0.9 s. Subsequently, we switch on a second ODT beam along the vertical z-axis to form a crossed ODT and continue with the last stage of evaporative cooling for 2 s [47], until the SSP is reached. During the entire evaporation sequence, a magnetic field of $B = 2.43$ G, pointing opposite to gravity along our z-direction, is maintained. The final trap geometry is cigar-shaped with harmonic frequencies $\omega_{x,y,z} = 2\pi \times (225, 37, 165)\,\mathrm{s}^{-1}$. After the initial-state preparation (SSP), we apply our phase-scrambling protocol. For that, without any additional waiting time after the evaporative cooling, we change the B-field to 1.65 G deep in the ID regime. Here, we allow the system's global phase to freely evolve for $t_{\mathrm{S}} = 20$ ms. We have explored two types of protocols: jumping, which results in an effective ≈ 1 ms change of the B-field due to the finite time response of the system, and ramping within 20 ms. We observe a similar scrambling behavior in $\Delta\Phi$ for both the jump and the ramp protocol. We complete our phase-scrambling sequence by jumping the B-field back to its initial value and by letting the system evolve for a variable hold time t_{h}. Finally, we perform a matter-wave interference-type experiment during time-of-flight (TOF) expansion and record the resulting interference pattern by absorption imaging. A TOF duration of 26.5 ms ensures a mapping onto momentum space. The imaging beam propagates along $\tilde{x}$ in the horizontal x–y-plane at an angle of $\sim 45^\circ$ with respect to the weak trap axis along y.

C. Tuning the scattering length.

To connect the experimental B-field values with the contact scattering length a_{s}, we use the well established formula for overlapping Feshbach resonances $a_{\mathrm{s}}(B) = a_{\mathrm{bg}} \prod_i (1 - \Delta B_i/(B - B_{0,i}))$ [48], with $B_{0,i}$ the poles, ΔB_i the corresponding distance from the pole to the zero-crossing and a_{bg} the (local) background scattering length. We determine the poles and zero-crossings in our B-field region of interest by performing loss spectroscopy and thermalization measurements. Starting from a thermal cloud prepared at 2.55 G we first ramp the magnetic field to the final value within 5 ms, then lower the trap depth to its final value within 50 ms, and wait an additional hold time of about 400 ms. In absence of Feshbach resonances, we typically end up with a thermal gas of 5×10^5 atoms with a temperature of about 500 nK. When scanning the magnetic field in our region of interest, we observe several atom loss features together with peaks in the atom cloud temperature, which we fit with gaussian functions to extract the positions of the poles $B_{0,i}$ and the widths ΔB_i.

The value of the background scattering length of ^{164}Dy is a more subtle topic, as several measurements give varying values in the range between 60–100 a_0 [49]. These measurements were using different methods (e. g. cross-thermalization, theory-experiment comparisons of oscillation frequencies), different initial states (thermal gases and quantum droplets) and were performed at different magnetic fields. Especially the existence of very broad resonances at higher magnetic fields [50] will affect the measured local background scattering lengths. Therefore, we set the value of a_{bg} in such a way that the B-to-a_{s} conversion reproduces the calculated critical scattering length $a_{\mathrm{s}} = 91\,a_0$ at the experimentally estimated phase transition point between BEC and SSP around 2.5 G. This gives a value of $a_{\mathrm{bg}} = 73\,a_0$ which lies within the error bars of the latest published value of $a_{\mathrm{bg}} = 69(4)\,a_0$ [49]. Extended Data Figure 1 shows the resulting calculated B-to-a_{s} conversion from which we estimate $a_{\mathrm{s,SSP}} = 88\,a_0$ at 2.43 G in the SSP and $a_{\mathrm{s,ID}} = 77\,a_0$ at 1.65 G in the ID as used in the experiment.

D. Interference pattern analysis.

Our analysis is similar to the one described in Ref. [19]. We record $q = 30$–100 experimental repetitions for each parameter set $\mathscr{P}$. Each recorded picture i ($i = 1 \ldots q$) is processed by first subtracting the thermal background via a symmetric 2D-Gaussian fit to the wings of the density distribution. Next, we recenter the image of the degenerate cloud and integrate its central region, where the matter-wave interference signal is concentrated, along the z-direction within $\pm 2\,\mu\mathrm{m}^{-1}$. We

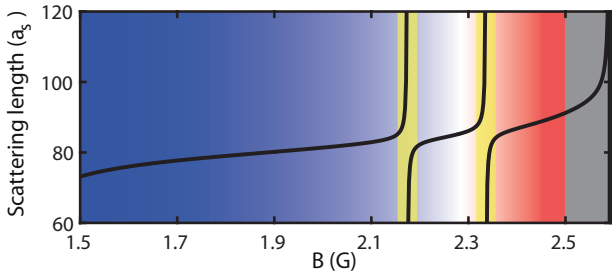

Extended Data Figure 1 | Estimated scattering length. Calculated B-to-a_s conversion for ^{164}Dy. Red and blue shaded areas indicate the SSP and the ID region, respectively. The grey area indicates the BEC region, while the yellow areas indicate regions around the two narrow Feshbach resonances located at 2.174 G and 2.336 G where we observe increased atom loss. We estimate $a_{s,SSP} = 88\,a_0$ in the SSP at 2.43 G and $a_{s,ID} = 77\,a_0$ in the ID at 1.65 G.

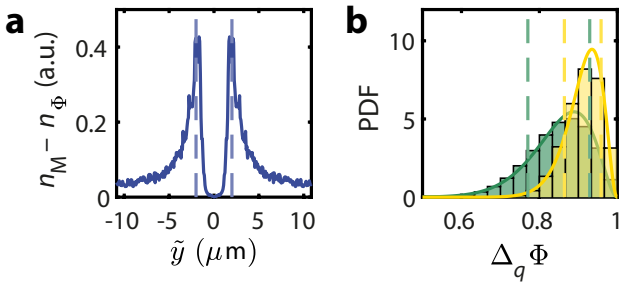

Extended Data Figure 2 | Wavelength of the modulation and finite-sampling effect. a, Difference between incoherent and coherent mean of the density profiles in the ID regime (1.65 G), peaking at the modulation wavelength $d \simeq \pm 2\,\mu$m (dashed lines). **b,** Histograms of 10^6 realisations (each) for calculations of $\Delta_q\Phi$ from uniformly random phases Φ_i, for $q = 35$ (green) and $q = 100$ (yellow) draws, respectively. The dashed vertical lines reflect the confidence interval enclosing 68.3 % ('one σ') of the calculated values. The solid lines reflect a Beta distribution with same mean and variance as the drawn distributions of $\Delta_q\Phi$ (no free fit parameters).

obtain a momentum density profile which we normalize by its sum. From such a momentum profile, a fast Fourier transformation (FFT) yields the 1D density profile $n_i(\tilde{y})$. An in-situ density modulation in an atomic cloud will lead to side peaks in $n_i(\tilde{y})$, symmetrically centred around the zero-momentum peak. To isolate the centre of this specific modulation, we calculate the incoherent and coherent means of $n_i(\tilde{y})$, which we denote $n_M(\tilde{y}) = \langle |n_i(\tilde{y})| \rangle_{\mathscr{P}}$ and $n_\Phi(\tilde{y}) = |\langle n_i(\tilde{y}) \rangle_{\mathscr{P}}|$, respectively. The incoherent mean n_M reflects the mean modulation amplitude of the cloud at the respective wavelength $\tilde{y}$. The coherent mean $n_\Phi \lesssim n_M$ if the phases of the interference pattern among the q repetitions at the respective $\tilde{y}$ are roughly constant, and $n_\Phi \to 0$ (and hence $n_\Phi \ll n_M$) if the phases are random. Therefore, the most pronounced difference $n_M - n_\Phi$ is observed for the ID regime (see Extended Data Fig. 2a). From the maximum of this difference we read off the modulation wavelength (or 'droplet distance') $\tilde{y} \equiv d$. The FFT phasors at d we call $P_i = n_i(d) = \rho_i \cdot e^{-i\cdot\Phi_i}$, yielding sets $\{P_1, \ldots, P_q\}_{\mathscr{P}}$. To characterise the distribution of phases Φ_i within our sets, we calculate the circular variance $\Delta\Phi = 1 - \frac{1}{q}\sqrt{\left(\sum_{i=1}^q \cos(\Phi_i)\right)^2 + \left(\sum_{i=1}^q \sin(\Phi_i)\right)^2}$ [37]. For a phase-coherent sample, and hence interference fringes stable within the envelope, $\Delta\Phi$ is small, whereas for an incoherent sample it approaches unity. To estimate the confidence intervals of our circular variance data we apply a bias-corrected accelerated bootstrapping scheme [32] for each $\mathscr{P}$, resampling 10^6 times from the respective q experimental values.

E. Effect of finite sample size

Even the circular variance $\Delta\Phi$ of a sample of q angles $\Phi_1, \ldots, \Phi_q$ drawn from a completely random distribution will approach unity only in the limit $q \to \infty$. To estimate the fully-incoherent limit of $\Delta\Phi$ for our finite q, we calculate 10^6 values for $\Delta_q\Phi$, each for q independent draws from a theoretical, uniform distribution in $[0, 2\pi)$. The histograms of $\Delta_q\Phi$ are shown in Extended Data Fig. 2b. The indicated one-σ confidence intervals are $[0.77, 0.93]$ for $q = 35$ and $[0.86, 0.96]$ for $q = 100$ draws. We note that the histograms of $\Delta_q\Phi$ follow a Beta distribution [51], even if one generalizes the underlying distribution of phases Φ_i to a von Mises distribution, of which the uniform distribution is just a degenerate case.

F. Interference pattern analysis and simple model of a droplet array

For simplicity let us consider here that the state is made of N_D identical droplets. In that case the total wavefunction of the system would be

$$\psi(x,y,z) = \sum_{j=1}^{N_D} f(x, y - R_j, z)\, e^{i\theta_j} \tag{1}$$

where R_j is the spatial coordinate of the jth droplet, θ_j is its phase, taken to be uniform over the droplet, and f is the wavefunction of a single droplet localized around $y = 0$. With such a wavefunction, the phasor extracted from one realization would be

$$P_i = \int dk_y \sum_{j_1, j_2 = 1}^{N_D} e^{ik_y(R_{j_1} - R_{j_2} - d)} e^{i(\theta_{j_1} - \theta_{j_2})} |\tilde{f}(k_y)|^2 \tag{2}$$

where $\tilde{f}$ is the Fourier transform of the function f and d is the distance between neighboring droplets $d = \langle R_{j+1} - R_j \rangle$. It simplifies in

$$P_i = \sum_{j_1, j_2 = 1}^{N_D} g(R_{j_1} - R_{j_2} - d)\, e^{i(\theta_{j_1} - \theta_{j_2})} \tag{3}$$

$$\approx g(0) \sum_j e^{i(\theta_{j+1} - \theta_j)} \tag{4}$$

with $g(y)$ the Fourier transform of $|\tilde{f}(k_y)|^2$, which is thus a peak function with a width of the order of the droplet size.

Formula (4) yields

$$A_{\mathrm{M}} = \langle |P_i| \rangle_{\mathscr{P}} \approx (N_{\mathrm{D}} - 1)\, g(0)\,, \tag{5}$$

which is essentially independent on the phase relation between the droplets and shows only a weak dependence on the droplets' shape. Here $\langle . \rangle_{\mathscr{P}}$ denote the average over an ensemble of realizations $\mathscr{P}$.

On the contrary the function $A_\Phi = |\langle P_i \rangle_{\mathscr{P}}|$ contains the average of the phases with

$$\frac{A_\Phi}{A_{\mathrm{M}}} = \frac{|\langle P_i \rangle_{\mathscr{P}}|}{\langle |P_i| \rangle_{\mathscr{P}}} \simeq |\langle \langle \mathrm{e}^{\mathrm{i}(\theta_{j+1} - \theta_j)} \rangle_j \rangle_{\mathscr{P}}|. \tag{6}$$

$\langle . \rangle_j$ denotes the average over the droplet array. The ratio A_Φ / A_{M} thus measures essentially the mean difference of phases between two neighboring droplets in the array. We also read from Eq. (4) that the phase of the phasor is $\Phi \approx \langle \theta_{j+1} - \theta_j \rangle_j$.

The circular variance $\Delta\Phi$ for q realizations can be expressed as

$$\Delta\Phi = 1 - \frac{1}{q} \sqrt{\sum_{i_1=1}^{q} \mathrm{e}^{\mathrm{i}\Phi_{i_1}} \sum_{i_2=1}^{q} \mathrm{e}^{-\mathrm{i}\Phi_{i_2}}} \tag{7}$$

For a totally phase coherent state, $\Phi = 0$ for all realizations leading to $\Delta\Phi = 0$ while for a totally phase incoherent sample only the diagonal terms in (7) survive, leading to $\Delta\Phi = 1 - \frac{1}{\sqrt{q}}$ for q independent measurements.

G. Modelization by a Josephson junction array

Let us modelize the system by a set of independent droplets, each one having a number of particles N_j (whose average will be denoted $\overline{N_j}$) and a phase θ_j. The Hamiltonian of such a system is

$$H = \sum_j \left[\frac{\left(N_j - \overline{N_j}\right)^2}{2C_j} - J_j \cos\left(\theta_{j+1} - \theta_j\right) \right] \tag{8}$$

The first term is the "charging" energy of the droplet (corresponding to its mean interaction energy) with the "capacitance" C_j while the second term describes the Josephson tunnelling of particles between droplets with the Josephson amplitude J_j. This is the well known JJA description [39]. Such a description is well adapted if the droplets are reasonably well separated in space, and thus should work adequately when the SSP is established. For simplicity we assume in the subsequent calculations that all parameters C_j and J_j are independent of the droplet and their values are later denoted C and J respectively. In addition, C is taken as constant.

H. Time evolution for the JJA model

To follow the experimental protocol, we used the equilibrium state of our Hamiltonian as initial state and looked at its evolution when we applied quenches to the Hamiltonian. We took a set of 4 droplets with, for simplicity, periodic boundary conditions. First, we quenched our initial state with a Hamiltonian having a J_{S} much smaller than the original J for a given time t_{S}. This corresponds to a decrease of the tunneling between droplets and therefore lets them evolve independently from each other. Then, we quenched our state again by letting it evolve a time t_{h} with the original Hamiltonian (J). This means that we reinstate the original tunneling between the droplets which is what happens in the experimental protocol.

We then looked at the correlation function $|\langle \psi(t)| \langle \mathrm{e}^{\mathrm{i}\theta_{j+1}} \mathrm{e}^{-\mathrm{i}\theta_j} \rangle_j |\psi(t)\rangle|$ which corresponds to A_Φ / A_{M}.

Given the perfect coherence that exists in the JJA model described above, this correlation function would show undamped oscillations corresponding to the time periodic nature of a system with a finite number of frequencies. In order to make the plateaus apparent in the correlation function we have damped these oscillations by an artificial damping term $\mathrm{e}^{-\omega_k t}$ for the mode with a frequency ω_k. The choice of such damping rather than the usual constant exponential one, is to get rid efficiently of the high frequency oscillations without having to recourse to the coupling to a bath for example. It is clear that a more precise and microscopically correct way of including the damping should be considered, but as discussed in the main text, what mechanism leads to damping is a whole question in itself in this system.

From time 0 to t_{s}, this correlation function shows the decrease in A_Φ / A_{M} and corresponds qualitatively to the phase scrambling as can be seen in Extended Data Figure 3a. The first minimum in the figure and the corresponding time scale would correspond to the dephasing discussed in the main text. In total absence of residual coupling between the droplets one would have lost completely the phase coherence on this timescale. Because we have put a small but finite coupling J_{S} remaining between the droplets one can also see at later times a partial recovery of the phase coherence whose value is of course controlled by the value of J_{S}.

Furthermore, if looked up to time t_{h}, this correlation function shows the increase in A_Φ / A_{M} and therefore corresponds to the rephasing of the system as shown in Extended Data Figure 3b. In the calculation, the correlation does not go back to a value of 1, which means that the rephasing is not perfect, in contrast with the experiment. This happens since this simplified model has no energy dissipation mechanism. The initial state not being an eigenstate of the final Hamiltonian thus leads to a final state which is a thermal-like state (with possibly more complicated distributions than a simple thermal one), where the extra energy has been converted to a distribution over the eigenstates. An energy dissipation mechanism, for example via the normal part of the fluid, will thus be necessary to converge back to the initial state. Such extra effects can be potentially incorporated in subsequent studies.

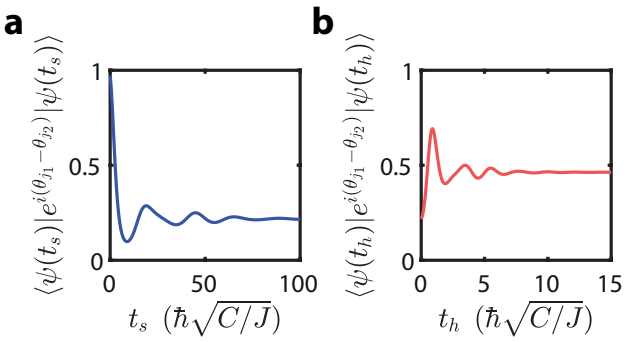

Extended Data Figure 3 | Theoretical predictions for the JJA model with parameters $J = 100$, $J_S = 1$, $C = 1$, $\hbar = 1$ and j_1, j_2 are neighbours. **a,** Evolution of the correlation when the droplets evolve independently from each other as a function of scrambling time t_S. **b,** Evolution of the correlation when the droplets are re-coupled to each other as a function of t_h with $t_S = 1000$ $[\hbar\sqrt{C/J}]$.

[44] Ronen, S., Bortolotti, D. C. E. & Bohn, J. L. Bogoliubov modes of a dipolar condensate in a cylindrical trap. *Phys. Rev. A* **74**, 013623 (2006). URL https://doi.org/10.1103/PhysRevA.74.013623.

[45] Wächtler , F. & Santos, L. Ground-state properties and elementary excitations of quantum droplets in dipolar Bose-Einstein condensates. *Phys. Rev. A* **94**, 043618 (2016). URL https://doi.org/10.1103/PhysRevA.94.043618.

[46] Ilzhöfer, P. *et al.* Two-species five-beam magneto-optical trap for erbium and dysprosium. *Phys. Rev. A* **97**, 023633 (2018). URL https://doi.org/10.1103/PhysRevA.97.023633.

[47] Trautmann, A. *et al.* Dipolar Quantum Mixtures of Erbium and Dysprosium Atoms. *Phys. Rev. Lett.* **121**, 213601 (2018). URL https://doi.org/10.1103/PhysRevLett.121.213601.

[48] Chin, C., Grimm, R., Julienne, P. S. & Tiesinga, E. Feshbach resonances in ultracold gases. *Rev. Mod. Phys.* **82**, 1225–1286 (2010). URL https://doi.org/10.1103/RevModPhys.82.1225.

[49] Ferrier-Barbut, I. *et al.* Scissors Mode of Dipolar Quantum Droplets of Dysprosium Atoms. *Phys. Rev. Lett.* **120**, 160402 (2018). URL https://doi.org/10.1103/PhysRevLett.120.160402.

[50] Maier, T. *et al.* Broad universal Feshbach resonances in the chaotic spectrum of dysprosium atoms. *Phys. Rev. A* **92**, 060702 (2015). URL https://doi.org/10.1103/PhysRevA.92.060702.

[51] Evans, M., Hastings, N. & Peacock, B. Beta distribution. In *Statistical Distributions*, chap. 5, 34–42 (Wiley, New York, 2000), 3 edn. URL https://doi.org/10.1002/9780470627242.

Appendix

B Extensive Feshbach scans

The following appendix collects the extensive Feshbach spectroscopy required for Ref. [Dur20]. These exploratory surveys were performed with a resolution of 200 mG in order to identify possible FRs of width greater than ∼1 G. All the experimental conditions are kept constant beside the laser locking parameters necessary to change the isotopic combination. Our investigation covered the following mixtures:

- ^{166}Er-^{164}Dy in Fig. B.1,
- ^{168}Er-^{164}Dy in Fig. B.2,
- ^{170}Er-^{164}Dy in Fig. B.3,
- ^{166}Er-^{161}Dy in Fig. B.4,
- ^{167}Er-^{161}Dy in Fig. B.5,
- ^{168}Er-^{161}Dy in Fig. B.6,
- ^{170}Er-^{161}Dy in Fig. B.7.

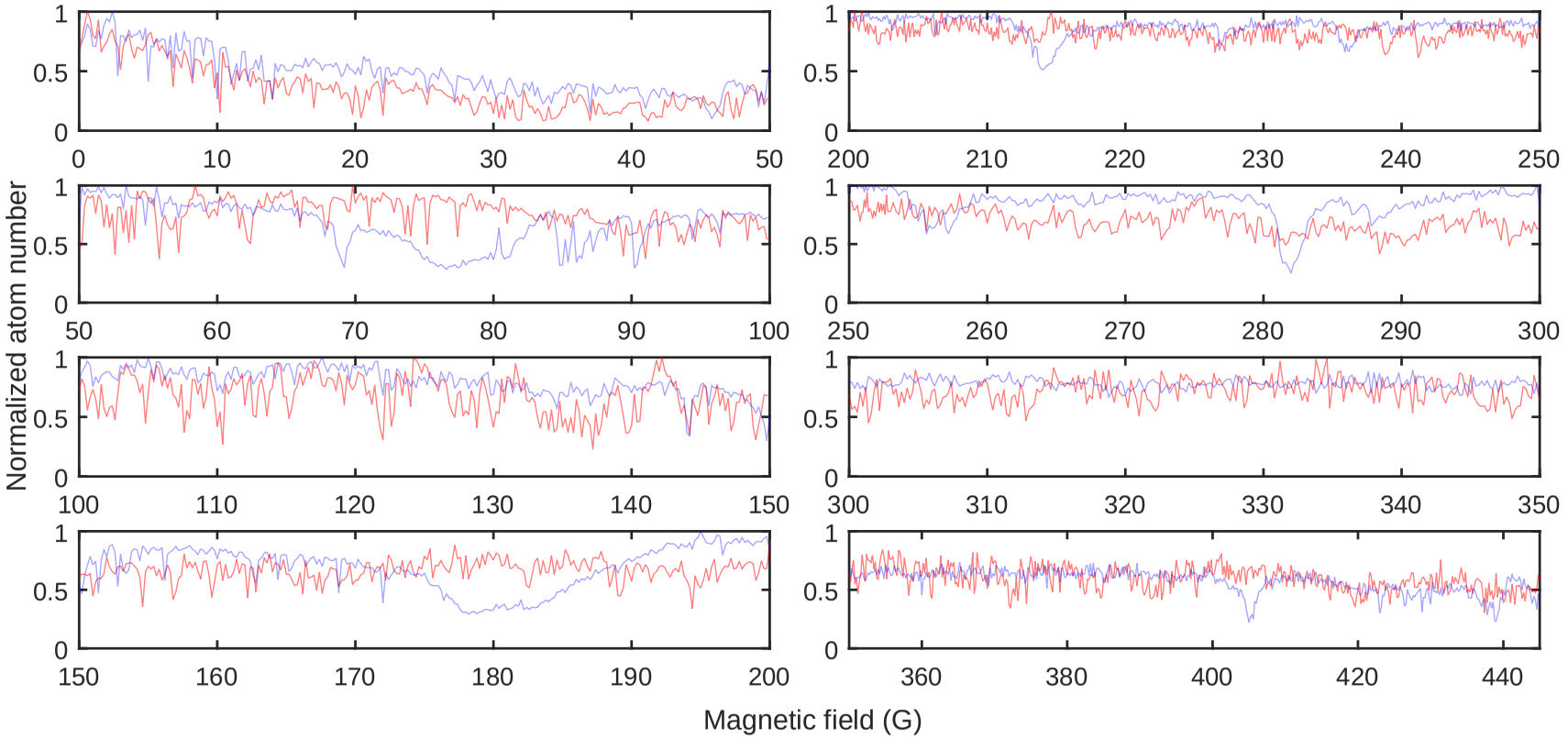

Figure B.1: Exploratory trap-loss spectroscopy in the mixture ^{166}Er-^{164}Dy (red and blue curves respectively) performed with a stepsize of 200 mG. For the ease of reading, the atom numbers are normalized to the maximum of each panel. Each point consists of an average over two to four experimental repetitions.

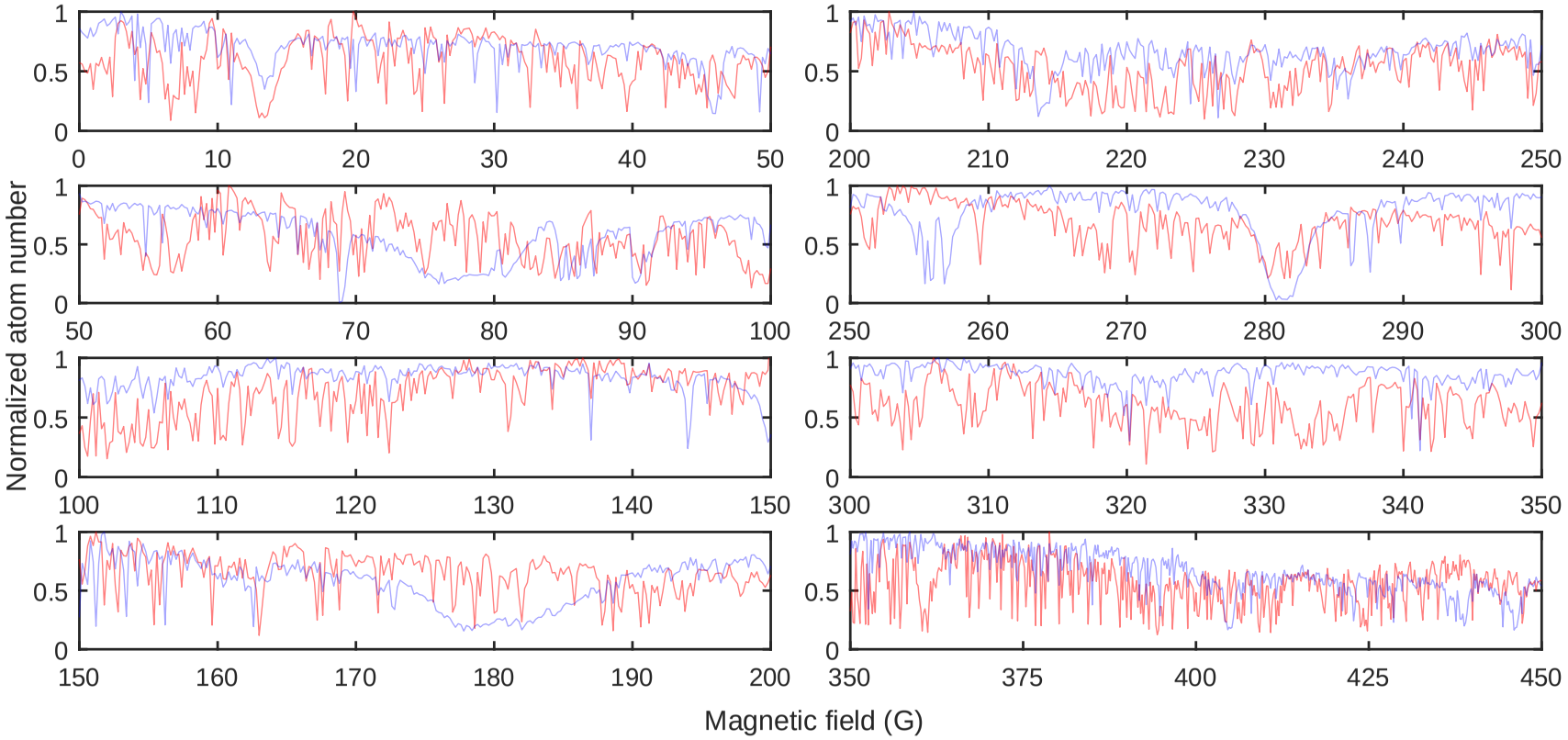

Figure B.2: Exploratory trap-loss spectroscopy in the mixture ^{168}Er-^{164}Dy (red and blue curves respectively) performed with a stepsize of 200 mG. For the ease of reading, the atom numbers are normalized to the maximum of each panel. Each point consists of an average over two to four experimental repetitions.

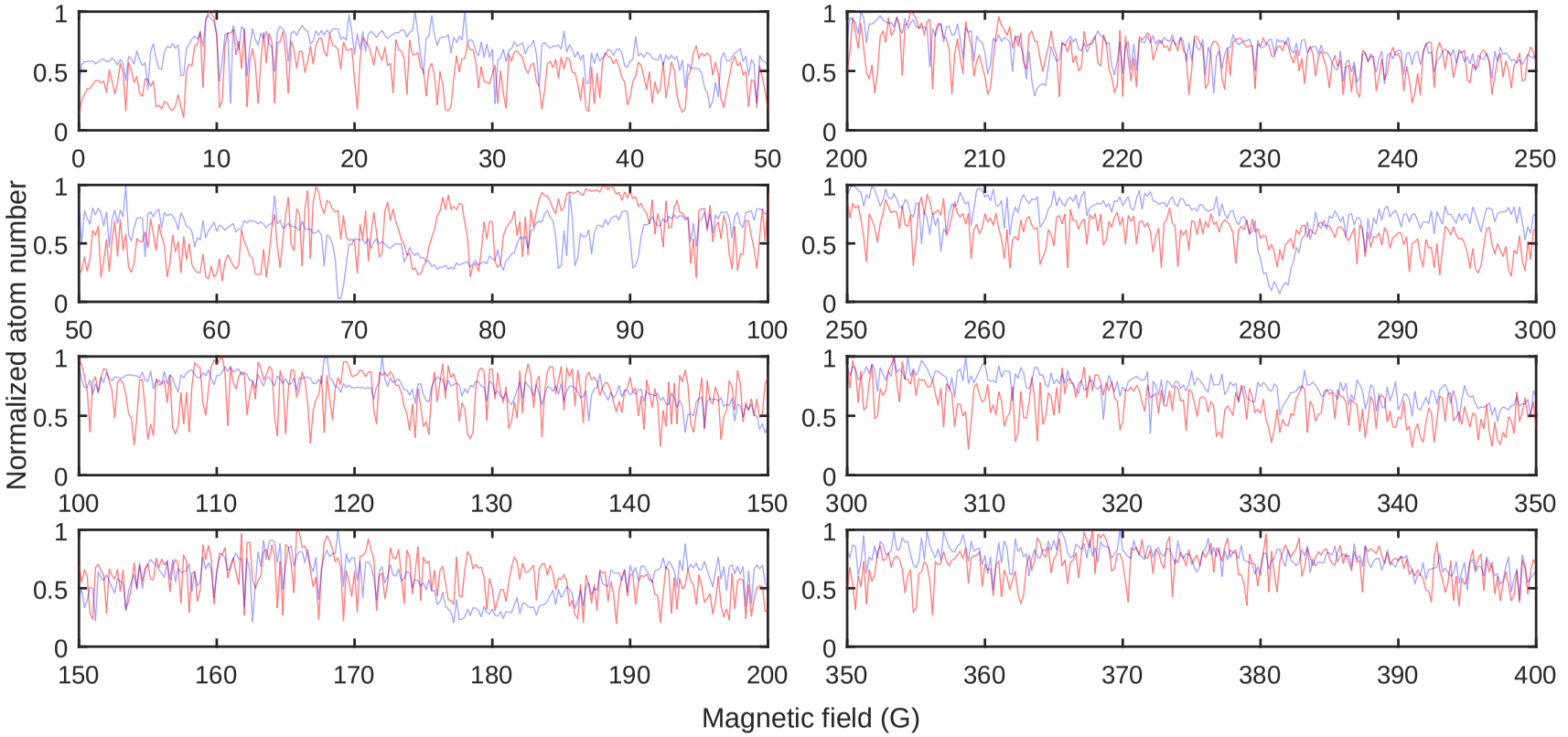

Figure B.3: Exploratory trap-loss spectroscopy in the mixture ^{170}Er-^{164}Dy (red and blue curves respectively) performed with a stepsize of 200 mG. For the ease of reading, the atom numbers are normalized to the maximum of each panel. Each point consists of an average over two to four experimental repetitions.

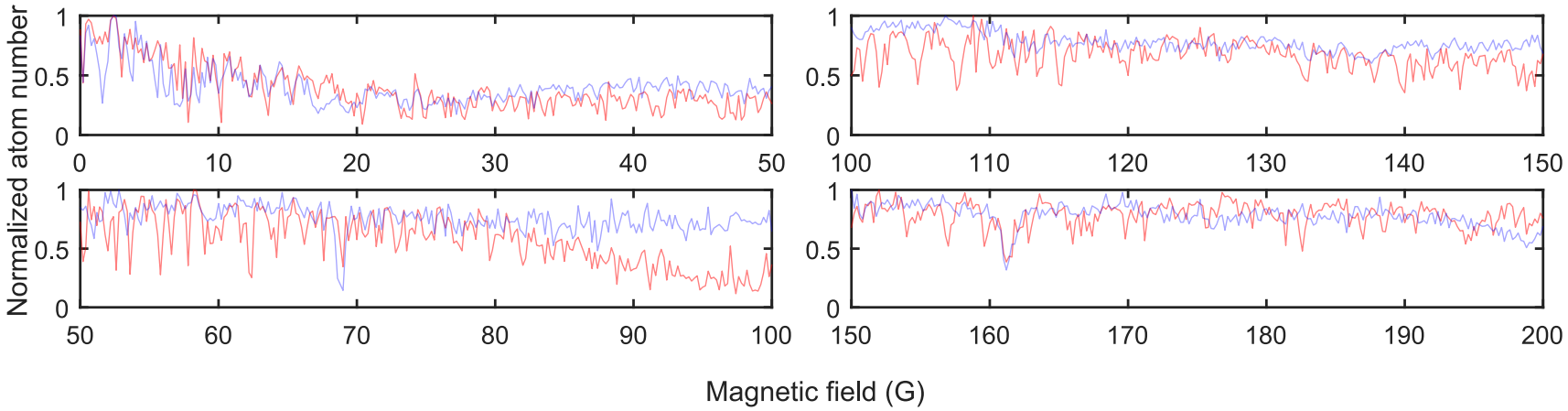

Figure B.4: Exploratory trap-loss spectroscopy in the mixture ^{166}Er-^{161}Dy (red and blue curves respectively) performed with a stepsize of 200 mG. For the ease of reading, the atom numbers are normalized to the maximum of each panel. Each point consists of an average over two to four experimental repetitions.

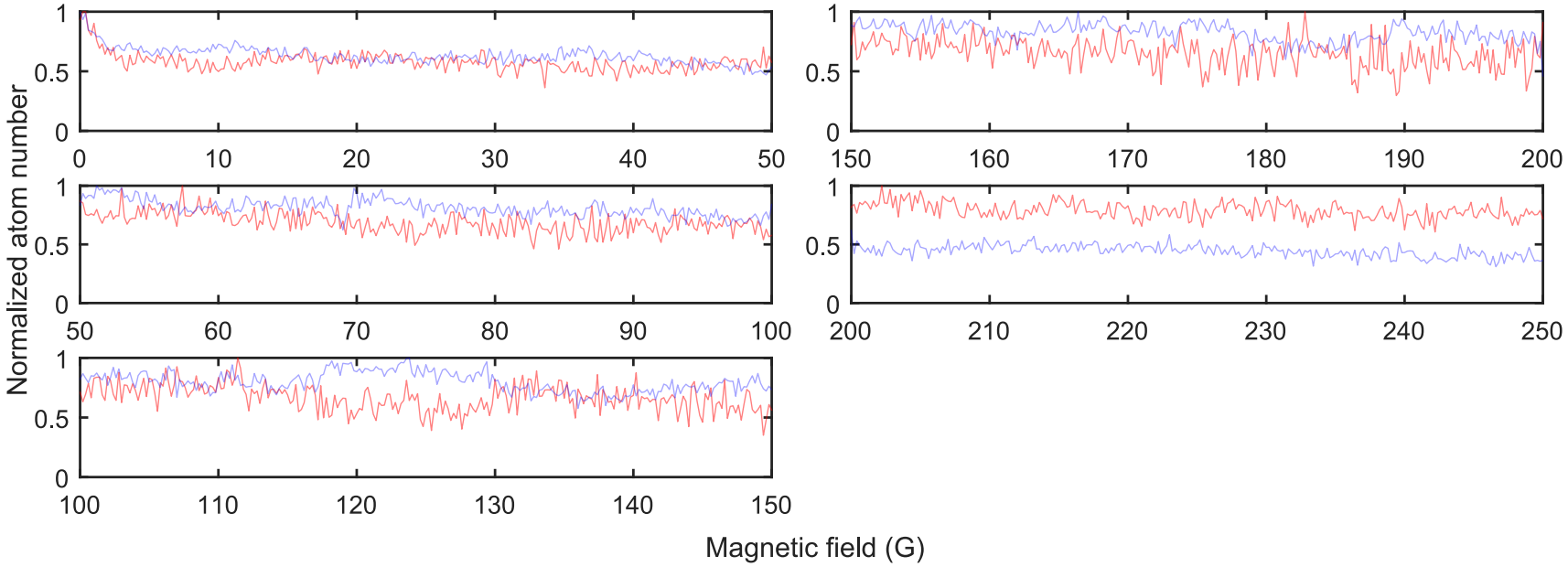

Figure B.5: Exploratory trap-loss spectroscopy in the mixture ^{167}Er-^{161}Dy (red and blue curves respectively) performed with a stepsize of 200 mG. For the ease of reading, the atom numbers are normalized to the maximum of each panel. Each point consists of an average over two to four experimental repetitions.

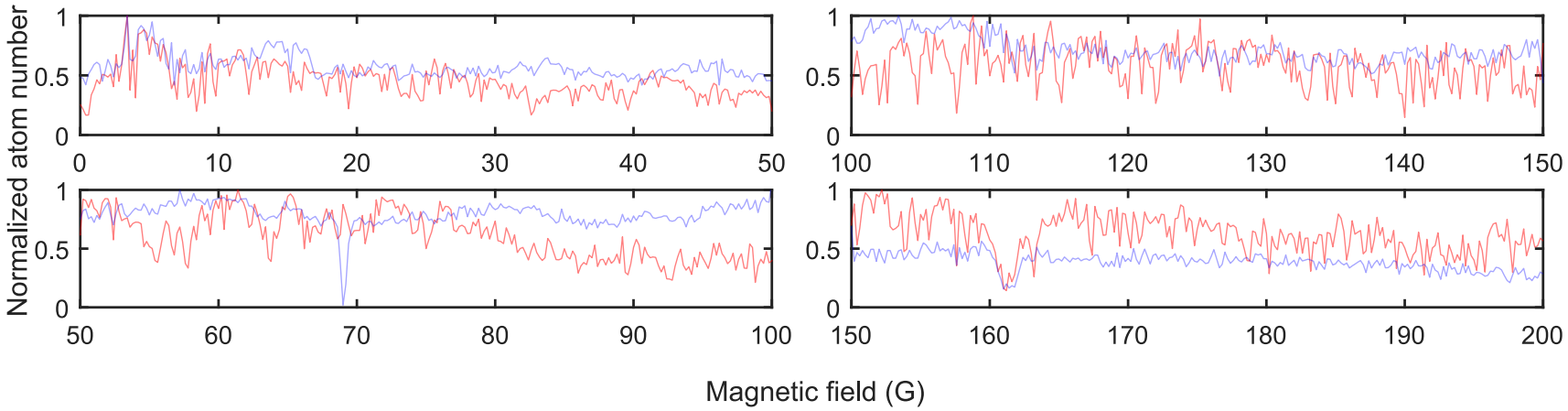

Figure B.6: Exploratory trap-loss spectroscopy in the mixture ^{168}Er-^{161}Dy (red and blue curves respectively) performed with a stepsize of 200 mG. For the ease of reading, the atom numbers are normalized to the maximum of each panel. Each point consists of an average over two to four experimental repetitions.

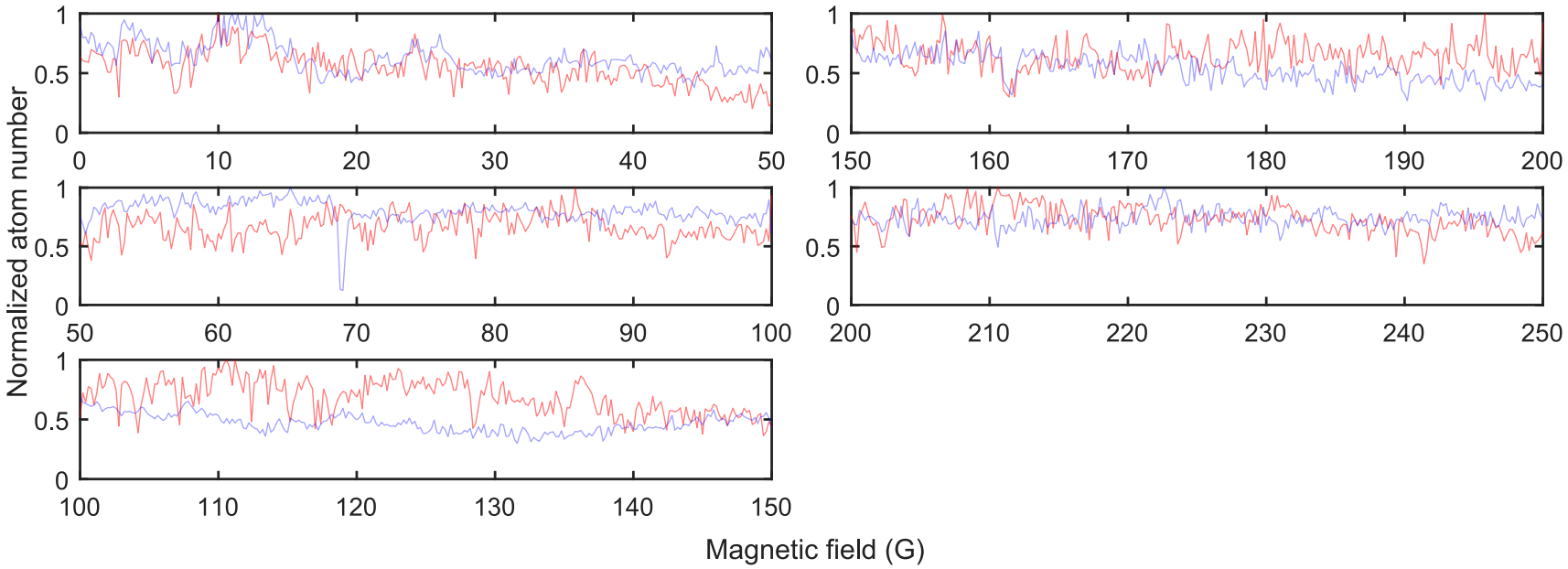

Figure B.7: Exploratory trap-loss spectroscopy in the mixture ^{170}Er-^{161}Dy (red and blue curves respectively) performed with a stepsize of 200 mG. For the ease of reading, the atom numbers are normalized to the maximum of each panel. Each point consists of an average over two to four experimental repetitions.

Appendix

C

Coil systems' cooling

In this appendix, additional information on the actual performance of the coils' water cooling system are reported together with a comparison to the simulated ones. Specifically, Fig. C.1 and Fig. C.2 summarize details about the large-field and the small-field coils respectively. The simulations are performed in SolidWorks© on the 3D-model and they assume perfect contact between the copper of the coils and the cooling surface. This simple model does not take in consideration either small gaps filled with thermal conductive glue or the isolation layer of the wire itself. The large-field coil is approximated with a solid copper block, heated by a homogeneous power density equivalent to the total power dissipated at the steady-state current of 100 A. Instead, for the small-field coils, the heating is modeled with an equivalent power density at the steady-state current of 10 A acting at the lower part of the copper cylinder.

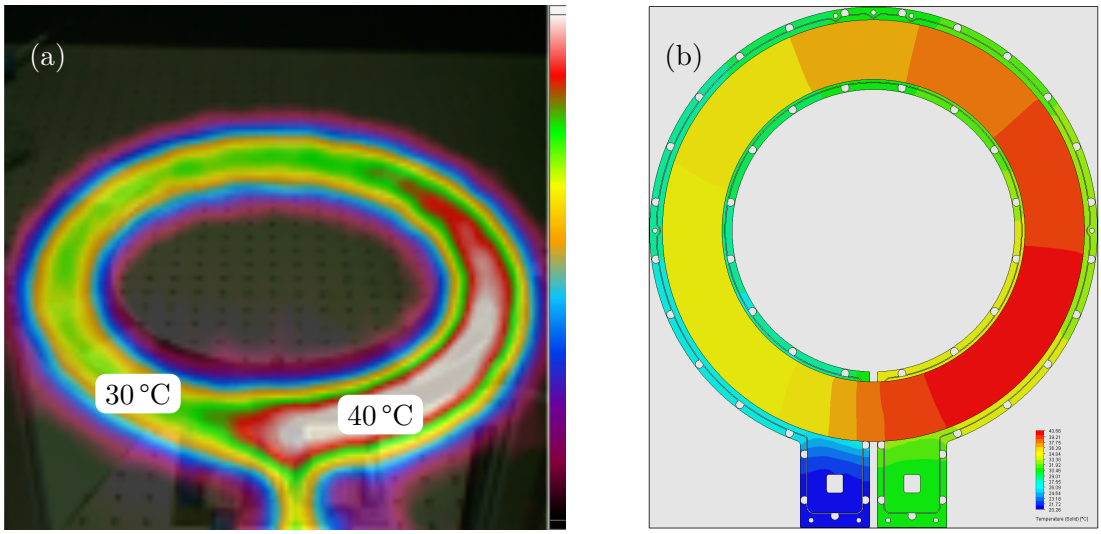

Figure C.1: Steady-state temperature for one of the large-bias/gradient coils at 100 A of constant operating current. The water runs clockwise from the inlet on the bottom-left of the figure to the outlet on the bottom right. (a) Temperature measured with an infrared thermal camera after a waiting time of a few minutes to ensure steady-state conditions. With ∼1.5 l/min of running water at about 23 °C, the coil temperature rises up to 30 °C at the inlet and 40 °C at the outlet of the water circuit. (b) Top view of the coil showing the simulated temperature with 1 l/min of running water at 20 °C. The increase in temperature of ∼11 °C at the warmest spot is consistent with the measured value.

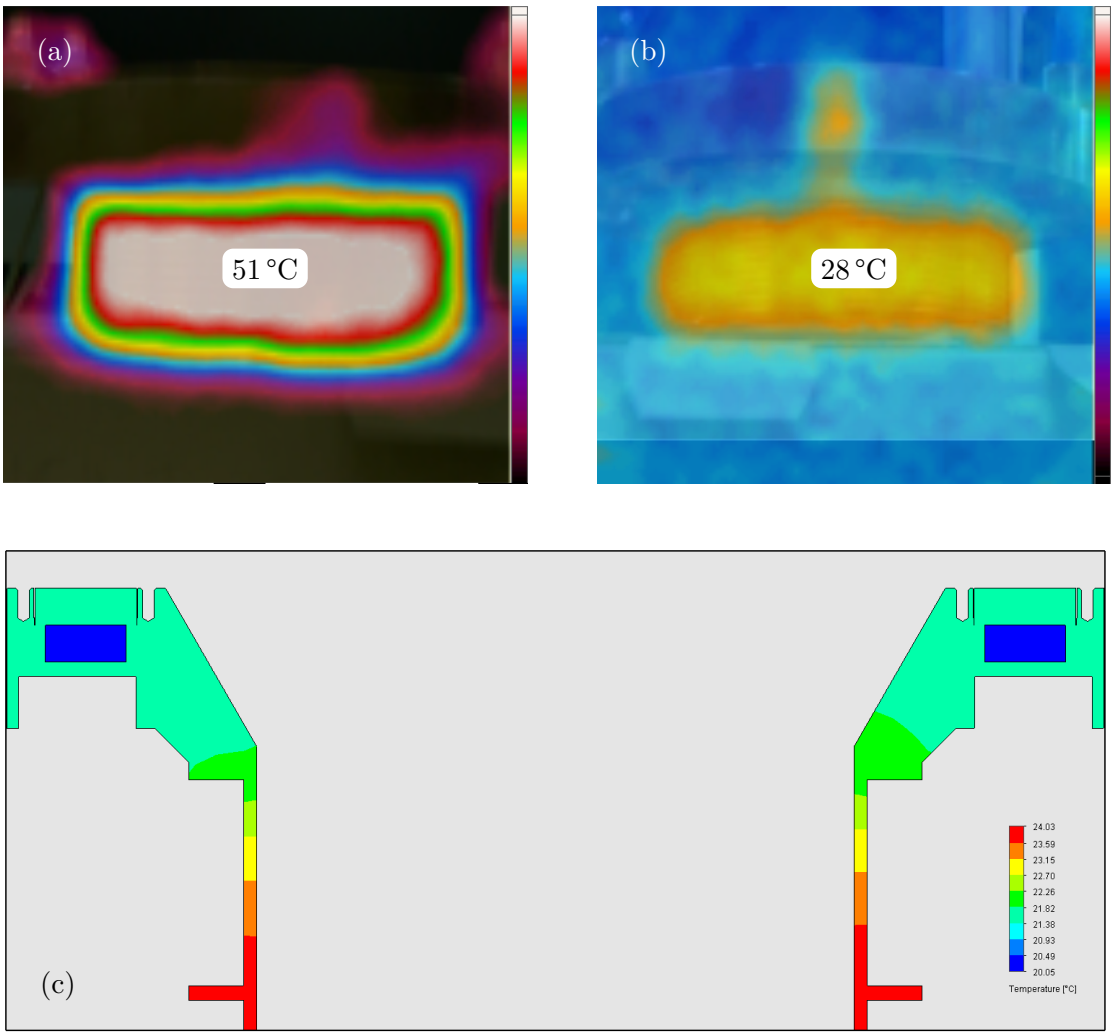

Figure C.2: Steady-state temperature of the inverted viewport coil module at 10 A of operating current. The measurement has been performed with an infrared thermal camera after a waiting time of a few minutes to ensure stable conditions. (a) Deactivating the water cooling, the coils temperature rises to about 50 °C. (b) With ∼1 l/min of running water at about 23 °C, the coils temperature rises up to 28 °C. (c) Sectional view of the copper mounting system showing the simulated temperature with 1 l/min of running water at 20 °C. The increase in the temperature of 4 °C is consistent with the measured value.

Bibliography

[Acv18] L. D. Augustovičová and J. L. Bohn, *Manifestation of quantum chaos in Fano-Feshbach resonances*, Phys. Rev. A **98**, 023419 (2018).

[Aik12] K. Aikawa, A. Frisch, M. Mark, S. Baier, A. Rietzler, R. Grimm, and F. Ferlaino, *Bose-Einstein condensation of erbium*, Phys. Rev. Lett. **108**, 210401 (2012).

[Aik14a] K. Aikawa, S. Baier, A. Frisch, M. Mark, C. Ravensbergen, and F. Ferlaino, *Observation of Fermi surface deformation in a dipolar quantum gas*, Science **345**, 1484–1487 (2014).

[Aik14b] K. Aikawa, A. Frisch, M. Mark, S. Baier, R. Grimm, and F. Ferlaino, *Reaching Fermi degeneracy via universal dipolar scattering*, Phys. Rev. Lett. **112**, 010404 (2014).

[And95] M. H. Anderson, J. R. Ensher, M. R. Matthews, C. E. Wieman, and E. A. Cornell, *Observation of Bose-Einstein condensation in a dilute atomic vapor*, Science **269**, 198–201 (1995).

[And05] M. Anderlini, E. Courtade, M. Cristiani, D. Cossart, D. Ciampini, C. Sias, O. Morsch, and E. Arimondo, *Sympathetic cooling and collisional properties of a* Rb-Cs *mixture*, Phys. Rev. A **71**, 061401 (2005).

[BÏ9] F. Böttcher, J.-N. Schmidt, M. Wenzel, J. Hertkorn, M. Guo, T. Langen, and T. Pfau, *Transient Supersolid Properties in an Array of Dipolar Quantum Droplets*, Phys. Rev. X **9**, 011051 (2019).

[Bai16] S. Baier, M. J. Mark, D. Petter, K. Aikawa, L. Chomaz, Z. Cai, M. Baranov, P. Zoller, and F. Ferlaino, *Extended Bose-Hubbard models with ultracold magnetic atoms*, Science **352**, 201–205 (2016).

[Bai18a] S. Baier, D. Petter, J. H. Becher, A. Patscheider, G. Natale, L. Chomaz, M. J. Mark, and F. Ferlaino, *Realization of a strongly interacting Fermi gas of dipolar atoms*, Phys. Rev. Lett. **121**, 093602 (2018).

[Bai18b] S. Baier, *Ultracold dipolar erbium atoms: From scattering phenomena to quantum simulations*, Ph.D. thesis, Faculty of Mathematics, Computer Science and Physics of the University of Innsbruck (2018).

[Bar18] V. Barbé, A. Ciamei, B. Pasquiou, L. Reichsöllner, F. Schreck, P. S. Żuchowski, and J. M. Hutson, *Observation of Feshbach resonances between alkali and closed-shell atoms*, Nature Physics **14**, 881–884 (2018).

[Bau14] K. Baumann, N. Q. Burdick, M. Lu, and B. L. Lev, *Observation of low-field Fano-Feshbach resonances in ultracold gases of dysprosium*, Phys. Rev. A **89**, 020701 (2014).

[Bec18] J. H. Becher, S. Baier, K. Aikawa, M. Lepers, J.-F. Wyart, O. Dulieu, and F. Ferlaino, *Anisotropic polarizability of erbium atoms*, Phys. Rev. A **97**, 012509 (2018).

[Beu35] H. Beutler, *Über absorptionsserien von argon, krypton und xenon zu termen zwischen den beiden ionisierungsgrenzen* $^2P^0_{3/2}$ *und* $^2P^0_{1/2}$, Zeitschrift für Physik **93**, 177–196 (1935).

[Bla11] S. Blatt, T. L. Nicholson, B. J. Bloom, J. R. Williams, J. W. Thomsen, P. S. Julienne, and J. Ye, *Measurement of optical Feshbach resonances in an ideal gas*, Phys. Rev. Lett. **107**, 073202 (2011).

[Blo05] I. Bloch, *Ultracold quantum gases in optical lattices*, Nature Physics **1**, 23–30 (2005).

[Blo08] I. Bloch, J. Dalibard, and W. Zwerger, *Many-body physics with ultracold gases*, Rev. Mod. Phys. **80**, 885–964 (2008).

[Blo12] I. Bloch, J. Dalibard, and S. Nascimbène, *Quantum simulations with ultracold quantum gases*, Nature Physics **8**, 267–276 (2012).

[Blu12] D. Blume, *Few-body physics with ultracold atomic and molecular systems in traps*, Reports on Progress in Physics **75**, 046401 (2012).

[Boh17] J. L. Bohn, A. M. Rey, and J. Ye, *Cold molecules: Progress in quantum engineering of chemistry and quantum matter*, Science **357**, 1002–1010 (2017).

[Bos24] S. N. Bose, *Plancks gesetz und lichtquantenhypothese*, Zeitschrift für Physik **26**, 178–181 (1924).

[Bra95] C. C. Bradley, C. A. Sackett, J. J. Tollett, and R. G. Hulet, *Evidence of Bose-Einstein condensation in an atomic gas with attractive interactions*, Phys. Rev. Lett. **75**, 1687–1690 (1995).

[Bra06] E. Braaten and H.-W. Hammer, *Universality in few-body systems with large scattering length*, Physics Reports **428**, 259 – 390 (2006).

[Bry77] H. C. Bryant, B. D. Dieterle, J. Donahue, H. Sharifian, H. Tootoonchi, D. M. Wolfe, P. A. M. Gram, and M. A. Yates-Williams, *Observation of resonances near 11 eV in the photodetachment cross section of the* H^- *ion*, Phys. Rev. Lett. **38**, 228–230 (1977).

[Bur98] J. P. Burke, J. L. Bohn, B. D. Esry, and C. H. Greene, *Prospects for mixed-isotope Bose-Einstein condensates in rubidium*, Phys. Rev. Lett. **80**, 2097–2100 (1998).

[Cap19] G. Cappellini, L. F. Livi, L. Franchi, D. Tusi, D. Benedicto Orenes, M. Inguscio, J. Catani, and L. Fallani, *Coherent manipulation of orbital feshbach molecules of two-electron atoms*, Phys. Rev. X **9**, 011028 (2019).

[Car09] L. D. Carr, D. DeMille, R. V. Krems, and J. Ye, *Cold and ultracold molecules: science, technology and applications*, New Journal of Physics **11**, 055049 (2009).

[Chi10] C. Chin, R. Grimm, P. S. Julienne, and E. Tiesinga, *Feshbach resonances in ultracold gases*, Rev. Mod. Phys. **82**, 1225–1286 (2010).

[Chi15] C. Chin, *Ultracold atomic gases going strong*, National Science Review **3**, 168–170 (2015).

[Cho16] L. Chomaz, S. Baier, D. Petter, M. J. Mark, F. Wächtler, L. Santos, and F. Ferlaino, *Quantum-fluctuation-driven crossover from a dilute Bose-Einstein condensate to a macrodroplet in a dipolar quantum fluid*, Phys. Rev. X **6**, 041039 (2016).

[Cho18] L. Chomaz, R. M. W. van Bijnen, D. Petter, G. Faraoni, S. Baier, J.-H. Becher, M. J. Mark, F. Wächtler, L. Santos, and F. Ferlaino, *Observation of roton mode population in a dipolar quantum gas*, Nat. Phys. **14**, 442 (2018).

[Cho19] L. Chomaz, D. Petter, P. Ilzhöfer, G. Natale, A. Trautmann, C. Politi, G. Durastante, R. M. W. van Bijnen, A. Patscheider, M. Sohmen, M. J. Mark, and F. Ferlaino, *Long-lived and transient supersolid behaviors in dipolar quantum gases*, Phys. Rev. X **9**, 021012 (2019).

[Cor02] E. A. Cornell and C. E. Wieman, *Nobel lecture: Bose-Einstein condensation in a dilute gas, the first 70 years and some recent experiments*, Rev. Mod. Phys. **74**, 875–893 (2002).

[Cou98] P. Courteille, R. S. Freeland, D. J. Heinzen, F. A. van Abeelen, and B. J. Verhaar, *Observation of a Feshbach resonance in cold atom scattering*, Phys. Rev. Lett. **81**, 69–72 (1998).

[Dav95] K. B. Davis, M. O. Mewes, M. R. Andrews, N. J. van Druten, D. S. Durfee, D. M. Kurn, and W. Ketterle, *Bose-Einstein condensation in a gas of sodium atoms*, Phys. Rev. Lett. **75**, 3969–3973 (1995).

[Dav20] E. T. Davletov, V. V. Tsyganok, V. A. Khlebnikov, D. A. Pershin, D. V. Shaykin, and A. V. Akimov, *Machine learning for achieving Bose-Einstein condensation of thulium atoms*, Phys. Rev. A **102**, 011302 (2020).

[dE09] Y. N. M. de Escobar, P. G. Mickelson, M. Yan, B. J. DeSalvo, S. B. Nagel, and T. C. Killian, *Bose-Einstein condensation of* ^{84}Sr, Phys. Rev. Lett. **103**, 200402 (2009).

[Deh08] B. Deh, C. Marzok, C. Zimmermann, and P. W. Courteille, *Feshbach resonances in mixtures of ultracold* ^{6}Li *and* ^{87}Rb *gases*, Phys. Rev. A **77**, 010701 (2008).

[DeM99] B. DeMarco and D. S. Jin, *Onset of Fermi degeneracy in a trapped atomic gas*, Science **285**, 1703–1706 (1999).

[DeS10] B. J. DeSalvo, M. Yan, P. G. Mickelson, Y. N. Martinez de Escobar, and T. C. Killian, *Degenerate Fermi gas of* ^{87}Sr, Phys. Rev. Lett. **105**, 030402 (2010).

[DeS17] B. J. DeSalvo, K. Patel, J. Johansen, and C. Chin, *Observation of a degenerate Fermi gas trapped by a Bose-Einstein condensate*, Phys. Rev. Lett. **119**, 233401 (2017).

[DM19] L. De Marco, G. Valtolina, K. Matsuda, W. G. Tobias, J. P. Covey, and J. Ye, *A degenerate Fermi gas of polar molecules*, Science **363**, 853–856 (2019).

[Dur20] G. Durastante, C. Politi, M. Sohmen, P. Ilzhöfer, M. J. Mark, M. A. Norcia, and F. Ferlaino, *Feshbach resonances in an erbium-dysprosium dipolar mixture*, arXiv:2006.06456 (2020).

[Ein24] A. Einstein, *Quantentheorie des einatomigen idealen gases*, Sitzungsber. Preuss. Akad. Wiss., Phys. Math. Kl. (1924).

[Ein25] A. Einstein, *Quantentheorie des einatomigen idealen gases. zweite abhandlung*, Sitzungsber. Preuss. Akad. Wiss., Phys. Math. Kl. (1925).

[End11] S. Endo, P. Naidon, and M. Ueda, *Universal physics of 2+1 particles with non-zero angular momentum*, Few-Body Systems **51**, 207–217 (2011).

[Eno08] K. Enomoto, K. Kasa, M. Kitagawa, and Y. Takahashi, *Optical Feshbach resonance using the intercombination transition*, Phys. Rev. Lett. **101**, 203201 (2008).

[Fan35] U. Fano, *Sullo spettro di assorbimento dei gas nobili presso il limite dello spettro d'arco*, Il Nuovo Cimento (1924-1942) **12**, 154–161 (1935).

[Fan61] U. Fano, *Effects of configuration interaction on intensities and phase shifts*, Phys. Rev. **124**, 1866–1878 (1961).

[FB16] I. Ferrier-Barbut, H. Kadau, M. Schmitt, M. Wenzel, and T. Pfau, *Observation of Quantum Droplets in a Strongly Dipolar Bose Gas*, Phys. Rev. Lett. **116**, 215301 (2016).

[FB18] I. Ferrier-Barbut, M. Wenzel, F. Böttcher, T. Langen, M. Isoard, S. Stringari, and T. Pfau, *Scissors mode of dipolar quantum droplets of dysprosium atoms*, Phys. Rev. Lett. **120**, 160402 (2018).

[Fer06] F. Ferlaino, C. D'Errico, G. Roati, M. Zaccanti, M. Inguscio, G. Modugno, and A. Simoni, *Feshbach spectroscopy of a* K-Rb *atomic mixture*, Phys. Rev. A **73**, 040702 (2006).

[Fes58] H. Feshbach, *Unified theory of nuclear reactions*, Annals of Physics **5**, 357 – 390 (1958).

[Fes62] H. Feshbach, *A unified theory of nuclear reactions. II*, Annals of Physics **19**, 287 – 313 (1962).

[Fey82] R. P. Feynman, *Simulating physics with computers*, International Journal of Theoretical Physics **21**, 467–488 (1982).

[Foo05] C. Foot, *Atomic physics*, Oxford master series in physics, Oxford University Press,

2005.

[Fri98] D. G. Fried, T. C. Killian, L. Willmann, D. Landhuis, S. C. Moss, D. Kleppner, and T. J. Greytak, *Bose-Einstein condensation of atomic hydrogen*, Phys. Rev. Lett. **81**, 3811–3814 (1998).

[Fri12] A. Frisch, K. Aikawa, M. Mark, A. Rietzler, J. Schindler, E. Zupanič, R. Grimm, and F. Ferlaino, *Narrow-line magneto-optical trap for erbium*, Phys. Rev. A **85**, 051401 (2012).

[Fri14] A. Frisch, M. Mark, K. Aikawa, F. Ferlaino, J. L. Bohn, C. Makrides, A. Petrov, and S. Kotochigova, *Quantum chaos in ultracold collisions of gas-phase erbium atoms*, Nature **507**, 475–479 (2014).

[Fri15] A. Frisch, M. Mark, K. Aikawa, S. Baier, R. Grimm, A. Petrov, S. Kotochigova, G. Quéméner, M. Lepers, O. Dulieu, and F. Ferlaino, *Ultracold dipolar molecules composed of strongly magnetic atoms*, Phys. Rev. Lett. **115**, 203201 (2015).

[Fry19] M. D. Frye, S. L. Cornish, and J. M. Hutson, *Prospects of forming high-spin polar molecules from ultracold atoms*, arXiv:1910.09641 (2019).

[Fuk07] T. Fukuhara, Y. Takasu, M. Kumakura, and Y. Takahashi, *Degenerate Fermi gases of ytterbium*, Phys. Rev. Lett. **98**, 030401 (2007).

[Gac10] G. Gligorić, A. Maluckov, M. Stepić, L. Hadžievski, and B. A. Malomed, *Transition to miscibility in linearly coupled binary dipolar Bose-Einstein condensates*, Phys. Rev. A **82**, 033624 (2010).

[Gad16] B. Gadway and B. Yan, *Strongly interacting ultracold polar molecules*, Journal of Physics B: Atomic, Molecular and Optical Physics **49**, 152002 (2016).

[Gar14] C. Gardiner and P. Zoller, *The quantum world of ultra-cold atoms and light*, Imperial College Press, 57 Shelton Street, Covent Garden, London, 2014.

[GM15] M. L. González-Martínez and P. S. Żuchowski, *Magnetically tunable Feshbach resonances in Li+Er*, Phys. Rev. A **92**, 022708 (2015).

[Gre16] D. G. Green, C. L. Vaillant, M. D. Frye, M. Morita, and J. M. Hutson, *Quantum chaos in ultracold collisions between Yb($^1S_0$) and Yb($^3P_2$)*, Phys. Rev. A **93**, 022703 (2016).

[Gre20] A. Green, H. Li, J. H. See Toh, X. Tang, K. C. McCormick, M. Li, E. Tiesinga, S. Kotochigova, and S. Gupta, *Feshbach resonances in p-wave three-body recombination within Fermi-Fermi mixtures of open-shell ^{6}Li and closed-shell ^{173}Yb atoms*, Phys. Rev. X **10**, 031037 (2020).

[Gri00] R. Grimm, M. Weidemüller, and Y. B. Ovchinnikov, *Optical dipole traps for neutral atoms*, Advances In Atomic, Molecular, and Optical Physics **42**, 95 – 170 (2000).

[Gri05] A. Griesmaier, J. Werner, S. Hensler, J. Stuhler, and T. Pfau, *Bose-Einstein condensation of chromium*, Phys. Rev. Lett. **94**, 160401 (2005).

[Grö16] M. Gröbner, P. Weinmann, F. Meinert, K. Lauber, E. Kirilov, and H.-C. Nägerl, *A new quantum gas apparatus for ultracold mixtures of K and Cs and KCs ground-state molecules*, Journal of Modern Optics **63**, 1829–1839 (2016).

[Gro17] C. Gross and I. Bloch, *Quantum simulations with ultracold atoms in optical lattices*, Science **357**, 995–1001 (2017).

[Guo16] M. Guo, B. Zhu, B. Lu, X. Ye, F. Wang, R. Vexiau, N. Bouloufa-Maafa, G. Quéméner, O. Dulieu, and D. Wang, *Creation of an ultracold gas of ground-state dipolar ^{23}Na^{87}Rb molecules*, Phys. Rev. Lett. **116**, 205303 (2016).

[Gut18] A. Guttridge, S. A. Hopkins, M. D. Frye, J. J. McFerran, J. M. Hutson, and S. L. Cornish, *Production of ultracold Cs*Yb molecules by photoassociation*, Phys. Rev. A **97**, 063414 (2018).

[Had02] Z. Hadzibabic, C. A. Stan, K. Dieckmann, S. Gupta, M. W. Zwierlein, A. Görlitz, and W. Ketterle, *Two-species mixture of quantum degenerate Bose and Fermi gases*, Phys. Rev. Lett. **88**, 160401 (2002).

[Han11] A. H. Hansen, A. Khramov, W. H. Dowd, A. O. Jamison, V. V. Ivanov, and S. Gupta, *Quantum degenerate mixture of ytterbium and lithium atoms*, Phys. Rev. A **84**, 011606 (2011).

[Har11] H. Hara, Y. Takasu, Y. Yamaoka, J. M. Doyle, and Y. Takahashi, *Quantum degenerate mixtures of alkali and alkaline-earth-like atoms*, Phys. Rev. Lett. **106**, 205304 (2011).

[Ši18] N. Šibalić and C. S. Adams, *Rydberg physics*, 2399-2891, IOP Publishing, 2018.

[Ilz18] P. Ilzhöfer, G. Durastante, A. Patscheider, A. Trautmann, M. J. Mark, and F. Ferlaino, *Two-species five-beam magneto-optical trap for erbium and dysprosium*, Phys. Rev. A **97**, 023633 (2018).

[Ilz19] P. Ilzh́ofer, M. Sohmen, G. Durastante, C. Politi, A. Trautmann, G. Morpurgo, T. Giamarchi, L. Chomaz, M. J. Mark, and F. Ferlaino, *Phase coherence in out-of-equilibrium supersolid states of ultracold dipolar atoms*, arXiv:1912.10892 (2019).

[Ilz20] P. Ilzhöfer, *Creation of dipolar quantum mixtures of erbium and dysprosium*, Ph.D. thesis, Faculty of Mathematics, Computer Science and Physics of the University of Innsbruck (2020).

[Ino98] S. Inouye, M. R. Andrews, J. Stenger, H.-J. Miesner, D. M. Stamper-Kurn, and W. Ketterle, *Observation of Feshbach resonances in a Bose-Einstein condensate*, Nature **392**, 151–154 (1998).

[Ino04] S. Inouye, J. Goldwin, M. L. Olsen, C. Ticknor, J. L. Bohn, and D. S. Jin, *Observation of heteronuclear Feshbach resonances in a mixture of bosons and fermions*, Phys. Rev. Lett. **93**, 183201 (2004).

[Jen04] A. S. Jensen, K. Riisager, D. V. Fedorov, and E. Garrido, *Structure and reactions of quantum halos*, Rev. Mod. Phys. **76**, 215–261 (2004).

[KÖ06] T. Köhler, K. Góral, and P. S. Julienne, *Production of cold molecules via magnetically tunable Feshbach resonances*, Rev. Mod. Phys. **78**, 1311–1361 (2006).

[Kai14] B. Kain and H. Y. Ling, *Polarons in a dipolar condensate*, Phys. Rev. A **89**, 023612 (2014).

[Ket99] W. Ketterle, D. S. Durfee, and D. M. Stamper-Kurn, *Making, probing and understanding Bose-Einstein condensates*, arXiv:cond-mat/9904034 (1999).

[Khl19] V. A. Khlebnikov, D. A. Pershin, V. V. Tsyganok, E. T. Davletov, I. S. Cojocaru, E. S. Fedorova, A. A. Buchachenko, and A. V. Akimov, *Random to chaotic statistic transformation in low-field Fano-Feshbach resonances of cold thulium atoms*, Phys. Rev. Lett. **123**, 213402 (2019).

[Koc08] T. Koch, T. Lahaye, J. Metz, B. Fröhlich, A. Griesmaier, and T. Pfau, *Stabilization of a purely dipolar quantum gas against collapse*, Nature Physics **4**, 218–222 (2008).

[Kos20] M. B. Kosicki, M. Borkowski, and P. S. Żuchowski, *Quantum chaos in Feshbach resonances of the ErYb system*, New Journal of Physics **22**, 023024 (2020).

[Kot11] S. Kotochigova and A. Petrov, *Anisotropy in the interaction of ultracold dysprosium*, Phys. Chem. Chem. Phys. **13**, 19165–19170 (2011).

[Kot14] S. Kotochigova, *Controlling interactions between highly magnetic atoms with Feshbach resonances*, Reports on Progress in Physics **77**, 093901 (2014).

[Kra09] S. Kraft, F. Vogt, O. Appel, F. Riehle, and U. Sterr, *Bose-Einstein condensation of alkaline earth atoms:* ^{40}*Ca*, Phys. Rev. Lett. **103**, 130401 (2009).

[Kra19] A. Kramida, Y. Ralchenko, J. Reader, et al., *NIST atomic spectra database*, National Institute of Standards and Technology, Gaithersburg (MD), 2019.

[Kri15] N. Krishnamurthy and C. K. Gupta, *Extractive metallurgy of rare earths*, CRC Press, 2015.

[Kuh16] S. Kuhr, *Quantum-gas microscopes: a new tool for cold-atom quantum simulators*, National Science Review **3**, 170–172 (2016).

[Kum17a] R. K. Kumar, P. Muruganandam, L. Tomio, and A. Gammal, *Miscibility in coupled dipolar and non-dipolar Bose–Einstein condensates*, J. Phys. Commun. **1**, 035012 (2017).

[Kum17b] R. K. Kumar, L. Tomio, B. A. Malomed, and A. Gammal, *Vortex lattices in binary Bose-Einstein condensates with dipole-dipole interactions*, Phys. Rev. A **96**, 063624 (2017).

[Lah07] T. Lahaye, T. Koch, B. Fröhlich, M. Fattori, J. Metz, A. Griesmaier, S. Giovanazzi, and T. Pfau, *Strong dipolar effects in a quantum ferrofluid*, Nature **448**, 672–675 (2007).

[Lah08] T. Lahaye, J. Metz, B. Fröhlich, T. Koch, M. Meister, A. Griesmaier, T. Pfau,

H. Saito, Y. Kawaguchi, and M. Ueda, *d-wave collapse and explosion of a dipolar Bose-Einstein condensate*, Phys. Rev. Lett. **101**, 080401 (2008).

[Lah09] T. Lahaye, C. Menotti, L. Santos, M. Lewenstein, and T. Pfau, *The physics of dipolar bosonic quantum gases*, Reports on Progress in Physics **72**, 126401 (2009).

[Law10] J. E. Lawler, J.-F. Wyart, and E. A. D. Hartog, *Atomic transition probabilities of Er i*, Journal of Physics B: Atomic, Molecular and Optical Physics **43**, 235001 (2010).

[LeB07] L. J. LeBlanc and J. H. Thywissen, *Species-specific optical lattices*, Phys. Rev. A **75**, 053612 (2007).

[Lep14] M. Lepers, J.-F. Wyart, and O. Dulieu, *Anisotropic optical trapping of ultracold erbium atoms*, Phys. Rev. A **89**, 022505 (2014).

[Ler11] A. D. Lercher, T. Takekoshi, M. Debatin, B. Schuster, R. Rameshan, F. Ferlaino, R. Grimm, and H.-C. Nägerl, *Production of a dual-species Bose-Einstein condensate of Rb and Cs atoms*, The European Physical Journal D **65**, 3–9 (2011).

[Liu18] L. R. Liu, J. D. Hood, Y. Yu, J. T. Zhang, N. R. Hutzler, T. Rosenband, and K.-K. Ni, *Building one molecule from a reservoir of two atoms*, Science **360**, 900–903 (2018).

[Lu10] M. Lu, S. H. Youn, and B. L. Lev, *Trapping ultracold dysprosium: A highly magnetic gas for dipolar physics*, Phys. Rev. Lett. **104**, 063001 (2010).

[Lu11a] M. Lu, N. Q. Burdick, S. H. Youn, and B. L. Lev, *Strongly dipolar Bose-Einstein condensate of dysprosium*, Phys. Rev. Lett. **107**, 190401 (2011).

[Lu11b] M. Lu, S. H. Youn, and B. L. Lev, *Spectroscopy of a narrow-line laser-cooling transition in atomic dysprosium*, Phys. Rev. A **83**, 012510 (2011).

[Lu12] M. Lu, N. Q. Burdick, and B. L. Lev, *Quantum degenerate dipolar Fermi gas*, Phys. Rev. Lett. **108**, 215301 (2012).

[Luc18] E. Lucioni, L. Tanzi, A. Fregosi, J. Catani, S. Gozzini, M. Inguscio, A. Fioretti, C. Gabbanini, and G. Modugno, *Dysprosium dipolar Bose-Einstein condensate with broad Feshbach resonances*, Phys. Rev. A **97**, 060701 (2018).

[Lud15] A. D. Ludlow, M. M. Boyd, J. Ye, E. Peik, and P. O. Schmidt, *Optical atomic clocks*, Rev. Mod. Phys. **87**, 637–701 (2015).

[Mai14] T. Maier, H. Kadau, M. Schmitt, A. Griesmaier, and T. Pfau, *Narrow-line magneto-optical trap for dysprosium atoms*, Opt. Lett. **39**, 3138–3141 (2014).

[Mai15a] T. Maier, I. Ferrier-Barbut, H. Kadau, M. Schmitt, M. Wenzel, C. Wink, T. Pfau, K. Jachymski, and P. S. Julienne, *Broad universal Feshbach resonances in the chaotic spectrum of dysprosium atoms*, Phys. Rev. A **92**, 060702 (2015).

[Mai15b] T. Maier, H. Kadau, M. Schmitt, M. Wenzel, I. Ferrier-Barbut, T. Pfau, A. Frisch,

S. Baier, K. Aikawa, L. Chomaz, M. J. Mark, F. Ferlaino, C. Makrides, E. Tiesinga, A. Petrov, and S. Kotochigova, *Emergence of chaotic scattering in ultracold Er and Dy*, Phys. Rev. X **5**, 041029 (2015).

[Mar78] W. C. Martin, R. Zalubas, and L. Hagan, *Atomic energy levels — the rare earth elements*, National Bureau of Standards, Washington, D.C. 20234, 1978, PB–282067.

[Mar17] A. M. Martin, N. G. Marchant, D. H. J. O'Dell, and N. G. Parker, *Vortices and vortex lattices in quantum ferrofluids*, Journal of Physics: Condensed Matter **29**, 103004 (2017).

[Mas14] P. Massignan, M. Zaccanti, and G. M. Bruun, *Polarons, dressed molecules and itinerant ferromagnetism in ultracold Fermi gases*, Reports on Progress in Physics **77**, 034401 (2014).

[McC06] J. J. McClelland and J. L. Hanssen, *Laser cooling without repumping: A magneto-optical trap for erbium atoms*, Phys. Rev. Lett. **96**, 143005 (2006).

[McC11] D. J. McCarron, H. W. Cho, D. L. Jenkin, M. P. Köppinger, and S. L. Cornish, *Dual-species Bose-Einstein condensate of* ^{87}Rb *and* ^{133}Cs, Phys. Rev. A **84**, 011603 (2011).

[McG00] I. McGill, *Rare earth elements*, American Cancer Society, 2000.

[McN06] J. M. McNamara, T. Jeltes, A. S. Tychkov, W. Hogervorst, and W. Vassen, *Degenerate Bose-Fermi mixture of metastable atoms*, Phys. Rev. Lett. **97**, 080404 (2006).

[Met99] H. J. Metcalf and P. van der Straten, *Laser cooling and trapping*, Graduate Texts in Contemporary Physics, Springer-Verlag New York, 1999.

[Mod01] G. Modugno, G. Ferrari, G. Roati, R. J. Brecha, A. Simoni, and M. Inguscio, *Bose-Einstein condensation of potassium atoms by sympathetic cooling*, Science **294**, 1320–1322 (2001).

[Mod02] G. Modugno, M. Modugno, F. Riboli, G. Roati, and M. Inguscio, *Two atomic species superfluid*, Phys. Rev. Lett. **89**, 190404 (2002).

[Mol14] P. K. Molony, P. D. Gregory, Z. Ji, B. Lu, M. P. Köppinger, C. R. Le Sueur, C. L. Blackley, J. M. Hutson, and S. L. Cornish, *Creation of ultracold* ^{87}Rb^{133}Cs *molecules in the rovibrational ground state*, Phys. Rev. Lett. **113**, 255301 (2014).

[Mos17] S. A. Moses, J. P. Covey, M. T. Miecnikowski, D. S. Jin, and J. Ye, *New frontiers for quantum gases of polar molecules*, Nature Physics **13**, 13–20 (2017).

[Mya97] C. J. Myatt, E. A. Burt, R. W. Ghrist, E. A. Cornell, and C. E. Wieman, *Production of two overlapping Bose-Einstein condensates by sympathetic cooling*, Phys. Rev. Lett. **78**, 586–589 (1997).

[Nay15] B. Naylor, A. Reigue, E. Maréchal, O. Gorceix, B. Laburthe-Tolra, and L. Vernac,

Chromium dipolar Fermi sea, Phys. Rev. A **91**, 011603 (2015).

[Ner20] E. Neri, A. Ciamei, C. Simonelli, I. Goti, M. Inguscio, A. Trenkwalder, and M. Zaccanti, *Realization of a cold mixture of fermionic chromium and lithium atoms*, Phys. Rev. A **101**, 063602 (2020).

[Ni08] K.-K. Ni, S. Ospelkaus, M. H. G. de Miranda, A. Pe'er, B. Neyenhuis, J. J. Zirbel, S. Kotochigova, P. S. Julienne, D. S. Jin, and J. Ye, *A high phase-space-density gas of polar molecules*, Science **322**, 231–235 (2008).

[Ott16] H. Ott, *Single atom detection in ultracold quantum gases: a review of current progress*, Reports on Progress in Physics **79**, 054401 (2016).

[PA18] L. A. Peña Ardila and T. Pohl, *Ground-state properties of dipolar Bose polarons*, Journal of Physics B: Atomic, Molecular and Optical Physics **52**, 015004 (2018).

[Pag15] G. Pagano, M. Mancini, G. Cappellini, L. Livi, C. Sias, J. Catani, M. Inguscio, and L. Fallani, *Strongly interacting gas of two-electron fermions at an orbital Feshbach resonance*, Phys. Rev. Lett. **115**, 265301 (2015).

[Pap06] S. B. Papp and C. E. Wieman, *Observation of heteronuclear Feshbach molecules from a* ^{85}Rb-^{87}Rb *gas*, Phys. Rev. Lett. **97**, 180404 (2006).

[Par12] J. W. Park, C.-H. Wu, I. Santiago, T. G. Tiecke, S. Will, P. Ahmadi, and M. W. Zwierlein, *Quantum degenerate Bose-Fermi mixture of chemically different atomic species with widely tunable interactions*, Phys. Rev. A **85**, 051602 (2012).

[Par15] J. W. Park, S. A. Will, and M. W. Zwierlein, *Ultracold dipolar gas of fermionic* ^{23}Na^{40}K *molecules in their absolute ground state*, Phys. Rev. Lett. **114**, 205302 (2015).

[Pas13] B. Pasquiou, A. Bayerle, S. M. Tzanova, S. Stellmer, J. Szczepkowski, M. Parigger, R. Grimm, and F. Schreck, *Quantum degenerate mixtures of strontium and rubidium atoms*, Phys. Rev. A **88**, 023601 (2013).

[PDS01] F. Pereira Dos Santos, J. Léonard, J. Wang, C. J. Barrelet, F. Perales, E. Rasel, C. S. Unnikrishnan, M. Leduc, and C. Cohen-Tannoudji, *Bose-Einstein condensation of metastable helium*, Phys. Rev. Lett. **86**, 3459–3462 (2001).

[Pet08] C. J. Pethick and H. Smith, *Bose-Einstein condensation in dilute gases*, 2 ed., Cambridge University Press, 2008.

[Pet12] A. Petrov, E. Tiesinga, and S. Kotochigova, *Anisotropy-induced Feshbach resonances in a quantum dipolar gas of highly magnetic atoms*, Phys. Rev. Lett. **109**, 103002 (2012).

[Pez18] L. Pezzè, A. Smerzi, M. K. Oberthaler, R. Schmied, and P. Treutlein, *Quantum metrology with nonclassical states of atomic ensembles*, Rev. Mod. Phys. **90**, 035005 (2018).

[Pil09] K. Pilch, A. D. Lange, A. Prantner, G. Kerner, F. Ferlaino, H.-C. Nägerl, and

R. Grimm, *Observation of interspecies Feshbach resonances in an ultracold Rb-Cs mixture*, Phys. Rev. A **79**, 042718 (2009).

[Pit16] L. Pitaevskii and S. Stringari, *Bose-Einstein condensation and superfluidity*, International Series of Monographs on Physics, Oxford University Press, Oxford, 2016 (eng).

[Pla06] M. Planck, *Vorlesungen über die theorie der wärmestrahlung*, Verlag von J. A. Barth, Leipzig, 1906.

[Rav18a] C. Ravensbergen, V. Corre, E. Soave, M. Kreyer, S. Tzanova, E. Kirilov, and R. Grimm, *Accurate determination of the dynamical polarizability of dysprosium*, Phys. Rev. Lett. **120**, 223001 (2018).

[Rav18b] C. Ravensbergen, V. Corre, E. Soave, M. Kreyer, E. Kirilov, and R. Grimm, *Production of a degenerate Fermi-Fermi mixture of dysprosium and potassium atoms*, Phys. Rev. A **98**, 063624 (2018).

[Rav20] C. Ravensbergen, E. Soave, V. Corre, M. Kreyer, B. Huang, E. Kirilov, and R. Grimm, *Resonantly interacting Fermi-Fermi mixture of* ^{161}Dy *and* ^{40}K, Phys. Rev. Lett. **124**, 203402 (2020).

[Rep13] M. Repp, R. Pires, J. Ulmanis, R. Heck, E. D. Kuhnle, M. Weidemüller, and E. Tiemann, *Observation of interspecies* ^{6}Li-^{133}Cs *Feshbach resonances*, Phys. Rev. A **87**, 010701 (2013).

[Rey86] M. W. Reynolds, I. Shinkoda, R. W. Cline, and W. N. Hardy, *Observation of inverse predissociation of spin-polarized atomic hydrogen at low temperatures*, Phys. Rev. B **34**, 4912–4915 (1986).

[Ric33] O. K. Rice, *Predissociation and the crossing of molecular potential energy curves*, The Journal of Chemical Physics **1**, 375–389 (1933).

[Rii94] K. Riisager, *Nuclear halo states*, Rev. Mod. Phys. **66**, 1105–1116 (1994).

[Roa02] G. Roati, F. Riboli, G. Modugno, and M. Inguscio, *Fermi-Bose quantum degenerate* ^{40}K-^{87}Rb *mixture with attractive interaction*, Phys. Rev. Lett. **89**, 150403 (2002).

[Rob00] J. L. Roberts, N. R. Claussen, S. L. Cornish, and C. E. Wieman, *Magnetic field dependence of ultracold inelastic collisions near a Feshbach resonance*, Phys. Rev. Lett. **85**, 728–731 (2000).

[Rob01] A. Robert, O. Sirjean, A. Browaeys, J. Poupard, S. Nowak, D. Boiron, C. I. Westbrook, and A. Aspect, *A Bose-Einstein condensate of metastable atoms*, Science **292**, 461–464 (2001).

[Ron06] S. Ronen, D. C. E. Bortolotti, D. Blume, and J. L. Bohn, *Dipolar Bose-Einstein condensates with dipole-dependent scattering length*, Phys. Rev. A **74**, 033611 (2006).

[Rum20] J. Rumble, *CRC handbook of chemistry and physics*, CRC Press, 2020.

[Rva17] T. M. Rvachov, H. Son, A. T. Sommer, S. Ebadi, J. J. Park, M. W. Zwierlein, W. Ketterle, and A. O. Jamison, *Long-lived ultracold molecules with electric and magnetic dipole moments*, Phys. Rev. Lett. **119**, 143001 (2017).

[Saf10] M. Saffman, T. G. Walker, and K. Mølmer, *Quantum information with Rydberg atoms*, Rev. Mod. Phys. **82**, 2313–2363 (2010).

[Sch01] F. Schreck, L. Khaykovich, K. L. Corwin, G. Ferrari, T. Bourdel, J. Cubizolles, and C. Salomon, *Quasipure Bose-Einstein condensate immersed in a Fermi sea*, Phys. Rev. Lett. **87**, 080403 (2001).

[Sch18] T. A. Schulze, T. Hartmann, K. K. Voges, M. W. Gempel, E. Tiemann, A. Zenesini, and S. Ospelkaus, *Feshbach spectroscopy and dual-species Bose-Einstein condensation of* ^{23}Na-^{39}K *mixtures*, Phys. Rev. A **97**, 023623 (2018).

[See18] F. Seeßelberg, N. Buchheim, Z.-K. Lu, T. Schneider, X.-Y. Luo, E. Tiemann, I. Bloch, and C. Gohle, *Modeling the adiabatic creation of ultracold polar* ^{23}Na^{40}K *molecules*, Phys. Rev. A **97**, 013405 (2018).

[Set00] J. Y. Seto, R. J. Le Roy, J. Vergès, and C. Amiot, *Direct potential fit analysis of the* $X^1\sigma_g^+$ *state of* Rb_2*: Nothing else will do!*, The Journal of Chemical Physics **113**, 3067–3076 (2000).

[Sil05] C. Silber, S. Günther, C. Marzok, B. Deh, P. W. Courteille, and C. Zimmermann, *Quantum-degenerate mixture of fermionic lithium and bosonic rubidium gases*, Phys. Rev. Lett. **95**, 170408 (2005).

[Smi20] J. C. Smith, D. Baillie, and P. B. Blakie, *Quantum droplet states of a binary magnetic gas*, arXiv:2007.00366 (2020).

[Spe75] D. Spence and T. Noguchi, *Feshbach resonances associated with Rydberg states of the hydrogen halides*, The Journal of Chemical Physics **63**, 505–514 (1975).

[Spi10] F. M. Spiegelhalder, A. Trenkwalder, D. Naik, G. Kerner, E. Wille, G. Hendl, F. Schreck, and R. Grimm, *All-optical production of a degenerate mixture of* ^{6}Li *and* ^{40}K *and creation of heteronuclear molecules*, Phys. Rev. A **81**, 043637 (2010).

[Sta04] C. A. Stan, M. W. Zwierlein, C. H. Schunck, S. M. F. Raupach, and W. Ketterle, *Observation of Feshbach resonances between two different atomic species*, Phys. Rev. Lett. **93**, 143001 (2004).

[Ste98] J. Stenger, S. Inouye, D. M. Stamper-Kurn, H.-J. Miesner, A. P. Chikkatur, and W. Ketterle, *Spin domains in ground-state Bose-Einstein condensates*, Nature **396**, 345–348 (1998).

[Ste09] S. Stellmer, M. K. Tey, B. Huang, R. Grimm, and F. Schreck, *Bose-Einstein condensation of strontium*, Phys. Rev. Lett. **103**, 200401 (2009).

[Stu07] J. Stuhler, A. Griesmaier, T. Koch, M. Fattori, and T. Pfau, *Magnetostriction in*

a degenerate quantum gas, Journal of Magnetism and Magnetic Materials **316**, 429 – 432 (2007), Proceedings of the Joint European Magnetic Symposia.

[Tö14] P. Törmä and K. Sengstock, *Quantum gas experiments*, Imperial College Press, 57 Shelton Street, Covent Garden, London, 2014.

[Tag08] M. Taglieber, A.-C. Voigt, T. Aoki, T. W. Hänsch, and K. Dieckmann, *Quantum degenerate two-species Fermi-Fermi mixture coexisting with a Bose-Einstein condensate*, Phys. Rev. Lett. **100**, 010401 (2008).

[Tak03] Y. Takasu, K. Maki, K. Komori, T. Takano, K. Honda, M. Kumakura, T. Yabuzaki, and Y. Takahashi, *Spin-singlet Bose-Einstein condensation of two-electron atoms*, Phys. Rev. Lett. **91**, 040404 (2003).

[Tak14] T. Takekoshi, L. Reichsöllner, A. Schindewolf, J. M. Hutson, C. R. Le Sueur, O. Dulieu, F. Ferlaino, R. Grimm, and H.-C. Nägerl, *Ultracold dense samples of dipolar RbCs molecules in the rovibrational and hyperfine ground state*, Phys. Rev. Lett. **113**, 205301 (2014).

[Tan18] L. Tanzi, C. R. Cabrera, J. Sanz, P. Cheiney, M. Tomza, and L. Tarruell, *Feshbach resonances in potassium Bose-Bose mixtures*, Phys. Rev. A **98**, 062712 (2018).

[Tan19] L. Tanzi, E. Lucioni, F. Famà, J. Catani, A. Fioretti, C. Gabbanini, R. N. Bisset, L. Santos, and G. Modugno, *Observation of a dipolar quantum gas with metastable supersolid properties*, Phys. Rev. Lett. **122**, 130405 (2019).

[Tey10] M. K. Tey, S. Stellmer, R. Grimm, and F. Schreck, *Double-degenerate Bose-Fermi mixture of strontium*, Phys. Rev. A **82**, 011608 (2010).

[Tie20] E. Tiemann, P. Gersema, K. K. Voges, T. Hartmann, A. Zenesini, and S. Ospelkaus, *Beyond Born-Oppenheimer approximation in ultracold atomic collisions*, Phys. Rev. Research **2**, 013366 (2020).

[Tim99] E. Timmermans, P. Tommasini, M. Hussein, and A. Kerman, *Feshbach resonances in atomic Bose–Einstein condensates*, Physics Reports **315**, 199 – 230 (1999).

[Tom19] M. Tomza, K. Jachymski, R. Gerritsma, A. Negretti, T. Calarco, Z. Idziaszek, and P. S. Julienne, *Cold hybrid ion-atom systems*, Rev. Mod. Phys. **91**, 035001 (2019).

[Tra18] A. Trautmann, P. Ilzhöfer, G. Durastante, C. Politi, M. Sohmen, M. J. Mark, and F. Ferlaino, *Dipolar Quantum Mixtures of Erbium and Dysprosium Atoms*, Phys. Rev. Lett. **121**, 213601 (2018).

[Tru01] A. G. Truscott, K. E. Strecker, W. I. McAlexander, G. B. Partridge, and R. G. Hulet, *Observation of Fermi pressure in a gas of trapped atoms*, Science **291**, 2570–2572 (2001).

[Vai15] V. D. Vaidya, J. Tiamsuphat, S. L. Rolston, and J. V. Porto, *Degenerate Bose-Fermi mixtures of rubidium and ytterbium*, Phys. Rev. A **92**, 043604 (2015).

[Vas12] W. Vassen, C. Cohen-Tannoudji, M. Leduc, D. Boiron, C. I. Westbrook, A. Tr-

uscott, K. Baldwin, G. Birkl, P. Cancio, and M. Trippenbach, *Cold and trapped metastable noble gases*, Rev. Mod. Phys. **84**, 175–210 (2012).

[vK02] E. G. M. van Kempen, S. J. J. M. F. Kokkelmans, D. J. Heinzen, and B. J. Verhaar, *Interisotope determination of ultracold rubidium interactions from three high-precision experiments*, Phys. Rev. Lett. **88**, 093201 (2002).

[vK04] E. G. M. van Kempen, B. Marcelis, and S. J. J. M. F. Kokkelmans, *Formation of fermionic molecules via interisotope Feshbach resonances*, Phys. Rev. A **70**, 050701 (2004).

[Vog20] K. K. Voges, P. Gersema, M. Meyer zum Alten Borgloh, T. A. Schulze, T. Hartmann, A. Zenesini, and S. Ospelkaus, *Ultracold gas of bosonic ^{23}Na^{39}K ground-state molecules*, Phys. Rev. Lett. **125**, 083401 (2020).

[VV04] G. F. Vander Voort, *Metallography and microstructures*, ASM handbook, vol. 9, ASM International, 2004.

[Wac15] L. Wacker, N. B. Jørgensen, D. Birkmose, R. Horchani, W. Ertmer, C. Klempt, N. Winter, J. Sherson, and J. J. Arlt, *Tunable dual-species Bose-Einstein condensates of ^{39}K and ^{87}Rb*, Phys. Rev. A **92**, 053602 (2015).

[Wan13] F. Wang, D. Xiong, X. Li, D. Wang, and E. Tiemann, *Observation of Feshbach resonances between ultracold Na and Rb atoms*, Phys. Rev. A **87**, 050702 (2013).

[Wan15] F. Wang, X. Li, D. Xiong, and D. Wang, *A double species ^{23}Na and ^{87}Rb Bose-Einstein condensate with tunable miscibility via an interspecies Feshbach resonance*, Journal of Physics B: Atomic, Molecular and Optical Physics **49**, 015302 (2015).

[Web03] T. Weber, J. Herbig, M. Mark, H.-C. Nägerl, and R. Grimm, *Bose-Einstein condensation of cesium*, Science **299**, 232–235 (2003).

[Wei09] H. A. Weidenmüller and G. E. Mitchell, *Random matrices and chaos in nuclear physics: Nuclear structure*, Rev. Mod. Phys. **81**, 539–589 (2009).

[Wen18] M. Wenzel, T. Pfau, and I. Ferrier-Barbut, *A fermionic impurity in a dipolar quantum droplet*, Physica Scripta **93**, 104004 (2018).

[Wer05] J. Werner, A. Griesmaier, S. Hensler, J. Stuhler, T. Pfau, A. Simoni, and E. Tiesinga, *Observation of Feshbach resonances in an ultracold gas of ^{52}Cr*, Phys. Rev. Lett. **94**, 183201 (2005).

[Wil08] E. Wille, F. M. Spiegelhalder, G. Kerner, D. Naik, A. Trenkwalder, G. Hendl, F. Schreck, R. Grimm, T. G. Tiecke, J. T. M. Walraven, S. J. J. M. F. Kokkelmans, E. Tiesinga, and P. S. Julienne, *Exploring an ultracold Fermi-Fermi mixture: Interspecies Feshbach resonances and scattering properties of ^{6}Li and ^{40}K*, Phys. Rev. Lett. **100**, 053201 (2008).

[Wil12] R. M. Wilson, C. Ticknor, J. L. Bohn, and E. Timmermans, *Roton immiscibility in a two-component dipolar Bose gas*, Phys. Rev. A **86**, 033606 (2012).

[Wu11] C.-H. Wu, I. Santiago, J. W. Park, P. Ahmadi, and M. W. Zwierlein, *Strongly interacting isotopic Bose-Fermi mixture immersed in a Fermi sea*, Phys. Rev. A **84**, 011601 (2011).

[Wu17] Y.-P. Wu, X.-C. Yao, H.-Z. Chen, X.-P. Liu, X.-Q. Wang, Y.-A. Chen, and J.-W. Pan, *A quantum degenerate Bose-Fermi mixture of ^{41}K and ^{6}Li*, Journal of Physics B: Atomic, Molecular and Optical Physics **50**, 094001 (2017).

[Xu17] F. Xu, J. Huang, and Q. Liu, *A hybrid two-component Bose–Einstein condensate interferometer for measuring magnetic field gradients*, Physics Letters A **381**, 865 – 868 (2017).

[Yan19] B. C. Yang, M. D. Frye, A. Guttridge, J. Aldegunde, P. S. Żuchowski, S. L. Cornish, and J. M. Hutson, *Magnetic Feshbach resonances in ultracold collisions between Cs and Yb atoms*, Phys. Rev. A **100**, 022704 (2019).

[Ye20] Z.-X. Ye, L.-Y. Xie, Z. Guo, X.-B. Ma, G.-R. Wang, L. You, and M. K. Tey, *Double degenerate Bose-Fermi mixture of strontium and lithium*, arXiv:2006.15654 (2020).

[Zha05] J. Zhang, E. G. M. van Kempen, T. Bourdel, L. Khaykovich, J. Cubizolles, F. Chevy, M. Teichmann, L. Tarruell, S. J. J. M. F. Kokkelman, and C. Salomon, *Expansion of a lithium gas in the BEC-BCS crossover*, AIP Conference Proceedings **770**, 228–237 (2005).

[Zha15] X.-F. Zhang, W. Han, L. Wen, P. Zhang, R.-F. Dong, H. Chang, and S.-G. Zhang, *Two-component dipolar Bose-Einstein condensate in concentrically coupled annular traps*, Scientific Reports **5**, 8684 (2015).

[ZK18] K. Zaremba-Kopczyk, P. S. Żuchowski, and M. Tomza, *Magnetically tunable Feshbach resonances in ultracold gases of europium atoms and mixtures of europium and alkali-metal atoms*, Phys. Rev. A **98**, 032704 (2018).

Acknowledgments

Here I am at the end of this long process of personal growth that lasted about five years called PhD. In these five years I got to know many people and I had the chance to meet even more of them. I had to face uplifting and upsetting moments, exciting hours, and frustrating situations which are intrinsic in experimental physics research done at its top level. Finding the right words to describe all this is quite challenging for me, nevertheless I will try my best.

The first thanks go to my supervisor *Francesca Ferlaino*. She gave me the possibility of joining a group competing at the leading edge of the investigation of nature and she trusted me for the development of an impressive experiment. In less than five years we saw this experiment growing with us, building something from scratch. I really pushed myself into this project and I am personally proud of what we achieved. I hope this will be the case for all my present and future colleagues working in this laboratory. Even brighter prospects will come, I am sure.

Another big thanks go to the people who assisted me with such hard work, which the PhD is. My team mates (*M.J.M.*, *A.T.*, *P.I.*, *M.S.*, *C.P.*, *M.N.*) and my old and new colleagues from the Ferlaino's group firstly, but also the whole ultracold group of the University of Innsbruck and the people participating in the DK-ALM. We shared a big part of our life, supporting and learning from each other. A special thanks goes to all the administration and mechanical and electronics workshop personnel of the University and IQOQI because all these big machines keep running just because of them. I wish the best to all of you.

There are tens of people I would like to acknowledge here, from my grandparents to my aunts and uncles, from university friends to schoolmates to my tireless holiday buddies. I tend to forget things but, believe me, I bring all of you in my heart every day. These words are for everyone of you who gave me a single smile over all these years.

During my PhD I had the chance to travel a lot, spending a significant amount of time away from the people I love. I am really grateful for this opportunity. Nonetheless, in a world which is more connected every day and in which people are constantly aware of each other, I understood the meaning of loneliness. During one of these journeys I lost a person without having the possibility to say goodbye. This achievement is also for you *Grandma*.

Love is what makes humanity alive. It can throw us from the brightest stars in the sky down to the darkest voids of our soul. Sometimes love paints the world with the most vivid colors and sometimes it drains all the energy we have, harming us and hurting our hearts. There is a person that I want to thank for all the good things she did in my life. I hope we can forgive each other for our mistakes.

T.K. entered my life in a way that I will never be able to forget. She put together the lost

pieces of myself, giving me renewed faith for what I believe in. Love is what makes us alive and, after so many years, I finally am. She taught me that our dreams are more important than anything and to follow them till they come true. Loving someone every single day poses its challenges but there is nobody I would rather face them with. Wherever this will bring us, being together is the only thing which matters. With you I am genuinely happy cause I understood the meaning of true love. You deserve the best that this life can donate. I love you so. Thank you!

Generally, I would not be the person I actually am without my friends from *Novaglie*. We are together since we came to life about 25 to 30 years ago. Ours is more than a simple friendship, we are the family we chose to have. We shared great moments and fights, and even though life is bringing us a bit further away from each other, I wish our friendship could last forever. Without you I am simply lost. I want to sit with all of you in 50 years at the bench of our hometown and laugh about every little thing which happened in our lives. To you I owe one of the greatest and most sincere thanks.

Lastly, all that I am goes back to the people closest to my heart. My family. My dad *S.D.*, my mum *P.P.*, and my sister *E.D.*. I think there exist no words able to describe what I have inside. Maybe for this reason I find sometimes hard to express my feelings and sometimes I forget to tell you how much I love you. Since I came to Innsbruck, I realized what it actually means living. I understood how you put myself and my happiness — and my sister's — in front of everything you might have wanted from your life. You pushed me to follow my own path without imposing anything on me. You believed in me in the same moment I opened my eyes for the first time. You raised and protected us despite all the efforts it required. Sometimes I forget to tell you that I love you all. You are the best family I could have dreamed for. You are the best father, the best mother, and the best sister. I am proud of you and I wish I could make you proud of me as well.

All this is for you family. You gave me more love than I could ever give you back.

Innsbruck, 31 August 2020 G. D.

Ringraziamenti

Eccomi alla fine di questo lungo processo di crescita personale durato cinque anni e chiamato PhD. In questi cinque anni ho conosciuto molte persone ed ho avuto la possibilità di incontrarne ancora di più. Ho dovuto affrontare sia momenti edificanti che di sconforto, ore eccitanti ed anche situazioni frustranti intrinseche nella ricerca in fisica sperimentale compiuta al suo massimo livello. Trovare le giuste parole per descrivere tutto ciò è compito arduo per me; ciononostante farò del mio meglio.

Il primo grazie va alla mia supervisor *Francesca Ferlaino*. Mi ha dato la possibilità di unirmi ad un gruppo all'avanguardia nello studio della natura, dandomi fiducia nello sviluppo di un esperimento così ambizioso. In meno di cinque anni abbiamo visto questo esperimento crescere con noi, costruendo qualcosa dal niente. Personalmente ho dato molto di me in questo progetto e sono fiero di ciò che abbiamo raggiunto. Spero che lo stesso possa valere anche per i miei colleghi presenti e futuri in questo laboratorio. Un avvenire ancora migliore è alle porte, ne sono certo.

Un altro grande grazie va a tutte le persone che mi hanno assistito in questo duro lavoro che è il PhD. I miei compagni di team (*M.J.M.*, *A.T.*, *P.I.*, *M.S.*, *C.P.*, *M.N.*) ed i miei vecchi e nuovi colleghi del gruppo della Francesca, così come l'intero ultracold group dell'università di Innsbruck e le persone partecipanti al DK-ALM. Abbiamo condiviso una parte importante della nostra vita supportandoci a vicenda ed imparando gli uni dagli altri. Un grazie speciale è dedicato a tutto il personale dell'amministrazione e dell'officina meccanica ed elettronica dell'università e dell'IQOQI poiché questa grande macchina continua a girare solo per merito loro. Auguro il meglio a tutti voi.

Ci sono decine di persone che vorrei ringraziare in queste righe, dai miei nonni alle mie zie e zii, dai soci dell'università ai compagni di scuola agli instancabili amici delle mie vacanze. Tendo ad essere smemorato ma fidatevi, vi porto tutti nel mio cuore ogni giorno. Queste parole sono per tutti voi che mi avete concesso anche solo un sorriso durante tutti questi anni.

Durante il mio dottorato ho avuto la possibilità di viaggiare molto, trascorrendo un notevole lasso di tempo lontano dalle persone che amo. Sono veramente grato per questa opportunità. Tuttavia, in un mondo ogni giorno sempre più connesso nel quale le persone sono costantemente al corrente di tutto, ho capito il significato del termine solitudine. Durante uno di questi viaggi ho perduto una persona senza la possibilità di dirle addio. Questa conquista è anche per te *nonna*.

L'amore è ciò che rende vivo l'essere umano. Ci può sbattere dalle stelle più luminose del cielo giù fino al nulla più buio della nostra anima. Talvolta l'amore dipinge il mondo con i colori più intensi e talvolta ci prosciuga di tutte le nostre energie facendoci del male e

ferendo i nostri cuori. C'è una persona a cui vorrei dire grazie per tutte le cose belle che ha portato nella mia vita. Spero di poterci perdonare per i nostri errori.

T.K. è entrata nella mia vita in un modo che non sarò mai capace di dimenticare, mettendo insieme i pezzi mancanti di me stesso e dandomi rinnovata fede per ciò in cui credo. L'amore ci rende vivi e, dopo tanti anni, finalmente lo sono anche io. Mi ha insegnato che i nostri sogni sono più importanti di ogni altra cosa e d'inseguirli finché non si realizzano. Amare qualcuno tutti i giorni pone costantemente delle sfide ma non c'è nessun altro con cui le affronterei. Ovunque questo ci porterà, essere insieme è l'unica cosa che conta. Con te sono sinceramente felice giacché comprendo finalmente il significato di amare. Ti meriti il meglio che questa vita ha da offrire. Ti amo così. Grazie!

In generale non sarei la persona che sono senza i miei amici di *Novaglie*. Ci conosciamo da quando siamo nati circa 25-30 anni fa. La nostra e più che una semplice amicizia. Noi siamo la famiglia che abbiamo scelto di avere. Abbiamo condiviso bei momenti e tante liti e, anche se la vita ci sta allontanando un poco gli uni dagli altri, spero che tutto questo possa durare per sempre. Senza di voi sono semplicemente perso. Voglio potermi sedere con tutti voi tra 50 anni alle panchine del nostro paese a ridere insieme per ogni piccola cosa accaduta nelle nostre vite. A voi devo uno tra i più grandi e autentici grazie.

Infine, tutto quello che sono lo devo alle persone più care del mio cuore. La mia famiglia. Mio papà *S.D.*, mia mamma *P.P.* e mia sorella *E.D.*. Non credo esistano parole capaci di descrivere ciò che provo dentro di me. Forse è per questa ragione che certe volte mi viene difficile esprimere i miei sentimenti e spesso mi dimentichi di dirvi quanto vi voglia bene. Da quando sono ad Innsbruck ho capito cosa significhi vivere. Ho capito come voi abbiate messo me e la mia felicità (e quella di mia sorella) prima di ogni cosa che possiate mai aver voluto dalla vostra vita. Mi avere spinto a seguire il mio percorso senza mai impormi niente. Avete creduto in me nel momento stesso in cui aprii i miei occhi per la prima volta. Ci avete cresciuto e protetto nonostante tutto l'impegno e la dedizione richiesti. Certe volte mi dimentico di dirvi che vi amo. Siete la famiglia migliore che potessi mai sognare di avere. Siete il miglior papà, la migliore mamma e la miglior sorella. Sono fiero di voi e spero di potervi rendere fieri di me.

Tutto questo è per voi famiglia. Mi avete donato più amore di quanto io potrò mai ricambiarvi.

Innsbruck, 31 August 2020 G. D.